Development of photoemission spectroscopy techniques for the determination of the electronic and geometric structure of organic adsorbates

Dissertation
zur Erlangung des naturwissenschaftlichen Doktorgrades der
Julius-Maximilians-Universität Würzburg

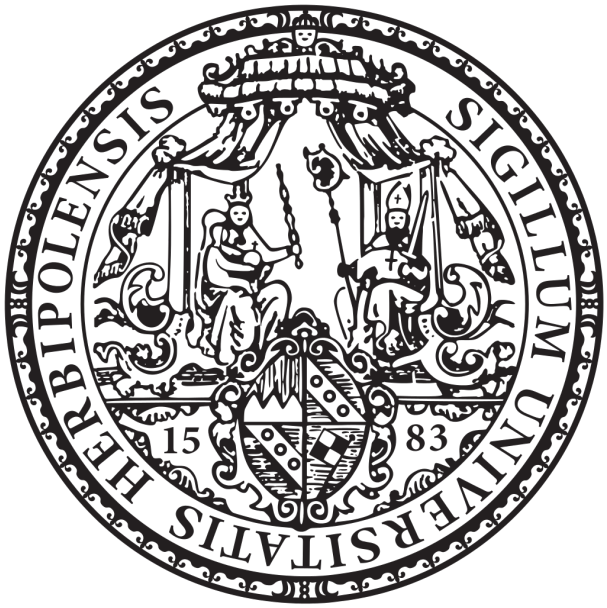

vorgelegt von

Christian Thomas Peter Metzger
aus Karlstadt

Würzburg 2020

Eingereicht am: 30.09.2020
bei der Fakultät für Physik und Astronomie

1. Gutachter: Priv. Doz. Dr. Achim Schöll
2. Gutachter: Prof. Dr. Bert Hecht
der Dissertation

Vorsitzende(r): Prof. Dr. Jens Pflaum
1. Gutachter: Priv. Doz. Dr. Achim Schöll
2. Gutachter: Prof. Dr. Bert Hecht
3. Prüfer: Prof. Dr. Haye Hinrichsen
im Promotionskolloquium

Tag des Promotionskolloquiums: 29.01.2021

Doktorurkunde ausgehändigt am:

Abstract

The projects presented in this thesis cover the examination of the electronic and structural properties of organic thin films at noble metal-organic interfaces. Angle-resolved photoemission spectroscopy is used as the primary investigative tool due to the connection of the emitted photoelectrons to the electronic structure of the sample. The surveyed materials are of relevance for fundamental research and practical applications on their own, but also serve as archetypes for the photoemission techniques presented throughout the four main chapters of this thesis. The techniques are therefore outlined with their adaptation to other systems in mind and a special focus on the proper description of the final state.

The most basic description of the final state that is still adequate for the evaluation of photoemission data is a plane wave. Its simplicity enables a relatively intuitive interpretation of photoemission data, since the initial and final state are related to one another by a Fourier transform and a geometric factor in this approximation. Moreover, the initial states of some systems can be reconstructed in three dimensions by combining photoemission measurements at various excitation energies. This reconstruction can even be carried out solely based on experimental data by using suitable iterative algorithms.

Since the approximation of the final state in the photoemission process by a plane wave is not valid in all instances, knowledge on the limitations of its applicability is indispensable. This can be gained by a comparison to experimental data as well as calculations with a more detailed description of the photoemission final state. One possible appraoch is based on independently emitting atoms where the coherent superposition of partial, atomic final states produces the total final state. This approach can also be used for more intricate studies on organic thin films. To this end, experimental data can be related to theoretical calculations to gain extensive insights into the structural and electronic properties of molecules in organic thin films.

Zusammenfassung

Die in dieser Arbeit vorgestellten Projekte behandeln die Untersuchung der elektronischen und strukturellen Eigenschaften organischer Dünnschichtfilme an Grenzflächen zwischen Edelmetallen und organischen Materialien. Als maßgebliche Messmethode wird die winkelaufgelöste Photoelektronenspektroskopie aufgrund der Verbindung der emittierten Photoelektronen mit der elektronischen Struktur der untersuchten Probe angewandt. Die verwendeten Materialien sind sowohl in der Grundlagenforschung als auch für praktische Anwendungen relevant, und dienen gleichzeitig auch als Beispiele für die Photoemissionstechniken, die in den vier Hauptkapiteln der Arbeit präsentiert werden. Diese Techniken werden daher auch bezüglich ihrer Übertragbarkeit auf andere Systeme dargestellt, wobei besonders auf die korrekte Beschreibung des Endzustands in der Photoemission eingegangen wird.

Die simpelste Beschreibung des Endzustands, die für die Auswertung von Photoemissionsdaten noch sinnvoll verwendet werden kann, stellt eine ebene Welle dar. Ihre Einfachheit ermöglicht eine relativ intuitive Interpretation von Photoemissionsdaten, da Anfangs- und Endzustand in dieser Näherung lediglich durch eine Fourier-Transformation und einen geometrischen Faktor verknüpft sind. Kombiniert man die Photoemissionsmessungen bei unterschiedlichen Anregungsenergien, lassen sich zusätzlich die Anfangszustände bestimmter Systeme in guter Näherung dreidimensional rekonstruieren. Mit Hilfe geeigneter iterativer Algorithmen ist diese Rekonstruktion darüber hinaus mit ausschließlich experimentellen Daten realisierbar.

Da die Näherung des Endzustands mit einer ebenen Welle nur unter bestimmten Bedingungen ausreichend präzise das reale System widerspiegelt, ist die Kenntnis über die Grenzen ihrer Anwendbarkeit von Bedeutung. Dies kann über den Vergleich mit experimentellen Daten sowie Rechnungen mit detailierteren Beschreibungen des Endzustands in der Photoemission geschehen. Ein möglicher Ansatz basiert auf unabhängig voneinander emittierenden Atomen, deren kohärent überlagerte, partielle Endzustände den gesamten Endzustand formen. Dieser Ansatz kann des Weiteren für komplexere Untersuchungen an organischen Dünnschichten verwendet werden. So können über den Vergleich von experi-

mentellen Messung mit theoretischen Rechnungen umfangreiche Einblicke auf die strukturellen und elektronischen Eigenschaften der Moleküle in organischen Dünnschichten gewonnen werden.

Contents

1 Introduction

In the last two decades, organic electronics have increasingly made their way into applications traditionally dominated by inorganic compounds [1]. With the advent of organic LEDs in TVs and smartphones, they nowadays also make up objects found in every-day life [2–4]. There are several causes for the expanded use of organic (opto-)electronic devices: one feature that makes them attractive in places where conventional semiconductors struggle is their flexibility. Organic materials can be bent in almost any shape, in stark contrast to their rigid inorganic equivalents. Due to this reason alone they already fill some niches like curved and bendable electronic displays, as well as applications on uneven surfaces. Solar cells based on organic materials are also narrowing the efficiency gap to their inorganic counterparts [5, 6]. Another economic benefit is the low cost of manufacture, since many devices can simply be printed on top of a suitable substrate [2]. The light weight of carbon and the majority of elements found in organic molecules promotes their use in portable equipment. Meanwhile, the field of organic chemistry provides an ever growing number of organic substances adding to the over 20 million ones that are already known at the time of this writing [7].

Due to the vast amount of available organic compounds and combinations thereof trying to improve specific material attributes in a trial-and-error approach is a futile effort. Fortunately there is an alternative: fundamental material research can provide an understanding of the physical processes governing the (opto-)electronic properties that can be adapted to augment existing devices and to develop entirely new applications. This type of research is usually not performed on actual devices or even prototypes, but on deceptively basic archetype samples. Instead of circuits and mechanisms present in a functioning device, their complexity might be reduced to the interface between two compounds or even to just a single bulk material. This deliberate limitation in complexity makes it easier to precisely pinpoint the material properties and their origin. The second pillar next to experimental studies are theoretical frameworks that describe the behavior of the involved particles. The ultimate goal is to relate the emergence of specific material features to properties of fundamental matter by altering the individual parameters underlying the theory. This type of research then provides the foundation to select the most suitable needles in the haystack of materials for a desired application.

The studies presented in this thesis address both the experimental and the theoretical

component of this endeavor. The common idea of the projects is to gain insight into a sample by exploiting the connection of electrons emitted under illumination with vacuum ultraviolet light with its material properties. The experimentally gathered information is contrasted to simulations of the same process that are explicitly implemented for this purpose.

The thesis will continue with the theoretical background of angle-resolved photoemission spectroscopy in chapter 2. This experimental method is the principle analytical tool of the thesis and forms the basis for more specific photoemission techniques for the extraction of structural and electronic information. The chapter also contains an overview of the suitable descriptions of the wave function of the electrons participating in the photoemission process.

In chapter 3 experimental concepts pertaining the measurements are laid out. This includes the auxiliary technique of low-energy electron diffraction that is used to obtain structural information about the periodic lattice of the substrate and molecular layer. The preparation procedures of the substrate and the molecular thin film under ultra-high vacuum conditions is elaborated. Lastly, the momentum microscope that is used to gather the photoemission data and the treatment of the instrument-related experimental artifacts is also presented here.

After the theoretical and experimental foundations are set, the first study in chapter 4 will showcase the capabilities and shortcomings of approximating the photoemission final state with a simple plane wave. An evaporated monolayer of the molecule pentacene on top of an Ag(110) substrate is surveyed at different photon energies in a process that has been labeled *orbital tomography* [8, 9]. Fluctuations in the measured photoemission intensity recorded at different photon energies point towards a deviation from a plane wave final state in the experiment. Nevertheless, the phase information is recovered from the experimental data and the highest occupied molecular orbital is successfully reconstructed in real space.

In chapter 5 we will go beyond the plane wave final state and take a look at the photoemission simulation tool that has been developed to this end for this thesis. After a brief explanation of the handling of the program, simulations with the photoemission tool will be compared to experimental data on increasingly complex model metal-organic systems that are assessed in concise photoelectron spectroscopy studies.

Chapter 6 deals with the layer-by-layer structure determination of molecules in thin films. The technique is showcased on the example of a pentacene bilayer grown on an Ag(110) substrate. The discussion of the calculations in this chapter will be particularly thorough to clarify how the method can be transferred to other systems. The results of this study are summarized and published in *Physical Review B* [10].

The last main topic of the thesis, presented in chapter 7, concerns the suitability of the plane wave approximation for the final state for truly three-dimensional molecules, a class of molecules where it was previously thought to be inapplicable [11]. The archetype system of an evaporated monolayer of C_{60} on an Ag(110) substrate is characterized electronically and structurally before comparing the experiment to simulations with a plane wave final state. Contrary to the expectations of the community, these simulations compare favorably to simulations with the more complex final state encoded in the photoemission tool and the experiment. A synopsis of this work has been peer-reviewed and published in *Physical Review B* [12].

The results of the main chapters are summarized in chapter 8 and possible future projects connected to the ones presented in this thesis are proposed. These include advancing the discussed techniques into the time-domain via pump-probe schemes to unravel dynamic, time-dependent phenomena. Another promising field is the modification of surface states of topological materials with organic thin films adsorbed at the surface. This as of yet barely explored topic might uncover novel electronic features at the substrate-organic interface and will enable the tailoring of the electronic states for specific material properties.

2 Photoemission spectroscopy

In the following chapter the theoretical background behind the main investigative tool of this thesis is presented.

2.1 Basic principles

The backbone of most of the work in this thesis is the so-called *photoelectric effect*. The phenomenom was discovered towards the end of the 19th century, when H. Hertz noticed a peculiar behavior during his experiments with ultraviolet light [13] which set off further studies within the scientific community [14, 15]. They were able to show that if a metal is illuminated with light below a maximal wave length, it will emit electrons whose kinetic energy is related to the light's wave length, but not to its intensity. This behavior was quite surprising at the time since it cannot be described using Maxwell's equations for electronmagnetic waves. It was subsequently explained in 1905 by A. Einstein [16] by quantizing the electromagnetic field into photons: A photon is fully absorbed by an electron which can then leave its host material. To do so the photon energy E_{ph} needs to be greater than the work function Φ plus the binding energy of the electron E_{bin}. The work function equals the potential step between the Fermi energy E_{F} and the vacuum level E_{vac} at the surface of the sample and is dependent on the material composition and its microscopic surface structure. The binding energy is increased the less energy an electron has and defined to be $E_{\mathrm{bin}} = 0$ at the Fermi energy E_{F}. Since the total energy is conserved in this process, the kinetic energy of the electron E_{kin} afterwards can be calculated using the equation [17]

$$E_{\mathrm{kin}} = E_{\mathrm{ph}} - \Phi - E_{\mathrm{bin}} \, . \tag{2.1}$$

By illuminating a sample with light of a known energy and recording the kinetic energy of the emitted electrons, one can therefore gain insight into the electrons *inside* the system. Electrons with a low binding energy are for example responsible for the chemical bonding as well as other highly relevant sample characteristics, like electronic conductance and responses to optical excitation. This technique is therefore routinely utilized to determine

various material properties and labeled **P**hoto**E**mission **S**pectroscopy (**PES**). Fig. 2.1 displays the energy transfer involved in a typical experiment.

Even strongly bound electrons can be excited and detected with sufficiently energetic X-ray photons which gives access to the weakly hybridizing electronic *core levels* of the inner atomic shells [19]. The binding energy of these core levels are specific for each element and can thus be used to establish which elements are present within a sample. The precise values for the binding energies are also affected by the chemical surroundings of an atom. This *chemical shift* was thoroughly studied and its application pioneered by K. Siegbahn in the mid-twentieth century [20, 21]. The chemical shift of core levels can be analyzed with a suitable spectrometer and used to gain insight into the valence states and chemical bonding.

Furthermore, the quantity of the respective element is connected to the measured photoemission intensity which enables the determination of the stoichiometry. There are several additional factors to the measured intensity, one of which is the finite inelastic scattering length of the excited photoelectrons inside the system. Inelastic scattering occurs when an electron loses (or gains) energy in an interaction event with another particle in the sample. The inelastic mean free path $\lambda(E_{\mathrm{kin}})$ is material dependent, but generally shortest around $E_{\mathrm{kin}} \approx 50\,\mathrm{eV}$ as shown in the log-log graph Fig. 2.2 [22, 23].

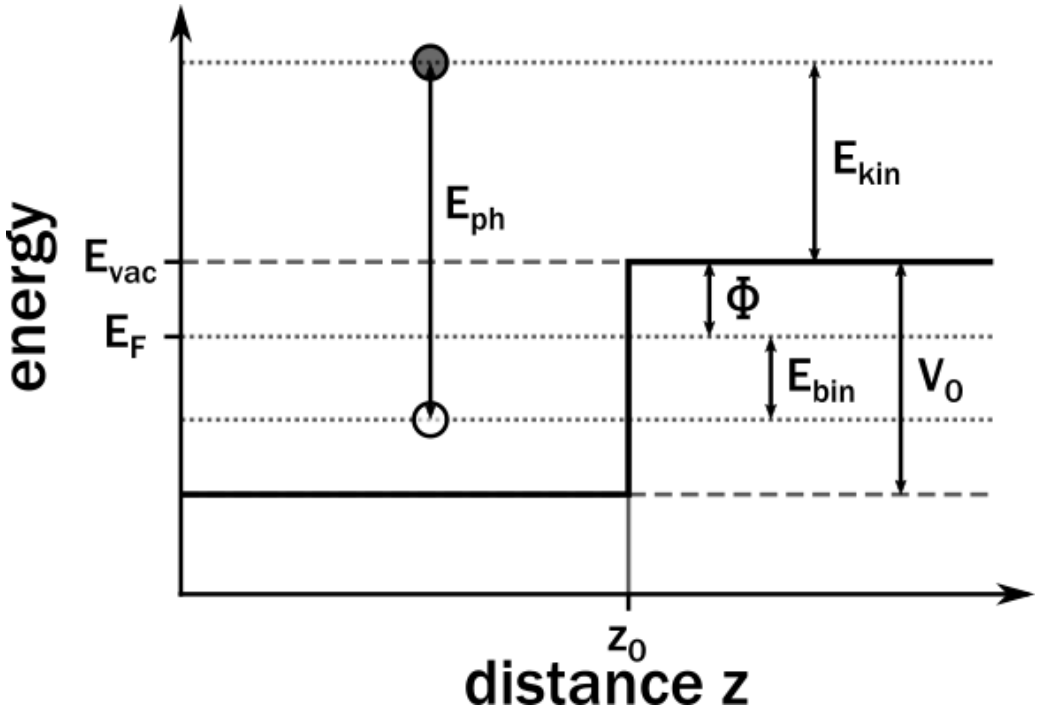

Figure 2.1: Schematic visualization of a photoemission experiment. A photon transfers its entire energy E_{ph} to an electron with binding energy E_{bin} which gets excited above the vacuum level E_{vac} and leaves the sample. Adapted from [18].

In this work, this type of spectroscopy with X-rays (**X**-ray **P**hotoelectron **S**pectroscopy (**XPS**)) is utilized to determine the thickness of adsorbed layers of organic molecules on top of non-organic substrates. Since the elements in the substrates are different from the carbon-based adsorbates, one can use either the damping of the substrate's core level features or the rise in intensity of the adsorbate's core levels with increased film thickness to quantify the height of the adsorbed thin film. The photoemission intensity from a substrate feature $I_{\mathrm{Sub}}(L)$ buried beneath a molecular film of height L can be extracted by a comparison with the signal strength on the clean substrate $I(0)$. Using $L = n\,L_0$ with the thickness of a single layer L_0, number of completed monolayers $n \in \mathbb{N}_0$, and the coverage in the top-most molecular layer $x \in [0, 1]$ the intensity is approximately given by

$$I_{\mathrm{Sub}}(n, x) = I_{\mathrm{Sub}}(0, 0)\left(x\,\exp\left(-\frac{(n+1)\,L_0}{\lambda(E_{\mathrm{kin}})}\right) + (1-x)\,\exp\left(-\frac{n\,L_0}{\lambda(E_{\mathrm{kin}})}\right)\right)\,. \quad (2.2)$$

On the other hand, the features produced by an element that is only present in the adlayer, e.g. the carbon 1s peak, will rise in the XPS spectrum with increasing film thickness. Since a molecule that adsorbs on top of another one blocks some of its emitted electrons, the photoemission intensity of adlayer features is dependent on how the molecules grow

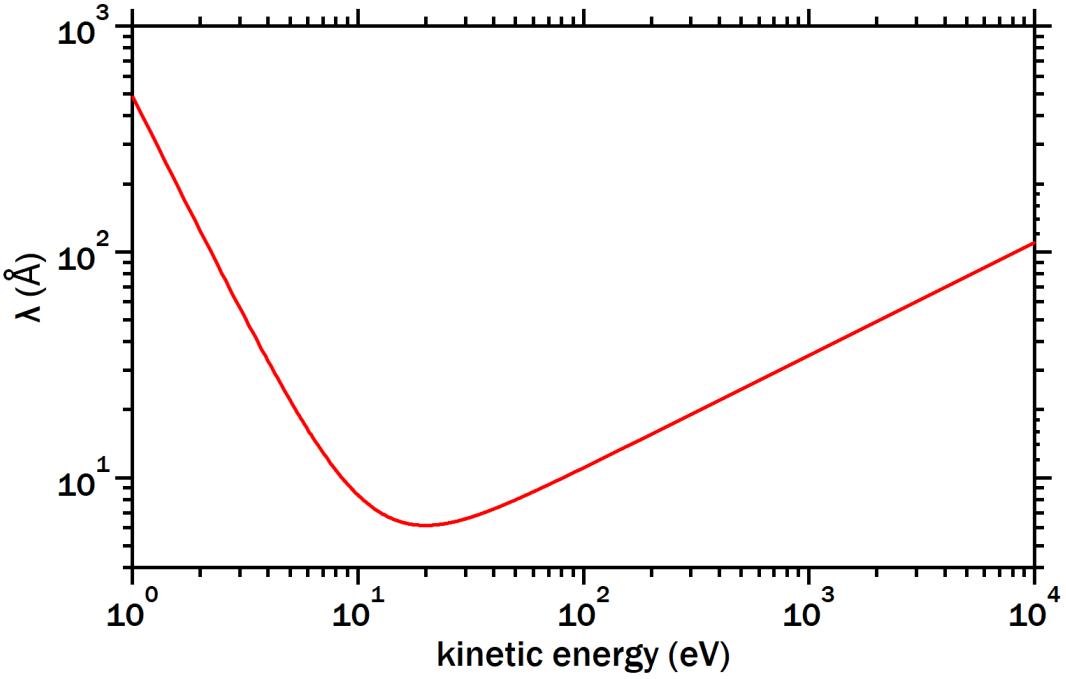

Figure 2.2: Universal curve for the inelastic mean free path of electrons with the kinetic energy dependence of organic compounds from [22] in a log-log plot.

on the substrate. The molecules surveyed in this thesis conveniently all exhibit a layer-by-layer growth on the clean substrates. We can therefore estimate the expected dependency of the molecular signals with increasing film thickness: up until the completion of the first monolayer $n = 0$, none of the photoelectrons emitted towards the detector are inelastically damped since the vacuum starts immediately above the molecules. The molecular features $I_{\mathrm{Mol}}(n, x)$ will therefore rise linearly with the coverage $x \in [0, 1]$. The intensity of a single completed molecular layer I_{Mono} can be used as a reference for a particular core level and experimental setup. Starting from the adsorption of molecules in the second layer $n > 1$, the signal from the lower layers will be exponentially damped by the finite mean free path of the photoelectrons through the thin film. The signal of the molecular features nonetheless continues to increase due to the additional signal from the top-most layer. As the thickness of the adlayer increases, the intensity converges towards and saturates at the level where any additional molecule blocks as many photoelectrons from below as it emits itself. This behavior is modeled by the equation

$$I_{\mathrm{Mol}}(n, x) = I_{\mathrm{Mono}} \left(x \, \exp\left(- \frac{n \, L_0}{\lambda(E_{\mathrm{kin}})} \right) + \sum_{n_i=1}^{n} \exp\left(- \frac{(n_i - 1) \, L_0}{\lambda(E_{\mathrm{kin}})} \right) \right) . \tag{2.3}$$

Note that if the measurement is performed at an angle Θ between the surface normal vector and the analyzer, the photoelectrons have to traverse a longer path inside the sample on their trajectory to the analyzer. This increases the "effective" thickness of the layer in the equations by a factor of $1/\cos\Theta$.

In general, the photoemission intensity I_i from an initial state Ψ_i into a final state Ψ_f can be described by time-dependent pertubation theory for weak excitations with **F**ermi's **G**olden **R**ule (**FGR**) [24, 25]:

$$I_{i,f} \propto \left| \langle \Psi_f | H_{\mathrm{exc}} | \Psi_i \rangle \right|^2 \cdot \delta\big[\hbar\omega - \Phi - (E_f - E_i)\big] \tag{2.4}$$

with final state wave function Ψ_f and interaction Hamiltonian H_{exc} between the (classical) light field and the system. The delta function ensures the energy conservation during the process.

Wave functions Ψ of an entire electron system are usually quite challenging to handle. For the evaluation of the experiments performed in this thesis however, it is acceptable to neglect the interaction of the emitted photoelectron with the remaining particles as well as any relaxation processes (*sudden approximation* [24]). Many-body effects can have a significant impact in the photoemission data in other cases, and the sudden approximation is not generally valid [26, 27]. Especially in strongly correlated systems the screening of the photohole left behind by the emitted electron has a strong impact on the photoemission

spectrum [17]. A more thorough introduction into the electronic wave functions will be given in the later sections of this chapter. For now, we use this approximation to factorize the many-particle wave function Ψ^N of N electrons into two components [28]: the wave function of the N-1 electron system $\Psi^{N\text{-}1}$ that can be neglected for our systems; and the wave function of the single electron emitted in the photoemission process ψ. This can be done both for the initial and final state of the electron ψ_i and ψ_f to simplify the many-particle problem of eq. (2.4) into a one-electron equation:

$$I(n) \propto \left|\langle\psi_f|H_{\text{exc}}|\psi_i\rangle\right|^2 \delta\big[\hbar\omega - \Phi - (E_f - E_i)\big] \; . \tag{2.5}$$

H_{exc} can be obtained with the momentum operator $\mathbf{p}+e\mathbf{A}$, where $\mathbf{A}$ is the vector potential of the field and e the elementary charge. This yields the Hamiltonian of the entire system H [25]:

$$H = \frac{1}{2m_0}\left(\mathbf{p}+e\mathbf{A}\right)^2 - e\phi + V = \frac{\mathbf{p}^2}{2m_0} + \frac{e}{2m_0}\big(\mathbf{Ap}+\mathbf{pA}\big) + \frac{e^2}{2m_0}\,\mathbf{A}^2 - e\phi + V \tag{2.6}$$

with the electron mass m_0 and the potential energy V due to the other particles of the system. The equation can be simplified by applying the dipole approximation and the Coulomb gauge $\nabla\mathbf{A} = 0$ and $\phi = 0$. This is justified due to the large light wave length ($\sim$ 100 nm) used in this work compared to the extent of the molecular wave functions ($\sim$ 1 nm) [25]. The light elements that make up the organic molecules also generate relatively small potential gradients within the sample. The last term proportional to $\mathbf{A}^2$ can be neglected for sufficiently weak light fields:

$$H = \left(\frac{\mathbf{p}^2}{2m_0} + V\right) + \frac{e}{m_0}\mathbf{Ap} = H_0 + H_{\text{exc}} \; . \tag{2.7}$$

So far we have taken only the energy conservation during the photoemission process into account which is sufficient to discuss angle-integrated spectra. On top of the insights that can be gained this way, a considerable amount of information is hidden within the angle-dependence of the emission. Using the conservation of momentum, the wave vector $\mathbf{k}$ of the photoelectron is immediately connected to the wave vector $\mathbf{k}_{\text{in}}$ of the electron inside the system. This relation has historically been used for an easy access into the band structure of solids and remains a prevalent tool for this purpose [19,25]. To perform a conventional **A**ngle **R**esolved **P**hoto**E**mission **S**pectroscopy (**ARPES**) experiment, the polar and azimuthal angles Θ and ϕ of the photoelectrons emitted into the upper hemisphere above the sample at a specified kinetic energy E_{kin} are recorded – see Fig. 2.3 for the experimental geometry.

With the measured angles and kinetic energy of the photoelectron $E_{\text{kin}} = \frac{\hbar^2\mathbf{k}}{2m_0}$, the

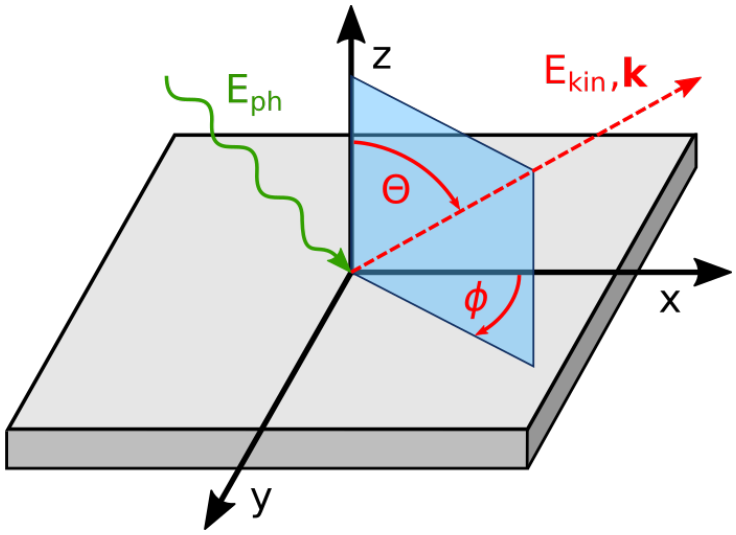

Figure 2.3: Depiction of the experimental geometry in an ARPES experiment. A photon with energy E_{ph} (green) excites a photoelectron wave (red) from the sample that propagates away with the kinetic energy E_{kin}, wave vector $\mathbf{k}$ and at angles Θ and ϕ.

Cartesian components of the wave vector inside the system $\mathbf{k}_{\mathrm{in}} = (k_{\mathrm{x}}, k_{\mathrm{y}}, k_{\mathrm{z}})$ can be determined through

$$k_{\mathrm{x}} = \frac{1}{\hbar}\sqrt{2m_0 E_{\mathrm{kin}}}\,\sin\Theta\,\cos\phi \tag{2.8}$$

$$k_{\mathrm{y}} = \frac{1}{\hbar}\sqrt{2m_0 E_{\mathrm{kin}}}\,\sin\Theta\,\sin\phi\,. \tag{2.9}$$

Unlike the wave vector components parallel to the surface, the perpendicular k_{z}-component is not conserved when the photoelectrons is transmitted from the sample into the vacuum above. This is due to the potential step $V_0 < 0$ in this direction, which is absent parallel to the surface. This potential step is also referred to as the *inner potential*. k_{z} is therefore reduced to

$$k_{\mathrm{z}} = \frac{1}{\hbar}\sqrt{2m_0(E_{\mathrm{kin}}\cos^2\Theta + V_0)}\,. \tag{2.10}$$

2.2 Density functional theory

After these considerations of the photoemission process we will take a look into the components mentioned in eq. (2.4). The two elements in FGR that are necessary to interpret or even predict the photoemission data are the final and initial state Ψ_f and Ψ_i. In this section we will begin with the Ψ_i treatment since initial state properties are usually the

main target of material studies.

In 1925, E. Schrödinger postulated the basic equation for the wave functions in a quantum system and published it the year after [29]. In the non-relativistic, time-independent expression of the **S**chrödinger **E**quation (**SE**), the wave functions of an N-particle system are connected to the particle mass m_j, the potential V and the energy E by the relation

$$\left[-\sum_{j=1}^{N} \left(\frac{\hbar^2 \nabla_j^2}{2m_j} \right) + V(\mathbf{r}_1, \mathbf{r}_2, ..., \mathbf{r}_N) \right] \Psi(\mathbf{r}_1, \mathbf{r}_2, ..., \mathbf{r}_N) = E\Psi(\mathbf{r}_1, \mathbf{r}_2, ..., \mathbf{r}_N) \, . \tag{2.11}$$

The potential V of the Hamiltionian in the bracket on the left contains the interaction between the particles and can therefore get almost arbitrarily complex. But even before considering V, the large number of particles N prevents finding a direct solution to the equation in any real system.

2.2.1 The many-body problem

To comprehend just how intractable the many-particle issue is, one can consider the example of calculating the electronic wave function of benzene (C_6H_6) on a very rough ($10 \times 10 \times 10$) grid of real space positions. Assuming the atomic cores to be stationary, the number of particles/electrons in the calculation N is six per carbon and one per hydrogen atom, and thus $N = 6 \cdot 6 + 6 = 42$. For each of the 10^3 possible voxel the potential from the cores plus that of the other 41 electrons at each voxel of the grid has to be taken into account. This means that there is a total $1000^{42} = 10^{126}$ possible combinations – for a simple benzene ring. Disregarding the calculation, just (temporarily) storing such an amount of information is not feasible. This unfavorable scaling of the many-body system therefore has to be overcome by suitable approximations.

The most common approach to tackle this issue and nevertheless arrive at reliable results is **D**ensity **F**unctional **T**heory (**DFT**) [30–32]. DFT is an integral part of the research in almost every branch of material science. For its discovery, the nobel prize in chemistry of 1998 was in part awarded to one of its pioneers, W. Kohn [33]. The central idea of DFT is to reduce the problem from a *many-* to a *single*-particle one. To this end, the interaction between the particles has to be approximated to reduce the complexity, see fig. 2.4 (a). This is achieved in two steps: First, instead of solving for the many-body wave function Ψ, the target is shifted towards acquiring the total particle density $n(\mathbf{r})$

$$n(\mathbf{r}) = \sum_{j}^{N} |\psi_j(\mathbf{r})|^2 \tag{2.12}$$

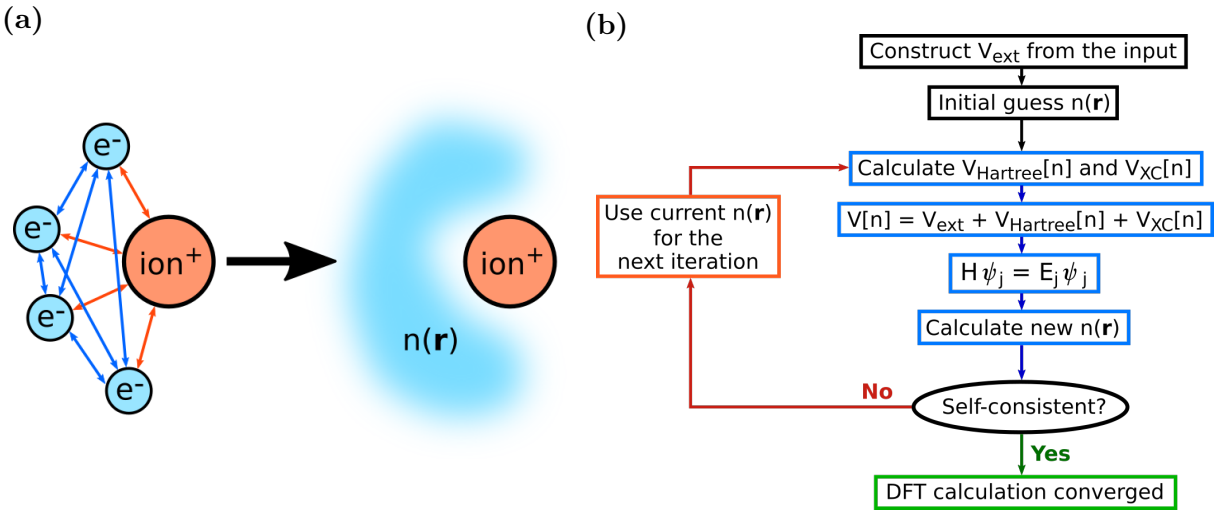

Figure 2.4: (a) The many-particle problem including individual electrons (left) is mapped onto a simpler single-particle problem that describes the electron density $n(\mathbf{r})$ instead (right). (b) Flowchart of a DFT calculation.

with normalized single-particle wave functions $\psi_j(\mathbf{r})$. Second, the interaction between the electrons that has been lost by dropping the additional dimensions is replaced with a *functional of the density*, $V[n] = V(n(\mathbf{r}))$:

$$V[n] = V_{\text{Ext}} + V_{\text{Hartree}}[n] + V_{\text{XC}}[n] \tag{2.13}$$

with the classical electron-electron and the static electron-nuclei interaction $V_{\text{Hartree}}[n]$ and V_{Ext}, respectively. The exchange-correlation functional $V_{\text{XC}}[n]$ contains all other contributions to the potential. The energy functional can then be used in a single-particle (Schrödinger) equation of decoupled electrons j:

$$\left[-\frac{\hbar^2\nabla^2}{2m} + V_{\text{Ext}}(\mathbf{r}) + V_{\text{Hartree}}[n] + V_{\text{XC}}[n] \right] \psi_j(\mathbf{r}) = E_j\psi_j(\mathbf{r}) \ . \tag{2.14}$$

This set of equations is one representation of the so-called *Kohn-Sham equations* published by W. Kohn and L. J. Sham in 1965 [34].

By minimizing the sum over all N particle energies in eq. (2.14), the ground state of this non-interacting system can be determined. What makes these collective relations so useful is that the particle density of this state is in principle identical to the particle density of the interacting system [30]. Calculating the lowest energy state of any real system is thus "only" a matter finding a suitable exchange-correlation functional $V_{\text{XC}}[n]$ and having sufficient computational resources. It should be stressed that the equivalence of the real and virtual system is by design only valid for the ground state.

A flowchart of the iterative steps in a typical DFT calculation is displayed in fig. 2.4 (b). The first step is guessing an initial density $n(\mathbf{r})$ based on the (approximately) known geometry and potential V_{Ext} of the atoms. From this density $V_{\mathrm{Hartree}}[n]$ and $V_{\mathrm{XC}}[n]$ of the chosen functional are determined. With the entire Hamiltonian assembled, eq. (2.14) is solved and and $\psi_j(\mathbf{r})$ used as an input for eq. (2.12). The updated $n(\mathbf{r})$ subsequently serves as starting point for the next iteration. At the end of each cycle, the current particle density is compared to the updated one. If their deviation is below a certain threshold, the calculation is declared to be converged. Depending on the chosen input parameters and functional, it is possible that the simulation moves towards a local instead of the global minimum. The convergence criterion might then be reached in the local minimum or the calculation could not converge at all. If the iteration loop completes successfully, the final result provides the electronic binding energies, real space orbitals and dipole moments among other parameters.

2.2.2 Linear combination of atomic orbitals

In principle, one can choose from an infinite amount of basis sets to construct the particle wave functions with. Two of those are especially common and useful: a plane wave basis set which works best for Bloch waves in extended solids; and a Gaussian basis set which relies on the atomic solutions in a spherically symmetric potential. The latter is a good choice for non-periodic systems (e.g. isolated molecules) and the one described in this section.

Since the collection of atoms into a molecule reduces the symmetry of the potential $V(\mathbf{r})$, solving the Kohn-Sham equations for molecules is significantly more complicated than for individual atoms. The potential surface inside a molecule can be built from the superposition of the potentials of its composite atoms, thus one can relate the solutions of the atomic SE to those of the molecule. Labeled after its mathematical definition, the **L**inear **C**ombination of **A**tomic **O**rbitals (**LCAO**) was first popularized by Lennard-Jones in 1929 [35]. It states that the wave function of a molecular orbital ψ_{Mol} can be assembled from the sum over atomic wave functions $\psi_{\mathrm{Atom,j}}$ of type j of all involved atoms a in the molecule multiplied by a weighting coefficient $c_{a,j}$ for each component [36]

$$\psi_{\mathrm{Mol}}(\mathbf{r}) = \sum_a \sum_j c_{a,j}\, \psi_{\mathrm{Atom},j}(\mathbf{r}) \; . \tag{2.15}$$

Neighboring atomic orbitals with closely matching binding energies (before interactions are taken into account) tend to exhibit a stronger hybridization than those further apart. For organic molecules with just a few different elements this commonly results in com-

posite states based on only a single type of orbital. Additionally, hybridization can only arise if the wave functions of adjacent atoms have some overlap in real space. There are two frequently used abbreviations for the molecular orbitals in the valence region: the **H**ighest **O**ccupied **M**olecular **O**rbital (**HOMO**) and the **L**owest **U**noccupied **M**olecular **O**rbital (**LUMO**). Starting from these states, the HOMO-1 is the second-highest occupied orbital, the HOMO-2 the third-highest and so forth. In the unoccupied region, the nomenclature LUMO+x with $x \in \mathbb{N}$ follows the same pattern towards increasingly lower binding energies.

When using this approach, the wave functions can be reproduced with the correct symmetry even in the presence of Coulomb potentials of neighboring atoms which distort the spherical symmetry around each core. However, the representation of these wave functions in an arbitrary potential requires spherical harmonic terms with orbital quantum numbers of a high order. If the potential of the neighboring atoms is large and non-symmetric around the atoms, the approximation will therefore be computationally more taxing the more orbital quantum numbers are necessary to reproduce the symmetry. Which order of orbital quantum numbers are included in the calculation is different from system to system and furthermore depends on the desired accuracy. This connection between atom and molecule is usually satisfactory for most applications and makes the resulting molecular orbitals intuitive to interpret and handle in calculations. In the spherically symmetric potential around each atom, the radial and angular components $R(r)$ and $Y(\hat{\mathbf{r}})$ of the wave function ψ_{Atom} can be decoupled from one another [36]:

$$\psi_{\text{Atom}}(\mathbf{r}) = \sum_{n} \sum_{l,m} R_{n,l}(r)\, Y_{l,m}(\hat{\mathbf{r}}) \; . \tag{2.16}$$

The radial wave functions for hydrogen-like atoms can be calculated exactly and lead to so-called **S**later-**T**ype **O**rbitals (**STO**). These are proportional to the product of a polynomial and an exponential function of the distance r from the nucleus. There is a significant downside to employing STO in DFT calculations: overlap integrals between two electrons are computationally complex. Instead of STO, the common alternative is to use **G**aussian-**T**ype **O**rbitals (**GTO**) instead. This makes the integrals easier to handle since the integral over two Gaussian functions is just a single Gaussian with its center in between the two constituents. A Gaussian function diverges from an STO close to the origin, where it is too flat for $r \to 0$. It also decays too fast at higher r. To nevertheless replicate the STO, one can use the sum over several Gaussian functions instead of just a single one. Fig. 2.5 displays how the STO for $R_{1,0}(r)$ (black) is approximated by a single Gaussian (yellow) and linear combinations of two (orange) and three (red) Gaussian functions of different widths and heights. In practice, the amount of Gaussian functions per STO is chosen depending on the element and the desired complexity of the calculation.

Such a combination of several Gaussians into one function is called a *contracted Gaussian function* or *basis function*. The minimal set of basis functions to describe an atom has to contain at least one basis function per two electrons, so that each electron can occupy its own state. Further basis functions improve the accuracy, which can be illustrated on the example of lithium: the bare minimum of two basis functions is sufficient to describe the electrons in the 1s and 2s orbitals in ground state. When lithium is bound in a molecule or solid, the breaking of the spherical symmetry is reproduced better with an additional p-type basis function. Thus, the polarization due to the neighboring atoms can be represented in the DFT. The common abbreviation to tell how many Gaussian functions are contained for each STO is "nG", where n is the number of Gaussians per STO.

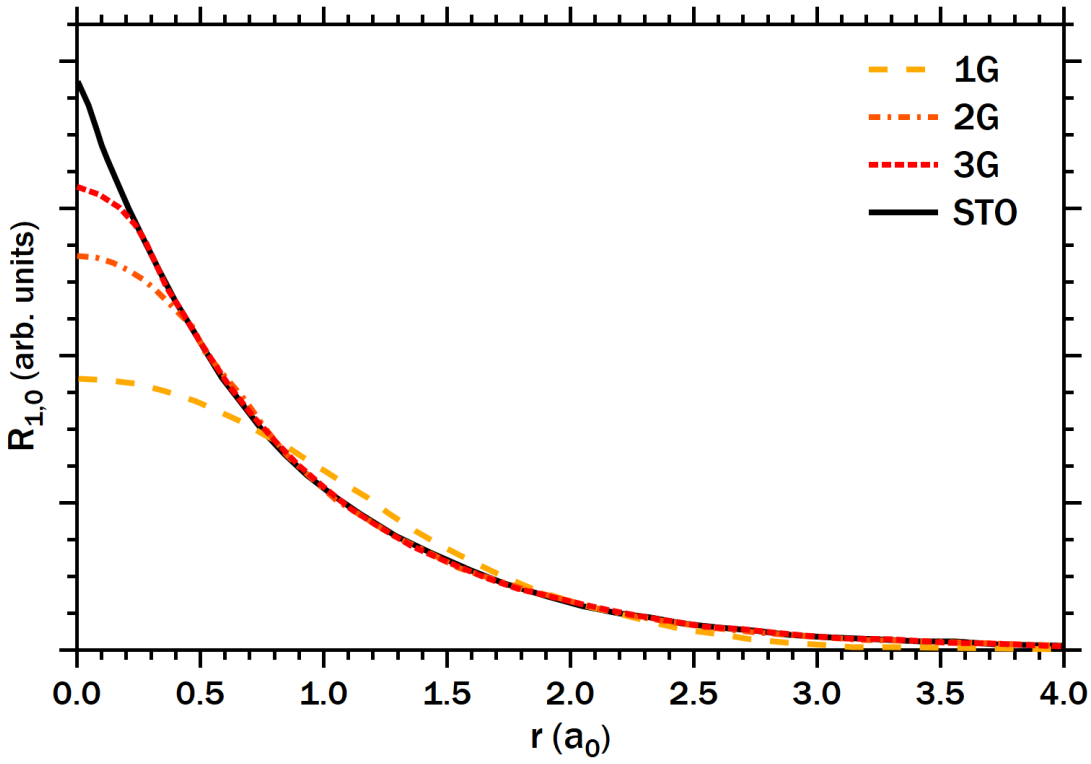

Figure 2.5: Approximation of the radial wave function $R_{1,0}(r)$ of a Slater-type orbital (black) with a linear combination of one (yellow), two (orange) and three Gaussian functions (red).

2.3 Final state approximations

Just like for the determination of molecular initial states, the final states are described by the solutions to the SE. In this case however, the time-independent DFT laid out in section 2.2 cannot be employed because it is not valid for any excitations. The increase in computational power in the last decade has made time-dependent DFT a feasible option [37,38]. Unfortunately it is still exceedingly time-consuming and too limited for some of the projects in this thesis. Due to the unfavorable scaling of the SE with the number of electrons, the final states have to be determined with another approach instead of DFT to calculate any real system. Furthermore, an accurate description is even more elaborate than for the initial states because the outgoing photoelectron wave of an emitting atom might interact with nearby atoms. Atoms which do not participate in forming the initial state could thus still play a role in the determination of the final states.

The type and complexity of the theoretical treatment is strongly dependent on both the material system and on the excitation parameters. E.g. the cross section of elastic scattering scales with increasing atomic numbers Z. For many organic systems comprised mainly of carbon ($Z = 6$) and hydrogen ($Z = 1$) this means that elastic scattering is only relevant at the substrate atoms [11]. Yet even when grown on a high-Z material, the strong inelastic damping in the kinetic energy range in common ARPES experiments ($\sim 15 - 40\,\mathrm{eV}$) only leaves a featureless, angle-independent background in the detected signal. This background *does* contain useful information on the excited particles and phenomena, but is not generally necessary to gain knowledge on the material properties if the directly emitted photoelectrons are thoroughly analyzed.

Three approaches for the final states are used for the simulations in this thesis: the *plane wave* approximation, the *independent atomic center* approximation, and an *expanded independent atomic center* approximation which includes elastic scattering events.

2.3.1 Independent atomic center approximation

The **I**ndepentent **A**tomic **C**enter (**IAC**) approximation [39] is conceptually closely related to the LCAO. The principle idea is once more the construction of the total wave function from atomic contributions. In case of the IAC, the final state of the entire system ψ_f is built from the coherent superposition of the partial final states of each atom a. The partial final states $\psi_{f,a}$ are calculated by solving the SE in the (approximately) spherically symmetric potential around each atom (see supporting online material of [40]). The equation is solved for the kinetic energy E_{kin} of the electrons after excitation which can be calculated from eq. (2.1).

There is an intuitive way to get to the final state in several steps. First of all, one can

start from the solution within the empty space far from any atom and potential. A viable solution to the SE of this problem is a plane wave $e^{i\mathbf{kr}}$ with wave vector $k = \sqrt{2mE_{\text{kin}}}/\hbar$ corresponding to the free electron mass m and its energy E_{kin}. The spherical symmetry in free space enables the separation of the total wave function into an angular and a radial component. This decoupling is directly apparent when the plane wave is rewritten using Rayleigh's plane wave expansion [41]

$$e^{i\mathbf{kr}} = 4\pi \sum_{l=0}^{\infty} \sum_{m=-l}^{l} i^l j_l(kr) Y_{l,m}(\hat{\mathbf{r}}) Y^*_{l,m}(\hat{\mathbf{k}}) \tag{2.17}$$

with orbital and angular quantum numbers l, m, spherical Bessel functions j_l and spherical harmonics $Y_{l,m}$. $\hat{\mathbf{r}}$ and $\hat{\mathbf{k}}$ indicate the unit vectors in the direction of $\mathbf{r}$ and $\mathbf{k}$, respectively. But what changes when an atom is inserted at the origin of the system? Due to the angle-independent Coulomb potential the spherical symmetry around $r = 0$ is not affected. The angular wave function can therefore still be decoupled from the radial one and spherical harmonics remain a possible solution for the angle-dependency. The atomic potential nevertheless attracts the electron which distorts the radial wave function in close proximity to the atom. Such a plane wave deformed by the presence of a Coulomb potential is called a *Coulomb wave* [42]. The radial wave function of a Coulomb wave $R_l(kr, \alpha)$ ultimately resolves to [43]

$$R_l(kr, \alpha) = (2kr)^l \, \frac{|\Gamma(l + 1 + i\alpha)|}{\Gamma(2l + 2)} \, e^{\left(-i\mathbf{kr} - \frac{\pi\alpha}{2}\right)} \, {}_1F_1(l + 1 - i\alpha, 2l + 2, 2ikr) \tag{2.18}$$

where $\alpha = -Z_{\text{ion}}/k$ is a measure of how strong the (partially) ionized atom pulls on the electron compared to its wave vector and therefore its kinetic energy. ${}_1F_1$ is the confluent hypergeometric function. Fig. 2.6 displays the radial wave function of the plane wave $j_0(kr) = R_0(kr, 0)$ (black) and Coulomb waves $R_0(kr, \alpha)$ with $Z = 0.5$ (red) and $Z = 1.0$ (blue) for $k = 0.1285\,\text{Å}^{-1}$ and $l = 0$. The change in the general curve shape is directly connected to electrodynamics: if the atom carries no residual charge ($Z_{\text{ion}} = 0 \rightarrow \alpha = 0$), the electron is moving through a flat potential surface and the Coulomb wave equals a plane wave. For increasing $Z_{\text{ion}} > 0$ the electron effectively has an enhanced kinetic energy in the vicinity of the atom. This in turn amplifies the oscillation frequency of the radial wave function, just like an increased wave vector in $e^{i\mathbf{kr}}$. The influence of the atom decays with $1/r$ and thus vanishes for $r \rightarrow \infty$. Only a phase shift compared to the plane wave remains far from the atom. Also, higher kinetic energies lower the impact of the atomic potential for a fixed Z_{ion} – the energy gain close to the atom simply becomes negligible compared to E_{kin}. The whole effect therefore scales with the wave vector $k = \sqrt{2mE_{\text{kin}}}/\hbar$.

The next aspect to consider is the presence of other atoms within the molecule or solid:

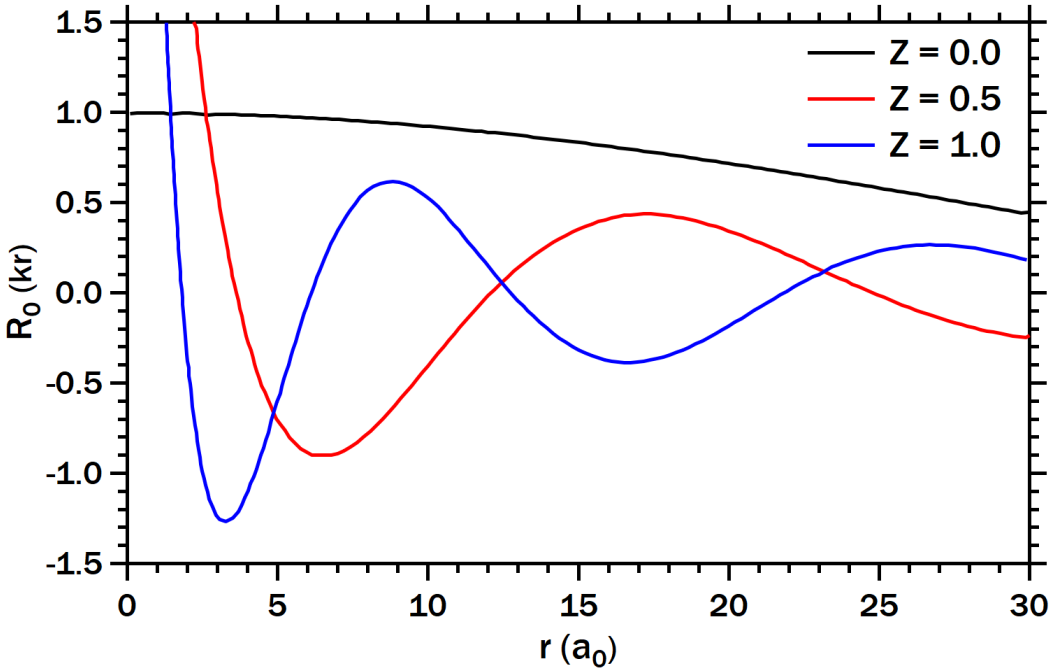

Figure 2.6: Radial wave function of a plane wave $Z = 0.0$ (black) compared to a Coulomb wave for $Z = 0.5$ (red) and 1.0 (blue) for $k = 0.1285\,\text{Å}^{-1}$ and $l = 0$ [43]. The deviation of the Coulomb wave from the plane wave is enlarged at higher $Z \propto \alpha$ and lower r.

the total final state ψ_f is assembled from individually emitting atoms a which are located at different positions $\mathbf{R}_a$ in real space. For a certain wave vector $\mathbf{k}$, the partial electron waves from each atom will therefore acquire a phase shift due to the path difference $e^{-i\mathbf{k}\mathbf{R}_a}$. Once the electronic waves leave the atom, they are still inside the sample and not immediately in empty space. There they can excite and interact with other particles like e.g. electrons, phonons and plasmons. The inelastic scattering length is on the order of $\sim 1\,\text{nm}$ in the typical energy range for ARPES experiments (see fig. 2.2). The diffuse inelastic background is not explicitly included in this final state, but the damping of the unscattered electrons is represented by a factor $D_a(\mathbf{k})$. The exponential decrease in intensity is dependent on the the direction and magnitude of the wave vector $\mathbf{k}$. It is dependent on the polar angle Θ_{in} of the electron inside the sample towards the surface and the k-dependent inelastic scattering cross section [22,44]. Since it takes longer for the electron to penetrate into the vacuum the further the emitting atom is from the surface at

R_{surface}, it is also a function of the distance $R_{z,a}$ of atom a from the surface. Put together, this results in a damping factor

$$D_a(\mathbf{k}) = \exp\left(- \frac{|R_{z,a} - R_{\text{surface}}|}{\lambda(k)\cos(\Theta_{\text{in}})} \right) . \tag{2.19}$$

There is one more influence on the phase of the electron to consider before one arrives at the complete final state wave function. The presence of the atomic potential affects the wave function which leads to the Coulomb wave displayed in eq. (2.18). As mentioned above, this distortion also leaves its trace in a phase shift when the electron is entirely separated from the atom at $r \to \infty$. Since this phase shift $\delta_a^l(k)$ is a function of the atomic potential, it is also dependent on the atom a. With these additional factors examined, we can now sum up the total final state ψ_f from the partial final state wave functions

$$\psi_f = \sum_a \psi_{f,a} = 4\pi \sum_a \sum_{l=0}^{\infty} \sum_{m=-l}^{l} i^l R_l(kr) Y_{l,m}(\hat{\mathbf{r}}) Y^*_{l,m}(\hat{\mathbf{k}}) D_a(\mathbf{k}) \delta_a^l(k) e^{-i\mathbf{k}\mathbf{R}_a} . \tag{2.20}$$

Please note that the kinetic energy and wave vector here are those *inside* the sample. In order to predict the measurement of an ARPES experiment *at the detector*, the reduction of k_z at the potential step V_0 at the surface is taken into account with eq. (2.10).

This description based on the IAC approximation is employed for the majority of simulations in this thesis. Up to this point, there is no term associated with elastic scattering. If elastically scattered electrons have a relevant amplitude in an ARPES experiment, an extension of the unscattered IAC final state is necessary.

2.3.2 Elastic electron scattering

Starting from eq. (2.20), elastically scattered electrons can be included in the final state through additional terms alongside the unscattered ones. We will stay within a one-step model of the photoemission, but nevertheless describe it using the terminology of a (technically less correct) multi-step process. This makes the theory more accessible and easier to understand. There are two components to a scattering event: the propagation of an electron wave from an atom a towards the scattering atom b; and the scattering of the wave at the electrostatic potential around that atom. The propagator inside the system is a type of *Green's functions* $G_{a,b}$, which is a measure of the probability of the

electronic transport from site a to b [24]. It is dependent on the vectorial atomic separation $\mathbf{R}_{ab} = \mathbf{R}_b - \mathbf{R}_a$, the wave vector and the angular and magnetic quantum numbers [45–47]:

$$G_{a,b}^{l_1,m_1,l_2,m_2}(k) = -4i\pi k \sum_{l_3=0}^{\infty} \sum_{m_3=-l}^{l} (-i)^{l_3}(-1)^{l_1-l_2+m_2}\, h_{l_3}^{(1)}(kR_{ab})\, Y_{l_3,m_3}(\hat{R}_{ab}) \int_{\Omega} Y_{l_1,m_1}(\hat{\mathbf{r}}) Y_{l_2,-m_2}(\hat{\mathbf{r}}) Y_{l_3,m_3}(\hat{\mathbf{r}}) d\hat{\mathbf{r}} \tag{2.21}$$

with the spherical Hankel function of the first kind $h_{l_3}^{(1)}(kR_{ab})$. How the electron is scattered elastically upon reaching atom b can be described by a scattering matrix $t_b^l(k)$. For a seamless integration into the calculation it is convenient to use a matrix with a dependency on orbital momentum components. $t_b^l(k)$ contains the l-dependent phase shifts that an electron wave with wave vector k acquires once the elastic scattering event at atom b is concluded. These two factors are sufficient to draw up an additional term in the final state that describes the singly scattered electronic wave function ψ_{f,Sca_1}:

$$\psi_{f,\mathrm{Sca}_1} = 4\pi \sum_{a} \sum_{b\neq a} D_b(\mathbf{k}) e^{-i\mathbf{k}\mathbf{R}_b} \sum_{l_1=0}^{\infty} \sum_{m_1=-l}^{l} i^{l_1} R_{l_1}(kr) Y_{l_1,m_1}(\hat{\mathbf{r}}) \delta_a^l(k) \sum_{l_2=0}^{\infty} \sum_{m_2=-l}^{l} Y_{l_2,m_2}^*(\hat{\mathbf{k}}) G_{a,b}^{l_1,m_1,l_2,m_2}(k)\, t_b^{l_2}(k)\ . \tag{2.22}$$

The strong dependence of ψ_{f,Sca_1} on parameters attributed to atom a is not accidental: The scattered wave function is built upon an electron emitted from an initial state around atom a, so ψ_{f,Sca_1} also contains parts of the final state wave function $\psi_{f,a}$.

The total final state including single elastic scattering events is the coherent superposition of both available channels: the non-scattered, directly emitted amplitude of eq. (2.20), and the single scattering amplitude eq. (2.22):

$$\psi_{f,\text{single-scattering}} = \psi_f + \psi_{f,\mathrm{Sca}_1}\ . \tag{2.23}$$

Multiple scattering can be implemented by repeating the idea of the approach above for subsequent scattering atoms. For each additional scattering event, the Green's function and scattering matrix of the last scattering incidence have to be multiplied into the wave function. The damping and path difference have to be updated as well. It is also important to include scattering events in which the electron bounces back and forth between two atoms in the summation over all scattering atoms. As an example, the equation for the

partial wave function of electrons that have been elastically scattered twice ultimately resolves to

$$\psi_{f,\mathrm{Sca}_2} = 4\pi \sum_a \sum_{b\neq a} \sum_{c\neq b} D_c(\mathbf{k}) e^{-i\mathbf{k}\mathbf{R}_c} \sum_{l_1=0}^{\infty} \sum_{m_1=-l}^{l} i^{l_1} R_{l_1}(kr) Y_{l_1,m_1}(\hat{\mathbf{r}}) \delta_a^l(k) \\ \sum_{l_2=0}^{\infty} \sum_{m_2=-l}^{l} Y^*_{l_2,m_2}(\hat{\mathbf{k}}) G_{a,b}^{l_1,m_1,l_2,m_2}(k)\, t_b^{l_2}(k)\, G_{b,c}^{l_1,m_1,l_2,m_2}(k)\, t_c^{l_2}(k)\ . \tag{2.24}$$

In this manner, the final state wave function including n times elastically scattered electrons $\psi_{f,\text{n-scattering}}$ is the coherent superposition of the partial wave functions at each step along the way:

$$\psi_{f,\text{n-scattering}} = \psi_f + \psi_{f,\mathrm{Sca}_1} + \psi_{f,\mathrm{Sca}_2} + ... + \psi_{f,\mathrm{Sca}_n}\ . \tag{2.25}$$

2.3.3 Plane wave approximation

One of the simplest final states that can still be successfully employed in calculations is a plane wave. The **P**lane **W**ave **A**pproximation (**PWA**) was first employed in the 1970s [48, 49], but subsequently fell out of use in favor of more elaborate treatments [50]. Decades later, it was rediscovered for its application to planar organic molecules in 2009 by Puschnig et al. [40]. Their group applied the PWA to ARPES measurements of a pentacene multilayer and a sexiphenyl monolayer on Cu(110) with a remarkably good fit to the experimental data. It has subsequently been used to gather structural and electronic information from photoemission experiments [8, 51–53].

We will start by examining how the PWA simplifies the photoemission equations. Using a plane wave final state $\psi_f = e^{i\mathbf{k}\mathbf{r}}$ in FGR eq. (2.5) the photoemission matrix element M_{if} can be transformed by using the relation $H_{\text{exc}} = H^\dagger_{\text{exc}}$ of the Hermitian Hamiltonian H_{exc} to

$$M_{if} = \langle\psi_f|H_{\text{exc}}|\psi_i\rangle = \langle\psi_f|H_{\text{exc}}|\psi_i\rangle^{**} = \langle\psi_i|H^\dagger_{\text{exc}}|\psi_f\rangle^* = \langle\psi_i|H_{\text{exc}}|\psi_f\rangle^* \tag{2.26}$$

with * denoting the complex conjugate and † the transposed complex conjugate of an element. The Hamiltionian now effectively acts upon the final – instead of the initial – state. In the next step, we resolve the bra-ket notation into an integral over all of real space. We will also use the momentum form of the Hamiltonian and insert $H_{\text{exc}} = \mathbf{A}\cdot\mathbf{p}$:

$$\langle\psi_i|H_{\text{exc}}|\psi_f\rangle^* = \int_{\mathbb{R}^3} \psi_i^*\, (\mathbf{A}\cdot\mathbf{p})^*\, \psi_f^*\ . \tag{2.27}$$

When a real-valued $\psi_i^* = \psi_i$ initial state and the plane wave final state $\psi_f = e^{i\mathbf{kr}}$ are inserted the equation resolves to

$$\int_{\mathbb{R}^3} \psi_i^* \left(\mathbf{A}\cdot\mathbf{p}\right)^* \psi_f^* = \int_{\mathbb{R}^3} \psi_i \left(\mathbf{A}\cdot\mathbf{p}\right)^* e^{-i\mathbf{kr}} = \int_{\mathbb{R}^3} \psi_i \left(\mathbf{A}^*\cdot(i\hbar\nabla)\right) e^{-i\mathbf{kr}} \,. \tag{2.28}$$

The final result has a peculiar connection to the Fourier transform of the wave function of the initial state $\mathcal{F}(\psi_i) = \widetilde{\psi}_i$

$$\int_{\mathbb{R}^3} \psi_i \left(\mathbf{A}^*\cdot(i\hbar\nabla)\right) e^{-i\mathbf{kr}} = -\hbar\,\mathbf{A}^*\cdot\mathbf{k}\int_{\mathbb{R}^3} \psi_i\, e^{-i\mathbf{kr}} \rightarrow \mathcal{A}(\mathbf{k}) \propto M_{if} = -\hbar\,\mathbf{A}^*\cdot\mathbf{k}\cdot\widetilde{\psi}_i \,. \tag{2.29}$$

The dependencies of the photoemission intensity $I(\mathbf{k}) = |\mathcal{A}(\mathbf{k})|^2 \propto |M_{if}|^2$ are hence reduced to the experimental geometry $|\mathbf{A}^*\cdot\mathbf{k}|^2 = |\mathbf{A}\cdot\mathbf{k}|^2$ and the Fourier transform of the initial state $|\widetilde{\psi}_i|^2$. This makes the PWA very appealing: the expected **P**hotoelectron **M**omentum **M**ap (**PMM**) can be almost intuitively predicted by looking at the molecular initial state (calculated with DFT) and factoring in the known experimental geometry.

Before discussing its details, we will see how the PWA can actually be derived from the more accurate IAC approximation [39, 40]. The simplifications we have to use will shed light on some of the shortcomings of using a plane wave final state. The photoemission intensity $I(\mathbf{k})$ from a single molecular orbital in the absence of scattering is determined by inserting the initial state from eq. (2.15) and the final state eq. (2.20) into FGR eq. (2.5):

$$I(\mathbf{k}) \propto \left|\langle\psi_f(\mathbf{k})|H_{\mathrm{exc}}|\psi_i\rangle\right|^2 = \left|\sum_a\sum_j c_{a,j}\, e^{-i\mathbf{kR}_a}\sum_{l=0}^{\infty}\sum_{m=-l}^{l} M_{a,j,l,m}(k) Y_{l,m}^*(\hat{\mathbf{k}}) D_a(\mathbf{k}) \delta_a^l(k)\right|^2 \tag{2.30}$$

with the atomic matrix element of atom a and type j

$$M_{a,j,l,m}(k) = \int_{\mathbb{R}^3} \psi_{\mathrm{Atom},a,j}\, H_{\mathrm{exc}}\, i^l R_l(kr) Y_{l,m}\, .(\hat{\mathbf{r}}) \,. \tag{2.31}$$

Due to the partial filling of the 2p states of atomic carbon, the valence orbitals of organic molecules are usually also derived from carbon – specifically the C-2p_z orbitals aligned out of the molecular plane of planar molecules forming π orbitals. The binding σ orbitals aligned in parallel to the molecular plane can be expected to have a higher binding energy due to the stronger interaction with neighboring atoms. Hence, if the atomic matrix elements of the π orbitals can be approximated by neglecting all contributions from non-carbon atoms and atomic orbitals besides C-2p_z, $M_{a,j,l,m}(k)$ is identical for each (carbon) atom a and restricted to j = C-2p_z. This results in $\psi_{Atom,a,j} \rightarrow \psi_{\text{C-2p}_z}$ and $M_{a,j,l,m}(k) \rightarrow$

$M_{l,m}(k)$. The sum over all types of initial state orbitals j can be dropped. Note that after this transformation, the LCAO coefficients c_a retain their dependency on the atom a. The photoemission amplitude $|\mathcal{A}(\mathbf{k})| = \sqrt{I(\mathbf{k})}$ is then

$$\mathcal{A}(\mathbf{k}) \propto \sum_a c_a \, e^{-i\mathbf{k}\mathbf{R}_a} \sum_{l=0}^{\infty} \sum_{m=-l}^{l} M_{l,m}(k) Y^*_{l,m}(\hat{\mathbf{k}}) D_a(\mathbf{k}) \delta^l_a(k) \; . \tag{2.32}$$

Next, we will take a closer look at the potential surface inside the sample. The phase shifts $\delta^l_a(k)$ of the partial photoelectronic waves scale with the depth of the potential well around atom a. Since all the emitted, partial electronic waves stem from carbon, we only have to handle comparatively shallow potential wells ($Z_{\text{carbon}} = 6$). The resulting phase shifts are small and decrease further with increasing E_{kin}. Moreover, only the *relative* phase shifts between the partial electronic waves are relevant for the photoemission intensity. This is straightforward to imagine and also apparent from eq. (2.5), where a constant phase shift could be factorized out of the matrix element which would subsequently nullify itself when the absolute square of the matrix element is taken. The carbon atoms in a molecule are positioned in different chemical surroundings and hence do not exhibit identical potential wells. They are nevertheless very much alike. In combination with the already small absolute phase shifts, $\delta^l_a(k)$ can safely be neglected in this case.

The damping factors $D_a(\mathbf{k})$ also warrant a detailed examination. For two-dimensional molecules that are aligned perpendicular to the sample normal vector, the distance from each constituent atom to the surface is essentially the same. The damping factor is then identical for each atom within a molecular layer. In its most extreme case – a flat-lying monolayer adsorbed on a substrate – the damping factor can be disregarded without much of an effect. Even if the molecules are aligned along the surface normal vector, the compounds used in this thesis are rather small. While the inclusion of $D_a(\mathbf{k})$ *does* change the simulation, the damping will mostly affect the relative intensity of the molecular features in the PMM. Overall, the approximation $D_a(\mathbf{k}) = 1$ will certainly be less accurate than $\delta^l_a(k) = 1$ for the majority of molecular systems. One would expect that the incurred error will be relevant for the intensity, but not the position and shape of the molecular features in reciprocal space.

For a more convenient comparison we now turn to the assembly of the molecular initial state $\psi_{\text{Mol}} = \psi_i$ in the LCAO approximation of eq. (2.15). We can dismiss the dependence on the orbital type j for the above mentioned arguments and apply a Fourier transform on both sides of the equation:

$$\widetilde{\psi}_i(\mathbf{k}) = \sum_a c_a \, e^{-i\mathbf{k}\mathbf{R}_a} \, \widetilde{\psi}_{\text{C-2p}_\text{z}}(\mathbf{k}) \;\rightarrow\; \sum_a c_a \, e^{-i\mathbf{k}\mathbf{R}_a} = \frac{\widetilde{\psi}_i(\mathbf{k})}{\widetilde{\psi}_{\text{C-2p}_\text{z}}(\mathbf{k})} \; . \tag{2.33}$$

Inserting the right hand side of this equation and the approximations above into eq. (2.32) further simplifies $\mathcal{A}(\mathbf{k})$:

$$\mathcal{A}(\mathbf{k}) \propto \left(\sum_{l=0}^{\infty} \sum_{m=-l}^{l} \frac{M_{l,m}(k) Y_{l,m}^{*}(\hat{\mathbf{k}})}{\widetilde{\psi}_{\text{C-2p}_\text{z}}(\mathbf{k})} \right) \widetilde{\psi}_i(\mathbf{k}) \ . \tag{2.34}$$

At this point, we can compare our result to eq. (2.29), where we used a plane wave final state from the very beginning. In both cases the photoemission amplitude is dependent on the Fourier transform of the initial state, albeit multiplied by different factors. For the specific measurement geometry $\mathbf{A} \parallel \mathbf{k}$, both factors lose their angle-dependence and actually make the same predictions about the photoemission intensity [49, 54, 55]. The deviation between both models grows with increasing angle between $\mathbf{A}$ and $\mathbf{k}$. However, the difference in the angle dependence of the prefactors grows rather slowly [40]. The main reason is the single initial state $\psi_{\text{C-2p}_\text{z}} \propto Y_{1,0}$ combined with the photoemission selection rules $\Delta l = \pm 1$ and $\Delta m_l = 0, \pm 1$, which results in a weak angle-dependence. If the angle between $\mathbf{A}$ and $\mathbf{k}$ is small, the anticipated photoemission intensity is approximately the same for both approaches.

The simplicity of this approximation comes at the price of some significant drawbacks [11]: the PWA is not intricate enough to capture a lot of the physics in actual systems [38]. In practice, this means that not all of the information included in the measured data can be made use of, e.g. information contained within the circular dichroism. Since the photoemission matrix element with the PWA is identical for left- and right-circular polarized light, the circular dichroism signal is always predicted to be zero. This prediction evidently runs contrary to actual measurements, in which the circular dichroism carries information about the system and e.g. can be used to recover the phase information of molecular orbitals [56]. Like mentioned above, the PWA is generally more accurate the closer $\mathbf{A} \parallel \mathbf{k}$ [11]. At $\mathbf{A} \parallel \mathbf{k}$ the PWA happens to be in agreement with more detailed final state descriptions in the absence of relevant electronic scattering [49, 54, 55]. On the other hand, the comparison to experiment is generally least favorable for $\mathbf{A} \perp \mathbf{k}$, where the PWA always predicts absolutely no photoemission signal.

The neglected damping of the emitted electronic wave ($D_a(\mathbf{k}) = 1$) can be addressed by including an anolagous factor expressing the inelastic damping of the electron inside the system post hoc [57]. The final state inside the sample is damped with the inverse of the inelastic mean free path $\gamma = \frac{1}{\lambda}$, $\psi_f = e^{i\mathbf{kr}+\gamma(z-z_0)}$ for $z < z_0$. In the vacuum above the sample $z \geq z_0$, the final state behaves like an unmodified plane wave $\psi_f = e^{i\mathbf{kr}}$. This treatment does not necessarily result in a more correct result, but it can be used to determine qualitatively from which depth specific features in the PMM stem from. In

their study, Lüftner et al. [57] were able to discern the molecular from the metal substrate signal by comparing the simulation for damping values $\gamma = 0.25\,\text{Å}^{-1}$ and no damping $\gamma = 0\,\text{Å}^{-1}$. Features that were strongly affected by the damping could be assigned to the substrate below the organic monolayer and vice versa.

2.4 Real space orbital reconstruction

If the plane wave final state is a suitable approximation for a given system, it enables the reconstruction of the molecular initial state in real space from the experimental data [40]. The method has since been labelled *orbital tomography* and analyzed extensively [8, 9, 12, 52, 58–62]. Being able to image the real space wave function $\psi_i(\mathbf{r})$ from experimental data is an impressive feat on its own – and perhaps a little surprising considering the electronic wave function is not an observable quantity [63]. The related physical quantity that *is* observable is the absolute square of the wave function, the electron density $n(\mathbf{r}) = |\psi_i(\mathbf{r})|^2$. Nevertheless, the reconstructed wave functions are in decent agreement with ab-initio simulations and just like these can be interpreted as a mathematical tool that guides the evaluation of physical phenomena. In principle, the reconstructed real space wave function contains information on the hybridization of an molecule with its immediate surroundings. The potential surface inside and around the molecule also shapes the initial state and is therefore accessible from the same experiment. Since its inception, orbital tomography has proven to be a handy technique for a variety of issues in fundamental material science [8, 52, 61].

The successful reconstruction hinges on solving the *phase problem* of the measured photoemission signal. This issue arises because the ARPES experiment records the intensity, but not the amplitude of the emitted photoelectrons. Any photoemission amplitudes that are shifted by an arbitrary phase α will be indistinguishable from one another: $I(\mathbf{k}) = |\mathcal{A}(\mathbf{k})\, e^{i\alpha}|^2 = |\mathcal{A}(\mathbf{k})|^2$. For example, this makes all anti-symmetry axes appear identical to symmetry axes. Without the phase information, the initial state wave function thus cannot be reconstructed properly by taking the inverse Fourier transform on both sides of eq. (2.29).

The phase problem is fairly common and not restricted to photoemission spectroscopy. It is especially prominent in the evaluation of X-ray crystallography experiments [64, 65] and the natural consequence of an intensity measurement of any kind of wave, whether classical or quantum mechanical. This prevalence of the phase problem turns out to be a boon to the orbital tomography technique: The topic is well researched [66, 67] and the findings of the scientific community can be adapted for ARPES experiments. Consequently, the phase retrieval algorithms that have been employed for ARPES on molecular

systems [62, 63, 68] were developed before the advent of orbital tomography and are essentially identical [69, 70].

Lüftner et al. devised and applied an algorithm specifically designed for the evaluation of ARPES experiments [63]. The approach is a revised version of an algorithm originally developed by Fienup in the late 1970s [69, 71]. Fig. 2.7 (a) displays how a single iteration is carried out. The photoemission magnitude is extracted from the square root of the measured intensity and an arbitrary phase is applied (**A**). An inverse Fourier transform yields the first guess of the real space orbital (**B**). If the molecular orbital is only weakly perturbed by the chemical surroundings in the sample, its extent in real space can be estimated from the size of the molecule. One can then define a confinement area, beyond which the wave function should vanish. The wave function outside of the area is multiplied by a suppression factor close to zero, leading to a constrained real space wave function (**C**). The result is Fourier transformed into reciprocal space (**D**). When the predicted magnitude at the end of an iteration matches the experimental magnitude within a designated error bar, the procedure is concluded and the correct phase determined. Otherwise, if this convergence criterion is not reached, the phase is kept as the input for the next iteration, but the magnitude is replaced with the experimental one. The next iteration follows the same four steps starting with the new guess of the phase.

In principle, there is a limitless variety of phase retrieval algorithms that can also be combined with one another. As an example, the issue of having to know the size of the confinement area in the algorithm above can be elimated by an adaptation of Marchesini et al. [70]. Kliuiev et al. recently modified their procedure for application in ARPES experiments [62, 68]. The algorithm does not require a priori knowledge of the extent of the wave function as the confinement area in real space is instead updated at each iteration and (if successful) settles into the correct shape.

Since the phase appears to be lost during the measurement the phase retrieval process begs the question of where the phase information originates from. The prerequisite to recover the phase from an intensity measurement alone is the so-called *oversampling condition* [71, 72]. In short, the ratio of the number of data points of known versus unknown amplitude $\sigma_{\mathrm{OS}} = N_{\mathrm{known}}/N_{\mathrm{unknown}}$ has to be greater than 2 to solve the underlying set of equations for both amplitude and phase. The additional redundancy of increasing σ_{OS} beyond 2 makes the algorithms more resistant against adverse experimental influences like a low signal-to-noise ration [63]. Suppressing the wave function beyond the confinement area essentially creates a large amount of data points with "known" amplitude. The inverse Fourier transform connects the resolution in reciprocal space $\Delta k_{\mathrm{x,y,z}}$ with the entire extent in real space $d_{\mathrm{x,y,z}} \propto (\Delta k_{\mathrm{x,y,z}})^{-1}$. A finer resolution in the experiment can thus boost the oversampling ratio σ_{OS}. For reference, Lüftner et al. achieved $\sigma_{\mathrm{OS}} \approx 150$ in their study [63].

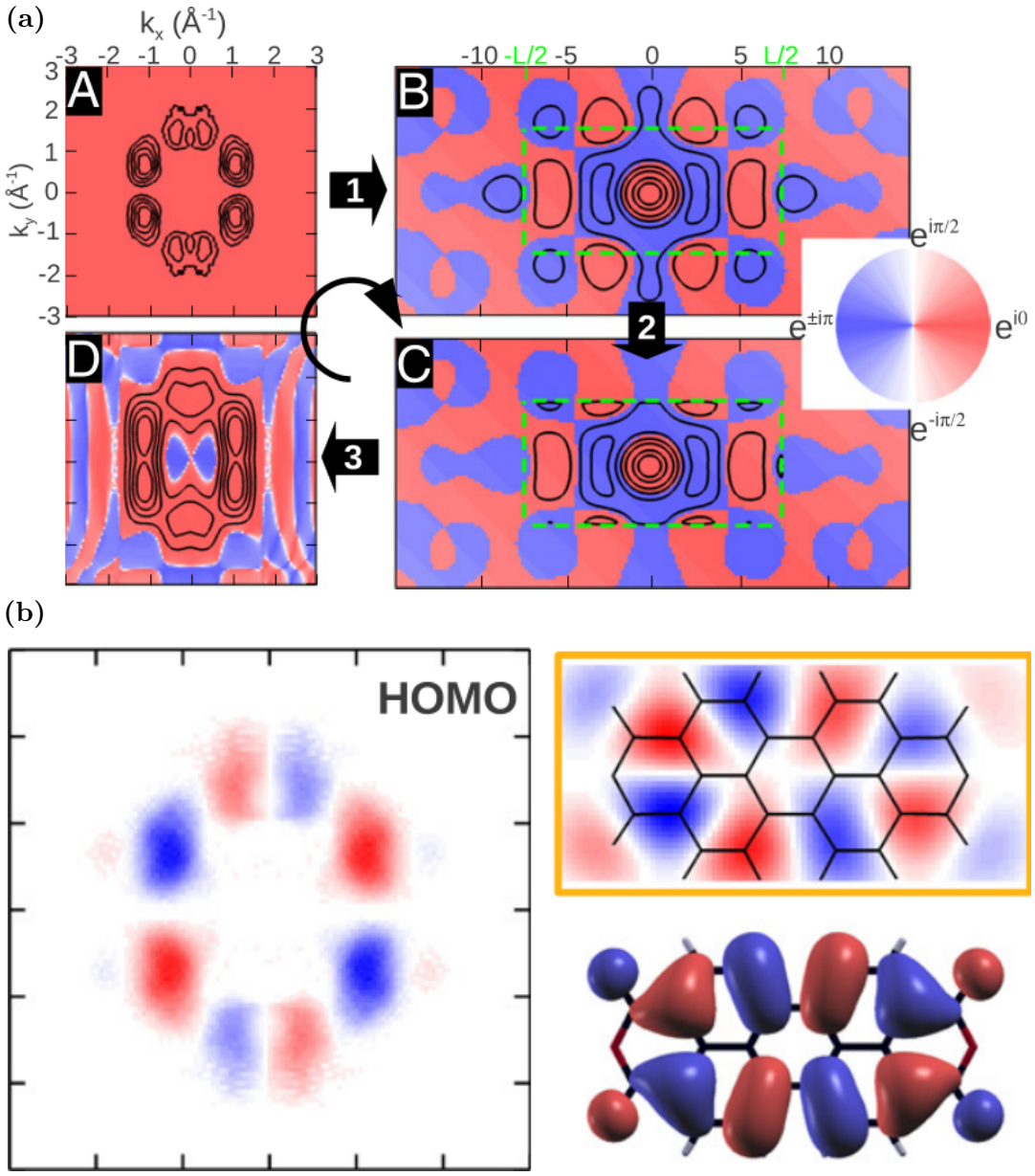

Figure 2.7: Iterative phase retrieval algorithm developed by Lüftner et al. [63]. (a) Description of a single iteration. Black lines indicate contour lines of identical magnitude while the color represents the phase: the photoemission magnitude $\sqrt{I(\mathbf{k})}$ with the current phase information (**A**) is translated into real space via an inverse Fourier transform. The magnitude of the result (**B**) is strongly suppressed outside a constraint area (**C**). A Fourier transform into reciprocal space leads to an updated PMM (**D**). Only the phase is kept from this output and used as the input alongside the experimental magnitude for the next iteration starting from (**A**). (b) Experimental PMM of HOMO of **P**erylene**T**etra**C**arboxylic **D**i**A**nhydride (**PTCDA**) for $E_{\mathrm{ph}} = 30\,\mathrm{eV}$ colored according to the retrieved phase information (left). Experimentally reconstructed real space orbital after 250 iterations (top right) in contrast to a DFT calculation (bottom right) drawn on the backdrop of the PTCDA molecule. Reprinted with author permission [63].

Besides retrieving the phase from experiment, the phase information can also be extracted from DFT calculations. This is the approach that Puschnig et al. chose in the initial publication in 2009 [40]. If the sample is well known and the hybridization sufficiently small, one can resort to the simulation of a gas phase molecule [73]. Nevertheless, retrieving the phase from the experiment is the more reliable approach the further the measured molecular system is from the simulation.

All of the aforementioned aspects apply both to the two- and three-dimensional orbital tomography. The three-dimensional reconstruction requires data taken at various photon energies to make several hemispherical "cuts" through the molecular orbital in reciprocal space. This adds the challenge of accurately normalizing the photoemission intensity of the experiment [61, 73]. We will take a look into this issue after discussing the technical details in the next chapter. Furthermore, the photoelectrons emitted with negative k_z in the direction of the sample are lost and cannot be detected with the currently available experimental setups. In a three-dimensional reconstruction, this data is usually extrapolated by relying on the symmetry of the isolated molecule. The adsorbed molecules certainly do not retain the same symmetry axes as in the gas phase, but it is a viable approach if the interaction between the molecule and its chemical surroundings are weak. Similarly, missing data points due to a limited photon electron energy range have to be approximated as well.

3 Experimental details and sample preparation

In the following chapter the details of the experimental setups and measurement methods are delineated. Since the topic of this thesis concerns the electronic and structural properties of molecules close to the sample surface, all experiments have to be conducted under **U**ltra-**H**igh **V**acuum (**UHV**) conditions. If they were to be done at ambient pressures, the sample would quickly be covered by contaminants within the air. On top of any undesired interaction with the molecules (e.g. oxidation) this would severely reduce the signal from the area of interest in the surface sensitive photoemission measurements. The UHV is generated and maintained by a multi-stage pumping system which achieve a base pressure on the order of 10^{-10} to 10^{-11} mbar.

3.1 Low-energy electron diffraction

A common technique to assess the structural order of surface lattices is through **L**ow-**E**nergy **E**lectron **D**iffraction (**LEED**) [74]. LEED is based on the coherent scattering of incoming electrons at the surface of a sample, see Fig. 3.1 (a): free electrons are supplied by thermal emission from a filament and accelerated towards the sample with the voltage U_{A}. Additional lens elements lateral to the flight path collimate the electronic beam into an area on the surface with a diameter of about 1 mm. Once at the surface, the electrons can scatter both elastically and inelastically with the atoms and molecules of the sample. Electrons which are reflected back into the upper hemisphere above the sample pass through a retarding voltage which inelastically scattered electrons do not have sufficient energy to penetrate. Electrons who did not lose any energy during their scattering events in the sample are subsequently accelerated by a high voltage $U_{\mathrm{Screen}} \approx 5\,\mathrm{kV}$ towards a fluorescence screen, where they can generate interference patterns that are recorded by a CCD camera.

If there is no long-range order within the sample the interference of the reflected electrons ultimately results in an incoherent and diffuse diffraction profile spread across all

angles. On the other hand, if the surface has a periodic structure the wave vectors for constructive interference can be calculated by the Laue condition [74]. For any real space lattice constructed from the lattice vectors $\mathbf{a}_1$, $\mathbf{a}_2$ and $\mathbf{a}_3$, there is a corresponding reciprocal lattice with reciprocal lattice vectors $\mathbf{b}_1$, $\mathbf{b}_2$ and $\mathbf{b}_3$. Elastic scattering events at this lattice occur for scattering wave vectors $\mathbf{G}_{hkl} = \mathbf{k}_{\text{out}} - \mathbf{k}_{\text{in}}$ where

$$\mathbf{G}_{hkl} = h\mathbf{b}_1 + k\mathbf{b}_2 + l\mathbf{b}_3 \qquad h,k,l\,\epsilon\,\mathbb{Z} \tag{3.1}$$

with incoming and outgoing wave vectors $\mathbf{k}_{\text{in}}$ and $\mathbf{k}_{\text{out}}$, respectively.

The primary electron kinetic energy E_{kin} is usually set between $10 - 200\,\text{eV}$ so that the electrons' wave length is on the order of the interatomic distances in the lattice [75]. As a secondary effect, electrons within this kinetic energy range have a relatively low inelastic mean free path $\lambda \approx 1\,nm$ (see fig. 2.2). The damping inside the sample is in fact so strong that the lattice becomes effectively almost two-dimensional from the perspective of the elastically reflected electrons. This causes the diffraction maxima to be spread along the entire k_z direction perpendicular to the surface with only small variations in the diffraction intensity.

Fig. 3.1 (b) shows an exemplary LEED pattern from a clean Ag(111) surface with an electron kinetic energy $E_{\text{kin}} = 90\,\text{eV}$. The central spot is blocked by the electron gun while the six-fold symmetry of the face-centered cubic silver cut at the (111)-plane is evident by the six diffraction spots at higher polar angles. Using the known lattice constant of silver $a_{\text{silver}} = 4.08\,\text{Å}$ [76] and E_{kin} one could calibrate the LEED instrument to enable a quantitative structural analysis on other samples.

LEED patterns of molecular adsorbates can be quite challenging to unravel. A supporting software is therefore helpful which in this work is the *Spot-Plotter* package by P. Bayersdorfer [77].

3.2 Sample growth

The samples surveyed in this thesis are always prepared in the UHV chamber right before the measurement to achieve a pristine surface free of contaminants from the atmosphere. All samples consist of a noble metal substrate with an evaporated molecular thin film on top. To facilitate the best possible sample quality, the metal single crystals are first cleaned by bombardment with Argon^+ ions. The ions are targeted at the sample with an accelerating voltage of $U_a \approx 1\,\text{kV}$, where they collide with and physically remove the surface atoms. The process is controlled by monitoring the sample current $I_{\text{sample}} \approx 5\,\mu\text{A}$ necessary to keep the sample electrically neutral. The sputter duration is about 30 minutes and the sample tilted towards the incoming beam to prevent burying any adsorbate

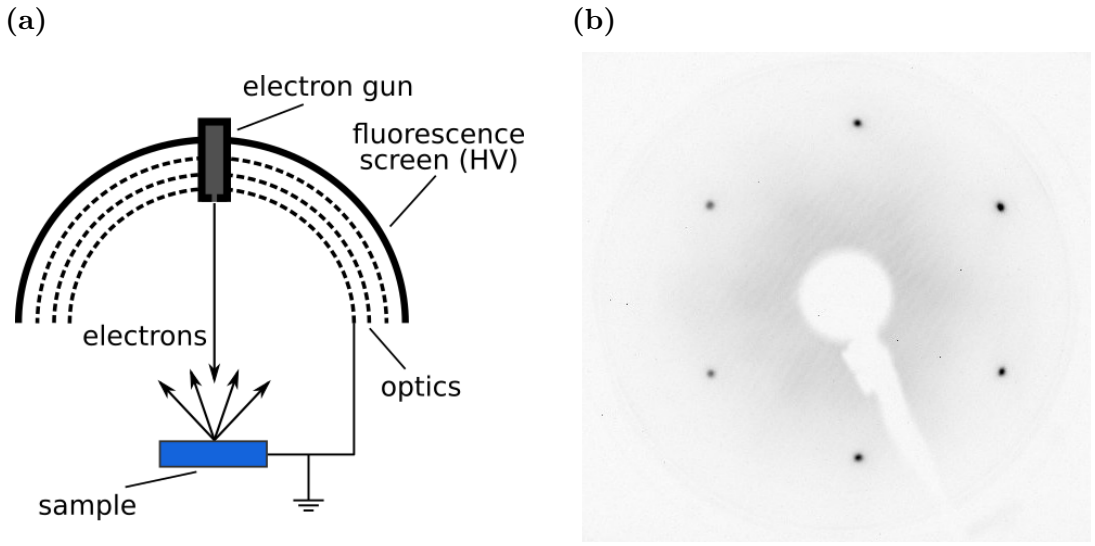

Figure 3.1: (a) Schematic LEED measurement setup. (b) Exemplary LEED pattern of a clean Ag(111) surface with a primary electron kinetic energy of $E_{\mathrm{kin}} = 90\,\mathrm{eV}$.

material in the bulk. If successful, the sputter procedure leaves a clean, but disordered and cratered surface. The clean surface is subsequently heated to about two thirds of the melting temperature in order to reestablish periodic order of the surface. The increased thermal energy during this annealing procedure lets the surface atoms migrate to energetically favorable positions. Since the bulk structure is unaffected by the sputtering and annealing, the surface atoms settle into the positions of the original structure orientation. Many surfaces exhibit surface reconstructions [78] that depend on the preparation conditions, but most noble metal surfaces can be prepared properly within a large range of annealing temperature and duration. To remove thicker films of contaminants, it can be necessary to carry out more than a single cleaning cycle. The successful preparation of a pristine surface is verified by a LEED experiment.

The next step in the sample fabrication is the evaporation of the organic material. The molecules are provided by a home-made thermal evaporator of simple, but reliable design: first, the molecules are inserted into a glass crucible ex situ. The crucible is then put into a metal socket mounted inside a UHV-tight tube. An electrically isolated tungsten wire is wound inside the socket and in situ heated electrically via two feedthroughs at the back of the tube. The metal socket ensures that the heat is distributed evenly across the crucible and the molecules inside. Two additional wires next to the crucible act as a thermocouple and provide a temperature gauge through a voltage measurement. During evaporation, the heating tungsten wire and the thermocouple are connected to a PID-controller which fixes the temperature at a specified value. The additional thermal energy enables some molecules to leave the crucible, travel through the vacuum and adsorb on the sample positioned opposite of the evaporator. The adsorption rate can be adjusted by varying

either the distance between sample and evaporator or the temperature inside the crucible. If the metal substrate is kept at room temperature, essentially every molecule that makes it to the surface sticks and remains on the sample. This is because the molecules leave the evaporator with very low, thermal kinetic energies and the evaporation temperature of the molecules inside the crucible bound by van-der-Waals forces is several hundred degrees Celsius. The molecules used in this thesis all have a purity of 99 % and higher and leave the crucible intact before chemical reactions at higher temperatures would destroy them.

Before a freshly filled evaporator can be used in a new experiment, the evaporation rate has to be calibrated. One method is the evaluation of photoemission intensities from core levels in XPS spectra, see section 2.1. To start out, one takes a reference XPS measurement of the clean metal substrate before evaporating any molecules. This spectrum is then compared to a second one after evaporation. The damping of the substrate features by the adsorbants can be used to determine the thickness of the organic thin film with eq. (2.2). Furthermore, the rise of features belonging to atoms inside the molecules also lend themselves for the calibration. Since carbon is present in any molecule, the C-1s signal is usually the most intense of the adsorbant features. A reference for this measurement can be established by heating a sample with an evaporated molecular multilayer on top to about the deposition temperature of the evaporator. In many cases – and for every material system in this thesis – the first molecular layer is more strongly bound to the metal substrate than further molecular layers to one another. Any material beyond the first monolayer thus desorbs during this temper procedure. The photoemission intensity of the C-1s peak of this sample then establishes the reference for a single monolayer.

Fig. 3.2 shows an exemplary calibration on an Ag(110) substrate of an evaporator filled with pentacene molecules. After the first evaporation of molecules with $t_{\mathrm{eva}} = 70\,\mathrm{min}$ and $T_{\mathrm{eva}} = 217\,^{\circ}\mathrm{C}$ corresponding to about 1-3 monolayers, the carbon 1s feature is recorded in the XPS experiment (black). Next, the sample is heated in the temper process to remove all but the first monolayer in contact with the silver substrate. As expected from the reduced coverage (red), the C-1s signal is reduced, while the silver features are increased in the subsequent XPS measurement. The damping of the spin-orbit split silver 3d features can be evaluated with eq. (2.2) and the known coverage $n_{\mathrm{after}} = 1$ after tempering to determine the coverage before tempering. The equivalent method of using the increase in the C-1s signal and eq. (2.3) is also possible and – if done correctly – yields the same result.

Before the evaluation of the peak intensities, the spectra have to be cleared of spurious photoemission satellites caused by the non-monochromatized Aluminum K_{α} X-ray source [79]. The most intense photon line of the $\mathrm{K}_{\alpha_{1,2}}$ transiton has an energy of $E_{\mathrm{ph}} = 1486.6\,\mathrm{eV}$, but there are several additional transitions that generate photons at other energies as well. Two minor contributions stem from the K_{α_3} and K_{α_4} lines with a

photon energy of $\Delta E_{\alpha_3} = 9.8\,\text{eV}$ and $\Delta E_{\alpha_4} = 11.8\,\text{eV}$ above the $K_{\alpha_{1,2}}$ line, respectively. They have a relative intensity of 6.4 % and 3.2 % compared to the main $K_{\alpha_{1,2}}$ line. The other spurious photon lines are not strong enough to influence any part of our evaluation. All spectra shown in fig. 3.2 have been corrected for these XPS satellites.

The lowest error bar in the evaluation is achieved by analyzing the photoemission features with the highest intensity and therefore best signal-to-noise ratio. This corresponds to the silver $3d_{5/2}$ level for the substrate and the carbon 1s for the molecular thin film. To get an estimate for the mean free path λ of electrons in the organic material, one can resort to a study on organic Alkanethiols by Lamont et al. [44]. We choose these values instead of Seah et al. [22] since the former are more precise and closer to the molecules examined in this thesis (even though our E_{kin} is slightly outside their surveyed range). The inelastic mean free path of photoelectrons from the C-1s and Ag-$3d_{5/2}$ features is then about $\lambda_{\text{C-1s}} = 28.1\,\text{Å}$ and $\lambda_{\text{Ag-3d}_{5/2}} = 26.8\,\text{Å}$. The high mean free path compared to the thickness of the molecular thin film means that the damping of the substrate features is rather low (see fig. 3.2). On the other hand, the height of the C-1s peak is very sensitive to the coverage in this regime. We will thus calibrate the evaporator with the C-1s feature to increase the precision of the evaporation rate, since it is possible to prepare a monolayer through the temper procedure in this case. Nevertheless, there are other combinations of materials where the temper procedure is not possible or reliable and the calibration has to be done using the substrate features instead. The intensity of the C-1s feature is extracted by integration over the entire area after subtracting a linear background. After the tempering process, the C-1s peak decreases to $I_{\text{C,after}} = (0.679 \pm 0.014)\, I_{\text{C,before}}$. With the known coverage $n_{\text{after}} = 1$, $x_{\text{after}} = 0$ we calculate the coverage by applying eq. (2.3) with the extracted intensities of the carbon 1s features. Unfortunately, the interlayer distance L_0 is not known for this system. On Cu(110) however, Söhnchen et al. evaluated a very low spacing of $L_0 = 1.9\,\text{Å}$ [80]. In the absence of other data we will use this value for L_0, even though one could expect a slightly higher distance for the chemically less reactive Ag(110) surface. The inaccuracy we incur is below $\sim 1\,\%$ since the inelastic mean free path is an order of magnitude larger compared to the film thickness $\lambda \gg L$.

These numbers in eq. (2.3) yield an initial coverage after evaporating for 70 min of $n_{\text{before}} = 1$, $x_{\text{before}} = (0.51 \pm 0.03)$, corresponding to (1.51 ± 0.03) monolayers. The resulting evaporation rate at $T_{\text{eva}} = 217\,°\text{C}$ is therefore one monolayer per $(46.5 \pm 1.0)\,\text{min}$.

LEED experiments complement every step of the XPS measurements above. The temperature onset at which molecules leave the evaporator is quickly determined by the damping of substrate spots in the LEED pattern. The same effect also expedites the production of a multilayer sample for the temper procedure, as one can simply deposit material until the substrate features vanish. Lastly, the interaction between metal substrate and the first monolayer on top commonly results in a characteristic adsorption

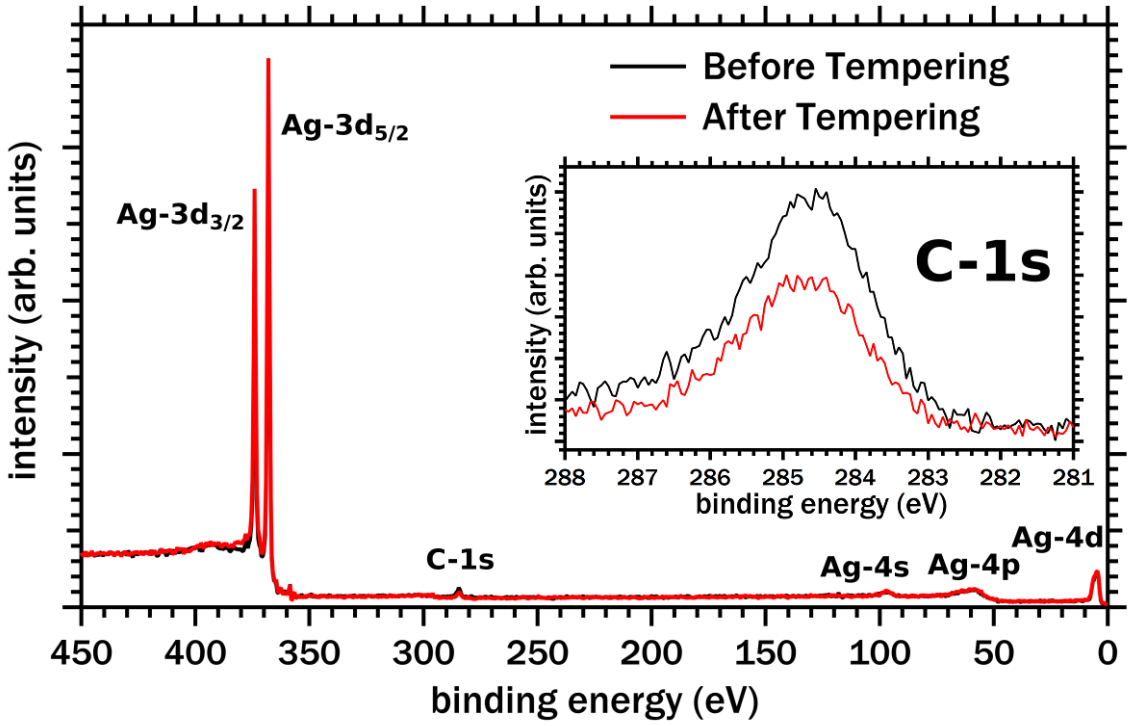

Figure 3.2: Calibration of the evaporation rate using XPS with photons from an Aluminum K_α source ($E_{\text{ph}} = 1486.6\,\text{eV}$). Pentacene thin film grown on Ag(110) before (black) and after tempering down to a single layer (red). All spectra have been cleared of satellites arising from the non-monochromatized X-ray source. The inset shows a detailed scan around the carbon 1s core level.

lattice that is probed by the LEED measurement. This pattern can then be compared to literature or previous experiments.

With the calibrated evaporator ready to go, there is still one easily overlooked detail when growing multilayer systems. The different chemical environment can result in a layer-dependent superstructure and density of molecules. For example, an amount of material that precisely completes the first molecular layer might not fit for a full coverage of a second layer on top [10]. If the additional layers grow with a periodic order, a LEED measurement can reveal the molecular density and the evaporation recipe can be adjusted accordingly.

Even when taking into account that most molecules end up on the interior chamber walls instead of on the sample, a single filling of the crucible is sufficient for a vast amount of preparations. Considering the low coverage of the substrate, an evaporator is only exchanged to take it to another research facility, maintenance or to replace the type of molecule with another one.

3.3 Momentum microscopy

The instrument used to gather the experimental ARPES data for this work is a so-called **P**hoto**E**lectron **M**omentum **M**icroscope (**PEMM**) [81]. Its experimental design is illustrated in Fig. 3.3. Photoelectrons emitted into the upper hemisphere above the sample are accelerated towards the microscope optics by the applied high voltage. Once inside the apparatus, they are separated according to their kinetic energy and angle within the **H**emispherical **D**eflection **A**nalyzer (**HDA**). The second HDA is not essential to the operation of the PEMM, but corrects an abberation caused by the ellipsoidal trajectory of the electrons [82]. In the $\sim 1/r$ potential inside the HDA all electrons move on ellipsoids that coincide at the entrance slit (by default) and after each full rotation $\alpha = 360\,^\circ$. Cutting the ellipses at a certain position produces an abberation $\propto \alpha^2$ between electrons of different E_{kin} and/or entrance angle that is most severe after moving through a single HDA with $\alpha = 180\,^\circ$. A second, identical analyzer positioned right after the first one thus makes the electrons complete the full ellipsoid $\alpha = 360\,^\circ \widehat{=} 0\,^\circ$ [83]. This erases the projection abberation, improving the resolution of the spectrometer. A two-dimensional **M**ulti-**C**hannel **P**late (**MCP**) is located in the Fourier plane of the experiment and detects the electrons at the selected E_{kin} for each $(k_{\mathrm{x}}, k_{\mathrm{y}})$ tuple in parallel. The raw data is recorded by a CCD camera behind the MCP and read out with a software on a connected computer.

The best possible wave vector resolution of momentum microscopes at the time of this writing is about $\Delta k = 0.0049\,\mathrm{\AA}^{-1}$, while the energy resolution reaches $\Delta E = 12\,\mathrm{meV}$ [81]. These values are more than sufficient to resolve the broad molecular features in reciprocal space and binding energy which we probe in this work. The instrument can also be outfitted with an optional state-of-the-art, two-dimensional spin filter that is positioned behind the HDA [84]. In a nutshell, a PEMM is a modified photoemission electron microscope with the detector plate in the Fourier plane of the electron beam path. The same device can still be used to image the sample in real – instead of reciprocal – space by applying different voltages to the lens elements. The real space mode is also used to align the sample relative to the photon beam and microscope optics as well as to identify and avoid physically damaged areas on the surface.

The twin-analyzer scheme eliminates one projection abberation, but there are more factors that have to be addressed and corrected in the raw data. The detector is subject to a non-zero noise level even if no photoelectrons are emitted from the sample towards the MCP. A reference picture of this *darkfield* $I_{\mathrm{darkfield}}$ can be taken while the photon beam is blocked before entering the chamber. Once the light is turned on and photoelectrons hit the MCP, there is another issue due to manufacturing reasons of the MCP. Not all pixels on the multi-channel plate are identical and equally sensitive to incoming electrons

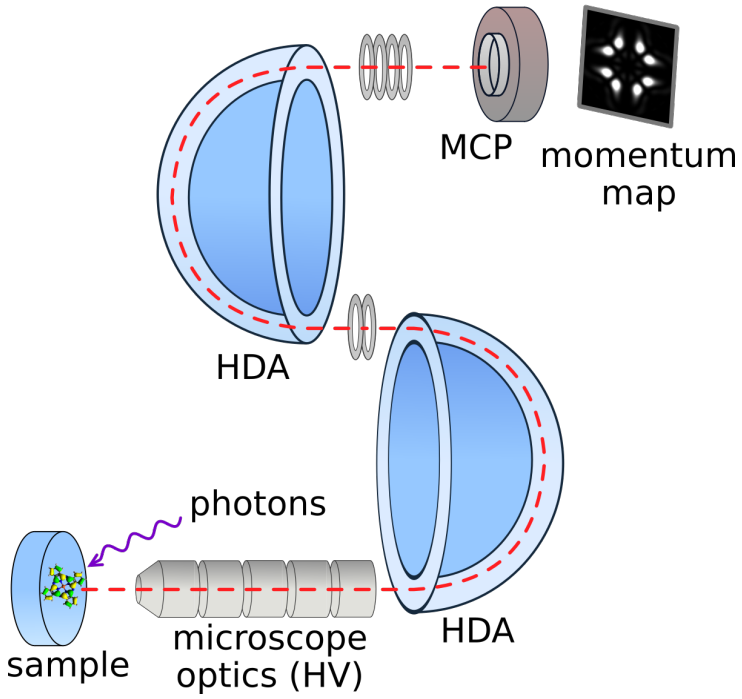

Figure 3.3: Photoelectron momentum microscope setup for the parallel detection of electrons at specific (k_x, k_y) tuples at a chosen kinetic energy.

which results in a position-dependent response function of the detector. To correct for this *brightfield* imperfection, a reference picture $I_{\text{brightfield}}$ is recorded by using a mercury lamp with a large illumination area on the sample. The light intensity profile that the PEMM analyzes in real space mode is virtually flat, so that any deviation from a constant intensity profile can be attributed to the response function of the MCP. Using these two references, any measured intensity profile I_{raw} can be corrected with the equation

$$I_{\text{corrected}} = \frac{I_{\text{raw}} - I_{\text{darkfield}}}{I_{\text{brightfield}}} \,. \tag{3.2}$$

All PMM shown in this thesis are treated this way and hence show $I_{\text{corrected}}$.

The response function of photoemission spectroscopy detectors is generally dependent on the kinetic energy of the photoelectrons E_{kin} [85, 86]. This *analyzer transmission function* has to be known or calibrated before a quantitive analysis of features at different E_{kin} can be attempted [87]. For the PEMM however, the transmission function at each (k_x, k_y) tuple is independent from E_{kin} [81], so no additional correction has to be applied.

Normalizing the intensities of different photon energies E_{ph} poses a far bigger challenge [73]. The photon flux for all experiments shown in this thesis is measured by a gold mesh in the path of the light. The grid is the last element that the photons pass before impinging

on the sample. A fraction of the photons hits the grid and generates a voltage U_{grid} against ground that is used as a measure of the total photon flux. This kind of gauge is unfortunately riddled with experimental uncertainties. Even though the grid is made of tightly packed, thin wire, the light beam only illuminates a few strands at a time. Depending on the trajectory of the light beam with changing E_{ph}, the beam might hit one additional wire or one less which woud distort the voltage measurement. The profile of the photon wave front naturally influences the voltage as well. Furthermore, there are several possible excitation channels – like (surface) plasmons and photoelectrons – but only some of them leave a trace in the voltage measurement. These effects are also energy dependent and influenced by the cleanliness of the surface of the gold mesh. We rely on the experimental data on the photoelectron cross section $\mu(E_{\mathrm{ph}})$ by Hagemann et al. [88] which are included in two overviews Henke et al. presented in [89] and tabulated in [90]. Missing values for $\mu(E_{\mathrm{ph}})$ have been interpolated linearly from the experimental points. Using these data sets, the measured intensity I_{raw} can approximately be normalized with the equation [91, 92]

$$I_{\mathrm{normalized}} = \frac{\mu(E_{\mathrm{ph}})\, E_{\mathrm{ph}}}{U_{\mathrm{grid}}\, t_{\mathrm{int}}}\, I_{\mathrm{raw}} \tag{3.3}$$

with the integration time per kinetic energy step t_{int} set in the scan.

For a quantitive analysis, the position where an electron hits the MCP has to be related to the wave vector components k_{x} and k_{y}. To this end, the scaling in reciprocal space can be calibrated via the high-symmetry points of the substrate [73]. Before the actual measurement, we evaluate the position of the known distance $\overline{\Gamma\mathrm{Y}} = 0.73\,\mathrm{\AA}^{-1}$ on the clean Ag(110) surface [93]. The scaling is linear across the detector [81, 94], aside from possible stray fields and inhomogeneities at the very edge. At the same time as fixing the scaling, th measurement also establishes the position of the Γ-point located right between both Y-points.

An alternative calibration method is by means of photoelectrons emitted with the maximum possible parallel wave vector $k_{\parallel}$ and $k_{\mathrm{z}} \approx 0$ [10]. If this condition is satisfied on the MCP, a circular *photoemission horizon* is clearly visible by a sudden drop in photoemission intensity. Note that depending on the chosen E_{kin} and the wave vector scaling the horizon might lie partially or entirely beyond the MCP. If the horizon is visible on the detector, the connection of the wave vector with the kinetic energy $E_{\mathrm{kin}} = \frac{\hbar^2 k^2}{2m_0}$ at the edge of the photoemission horizon $k = k_{\parallel}$ determines the scaling. For the known E_{kin}, the total wave vector at the horizon is

$$k = \frac{\sqrt{2m_0 E_{\mathrm{kin}}}}{\hbar}\,. \tag{3.4}$$

This kind of calibration of the wave vector scaling still leaves an azimuthal rotation around the k_z axis undefined. Mapping $k_{\parallel}$ onto (k_x, k_y) requires measuring features of known symmetry to determine the azimuthal rotation.

In conclusion, the first method has the advantage of defining both k_x and k_y and being independent from the excitation parameters. Its drawback is that it necessitates a measurement of the clean substrate or a sharp feature of well-known position in reciprocal space. On the other hand, the second method can be carried out on the fully prepared sample. The photoemission horizon has to be visible on the MCP, however, and the azimuthal angle is only determined through bands or orbitals of known symmetry.

4 Orbital reconstruction on two-dimensional molecules

In this chapter we will analyze experimental ARPES data and reconstruct the wave functions of a molecular orbital in real space with a plane wave final state introduced in in section 2.4. On first sight, one might question the purpose and benefit of this endevour. The relevance of having a tangible representation of physical phenomena should not be underestimated. There are of course more elaborate final state descriptions which are universally more accurate than a plane wave approximation [38, 95, 96]. However, they are also computationally more expensive and challenging to implement. The simple connection of the measured ARPES data in reciprocal space with the real space orbitals is also lost. E.g., the elongation of a molecular orbital in the direction of another molecule in real space is intuitively understood as hybridization even without a complementary theoretical calculation.

The concept of electron orbitals is also accompanied by the philosophical question of whether wave functions actually exist in reality or just as a convenient mathemtical construct. The "Copenhagen" interpretation of wave functions views them as an abstract mathematical tool that does not have to exists in the real, physical world [97]. This interpretation is the most prevalent among scientists and most commonly taught in physics and chemistry courses [98]. Even though the concept of wave functions has been around for about a century, this question is still open to debate. The inclined reader is refered to an essay on the metaphysical aspect of orbitals by Schwarz [99].

The two-dimensional electron density $\left|\psi_i(\mathbf{r})\right|^2$ of the pentacene HOMO and LUMO has been experimentally determined through scanning tunneling microscopy by Repp et al. already in 2005 [100]. They measured the position-dependent gradient of the tunneling current dI/dV using a tip functionalized with a pentacene molecule. The sub-molecular real space resolution in combination with DFT calculations of the isolated molecule enabled the authors to identify the HOMO and LUMO. However, the wave functions $\psi_i(\mathbf{r})$ have not been uncovered, but the position of the nodes in the electron density nevertheless permits an assertion about the phase relation between the individual molecular features.

Reconstructing the wave function without making assumptions requires additional information about a molecular orbital which is for example contained in the photoemission

signal of an ARPES experiment [63]. The technique of determining molecular wave functions from experimental ARPES data – whether alone or in conjuction with theory calculations – is usually labelled *orbital reconstruction*. This type of reconstruction relies on the plane wave final state described in subsection 2.3.3. It is therefore tied to the applicability of the PWA for a given system. The first orbital reconstruction was performed by Puschnig et al. on a monolayer of sexiphenyl evaporated on Cu(110) [40]. They reconstructed the wave function of the former HOMO and LUMO of the molecule in a decent agreement with DFT calculations for a two-dimensional cut through reciprocal space at $E_{\mathrm{kin}} = 33.1\,\mathrm{eV}$ (HOMO) and $34.7\,\mathrm{eV}$ (LUMO), respectively.

In this chapter, we will propel the orbital tomography technique into the third dimension. So far, two comparable studies on a monolayer of another archetype molecule have been published [61, 73]. Both of them reconstructed the HOMO and LUMO of PTCDA on an Ag(110) substrate. We will focus on the reconstruction of the HOMO of another organic molecule – pentacene – from a sample of an evaporated pentacene monolayer on top of Ag(110).

Just like the other works of orbital reconstruction, we will employ the plane wave approximation for the final state. The difference of the PWA to an IAC final state including multiple electron scattering is briefly discussed for the isolated pentacene HOMO by Krüger in [95]. He specifically analyzed the predictions for the circular dichroism as well as the **P**hotoelectron **M**omentum **M**ap (**PMM**) for the experimental geometries $\mathbf{A} \parallel \mathbf{k}$ and $\mathbf{A} \perp \mathbf{k}$. For now, we tentatively state that they are comparable for our experimental geometry and that the PWA is a suitable approximation for our system. We will go into the details later in the discussion in this chapter.

4.1 Sample selection and preparation

The first step for this project is selecting a suitable molecule that makes up the organic thin film. The use of the plane wave approximation dictates that the final state of the organic layer should be well describe by a plane wave. One aspect of the photoemission process that is entirely absent in a plane wave final state is the elastic scattering of photoelectrons at the atoms inside the molecule. The strength of this electron scattering is tied to the potential surface inside the system, which in turn is dependent on the atomic number [11]. This means that in order to minimize the intensity of elastically scattered electrons, the molecule has to be comprised exclusively of atoms with low atomic numbers. It should also be fairly large so that any elastic scattering that *does* occur is diffuse and spread across all angles. The reason being that the real space extent of the molecular initial state correlates with the sharpness of the elastically scattered features in reciprocal space. The

intensity from scattered photoelectrons can in this case be separated from the unscattered signal without difficulty. Another course of action is using the low inelastic mean free path at the typical energies of an ARPES experiment [22] to suppress the elastically scattered signal even further. The inelastically scattered photoelectrons produce only a diffuse background that can be filtered out just like above. It is therefore advisable to evaporate only a single monolayer on the substrate, so that the primary electrons immediately enter the vacuum above the sample on their trajectory to the detector. For a photoelectron to be scattered elastically, it has to move at least some distance inside the sample, during which time it can scatter inelastically. Furthermore, the probability of being scattered in the direction of the detector is comparatively small for the kinetic energies in a typical ARPES experiment ($\sim 10 - 120\,\mathrm{eV}$). Fig. 4.1 shows the angle-dependent cross section of electrons scattered elastically at a carbon (solid lines) and at a silver atom (dashed lines) for various kinetic energies. The calculations are based on the muffin-tin approximation for the potential around the atom and performed with the *Electron Diffraction in Atomic Clusters* code (EDAC) of de Abajo et al. [101].

There are minor and negligible side maxima for silver ($Z_{\mathrm{Ag}} = 47$) and carbon ($Z_{\mathrm{C}} = 6$),

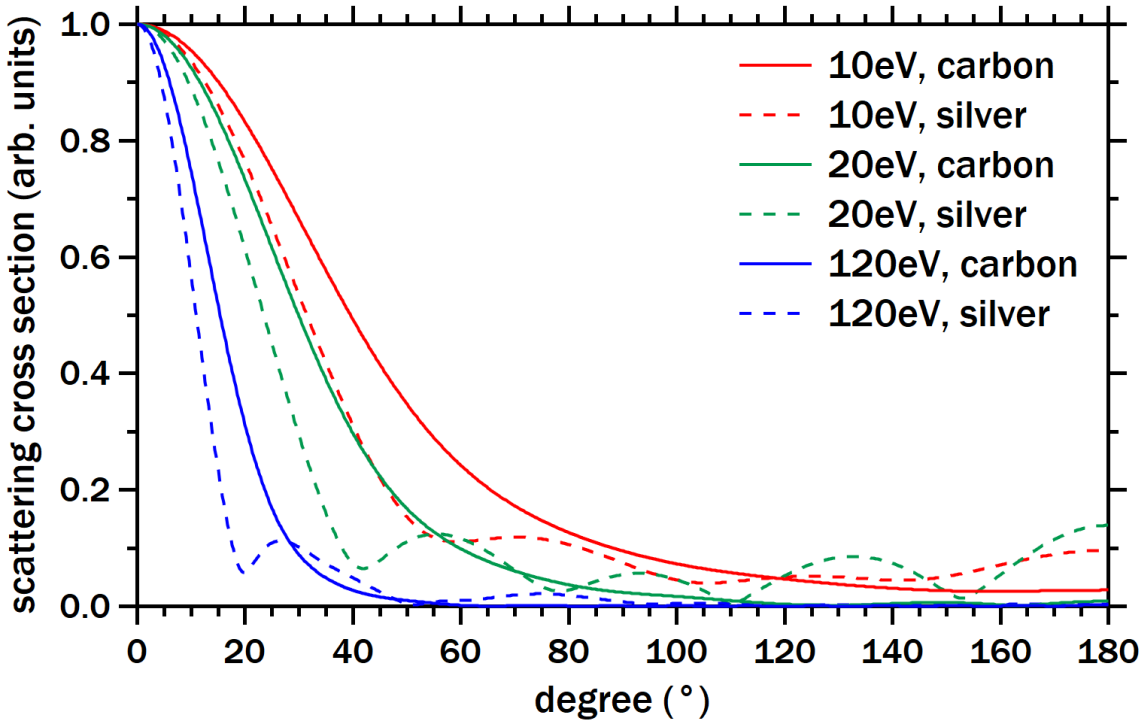

Figure 4.1: Angle-dependent cross section of electrons elastically scattered at a carbon (solid lines) and silver atom (dashed lines) for electron kinetic energies of $E_{\mathrm{kin}} = 10\,\mathrm{eV}$ (red), $20\,\mathrm{eV}$ (green) and $120\,\mathrm{eV}$ (blue). Zero degrees (forward scattering) is the dominant scattering direction in the entire relevant energy range, especially for carbon and at higher kinetic energies.

respectively, but forward scattering is the main deflection direction across the entire energy range. Photoelectrons that are emitted from the monolayer cannot reach the detector through forward scattering only, however, since the the vacuum begins immediately above the organic layer. One available scattering channel is the deflection within the molecular layer, which requires scattering events accumulating to about 90° plusminus the acceptance angle of the detector. Alternatively, the photoelectrons can be backscattered at the silver substrate. Both pathways are far less likely than forward scattering and are further damped by the long trajectory within the sample.

One molecule that meets all the criteria is the organic molecule *pentacene*. Its structure is displayed in fig. 4.2. Pentacene is made up exclusively of low-Z elements, namely carbon (black) and hydrogen (gray). Pentacene has three symmetry axes through its center and along each Cartesian plane and is two-dimensionally flat in the gas phase. The molecule thus resembles five benzene rings linearly glued to one another at the edges and surrounded by hydrogen atoms in the molecular plane. It has the additional benefit of being a well-studied archetype molecule both in fundamental research and and for prototype devices [102–104]. Many of its characteristics are already known, especially concerning the growth on various substrates [80, 105–107]. Neighboring molecules also do not have any relevant overlap of molecular orbitals in the valence region (unless stacked on top of each other). The molecular orbitals are therefore very close to those of the isolated molecule. A first procedure for the synthesis of pentacene was already published in 1912 [108]. One straightforward reason for the popularity of pentacene is found in its material properties: several publications in the early 2000s already indicated that it has a high charge mobility and exciton diffusion length [109, 110], making it a suitable candidate in organic solar cells [111, 112] and thin film transistors [113–115]. Electronic devices based on organic materials like pentacene are also flexible and can thus cover on any kind of (curved) surface or be used in foldable applications [116–119]. The manufacturing process is also cheap and simple, since the molecules can simply be printed on a substrate [120–122]. Today, it is widely available and inexpensive to produce which benefits its application in devices as well as in fundamental research.

Just like for the choice of molecule, the substrate has to fulfill several requirements. The first prerequisite is that the molecules can grow in a phase with a single orientation on the surface. While it is not categorically impossible to reconstruct the molecular wave functions in the presence of several domains, the signal from each inequivalent domain would have to be disentangled. The reason being that for the reconstruction of *one* molecular orbital, each tuple in reciprocal space has to have exactly *one* value for the phase. If there is more than one domain, e.g. with a different azimuthal alignment, their photoemission signal might overlap for some emission angles, destroying this one-to-one correspondence. Depending on the system at hand, possible methods to untie degenerate

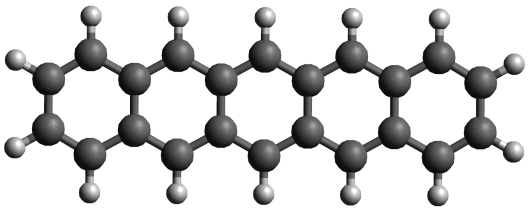

Figure 4.2: Pentacene structure and elemental makeup. The molecule is composed of five hexagons made of carbon (black) and laterally surrounded by hydrogen atoms (gray). Pentacene has a flat, two-dimensional geometry when a single molecule is isolated in the gas phase.

orbitals would include fitting routines and/or a clever choice of light polarization. The two-fold symmetry of pentacene implicates that the substrate can at most be two-fold symmetric as well. Using a substrate with a higher symmetry would result in the growth of several energetically equivalent domains that are not all aligned identically. In principle, such a system could still be used for the orbital reconstruction, but only if the domain size is bigger than the measurement spot in the ARPES experiment. For the current generation of PEMM instruments, the domain sizes would have to be on the order of $\sim 10\,\mu m$ [123]. A further reduction of the measurement spot below $1\,\mu m$ has recently been achieved on other instruments [124, 125], but can lead to issues due to the increased spherical abberation [126]. For comparison, the typical molecular domain size on noble metal surfaces is on the order of the terrace size and hence roughly $\sim 200\,nm$ (with the commercially available orientation accuracy of $\geq 0.1\,\%$ [127, 128]). The connection to the terrace size is related to the diffusion of the molecules on the substrate during the growth process. The energetically most advantageous adsorption site is in the valley next to a step edge where a single molecule is laterally covered by the atoms in the rising edge. If the diffusion length of the molecules is sufficiently high to reach these edges, the growth of each domain will start from there and at best cover a single terrace. If the diffusion length is lower, e.g. at lower temperatures during the growth process, the molecules will form additional condensation centers and the average domain size will decrease.

The second condition for this study is that the hybridization between the substrate and the molecules is so low, that it can be neglected without much of an error. Note that this is only relevant for the reconstruction of a mostly unperturbed molecular orbital as we aim to do here. There is no restriction for the reconstruction of a hybridized or even completely delocalized wave function. The most substantial change from a localized molecular orbital to a delocalized wave function is the method of phase retrieval, which would involve periodic boundary conditions. A variety of materials fulfill this prerequisite, including the noble metals copper, silver and gold. These elements have the advantage of being quickly and reliably conditioned via argon ion bombardment and a subsequent

annealing procedure as described in section 3.2. Even though it is not the target of this project, this particular metal-organic interface also serves as a model for a real electronic device, where the functional organic element has to be attached to the power grid via a metal connection. Moreover, the metal substrates are highly conductive, so there is no issue with charging during the photoemission experiment. Lastly, the valence region in the vicinity of the Fermi edge has a fairly uniform density of states, which simplifies the separation of the molecular features from the substrate background in the photoemission experiment. This valley of sp-bands extends a few electronvolt from the Fermi edge and is followed by more strongly bound d-bands [129, 130].

To satisfy all of the aforementioned conditions, we choose the two-fold symmetric surface of a silver (110) substrate. The main reason for this – instead of the other – noble metals is that a suitable growth phase of flat-lying pentacene on Ag(110) was already found and published by Wang et al. in 2004 [131]. All molecules of the lattice are located at equivalent adsorption sites and are uniformly aligned along the [001] direction of the substrate. The interaction between the substrate and the molecular layers is therefore strong enough to impose a commensurate superstructure on the molecular adlayer. The hybridization of the valence orbitals is nevertheless approximately negligible [10]. This trend is in line with the findings on samples of a monolayer of the model molecule PTCDA on Ag(110), where the substrate-molecule interaction is noticable, but small [8, 132]. The region of flat 5sp-bands extends from the Fermi edge to about $E_{\mathrm{bin}} \approx 3\,\mathrm{eV}$, beyond which the 4d-bands are located ($E_{\mathrm{bin}} \approx 4 - 8\,\mathrm{eV}$ [133, 134]). Of the three stable elements in group 11 of the periodic table of elements, that is the largest plateau with a flat density of states [130].

The photoemission experiments are conducted at the NanoESCA beamline at the ELETTRA synchrotron in Trieste [135]. The beamline is equipped with a PEMM [123] and the photon energy can be varied in the relevant range ($E_{\mathrm{ph}} \approx 20 - 140\,\mathrm{eV}$) by changing the undulator parameters in the electron beam path. Even lower photon energies would be desirable for this experiment, but the photon flux drops too rapidly below $E_{\mathrm{ph}} \approx 22\,\mathrm{eV}$ to record any meaningful data. The two undulators in front of the beamline are set to generate left-circularly polarized light from the acceleration of the electrons in the storage ring. Before the photoemission experiments, the Ag(110) substrate is cleaned and prepared in the UHV chamber as described in section 3.2. Following the verification of the pristine substrate with LEED, the molecules are evaporated from the home-made thermal evaporator. The evaporator was previously calibrated with the described temper procedure in the lab at the university of Würzburg.

Fig. 4.3 (a) shows the LEED pattern of the fully prepared pentacene/Ag(110) sample at an electron kinetic energy of 14 eV. The diffraction spots of the silver substrate (blue)

lie beyond the detection range at this low energy, but are still visible at higher E_{kin} due to the low coverage (not shown). The pentacene molecules arrange themselves in a periodic lattice with larger lattice constants than the substrate and cause the prominent diffraction spots on the screen. With the substrate surface vectors $\mathbf{a}_1 = (2.89\,,\,0)\,\text{Å}$ and $\mathbf{a}_2 = (0\,,\,4.08)\,\text{Å}$ from the known lattice of silver [76], the superstructure matrix is determined to be $(\,3\,,\,-1\,/\,-1\,,\,4\,)$ (red). The appearance of additional features (indicated by green arrows) suggests that the molecular thin film is slightly thicker than just a single monolayer. As mentioned above, the molecules in this growth phase lie flat on the surface and align with the long molecular axis in the [001] direction of the Ag(110) substrate [131].

The **E**nergy **D**istribution **C**urve (**EDC**) of the photoemission intensity integrated over all detected angles is depicted in fig. 4.3 (b). The photon energy in this scan is set to $E_{\mathrm{ph}} = 30\,\text{eV}$ with left-circularly polarized light. The kinetic energy of the photoelectrons is recorded in steps of $\Delta E = 100\,\text{meV}$ and integrated over 800 ms at each step. There are three distinct features on top of the relatively flat Ag-5sp-bands which are framed by the Fermi edge at $E_{\mathrm{bin}} = 0\,\text{eV}$ on one side and the onset of the Ag-4d-bands at higher E_{bin} on the other. We ostensibly assign these to the pentacene HOMO-2 at $E_{\mathrm{bin}} = 3.1\,\text{eV}$, HOMO-1 at $E_{\mathrm{bin}} = 2.4\,\text{eV}$, the HOMO at $E_{\mathrm{bin}} = 1.2\,\text{eV}$, and the partially occupied LUMO at $E_{\mathrm{bin}} = 0.1\,\text{eV}$. The LUMO is (by definition) fully unoccupied in the gas phase, but can get partially or entirely filled with electrons when in contact with the substrate. This kind of fractional charge transfer is quite common at metal-organic interfaces [136–138]. Note

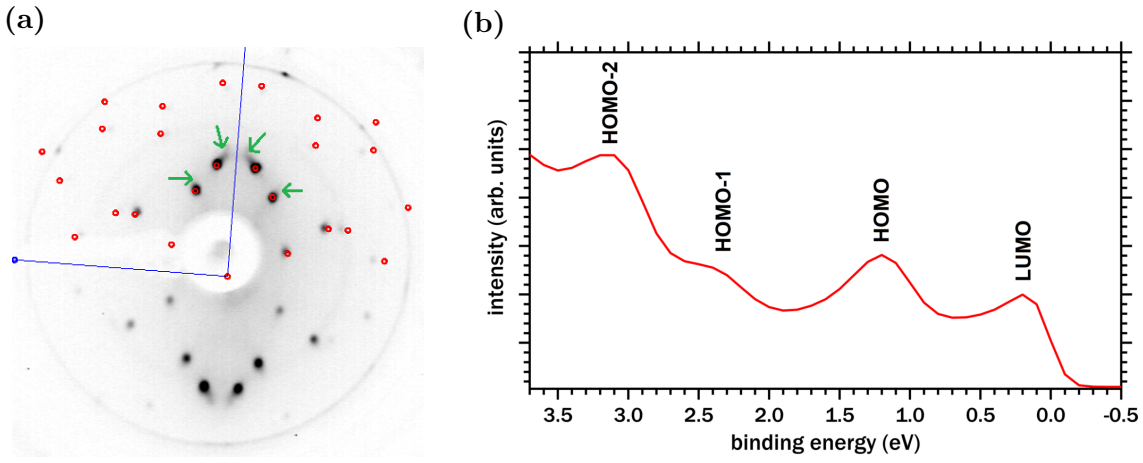

Figure 4.3: (a) LEED pattern of the pentacene monolayer/Ag(110) sample at $E_{\mathrm{kin}} = 14\,\text{eV}$. The unit cell vectors of the monolayer on top of the substrate (blue) are reproduced with the superstructure matrix $(\,3\,,\,-1\,/\,-1\,,\,4\,)$ (red). Faint addition spots (green arrows) indicate a thickness of slightly more than a monolayer. (b) Angle-integrated **E**nergy **D**istribution **C**urve (**EDC**) of the photoemission signal at a photon energy of 30 eV.

that we designate the orbitals according to the gas phase occupation to avoid confusion about the labels for different orbitals. The LUMO hence is not relabeled despite it being (partially) occupied.

4.2 Results and discussion

The raw data has to be corrected for various artifacts emerging in the measurement process as described in section 3.3. It is also rotated by 5 ° around the k_z axis so that the k_x axis points in the [001] direction of the substrate and is horizontal in all PMM. This aligns the long molecular axis along the k_x axis as well (compare with the evaluation of the LEED pattern in fig. 4.3 (a)). The light impinges at a polar angle $\Theta = 65\,°$ and at a $\phi = 5\,°$ angle to the $[1\bar{1}0]$ direction of the substrate towards positive k_y values of the photoelectrons. Next, the scaling factor between the pixel and wave vector values with the known $\overline{\Gamma Y} = 0.73\,\text{Å}^{-1}$ separation of the Ag(110) substrate is applied. In the following step of the data preparation, the PMM are mirrored and averaged – "*symmetrized*" – around the two known symmetry axis of the system, $k_x = 0$ and $k_y = 0$. Note that these are the symmetry axes of the system, but not of the entire photoemission experiment due to the left-circular light polarization and the small misalignment of the incoming light towards the high symmetry axis of the crystal. This is a largely inconsequential issue, but taken into account once we evaluate the effect of the light polarization later on. Fig. 4.4 shows the PMM at the maximum intensity of the pentacene HOMO ($E_{\text{bin}} = 1.2\,\text{eV}$) for a photon energy of $E_{\text{ph}} = 28\,\text{eV}$ and left-circularly polarized light impinging from below towards higher k_y values. The left panel (a) displays the asymmetric HOMO before and the right panel after the symmetry procedure is applied (b). This treatment affects the data in two ways: first, it gives an overall boost to the signal-to-noise ratio. Second, the photoemission intensity is especially low in these areas due to $\mathbf{A}$ being far from parallel to $\mathbf{k}$. It thus improves the applicability of the PWA, since the condition $\mathbf{A} \parallel \mathbf{k}$ is otherwise poorly fulfilled here [11]. Alternatively, one could discard data where the angle between $\mathbf{A}$ and $\mathbf{k}$ is large and refill them with symmetrically equivalent data points. This step is advantageous for the evaluation of the HOMO of PTCDA in [73] though, where the final state shows stronger deviations from a plane wave. Since the PWA works reasonably well even at these angles for our system, however, this step is not necessary for our evaluation.

In order to disentangle the molecular from the background signal we apply a fitting procedure to the EDC at each (k_x, k_y) tuple of the detector and for each photon energy. Fig. 4.5 (a) displays the EDC at $k_x = 1.00\,\text{Å}^{-1}$ and $k_y = 1.55\,\text{Å}^{-1}$ and $E_{\text{ph}} = 28\,\text{eV}$. The contribution of the molecular orbitals is extracted from the experimental data (black

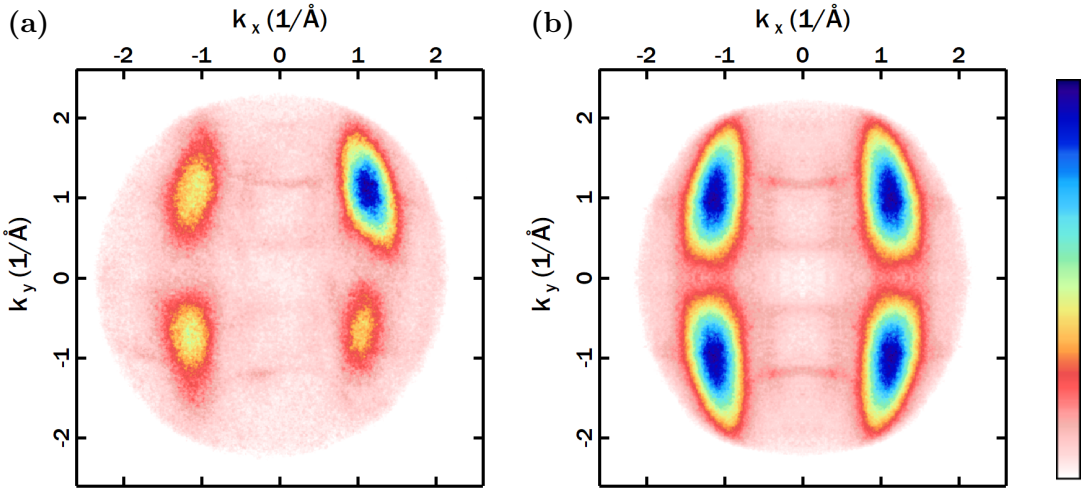

Figure 4.4: PMM of the pentacene HOMO recorded at $E_{\mathrm{ph}} = 28\,\mathrm{eV}$ and left-circularly polarized light before (a) and after symmetrization (b).

circles) via a fitting procedure that also contains the silver background and the Fermi edge. Before this main procedure, the position of the Fermi edge is established by a fit of the derivation of the Fermi edge around $E_{\mathrm{bin}} = 0\,\mathrm{eV}$. With the Fermi edge fixed, the subsequent main fit (red line) includes a Gaussian function for each molecular orbital plus an exponential function and an absolute offset for the silver background, all of which are multiplied by the Fermi function. Every parameter in the calculation is highly constrained to suppress erroneous fits. For example, the procedure removes possible misfits of a molecular orbital if its width is uncharacteristically large while its peak height is low. The code thus rarely succeeds in mistakenly fitting a silver feature with a molecular orbital. The code is applied to every $(k_{\mathrm{x}}, k_{\mathrm{y}})$ tuple and the fitted area of the Gaussian functions saved as the intensity of the respective orbital. The real space wave functions of the four molecular orbitals are calculated by DFT and shown next to their respective maximum. In general, the closer a state is to the Fermi edge, the higher its relevance for chemical interactions and material properties. Hence we will focus on the HOMO and LUMO in the following discussion.

Fig. 4.5 shows the resulting intensity of the fitted PMM for the HOMO (b) and LUMO (c). The orbitals compare favorably with simulations with a plane wave final state of the HOMO (d) and LUMO (e), verifying our earlier assignment of the molecular orbitals. The simulations are based on a DFT calculation of the isolated molecule with a 6-31G+ basis set and the B3LYP functional [139,140]. There are some minor deviations especially at the edges of the the detector plate in the experiment. The most likely explanation is the distorted projection of the trajectory of the photolelectrons close to the electronic lens elements. The very faint stripes of the HOMO in (d) at $(k_{\mathrm{x}}, k_{\mathrm{y}}) = (\pm 0.5, \pm 1.1)\,\mathrm{\AA}^{-1}$

are likely not visible in the experiment (b) due to background signal and the imperfect order of the molecules. This data treatment is repeated for all other recorded photon energies in the range of $E_{\mathrm{ph}} = [20\text{–}140]\,\mathrm{eV}$. The steps from one photon energy to the next get progressively larger towards higher E_{ph}: increments of $\Delta E = 0.5\,\mathrm{eV}$ between $[20\text{–}24]\,\mathrm{eV}$, then $\Delta E = 1\,\mathrm{eV}$ until 30 eV, $\Delta E = 2\,\mathrm{eV}$ until 82 eV, and finally nonuniform steps until 140 eV. The reason behind these increments is that the cross section of the molecular orbitals is expected to vary strongly between about $E_{\mathrm{ph}} = [20\text{–}30]\,\mathrm{eV}$ with a (fairly unsteady [61, 73]) decline afterwards.

The main challenge in comparing data taken at different photon energies is that undulators do not provide a constant photon flux for each energy. As described in section 3.3, we use the voltage generated at a gold mesh in the beam path as a gauge for the photon flux for each particular E_{ph}. All scans are normalized thus with the measured U_{grid} and the chosen integration time t_{int} according to eq. (3.3). The issue with this approach is the dependency of measured voltage on the cleanliness of the gold mesh. The mesh is not cleaned on a regular basis and thus gradually contaminated by adsorbates from the residual gas the longer it stays in the vacuum chamber. These contaminents in turn affect the energy-dependent photoelectron cross section $\mu(E_{\mathrm{ph}})$. The resulting ambiguity in the normalization results in an uncertainty of the intensity calibration on the order of 10–20 %. In comparison with the normalization, the darkfield and brightfield correction, fitting procedure and the statistical noise all have a significantly higher precision and barely contribute to the total uncertainty.

In the framework of the linear combination of atomic orbitals (see section 2.2.2), the molecular orbitals of pentacene in the valence region are almost exclusively based on the superposition of carbon $2p_z$ orbitals [40]. If a plane wave final state is applicable, the k_z dependence of the molecular orbitals should therefore be rather simple and comparable to that of a single $2p_z$ orbital. Deviations from the theoretically expected k_z-dependence can give insights into the photoemission process and the initial state in general, as well as into the applicability of the PWA in particular. Even though there is the fractional charge transfer into the molecular layer, the pentacene orbitals are almost unperturbed by the presence of the silver substrate and can be taken from the DFT on an isolated pentacene molecule. Hence we compare the experimental data to DFT calculations of a single molecule with a 6-31G+ basis set and the B3LYP functional. The initial states are then put into the photoemission matrix element calculation with a plane wave final state. It should also be mentioned at this point that the gold adsorption cross section used for the intensity normalization is fairly smooth in the surveyed energy range and is an unlikely source of any of the features we will discuss [90].

Fig. 4.6 displays the k_z dependence of the experiment (black circles) and the calculations

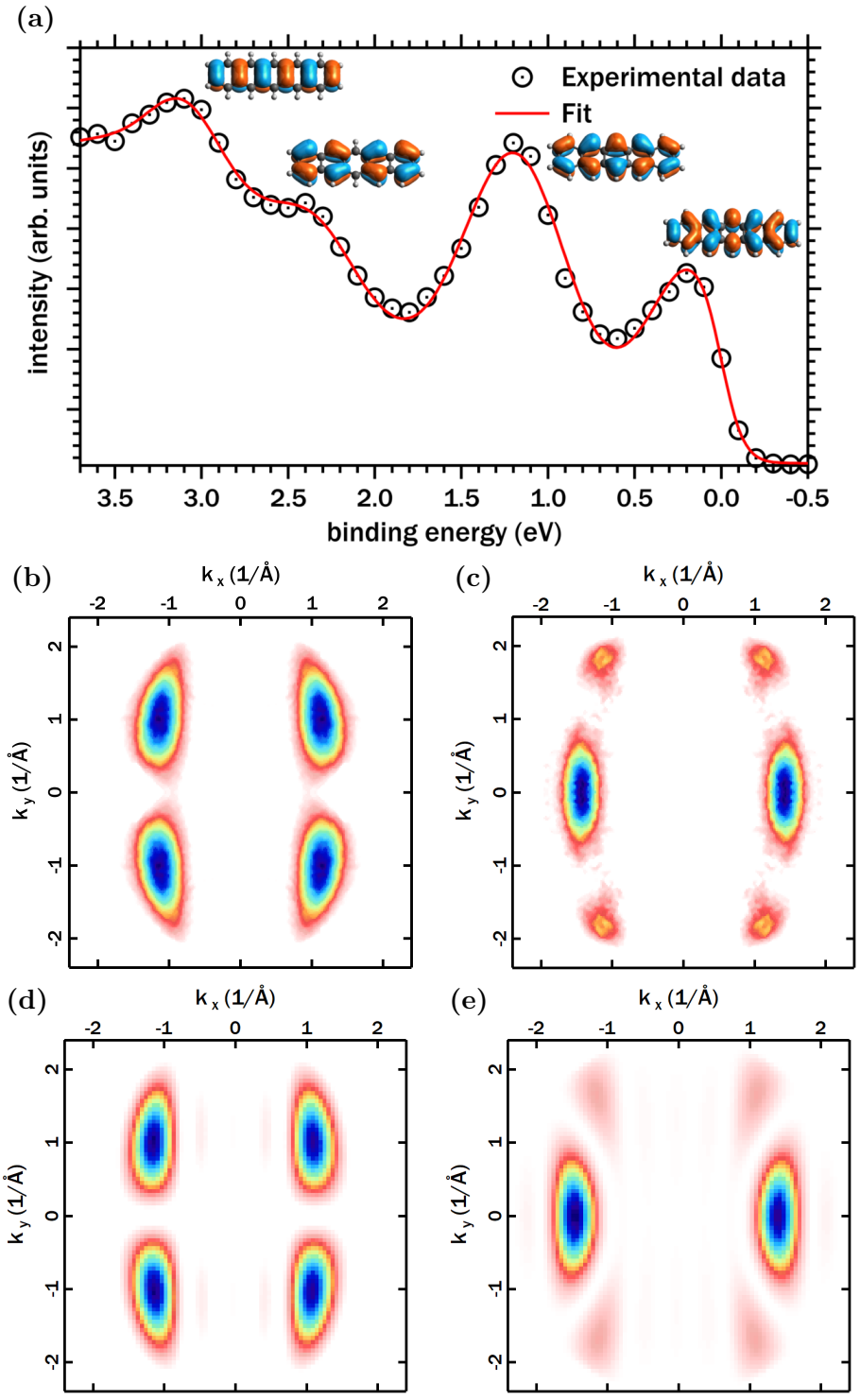

Figure 4.5: (a) Exemplary fit of the EDC for $E_{\mathrm{ph}} = 28\,\mathrm{eV}$ for $k_{\mathrm{x}} = 1.00\,\mathrm{\AA}^{-1}$ and $k_{\mathrm{y}} = 1.55\,\mathrm{\AA}^{-1}$. The experimental data (black circles) is in good agreement with the fit (red line). The DFT calculation of the orbital in real space is depicted next to each feature. The PMM of the resulting area of the HOMO (b) and LUMO (c) is in very good agreement to calculations of the isolated molecule with a plane wave final state for the HOMO (d) and LUMO (e).

(red line) for the HOMO $(k_x, k_y) = (1.10, 1.00)\,\text{Å}^{-1}$ (a) and $(0.90, 1.60)\,\text{Å}^{-1}$ (b), and of the LUMO $(1.40, 0.00)\,\text{Å}^{-1}$ (c) and $(1.40, 0.80)\,\text{Å}^{-1}$ (d). The wave vectors roughly correspond to the position of the main maximum (a,c) and the edge of the maximum (b,d) in $k_\parallel$. In general, the experimental data follows the main trend of the calculation, but decays faster towards higher E_{ph} and exhibits additional peaks and valleys in intensity. Starting with the HOMO in (a), the lowest photon energy is already on top of the expected maximum of the intensity curve. After a quick decline, a broad local maximum is found around $E_{\text{ph}} = 30\,\text{eV}$ (feature A), followed by another valley and a peak at $E_{\text{ph}} = 42\,\text{eV}$ (feature B). A smaller peak is located at $E_{\text{ph}} = 76\,\text{eV}$ (feature C). To check whether these features are dependent on the wave vector and/or the energy, we can contrast them to the HOMO at $(0.90, 1.60)\,\text{Å}^{-1}$ (b). The onset of the main intensity maximum is clearly visible in this data set due to the higher wave vector. There is no separated maximum at A, but the other two maxima are very similar. This is an indication that feature A has a dependence on the photoelectron wave vector, that is absent in B and C. To narrow down the origin of the features, one can compare these regions to the LUMO on the main maximum at $(1.40, 0.00)\,\text{Å}^{-1}$ (c). For reference, photoelectrons emitted from the LUMO have a binding energy that is 1.1 eV lower than for the HOMO. The kinetic energy of the photoelectrons from the LUMO and HOMO is therefore very slightly shifted for the same photon energy. All three features in (c) show an elevated intensity and features A and B are even more pronounced. On the edge of the maximum at $(1.40, 0.80)\,\text{Å}^{-1}$ (d), the features are a lot less prominent, but nevertheless visible.

Peaks similar to the ones found here also appear in the measurements of a monolayer of PTCDA on Ag(110) of Graus et al. [73]. There they found intensity maxima of the PTCDA HOMO and LUMO on their respective main features at slightly higher photon energies, around $E_{\text{ph}} = 36\,\text{eV}$ and $E_{\text{ph}} = 48\,\text{eV}$. These maxima are not as pronounced and on the edge of the error range of the experiment, however. They are also only evaluated for the single wave vector $k_\parallel$ at the maximum of the respective orbital in reciprocal space. Weiß et al. detected HOMO and LUMO maxima around $E_{\text{ph}} = 33\,\text{eV}$ on the same system and position in reciprocal space [61]. They suggest photoelectron scattering due to a shape resonance as a possible – admittedly speculative – cause of the increased intensity. Nevertheless, the appearance of intensity maxima at the same photon energies for different molecular orbitals also suggests an influence of the final state and/or the exciting light field in the photoemission process. The effect of the final state would have to be rather insensitive towards the direction of the wave vector $\mathbf{k}$ since the features B and C exhibit a similar increase in intensity for different final state wave vectors. The final state calculations of Bentmann et al. reported for a $BiAg_2$ surface alloy on Ag(111) give a hint on the role that the substrate might play [141]. In their photoemission study, they identified a strong dependence of the photoelectron final state on the photon

energy. Their calculation showed that the modulation was connected to the Bragg gap of Ag(111) at $E_{\mathrm{ph}} = 22\,\mathrm{eV}$. The gap and its effect on the final state wave function is dependent on the wave vector $\mathbf{k} = (k_{\mathrm{x}}, k_{\mathrm{y}}, k_{\mathrm{z}})$. The substrate in our work is also a silver single crystal (Ag(110)), so the same phenomenon could be responsible for the detected intensity variations in fig. 4.6. An alternative explanation is that the gold mesh used for the intensity normalization might be coated with adsorbants that differ strongly from the pure gold surface around these photon energies. In contrast to B and C, feature A has a stronger dependence on the wave vector as it appears more intense on the main maxima in reciprocal space (a,c) than on the edges (b,d). It is possible that a Bragg gap is nevertheless responsible for this variation as well. The wave vector $\mathbf{k}$ could be inside the gap for (a) and (c), but outside of it for (b) and (d).

Another possible cause is that the radial wave function of the unscattered final state is far from the spherical Bessel function of a plane wave and is better described by a Coulomb wave due to the potential well in the vicinity of the atoms (see subsection 2.3.1). However, this effect is likely limited because of the weakly corrugated potential surface around the light elements that make up the pentacene molecule and the electronic wave function that is spread across many atoms.

In summary, the question of the deviation from the expected E_{ph} dependence of the intensity unfortunately cannot be fully resolved from the present data set and the ones in literature. At the moment, the lack of theoretical data, e.g. with calculations of the unoccupied band structure of the Ag(110) substrate, appears to be the main roadblock to a deeper understanding of the measured intensity variations.

4.3 Real space orbital reconstruction

In this section, we will illustrate the reconstruction of the real space wave function of a molecular orbital from the experimental data. Our approach is dependent on the plane wave approximation of the final state as discussed in subsection 2.3.3 and the orbital reconstruction and phase retrieval of section 2.4. As an showcase of the technique, we will focus on retrieving the pentacene HOMO.

In addition to the artifact correction, background removal and normalization that is already applied from the previous section, the data has to be processed through a few more steps before it can be used as an input for the inverse Fourier transform on both sides of eq. (2.29). First, it is convenient to convert the hemispherical data tuple of the momentum maps in reciprocal space from (k_{x}, k_{y},E_{ph}) to orthogonal (k_{x}, k_{y},k_{z}) voxel. This enables us to perform the inverse Fourier transform which includes the integration of the

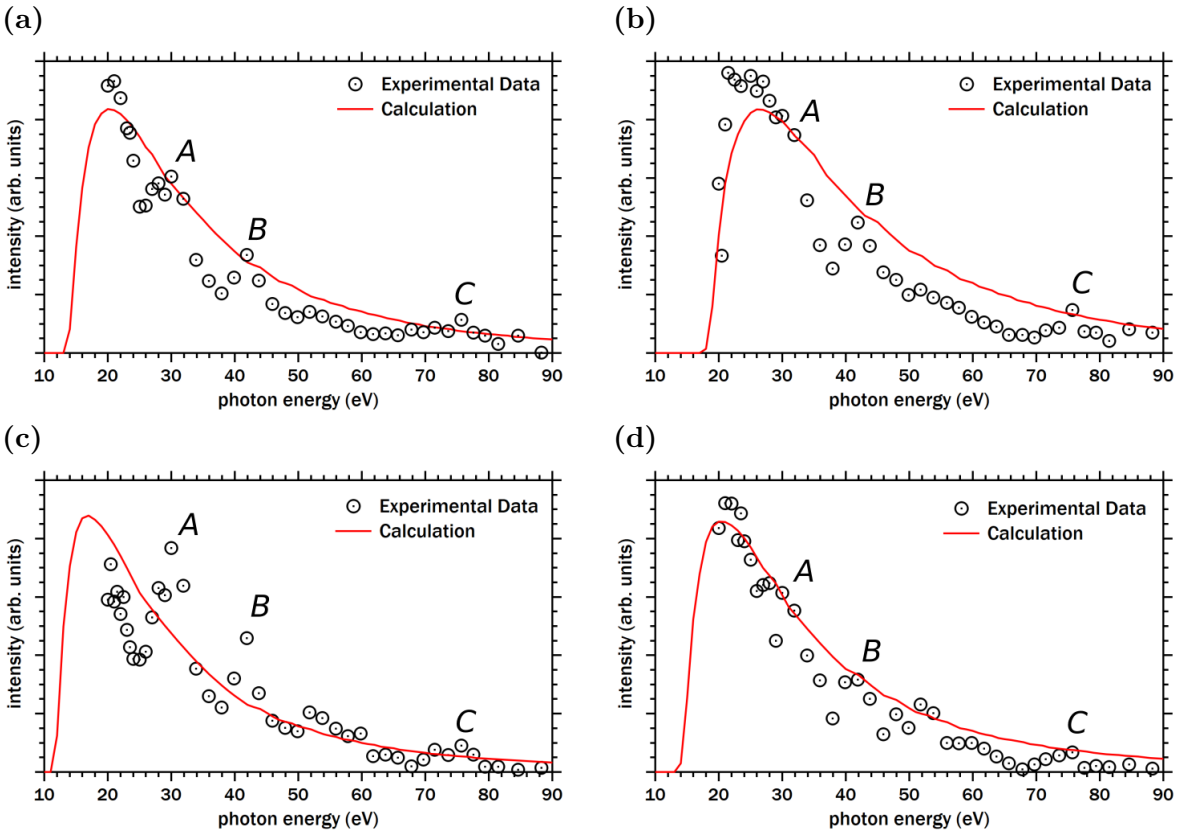

Figure 4.6: Intensity over photon energy of the HOMO for $(k_x, k_y) = (1.10, 1.00)\,\text{Å}^{-1}$ (a) and $(0.90, 1.60)\,\text{Å}^{-1}$ (b), and of the LUMO for $(1.40, 0.00)\,\text{Å}^{-1}$ (c) and $(1.40, 0.80)\,\text{Å}^{-1}$ (d). The experiment exhibits pronounced deviations from the trend expected with a plane wave final state for some photon energies and wave vectors. Indicated are the features A, B and C around $E_{\text{ph}} = 30$, 42 and 76 eV, respectively.

molecular orbital over the entire reciprocal space. The E_{ph} dependency can be converted to k_z through eq. (2.10) with $V_0 = 0\,\text{eV}$. One can also use the already calibrated k_x and k_y and the free electron dispersion $E_{\text{kin}} = \frac{\hbar^2 \mathbf{k}}{2m_0}$ and $\mathbf{k} = (k_x, k_y, k_z)$. In the new orthogonal coordinate system, the experimental data lies on hemispheres with varying diameter according to E_{kin} (E_{ph}) inside the sample that leave gaps of missing data in between them. To complete the data set, these missing values in the new coordinate system are interpolated linearly from the adjacent values in all three dimensions. This treatment fills the gaps within the range determined by $E_{\text{kin}} = E_{\text{ph}} - E_{\text{bin}} = [18.8, 138.8]\,\text{eV}$ which corresponds to a minimal and maximal wave vector $k_{\text{min}} = \sqrt{k_x^2 + k_y^2 + k_z^2} = 2.22\,\text{Å}^{-1}$ and $k_{\text{max}} = 6.04\,\text{Å}^{-1}$, respectively. Unfortunately, there is no experimental data on the photoemission intensity at the lower end $k < k_{\text{min}}$. This is an issue because the rising edge of the photoemission intensity of the main HOMO feature is not contained within the data set, as can be seen in fig. 4.6 (a). For (k_x, k_y) tuple with a low $k_{\parallel}$, the first data

point is already close or on the maximum of the curve. Judging from the theoretical calculations, the drop in intensity towards lower E_{kin} is rather steep and featureless. It is therefore well approximated by a linear dependence towards the origin of the coordinate system. The error caused by the cutoff at the upper end of the data set is minor, however, since the cross section of the HOMO for E_{ph} greater than about $\sim 80\,\mathrm{eV}$ is rather small. The intensity of the voxel beyond this side of the data range are set to $I(k > k_{\mathrm{max}}) = 0$.

The entire lower hemisphere with negative $k_{\mathrm{z}} < 0$ is also void of any experimental data. This area contains photoelectrons which cannot be recorded by the detector since they are emitted in the opposite direction towards the silver substrate. Nevertheless, filling these voxel is necessary for the integration over all of reciprocal space. We will therefore resort to the fact that the C-2$\mathrm{p_z}$ orbitals that make up the pentacene HOMO [40] are antisymmetric with respect to a mirror operation at the k_{x}-k_{y} plane. The mirror antisymmetry at $k_{\mathrm{z}} = 0$ is also in agreement with DFT calculations on the isolated molecule. In the *actual* experiment of pentacene molecules adsorbed on Ag(110), this symmetry is broken by the presence of the substrate on one side of the molecule and vacuum on the other. The distortion of the valence molecular orbitals in contact with noble metal substrates is generally small, however, and can be assumed to play a minor role for this specific case, as evidenced by the very good agreement to calculations with the isolated molecule shown in fig. 4.5. After all, the limited interaction between the organic layer and the substrate was originally part of the reason for selecting the Ag(110) substrate. This treatment concludes the assembly of the three-dimensional intensity matrix in reciprocal space $I(k_{\mathrm{x}}, k_{\mathrm{y}}, k_{\mathrm{z}})$.

The next step in the data preparation is the determination of the amplitude $\mathcal{A}(\mathbf{k})$ from the intensity matrix $I(\mathbf{k})$ which are connected by the absolute square of the amplitude matrix $I(\mathbf{k}) = |\mathcal{A}(\mathbf{k})|^2$. As outlined in section 4.3, the absolute square function of a complex number $\mathcal{A} \in \mathbb{C}$ is not an injective projection. The relation $\mathcal{A}(\mathbf{k}) = \sqrt{I(\mathbf{k})}$ is missing the phase factor $e^{i\alpha}$ that is crucial to the integral over all of reciprocal space in the inverse Fourier transform. The phase information is not directly recorded in the measurement of the photoemission intensity in ARPES and appears to be lost. Nevertheless, it is contained in the photoemission signal – albeit only implicated and hidden in the data – and can be retrieved with algorithms developed in and adapted from the X-ray diffraction community [62, 63, 68].

To this end, a two-dimensional PMM at a fixed k_{z} is extracted from the three-dimensional data cube. From the phase information of this plane we can establish the phase relation of the entire data set. As previously mentioned, this is possible because the molecular orbitals are based on atomic $\mathrm{p_z}$ orbitals, so there are no additional nodes with a phase change in k_{z} direction in each hemisphere. This is reflected in the experimental data by the absence of nodal planes in the same direction. The DFT calculation on the

isolated molecule is in agreement as well. When moving from the upper to the lower hemisphere, however, the antisymmetry plane of the p_z orbitals at $k_z = 0$ reverses the phase of the wave function in reciprocal space. This transition will be taken into account by inverting the recovered phase for $k_z \rightarrow -k_z$.

Fig. 4.7 (a) shows the k_x-k_y plane at $k_z = 2.00\,\text{Å}^{-1}$ that is extracted from the square root of the fitted intensity of the HOMO. The minor features around $(\pm 0.4, \pm 1.2)\,\text{Å}^{-1}$ are not part of the HOMO, but misfits of the silver bands which happen to have a binding energy, height and width comparable to the molecular orbital at this (k_x, k_y) tuple. Their contribution to the total signal is nevertheless relatively small. The initial phase guess is chosen to be random and shown in fig. 4.7 (b). In principle, one could pick any kind of phase information to start with, although some might be more prone to finding a local, instead of the global, true minimum in the phase retrieval process.

Before starting the calculation, the size of the input files is increased to a total extent of $83.1\,\text{Å}^{-1}$ centered around $(k_x,k_y) = (0,0)$ and the new pixel filled with zero magnitude and arbitrary phase. Since the total extent before and the resolution after the inverse Fourier transform are inversely proportional to one another, the padding in reciprocal space leads to a resolution in real space of $\Delta r = 0.0756\,\text{Å}$. Setting the magnitude to zero is justified because there is no intensity to be expected at these high $k_\parallel$ values even if they were recorded in the experiment. In our case, the amount of padding before the calculation is limited by the size of the random access memory (RAM) of the commercial computer on which the Fourier transform is performed. Enhancing the resolution even further would therefore be possible, but ultimately unnecessary, since the wave function in real space exhibits no features that cannot be easily resolved with the resolution of the calculation at hand.

The iterative phase retrieval procedure is carried out with the scheme developed by Lüftner et al. [63] described in seq. 4.3. The rectangular confinement (*support*) in real space is 180 Å , 78 Å and centered on the molecule. After the inverse Fourier transform in each iteration, the magnitude of the wave function outside of this box is reduced to 5 % of its value. To recapitulate the procedure, the wave function is then Fourier transformed back into reciprocal space and the magnitude replaced with the experimental one. The phase information is kept for the subsequent inverse Fourier transform, thereby completing one iteration.

The resulting PMM after 100 iterations is displayed fig. 4.7 (c) with the color indicating the phase. There are only two, opposite values of the phase, so it can be entirely projected from $\mathbb{C}$ to $e^{i\alpha} = \{-1, 1\} \in \mathbb{R}$. The phase of the main features is mostly converged after about 10 iterations, after which the details in areas of lower magnitude settle into their final value. The recovered phase of the HOMO has a symmetry axis along $k_x = 0$ and an antisymmetric one along $k_y = 0$. The spurious silver bands have the same symmetry

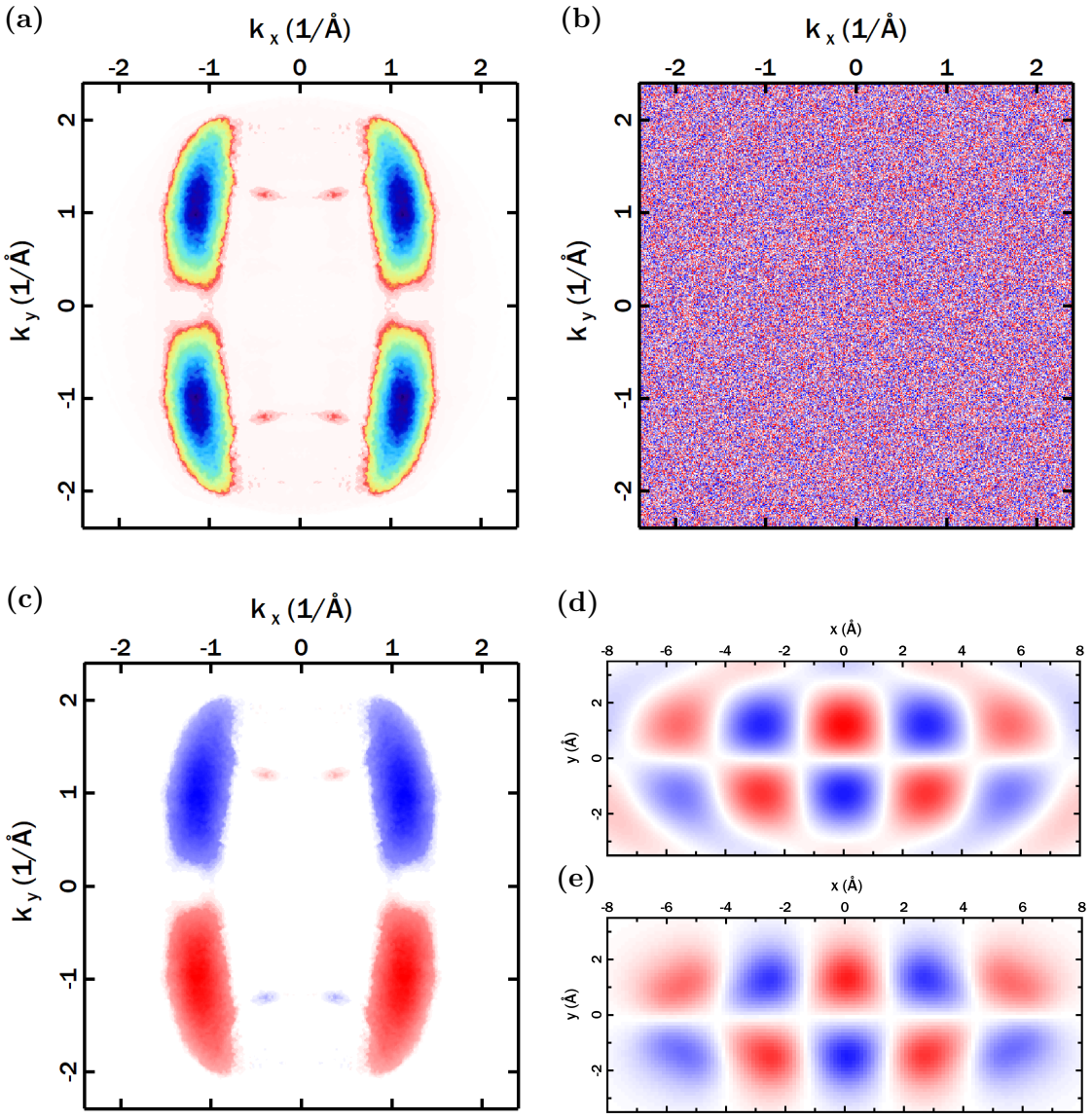

Figure 4.7: Phase retrieval for the pentacene HOMO for a wave vector of $k_z = 2.00\,\text{Å}^{-1}$. The symmetrized, experimental magnitude (a) is multiplied with a random phase (b) and put into the phase retrieval algorithm. The recovered amplitude after convergence is shown in (c) with phase information contained in the color. An inverse Fourier transformation of (c) leads to the experimentally determined two-dimensional real space HOMO (d), which is in decent agreement with a DFT calculation on the isolated molecule (e).

axes, but are inverted relative to the phase of the molecular orbital. The real space wave function of the HOMO from the inverse Fourier transform of fig. 4.7 (c) is shown in (d). The experimental result is in good agreement with the DFT calculation on the isolated molecule in (e), which is evidence that the phase recovery settled in the global minimum. The position, width and intensity of the ten main features fit well and the shape is also very much alike. The simplicity of the Fourier transform enables the intuitive interpretation of some of the features in real space: the maxima of the features in reciprocal space at $\sim 1.1\,\text{Å}^{-1}$, for example, are inversely proportional to the periodicity of the lobes in x direction $(2\pi)/(1.1\,\text{Å}^{-1}) = 5.7\,\text{Å}$. Going into the details, there are minor deviations between the reconstruction and the calculation: first, the wave function is not localized as strongly to the 10 main lobes in real space. On one hand, the molecule-molecule and molecule-substrate interaction in the experiment, albeit small, could result in a hybridization of the HOMO. The HOMO wave function is then spread out across the neighboring interaction partners and less confined to a single molecule. The DFT calculation cannot capture this behavior since it only contains a single pentacene molecule without the substrate or neighboring molecules. The signal might also be caused by the missing photoemission intensity of large (k_x,k_y) values outside of the detector plate in the experiment. Without them, the wave function could erroneously continue oscillating far from the molecule in real space. The spurious silver bands are too small in magnitude to cause the signal, but might contribute in a similar manner by their low frequency that is not negated by another signal. Note that the very small asymmetry in y direction is due to the support not being perfectly centered around the $y = 0$ symmetry axis.

Another likely source for at least parts of the deviations could be the final state which is not perfectly described by a plane wave, see the discussion of fig. 4.6.

The recovered phase information of the extracted two-dimensional plane at each pixel is now extended to all other k_z values with the same (k_x,k_y) values. Voxel in the same hemisphere share the same phase, while the phase is inverted at $k_\text{z} = 0$ and reversed for voxel from the opposite hemisphere. Similar to the two-dimensional reconstruction, the data is then padded with empty voxel and translated into real space with a three-dimensional Fourier transform. The limited RAM-size of the computer is a considerably bigger issue for the three-dimensional data set and limits the amount of padding that can be applied. The resolution is in real space is therefore markedly lower and amounts to $\Delta x, y = 0.26\,\text{Å}$ in x and y direction and $\Delta z = 0.20\,\text{Å}$ in z direction.

Fig. 4.8 displays exemplary two-dimensional excerpts of the reconstructed real space HOMO (upper half) compared to the DFT calculation on the isolated molecule (lower half). The phase of the wave function is again encoded in the color. Due to the symmetry axes of the orbital only the phase is flipped between the upper and lower half

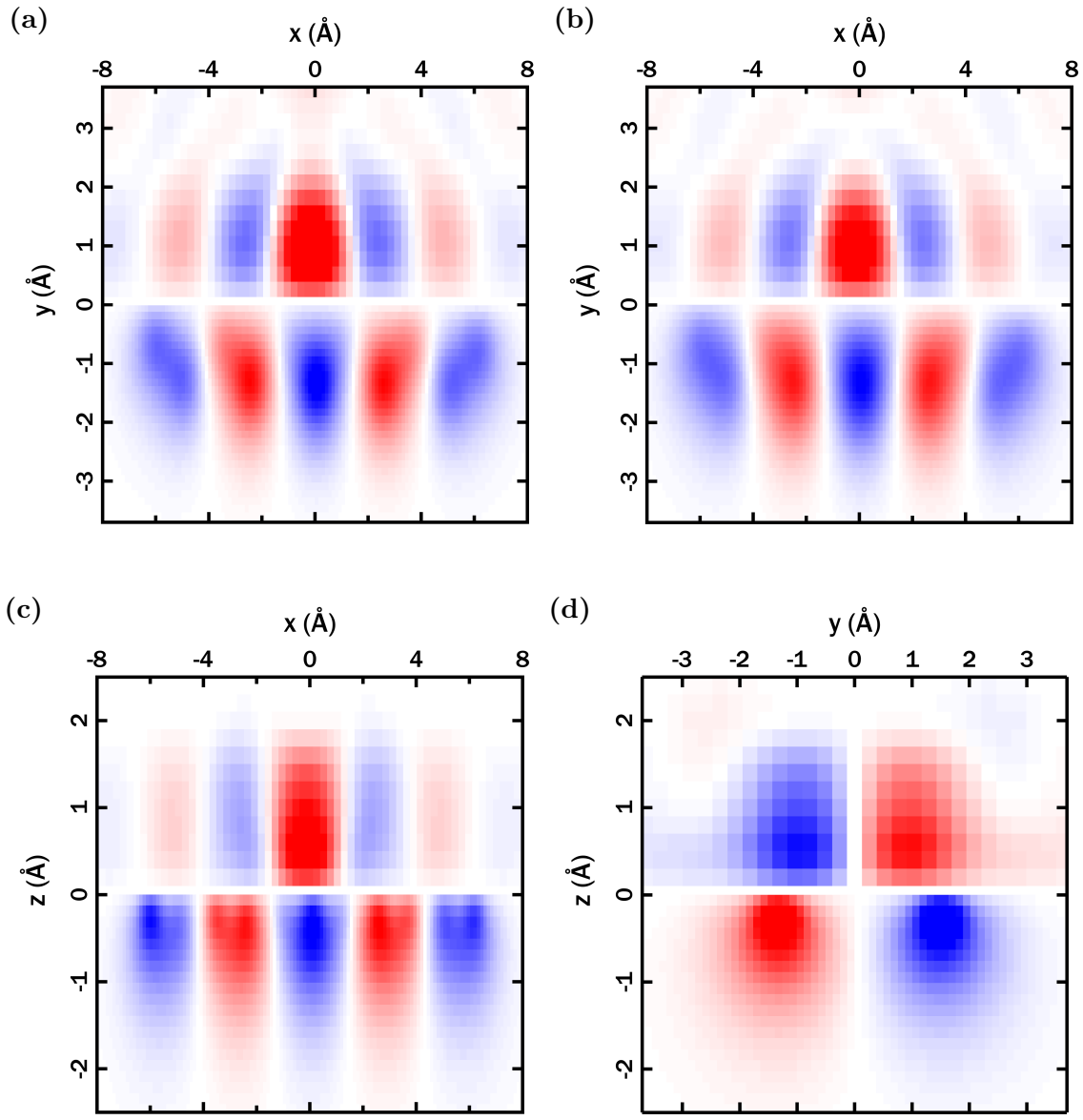

Figure 4.8: Two-dimensional excerpts of the three-dimensional reconstruction of the HOMO (upper half) compared to the DFT simulation (lower half) with the color indicating the phase. Shown are the x-y-plane for $z = 0.9\,\text{Å}$ (a) and $z = 1.2\,\text{Å}$ (b), the x-z-plane for $y = 1.1\,\text{Å}$ (c) and the y-z-plane for $x = 0.0\,\text{Å}$ (d). The experiment largely matches the simulation, but significant deviations occur in the intensity and extent of the features at the outer edges of the orbital.

while all other information is identical. The top-down view on the x-y-plane is shown for $z = 0.9\,\text{Å}$ in fig. 4.8 (a). The shape and position of the main lobes in the reconstruction is again in a decent agreement with the simulation. The periodicity in x direction is slightly smaller than expected: the node between the two outer-most features is positioned at $x = 4.15\,\text{Å}$ in the reconstruction and stretched by $\sim 5\,\%$ compared to the node at $x = 4.35\,\text{Å}$ in the simulation. As previously mentioned in the discussion of fig. 4.7, the wave function in the reconstruction is not as confined as in the simulation, which could be caused by the influence of the chemical surroundings around the molecule, the spurious silver signal and/or the missing signal at high $k_{\parallel}$ outside of the MCP detector. There is one additional aspect that does not factor in at the two-dimensional reconstruction: the extrapolated data at low $|k|$ determined by the lowest kinetic energy inside the system $E_{\text{kin,min}} = 18.8\,\text{eV}$. Another likely influence comes from the final state itself whose deviation is likely not negligible (see discussion of fig. 4.6). The theoretical calculation of a more realistic final state for this system would thus shed light on both the reconstruction and the E_{ph} dependence of the photoemission intensity.

The x-y-cut for $z = 1.2\,\text{Å}$ (b) is very similar in both the reconstruction and the simulation. This is to be expected due to the flat geometry of the pentacene molecule and the underlying C-$2p_z$ orbitals which have no new features in this direction and simply decay slowly in magnitude. In the reconstruction, however, a change in phase in positive y direction is clearly visible (and more so than already in (a)). The most probable cause for these phase changes is again the imperfect information due to the aforementioned arguments.

The excerpts in the bottom row show the x-z-plane for $y = 1.1\,\text{Å}$ (c) and the y-z-plane extracted at $x = 0.0\,\text{Å}$ (d). The comparison between reconstructed and simulated wave function qualitatively identical to the images in the upper row, and for the same reasons: the agreement is generally good with the reconstructed features being spread further out and their periodicity slightly increased in (c). The shape of the individual lobes is close to the simulation, but not entirely alike.

In conclusion, the real space reconstruction of the pentacene HOMO is successfully performed on the system of a monolayer of pentacene on top of Ag(110). The reconstructed wave function matches the simulation with a plane wave final state to a large extent. The deviations between both wave functions can be explained by a small hybridization of the molecular orbital in the experiment as well as missing data values, especially at low k_z values that cannot be accessed with the chosen photon energy range. Additionally, the plane wave approximation for the final state does not perfectly resemble the actual final state which results an error by applying the inverse Fourier transform to the reciprocal initial state wave function determined with the phase retrieval procedure.

For an overview over the entire reconstructed initial state, an oblique, projection of

the three-dimensional reconstruction of the pentacene HOMO is depicted in fig. 4.9. The molecular frame (black) is not reconstructed by this procedure, but included as guide to the eye. The isosurface traces the contour of 25 % of the maximal magnitude with the color again indicating the phase of the wave function.

Limits of orbital reconstruction

It is important to keep in mind that the reconstruction of molecular orbitals is linked to the plane wave approximation and all its drawbacks. These are discussed along with the derivation of the approximation in subsection 2.3.3. Due to this connection, the less applicable of an approximation the PWA is for a particular system, the worse the reconstructed orbital will represent the actual initial state of the system.

An additional experimental issue arises if more than a single state is detected at the same photoelectron kinetic energy in the experiment, e.g. for energetically degenerate

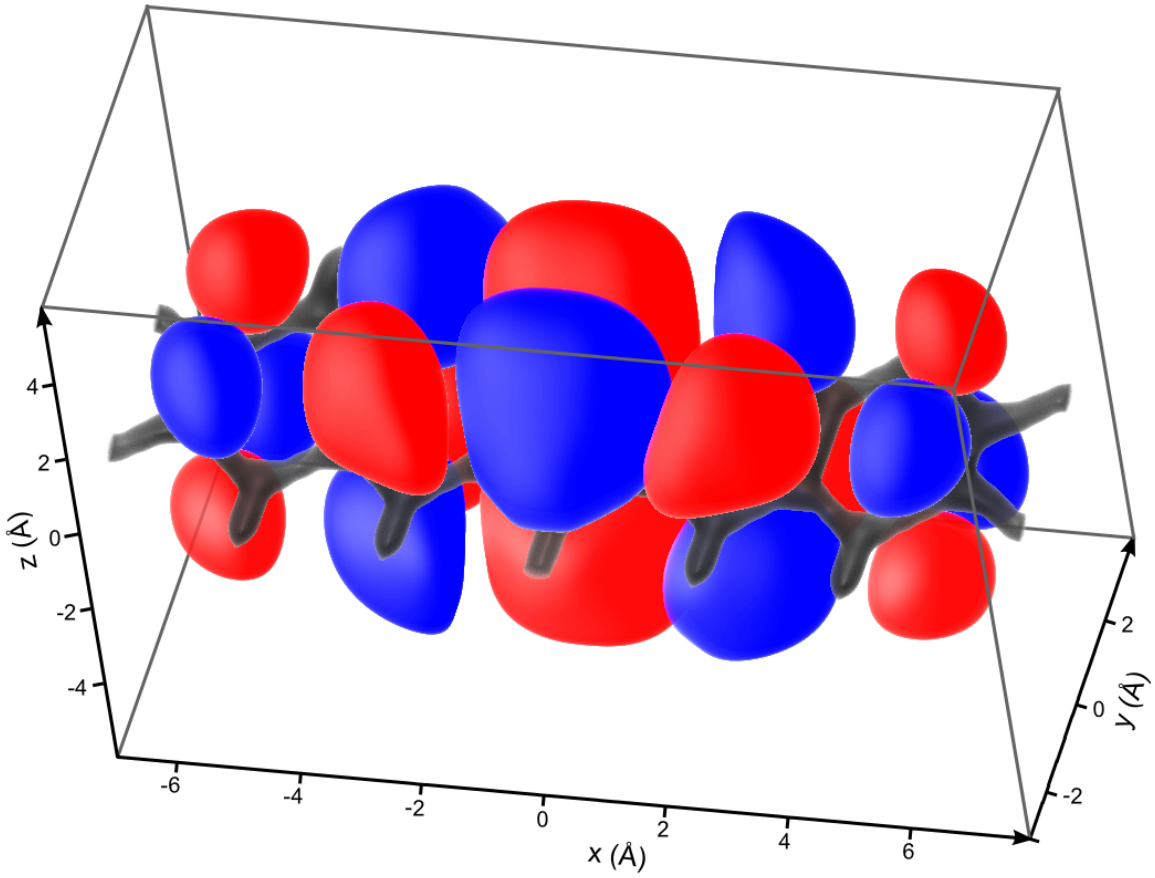

Figure 4.9: Three-dimensional reconstruction of the HOMO of pentacene in real space from experimental data. The structure of pentacene (black) is drawn to aid in the visualization and not part of the reconstruction. The threshold for the isosurface is set to 25 % of the maximal magnitude.

orbitals. In this case, the measured photoemission signal at a specific (k_x, k_y) tuple is not tied to a single value for the phase, but one for each of the individual orbitals. Since there is no one value for the orbital reconstruction through the inverse Fourier transform of eq. (2.29), the result will not match (any) of the real orbitals. Unless they are disentangled by some means, e.g. by fitting procedures or choosing a suitable substrate that separates them energetically [137], these orbitals cannot be successfully reconstructed. Note however, that if the PWA is applicable the experimental PMM might nevertheless be reproduced by the sum of photoemission simulations of each of the DFT-calculated initial states and a plane wave final state.

The condition of the light vector field being as close to parallel as possible to the wave vector $\mathbf{A} \parallel \mathbf{k}$ [11,38,40] can be circumnavigated to some extent. One way to mitigate this effect is by using a symmetry arguments of the sample: For example, one can use symmetry arguments to get discard the worst areas where the geometry approaches $\mathbf{A} \perp \mathbf{k}$ and replace them with symmetrically equivalent data from regions closer to $\mathbf{A} \parallel \mathbf{k}$ [73].

5 The expanded photoemission simulation tool

Calculations of the angle-resolved photoelectron momentum maps can usually not be done without the assistance of computers. It is therefore inevitable to implement the theoretical equations governing the photoemission process into an actual simulation tool. Comparing the calculated to the experimentally measured data then enables an understanding of the properties of the system. Furthermore, one can predict the expected outcome of a measurement prior to the actual data acquisition and if necessary alter the experiment accordingly.

In this vein, one major project behind this thesis was the creation of a tool to simulate the photoemission signal from organic molecules. The goal was to provide a fast and accessible code that runs on common, commercially available computers. It should also go beyond the PWA (see subsection 2.3.3 and chapter 4) and use final states based on the IAC approximation with optional elastic scattering (subsection 2.3.1 and 2.3.2). The tool is implemented in the user interface of the software *WaveMetrics IGOR Pro* which is commonly employed for data acquisition and processing within the surface science community [142]. Since it also has its own programming language that is very similar to *C* and quite powerful, IGOR Pro is a suitable platform to build the code on. The development of the tool started using version 6 of IGOR Pro [143] and has continued up until the the lastest version 8 [144]. The current tool is backwards compatible with IGOR Pro 6/7 and runs properly both in the 32- and 64-bit versions of the software.

In this chapter we will apply the program in the analysis of three short photoemission studies. Note that while the photoemission simulation is carried out within the program, the DFT calculation for the initial state wave functions is not. The initial state is generated by the *Gaussian 09* software package instead [145]. Gaussian 09 is a commercially available software for DFT calculations based on Gaussian type orbitals and the linear combination of atomic orbitals. It essentially follows the theoretical description laid out in section 2.2 with a variety of choices for the basis set, functional and many more parameters. Even though Gaussian 09 was used throughout this work for licensing reasons, the tool is nevertheless forward compatible with outputs created by the presently newest version Gaussian 16 [146]. A more detailed look into the principles that govern the pro-

gram behind the user interface is given in appendix A5. It contains the preparation of the input in advance of the calculation (appendix A5.1) as well as the procedure operation inside the tool (appendix A5.2).

Program validation and applications

Any program of this size exhibits computational errors ("bugs") and unexpected behavior under some conditions. A lot of these can be detected and already ironed out during the implementation of a new feature by checking each new step one at a time. To verify that the tool ultimately performs as intended however, the program has to be tested against some representative model cases eventually.

We will begin by comparing the experimental and simulated photoemission patterns of pentacene from the previous chapter 4 to those of the photoemission tool. Next, we will address the more complex system of the adsorption geometry of a monolayer of pyrphirin on an Ag(110) substrate [147]. For both of these systems the effects of elastic scattering can safely be neglected. This is not true for the last test model of carbon monoxide molecules on top of Pt(111). The tight localization of the initial state due to the small size of the molecule results in a PMM whose pattern is dominated by elastically scattered electrons.

5.1 Basic evaluation

Pentacene is already thoroughly analyzed with a plane wave final state in the previous chapter 4, where the ordered monolayer on top of an Ag(110) is studied. To briefly recapitulate, pentacene is a rather simple molecule that was among the first to have been used for orbital tomography in a thick multilayer for the publication by Puschnig et al. in 2009 [40]. In this configuration it exhibits a limited molecule-molecule and molecule-substrate hybridization and therefore lends itself as the first model system for testing the photoemission tool.

DFT calculations are performed on the isolated molecule with a STO 6-31+ basis set and the B3LYP functional. The initial states of the HOMO and LUMO are loaded into the photoemission tool and the inner potential set to $V_0 = -10\,\mathrm{eV}$ [10]. The kinetic energy belonging to each orbital is measured in the experiment. Lastly, the light incidence with a polar angle of $\Theta = 65\,^\circ$ and $\phi = 5\,^\circ$ towards the positive k_y direction of the photoelectrons is put into the tool. The light is left-circularly polarized. Fig. 5.1 shows the PMM after applying the symmetry procedure discussed in 4 for $E_\mathrm{ph} = 25\,\mathrm{eV}$. The corrected and fitted experimental PMM of the HOMO (a) and LUMO (b) is in very good agreement

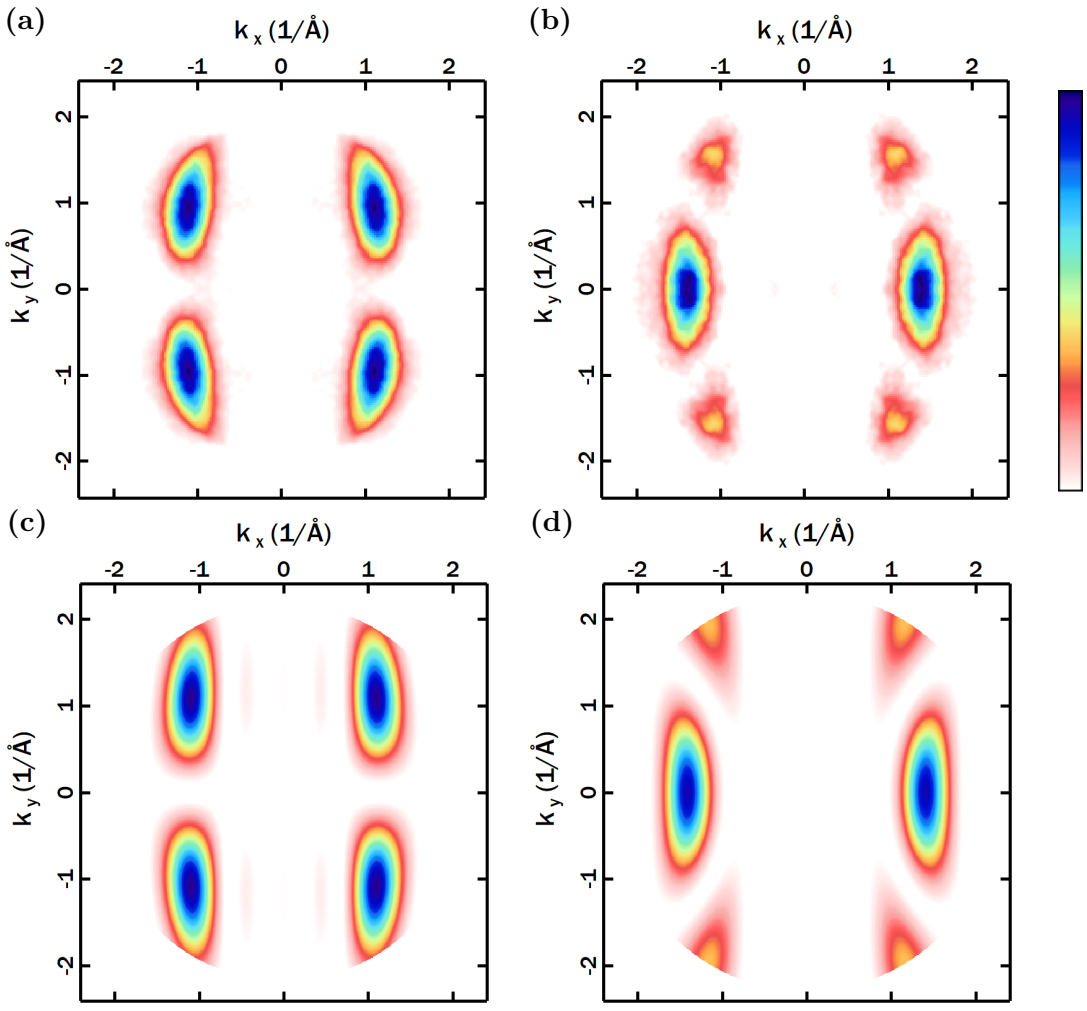

Figure 5.1: Symmetrized and fitted experimental PMM (top row) compared to the simulation (bottom row) of the HOMO (left column) and LUMO (right column) of a pentacene monolayer on Ag(110) at $E_{\mathrm{ph}} = 25\,\mathrm{eV}$.

with the simulations (c) and (d), respectively. As previously discussed in section 4.2, the features in the experiment are slightly distorted due to the inhomogeneous field of the lens elements close to the edge of the detector. They are also cut at higher k values beyond the finite extent of the MCP. The simulation of the HOMO (c) again predicts a faint signal at $(k_x, k_y) = (\pm 0.5, \pm 1.1)\,\text{Å}^{-1}$ that is likely not detectable in the experiment (a) due to the imperfect molecular lattice and interfering background noise. The calculated position and intensity distribution of the main compared to the side features in the LUMO (d) is also very close to the experimental data (b).

Since the final state should give a more reliable prediction even in cases where **A** is far from parallel to **k**, we can also compare the non-symmetrized PMM. Fig. 5.2 shows the non-symmetrized experimental PMM (top row) compared to the simulation (bottom

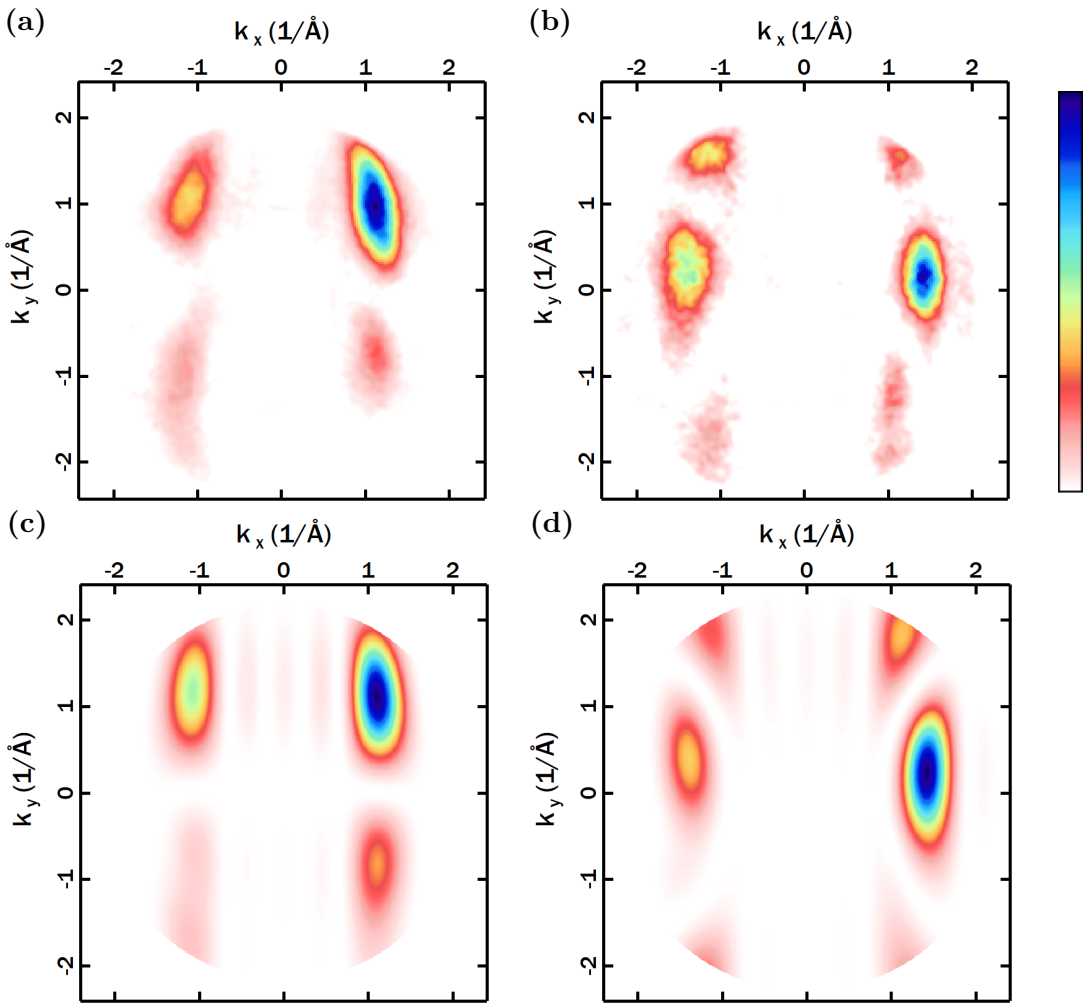

Figure 5.2: Non-symmetrized experimental (top row) and simulated PMM (bottom row) of the HOMO (left column) and LUMO (right column) of a pentacene monolayer on Ag(110) at $E_{\text{ph}} = 25\,\text{eV}$.

row) for the HOMO (left column) and the LUMO (right column). As expected, the molecular features are strongly dependent on the light polarization that breaks the pmm-symmetry of the sample. For $k_x, < 0$ and $k_y < 0$ the HOMO in (a) is visibly spread in k_y, whereas it is shifted slightly upward for $k_x, > 0$. Both of these signals are reproduced by the calculation in (c) as well as the relative intensity distribution. The LUMO in (b) is generally lopsided towards higher k_y values. The fit to the calculation in (d) is also decent, even though the relative intensity distribution in the upper quadrants is not ideal. The deviation could stem from the imperfect alignment of the experimental setup. The trajectories of the photoelectrons are not entirely symmetric around $k_{\parallel} = 0$ which results in the detector cutting the photoelectron signal at different (k_x, k_y) values depending on the azimuthal angle. Nevertheless, it could also be a hybridization of the LUMO with the silver substrate that shifts the spectral weight.

In conclusion, the successful replication of the pentacene valence orbitals is evidence of the proper implementation of the photoemission tool.

5.2 Determination of adsorption geometries

The geometric alignment of molecules at organic-inorganic interfaces plays a major role in the energy alignment and physical properties of a sample and ultimately of any organic device [148–154]. The determination of the growth structure of a molecular thin film on a substrate is therefore usually the first step in the examination of an unknown interface. Theoretical calculations can narrow down the possible adsorption configurations of the molecules to some extent, but are unfortunately not unambiguous [12]. At the current level of technology, they cannot be used to simulate the entire substrate plus the molecular layer; and even when reducing the molecular layer to a single molecule, they remain computationally taxing. However, when supplemented with LEED and ARPES experiments and simulations, the growth geometry of the molecules can be established quite efficiently. In the following, we will use this approach to determine the adsorption site and azimuthal rotation of the molecule pyrphyrin on an Ag(110) substrate.

Pyrphyrin was already synthesized in 1984 by Ogawa et al., but barely any further inquiry into its properties was conducted for the next three decades [155, 156]. Pyrphyrin and its derivations were finally "rediscovered" in the mid-2010s for their potential as a catalyst in the reduction of water [157–159]. The structure and composition of pyrphyrin is displayed in fig. 5.3. It is a two-dimensionally flat molecule in the gas phase composed of carbon (black), nitrogen (blue) and hydrogen (gray). The two hydrogen atoms in the center can be replaced with a transition metal atom to form a pyrphyrin derivate which altered physical and chemical properties. One promising candidate for the reduction of

water into hydrogen and oxygen is cobalt-pyrphyrin, which is an alternative to other, more expensive metals [160]. In the future, it might therefore become an important piece in the quest for sources of renewable energy. Nevertheless, there are also entirely different conceivable applications, like the controlled doping of a substrate at its surface.

An understanding of the growth of the molecules is indispensible for their application, since the electronic, physical and chemical properties are dependent on the molecular alignment in respect to one another and a substrate close to the reactive region. To this end, we determined the adsorption geometry of a monolayer of pyrphyrin on an Ag(111) substrate at room temperature in collaboration with Pavlo Kliuiev and Luca Castiglioni from the Department of Physics at the University of Zürich (UZH), who recorded the experimental data. They conducted the experiments at the NanoESCA beamline at the ELETTRA synchrotron in Trieste [135]. The molecules were synthesized and provided by Stephan Schnidrig and Roger Alberto from the Department of Chemistry at the UZH. This project provided preliminary information for parts of the eventual publication in [147].

Possible adsorption sites of pyrphyrin were previously narrowed down by a geometry relaxation in a DFT calculation performed by Yeliz Gurdal and Marcella Iannuzzi from the Department of Chemistry of the UZH. Their simulations deployed a single molecule at arbitrary positions and azimuthal rotations above the fixed silver substrate and relaxed it along the potential gradient to find local minima in the adsorption energy. The geometric alignment and adsorption energy of the five strongest bound configurations found via this method are shown in fig. 5.4.

The position and azimuthal rotation of the models differs strongly. Since the differ-

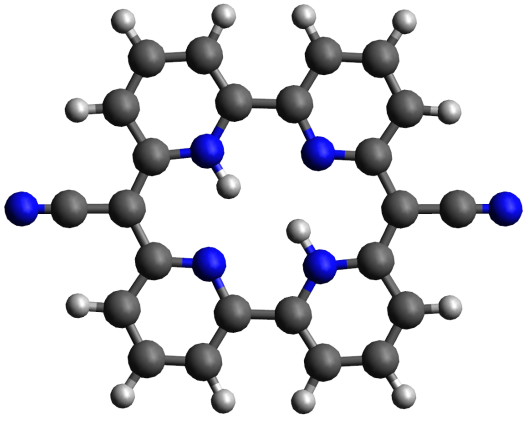

Figure 5.3: Pyrphyrin structure and elemental makeup. The molecule is made of carbon (black), nitrogen (blue) and hydrogen atoms (gray) and has a flat, two-dimensional shape in the gas phase. The center which is filled by two hydrogen atoms in pyrphyrine can be also filled with a transition metal instead, thereby creating a variety of possible derivates.

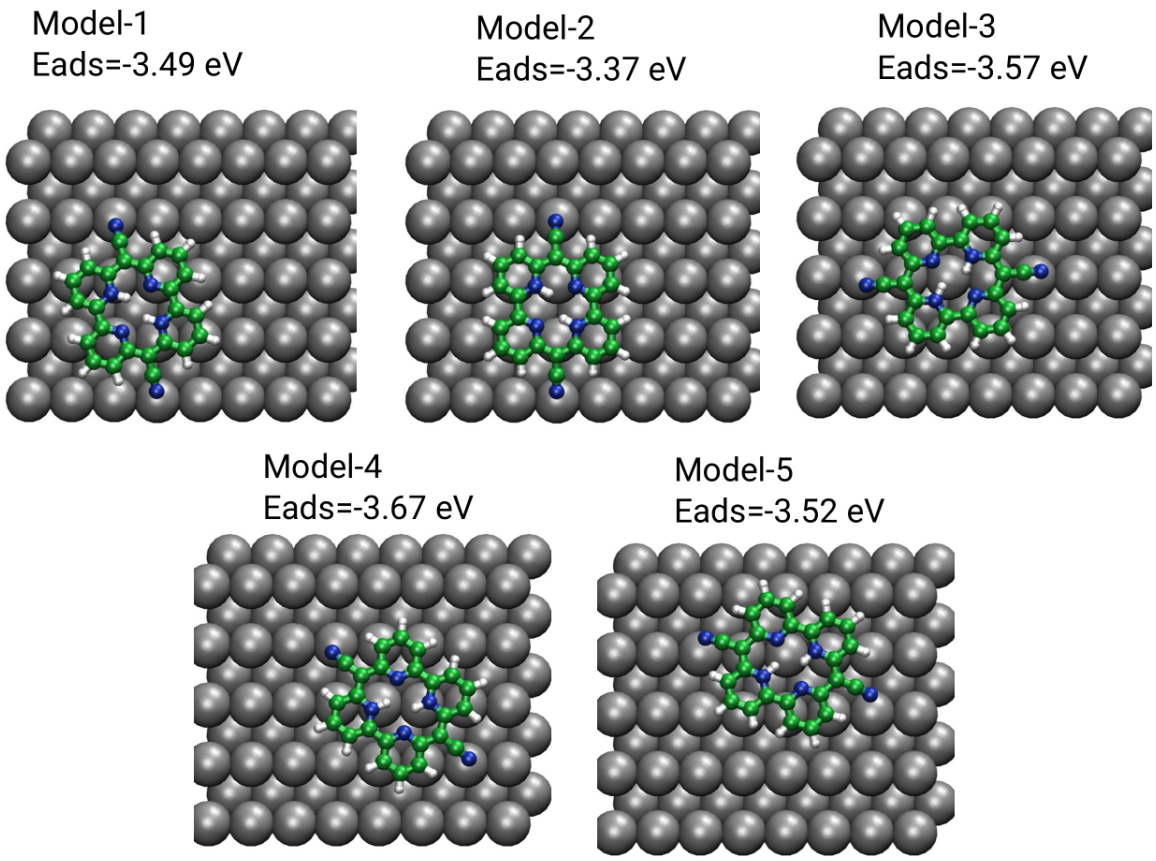

Figure 5.4: Possible adsorption geometries of pyrphyrin on Ag(110) according to the DFT simulation of a single molecule on the substrate. The calculated adsorption energy of the five models is indicated above the geometry. The relaxation was performed by Yeliz Gurdal and Marcella Iannuzzi from the University of Zürich [147].

ence in adsorption energy between the energetically lowest $E_{\text{ads,Model-4}} = -3.67\,\text{eV}$ and the second lowest configuration $E_{\text{ads,Model-3}} = -3.57\,\text{eV}$ is larger than the thermal energy at room temperature $\Delta E_{\text{ads}} = 100\,\text{meV} > E_{20^\circ\text{C}} = 25\,\text{meV}$, one could be tempted to declare Model-4 with the lowest adsorption energy as the proper growth geometry. However, there are many factors present in the actual sample and experiment that will alter the adsorption energy and that are absent in the calculation. The most crucial ones being the influence of neighboring molecules in the experiment and the presence of step edges and crystal defects, at which the growth of the molecular layer typically begins due to the additonal lateral bonding partners [161, 162].

Photoemission experiments are thus helpful to clarify the adsorption geometry. To this end, a monolayer of pyrphyrin is evaporated from a home-built thermal evaporator onto the Ag(110) substrate and illuminated by p-polarized light towards positive k_x and k_y values with a photon energy of $E_\text{ph} = 35\,\text{eV}$. Fig. 5.5 shows the experimental photoelectron momentum maps of the HOMO-2 (a), HOMO-1 (b) and HOMO (c). The background signal from the clean Ag(110) substrate has been previously measured and is already subtracted in these PMM. The asymmetry caused by the light impinging towards positive k_x and k_y values is clearly visible by the increased intensity in the upper right quadrant. All three molecular orbitals exhibit a clearly identifiable photoemission pattern.

To determine the geometry of the molecules that leads to this ARPES signal, DFT calculations for the initial states are performed on isolated pyrphyrin molecules with an STO 6-31+ basis set and the B3LYP functional. For each of the five models the energetically equivalent configurations due to the symmetry axes of the substrate are also calculated. The DFT initial states are then put into in the photoemission calculation along with the same parameters as in the experiment and the intensity of equivalent configurations

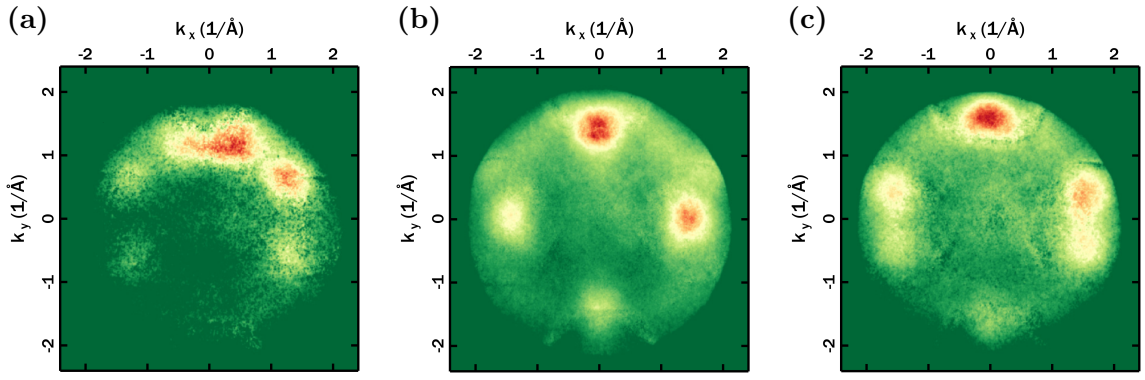

Figure 5.5: Experimental PMM of the HOMO-2 (a), HOMO-1 (b) and HOMO (c) for p-polarized light in the direction of positive k_x and k_y values and $E_\text{ph} = 35\,\text{eV}$. Courtesy of Pavlo Kliuiev.

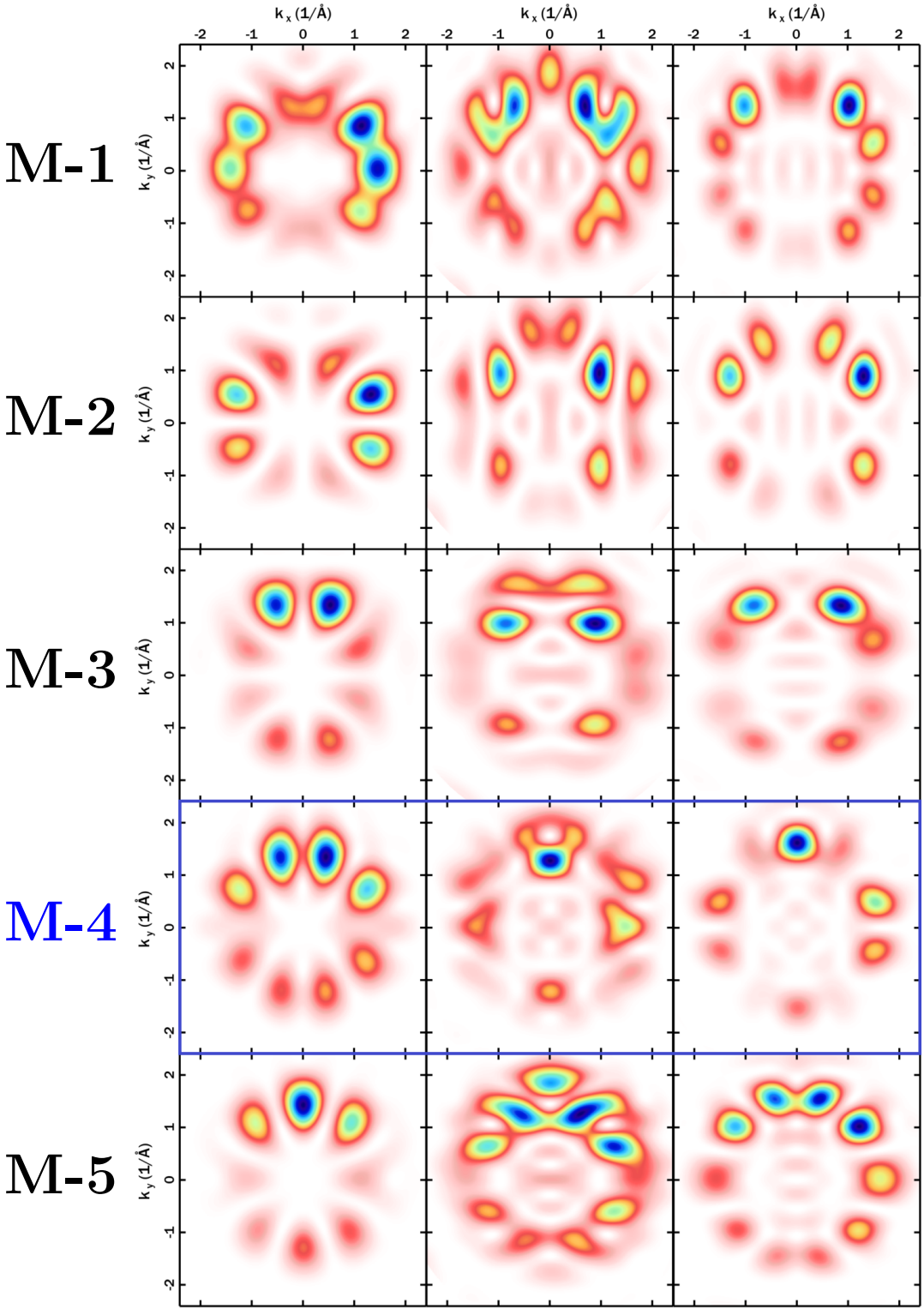

Figure 5.6: Calculated PMM of the HOMO-2 (left column), HOMO-1 (middle column) and HOMO (right column) for the five adsorption geometries with the lowest energy according to the DFT calculation. With the comparison to the experiment in fig. 5.5, Model-4 is unambiguously identified as the correct adsorption geometry.

added together. The resulting PMM are shown in fig. 5.6 for the HOMO-2 (left column), HOMO-1 (middle column) and HOMO (right column) for each model M-1 to M-5 (rows). Note that the simulated PMM extend to larger $k_{\parallel}$ values than the experiment, since the latter are cut by the limits of the MCP detector. The asymmetry in the PMM is caused by the light incidence and polarization that breaks the symmetry of the system.

The different models predict distinct photoemission distributions that can easily be separated from one another. In comparison with the experiment in fig. 5.5, the only set of PMM that agree with the experiment for all three molecular orbitals are calculated with the M-4 geometry. The positions of the molecular features in reciprocal space fits to the experiment and the relative intensities are also well reproduced.

The comparison of all three calculated molecular orbitals to the experiments leads to an unequivocal result in this growth study. Since the interaction between the substrate and molecular valence states is negligible in this case, the determination of the azimuthal (and polar) tilt of the pyrphyrin molecules is even feasible without the accompanying DFT relaxation. They nevertheless help to reduce the set of geometries that are initially tested and moreover give an indication for the adsorption sites of the molecules. The evidence for the latter is not as strong as for unambiguously determined tilt angles, however, since the molecular superstructure is not commensurable [147]. That means that while one molecule could adsorb in the position shown in in Model-4 in fig. 5.4, the majority of molecules occupy non-equivalent adsorption sites. This question cannot be fully settled from the experimental data at hand and would require further measurements, e.g. with scanning tunneling microscopy. If there is a limited amount of adsorption sites it can also be possible to analyze the photoemission signal from elastically scattered electrons to uncover the molecular adsorption sites. This approach based on the diffraction of photoelectrons will be examined in the following section.

5.3 Determination of adsorption sites via photoelectron diffraction

Not all photoelectrons that are measured in an experiment have to take a direct path to the detector. Some scatter elastically at the potential surface around the atoms in the sample before they enter the vacuum on their trajectory to the detector. The three steps of such an elastic scattering process – initial emission, scattering at a potential, transmission through the surface into the vacuum – are condensed into a physically more accurate one-step model in the photoemission tool. The mathematical basis for this description is laid out in subsection 2.3.2. Even though the elastic scattering component of the photo-

emission tool is still work in progress at the time of this writing, it can already be used in this analysis. Nevertheless, it involves more approximations and thus can be expected to be less accurate than the previous evaluations.

In this section, the photoemission tool will be used to determine the adsorption site and geometry of a sub-monolayer of carbon monoxide on top of the platinum (111) surface. The project was carried out in cooperation with Kay Waltar and Luca Castiglioni from the Department of Physics at the University of Zürich (UZH) and Peter Krüger from the Department of Materials Science at Chiba University. The target of this study was to obtain the geometric information of the carbon monoxide molecules at lower photon energies than in commonly used **X**-ray **P**hotoelectron **D**iffraction (**XPD**) experiments for this purpose. XPD is an established photoemission technique to aquire structural information from the angle-dependence of elastically scattered photoelectrons emitted from strongly bound core levels [163]. The data is usually straightforward to interpret in conjunction with theoretical simulations, e.g. via software packages like EDAC [101], since the fully occupied initial states are spherically symmetric [95]. The measured angle-dependence is therefore determined by the known light polarization and the scattering in the final state. This reliance on core level initial states unfortunately means that the same theory is not easily adapted to molecular valence orbitals. For molecular orbitals the angle-dependence of the initial state cannot be neglected as they extend over several atoms and have a non-spherical symmetry. The advantage of nevertheless using molecular instead of core orbitals for the geometry determination is that they are only weakly bound and thus require lower photon energies. This in turn enables the measurement of time- and angle-resolved photoemission data at high-harmonic generation setups [164–166] instead of only at free-electron laser facilities [167, 168]. The photoemission cross section of the molecular valence orbitals also conveniently increases for photon energies in the e**X**treme **U**ltra**V**iolet (**XUV**) instead of the X-ray range (compare section 4.2). The structural information can hence be gathered alongside the electronic and chemical information contained in the valence states using the same experimental setup and possible even in the very same scan.

In addition to this promising technique, the CO/Pt(111) system that is surveyed is also of high interest in its own right: platinum is widespread in many industrial applications as a catalyst in the oxidation of carbon monoxide [169]. Despite its everyday usage in cars and other machinery, the details of the catalysis at the platinum surface are not fully understood and still researched on a fundamental level [170, 171]. While the catalytic reaction retains some secrets, the adsorption site of several low coverage phases of this system have been explored through other experimental methods [172, 173] and DFT calculations [174]. Knowledge of the static geometric information of the isolated CO molecule was a useful step in assessing how the platinum surface promotes its oxidation.

The CO/Pt(111) system is therefore a suitable test case to check whether the photoemission tool arrives at the same adsorption site. If the static geometry can be verified, the aforementioned time-resolved ARPES techniques can subsequently build upon and expand this photoemission technique to track dynamic structural changes induced by an exciting pump pulse followed by a XUV probe pulse. These follow-up measurements can then provide novel insights closer to the actual chemical reactions on the Pt(111) surface.

The experiments of this project were conducted at the PEARL beamline of the Paul-Scherrer-Institut in Villigen, Switzerland [175]. The platinum sample surface is cleaned in the UHV by cycles of argon ion bombardment and annealing at elevated temperatures. To make sure that there is no interaction between neighboring carbon monoxide molecules, a sub-monolayer in the $(\sqrt{3}\mathrm{x}\sqrt{3})\mathrm{R}30^\circ$ superstructure is prepared on the Pt(111) substrate [176] and verified by a LEED experiment. Fig. 5.7 (a) shows the angle-integrated EDC of the photoemission experiment on the completed sample at a photon energy of 150 eV, p-polarized light and cooled down to 150 K. The prominent features in the occupied part of the spectrum can be assigned to the carbon monoxide 4σ, 5σ and 1π orbitals [177] as well as the platinum 5d bands. For the angle-resolved analysis, we will focus on the 5σ orbital at a binding energy of $E_{\mathrm{bin}} \approx 9\,\mathrm{eV}$. To this end, DFT calculation of the isolated carbon monoxide are performed with the STO 3-21 basis set and the B3LYP functional, as well as with a carbon monoxide molecule and the nearest platinum atoms below with a polarized doube-zeta basis set (DZP) and the CAM-B3LYP functional [178]. The latter calculations are included to gauge whether the hybridization of CO with the substrate is of relevance to the PMM, as can be expected from literature [174]. Fig. 5.7 (b) displays the resulting real space wave function of the isolated CO 5σ around the carbon (black) and oxygen atom (red) with the color of the wave function indicating its phase. The main contribution to the CO 5σ orbital are the carbon 2s and $2\mathrm{p}_\mathrm{z}$ orbitals as well as the oxygen $2\mathrm{p}_\mathrm{z}$ orbital (with the z-axis aligned parallel to the molecular axis).

Unlike the previously shown ARPES data sets in this thesis, the angle-resolved data in this experiment is recorded by rotating the sample within the UHV measurement chamber. Fig. 5.8 (a) displays the processed data of the 5σ orbital in a polar plot. The color indicates the deviation from the average intensity at each polar angle step $I(\Theta)$. A brighter/darker color thus signals that the photoemission intensity at this particular polar and azimuthal angle Θ and ϕ is above/below the average of all data points at the same Θ. The integration interval also contains spurious signal from the 1π orbitals which have some energetic overlap with the 5σ orbital. The data has been symmetrized (averaged) with the three-fold rotational symmetry of the Pt(111) substrate to boost the signal-to-noise ratio. While the first layer of the fcc-structure substrate is six-fold symmetric, this symmetry is reduced to three-fold if the second and subsequent layers are taken into account. The absolute intensity of the measurement strongly decreases and is therefore less

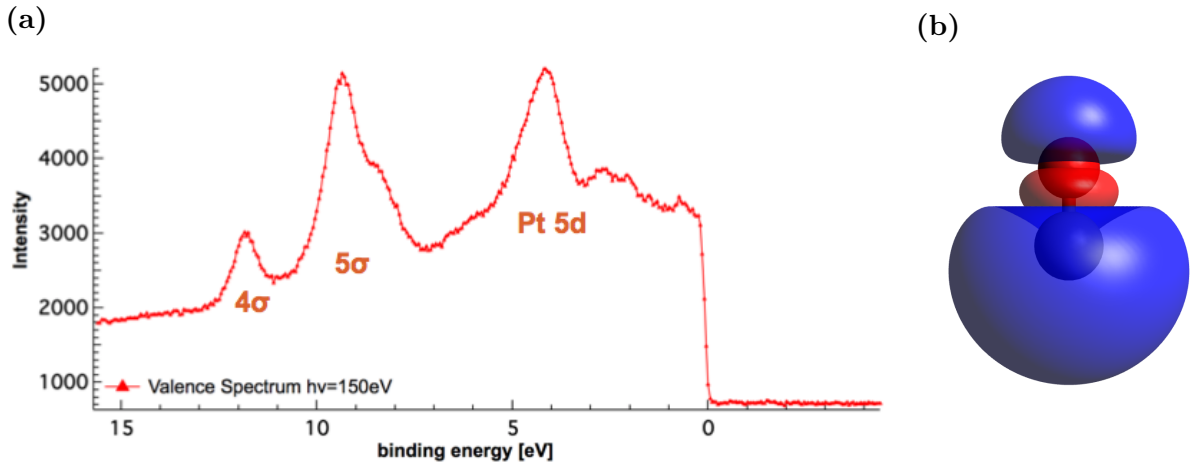

Figure 5.7: (a) Angle-integrated EDC of a sub-monolayer of carbon monoxide on top of Pt(111) at a photon energy of $E_{\mathrm{ph}} = 150\,\mathrm{eV}$ and temperature of 150 K. Courtesy of Luca Castiglioni. (b) Wave function of the CO 5σ orbital around the carbon (black) and oxygen atom (red).

reliable for polar angles above $\Theta \gtrsim 55°$.

Close to the center in the polar plot, the photoemission pattern shows the three-fold symmetry of the substrate that is also imposed by the symmetrization process. Towards higher polar angles, the features exhibit an almost six-fold symmetric intensity distribution. This can be explained by the dominance of backwards scattering at a 180 ° angle at the platinum atoms: in a three-step model of photoemission, photoelectrons that are emitted straight towards the substrate and backscattered have a shorter path inside the substrate than photoelectrons at higher polar angles. The former are then not damped as strongly by the finite inelastic mean free path. Hence, the lower the polar angle, the higher the ratio of photoelectrons that reach the second layer of the Pt(111) substrate, scatter elastically and arrive at the detector. It is the influence of these electrons that breaks the six-fold symmetry that would be expected if the elastic scatting occurred only at the very first platinum layer. Close to the surface normal vector in the interval of polar angles $\Theta = [10, 25]°$ there is a three-fold symmetric pattern of alternating higher and lower intensity (A). It is followed by another ring-shaped pattern for $\Theta = [25, 45]°$ that is close to six-fold symmetric with a more pronounced intensity variation (B). The intensity maxima of features A are rotated by about 30° with respect to the maxima of feature B for the same azimuthal angle ϕ. A third ring (C) further out at $\Theta = [45, 60]°$ also has an almost six-fold symmetric pattern that is rotated by 30° compared to feature B.

To extract the adsorption site from this data, photoemission matrix element calculations with the photoemission tool have been conducted with several different adsorption sites, heights and rotations of the carbon monoxide molecule. As mentioned above, the DFT calculations contained either the isolated carbon monoxide, or the carbon monox-

ide including the nearest platinum atoms below. Simulating matrix elements with elastic scattering enabled is considerably more complicated than those without. In the current version of the program, the agreement to the experiment can thus be expected to be affected by the additional approximations.

The position of the platinum substrate atoms was optimized in a DFT relaxation performed by Peter Krüger. For the photoemission calculation itself, the "Rotary Azimuthal Scan" Mode of the photoemission tool is used to replicate the experimental geometry. In preparation of more detailed calculations, the influence of the maximum scattering distance and the maximum number of scattering events are determined. In these tests it is found that atoms beyond a 10 Å radius around each emitting atom and more than twice-scattered electrons barely contribute to the calculated photoemission intensity.

The resulting photoemission intensity distribution for the parameters with the best agreement to the experiment is shown in fig. 5.8 (b). Just like in the experiment, with increasing polar angle the patterns have a symmetry that gets closer to being six- instead of three-fold. Starting at the center, the calculation shows a small intensity variation that is conceivable too small to be picked up in the experiment. Around $\Theta = 0°$, the finite angle resolution will also blur out the recorded intensity. Feature A at $\Theta = [10, 25]°$ exhibits clear deviations from the experiment. While there is an increase in intensity at the expected positions, the calculation predicts an increase that is almost as large in areas of slightly decreased intensity in the measurement. One possible explanation is that the inelastic damping in the calculation stops at the vacuum that is located at a fixed height above the sample. However, from the position of the carbon monoxide molecule above the platinum substrate one would expect that the damping of photoelectrons effectively stops at a lower height above the substrate, if the photoelectrons take a path at a higher polar angle away from the molecule. The setting in the simulation could therefore distort the ratio of photoelectron intensity scattered at the first versus at the second and at subsequent platinum layer. Nevertheless, the fixed height of the vacuum in the calculation underestimates the damping at low polar angles. With this explanation, the three-fold symmetric pattern of the measurement would thus only be reproduced by scattering on substrate layers beyond the second layer. On the edge between features A and B at $\Theta = 25°$, the six-fold intensity maxima are found in both images. Feature B also agrees well with the experiment: the almost six-fold variation in intensity is reproduced and the three-fold symmetry of every second intensity valley being slightly more pronounced is also present in both calculation and experiment. This is similar for the close to six-fold symmetric C at $\Theta = [45, 60]°$, where every second intensity maximum starts at slightly lower polar angles, but is less confined. The two drops in intensity between the maxima that are split by a slight increase in intensity are also visible in the experiment. The calculation shows distinct patterns towards even higher polar angles that cannot be seen

in the experiment. This is due to the total intensity dropping sharply beyond $\Theta = 60°$. Also, the small deviations in polar angles of the features in calculation and experiment can be explained by a slight mismatch in the simulated compared to the actual geometry. This could be improved by further tweaking the simulated geometry in a trial-and-error approach.

In the input of the calculation, the carbon molecule is in a top site above a platinum atom at an adsorption height of $d_{\text{Pt-C}} = 1.85\,\text{Å}$ and the oxygen atom pointing straight up separated by $d_{\text{C-O}} = 1.15\,\text{Å}$. The DFT calculation includes the platinum atom right below the carbon atom. These values match those found by experiments [172, 173] and DFT calculations [174] in literature. The inner potential is set to $V_0 = 14\,\text{eV}$ and the inelastic mean free path to 9.6 Å.

In summary, the elastic scattering component of the photoemission tool was tested against the experimental data of CO adsorbed on a Pt(111) substrate. The agreement between calculation and measurement is sufficient for the determination of the on-top adsorption site of CO with the carbon below the oxygen atom. Nevertheless, the match is not as good as for the previous evaluation cases in the absence of relevant elastic scattering in the current version.

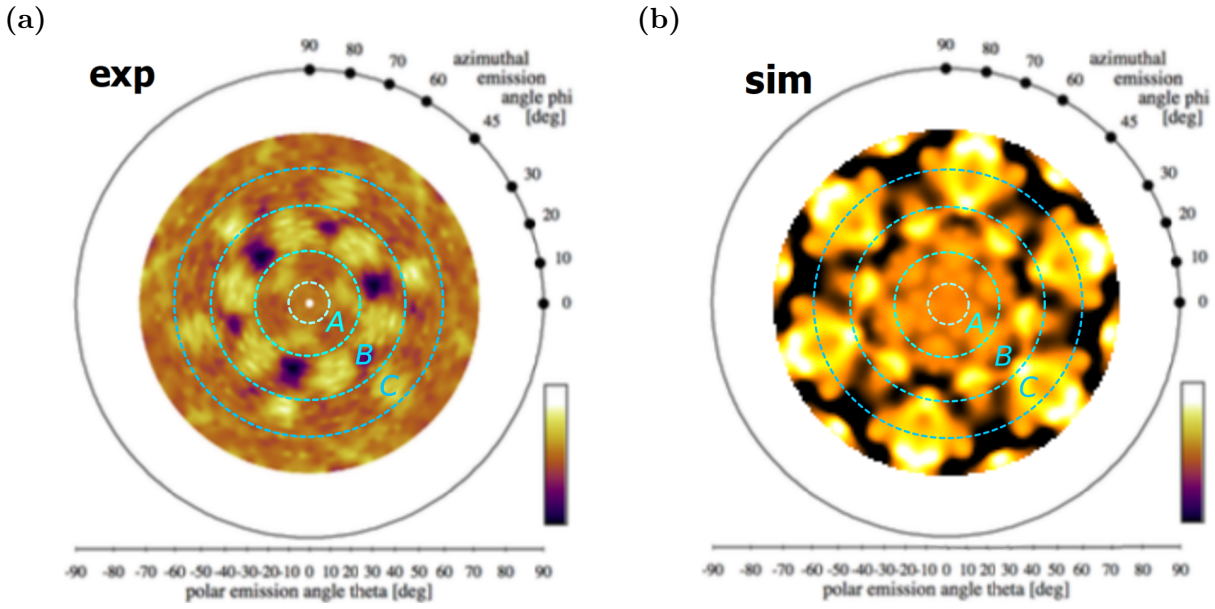

Figure 5.8: Polar plot of the experimental (a) and simulated photoelectron intensities (b) of the HOMO of carbon monoxide on top of Pt(111) at a photon energy of $E_{\text{ph}} = 150\,\text{eV}$. The color indicates the deviation from the average intensity at each polar angle. Picture (a) by courtesy of Luca Castiglioni.

6 Structure determination of adsorbates in multilayer films

The areas of interest we probe in this thesis are all at the junction of a crystal with a molecular thin film on top. In a sense, two realms described by fundamentally different physical models meet at these interfaces: delocalized electrons of a periodic lattice represented by Bloch waves and localized molecular orbitals built from the LCAO approximation. The crossover region can give rise to a variety of physical phenomena [151,179,180]. The interaction between the two materials is naturally dependent on the overlap of wave functions and the potential surface in the region. These electronic properties are in turn guided by the adsorption geometry of the molecules [181]. Hence, information on the molecular alignment is vital to studies of interface phenomena.

Besides shedding light on novel properties in fundamental research, interfaces are abundant in almost any kind of application of organic structures. The vast majority of organic devices are electronic and connected to a power source (or drain) at least temporarily during their lifetime. This means that at the very least there has to be a junction of the organic material and the (metal) connectors to facilitate the electronic transport. The region in the vicinity of the junction is subject to many interface phenomena like structural realignment and contact losses [182–184]. The effects are mostly detrimental to the electronic transport, but can be minimized if they are thoroughly probed and understood. Knowledge of the interface is even more crucial if the interface is a functional part that is integral to the operation of the device. This rationale is perhaps best summarized by Herbert Kroemer in his nobel lecture after receiving the nobel prize for physics in 2000: "The interface *is* the device" [185]. In these cases, the function and efficiency of the item is immediately tied to the interface properties.

In this chapter, we will tackle this issue with a spectroscopy technique based on ARPES measurements and calculations. The approach yields both the geometric structure and the electronic properties of the organic molecules. Our model system of a metal-organic interface is a thin film of pentacene grown on top of a silver substrate.

LEED experiments can be used to probe the lateral unit cell, but they do not reveal how the molecules are aligned within that cell. Any tilt or distortion of the molecular positions that would affect the interface properties thus has to be determined by a different technique.

Besides ARPES, one might alternatively or complementary use **S**canning **T**unneling **M**icroscopy (**STM**) [186], **N**ear **E**dge **X**-ray **A**bsorption **F**ine **S**tructure (**NEXAFS**) [187] and **X**-ray **S**tanding **W**ave (**XSW**) [188] techniques for this purpose. While STM measurements contain this information by default there are two major drawbacks. First of all is the limited precision to which the structure of molecules can be resolved. For a similar organic system for example, the resolution of the molecular tilt angle is markedly lower. The second issue is the extreme surface sensitivity of the tunneling current. If the area of interest is not directly at the surface then it's effect on the tunneling current is greatly suppressed. The accuracy of the geometry determination for molecules buried beneath the surface is therefore even further reduced. NEXAFS measurements on the other hand *can* penetrate the immediate surface of the sample. The same is true for XSW experiments, as long as the area of interest is either above the reflective substrate or the sample is highly ordered. Data interpretation is more engaging however, as the signal from different parts of the molecule can be difficult or even impossible to disentangle when simulations with different geometries match the experimental data.

ARPES measurements have the advantage of probing several layers deep into the sample, under certain conditions even without blending the information of different layers inseparably. This is mainly due to the additional detection of the angular dependence of the emitted photoelectrons which helps unravel similar signals from different components of the sample.

The well characterized pentacene/Ag(110) sample from the previous chapter presents a suitable starting point to look into this topic. By evaporating additional molecules on top of the first layer and following up with ARPES experiments one can establish this technique on the instance of a pentacene thin film atop Ag(110). For this proof of principle it is sufficient to increase the amount of molecules to about two monolayers. The major results of this study are published in *Physical Review B* [10].

6.1 Sample preparation

Fig. 6.1 depicts the exemplary growth mode of a pentacene dimer which can be expected to form according to studies of similar pentacene layers. While the molecules in the bulk phase are highly tilted with respect to each other [106, 189], the first few layers on top

of noble metal substrates do not generally align in this geometry right away [80, 105, 190] due to the interaction between the substrate and the organic thin film.

The first step in the preparation of the bilayer is cleaning the Ag(110) substrate with repeated cycles of Ar^+ ion bombardment and annealing as described in section 3.2. Once the cleanliness of the substrate is verified by a LEED experiment, pentacene from the previously calibrated evaporators is deposited for $t = 45\,\text{min}$ at a temperature of $T = 185\,°\text{C}$. With an evaporation time of $t_{ML} = 25\,\text{min}$ for the first monolayer, this corresponds to a coverage well above a single layer, but below two layers. One reason for this choice is to avoid depositing molecules in a third layer within the error bar of the evaporation rate. Opening a third layer would not undermine the demonstration of the technique, but unnecessarily complicate it. As we will illuminate below, the second layer is also denser than the first one, which alters the evaporation duration for a full layer.

The LEED pattern of the finished sample is shown in fig. 6.2 (a) for an electron kinetic energy of 14 eV. Some of the LEED spots can be explained by the $(\,3\,,\,-1\,/\,-1\,,\,4\,)$ superstructure matrix of the first layer (red), which was decoded in chapter 4. These molecules are aligned with their long molecular axis along the [001] direction of Ag(110) [131]. Deposition of more pentacene results in additional diffraction maxima (green) next to the spots originating from the first layer. This new set of spots is described by a $(\,5\,,\,2\,/\,-2\,,\,3\,)$ superstructure matrix. This second growth geometry ostensibly belongs to the second layer of pentacene.

Both layers thus grow commensurately with respect to the silver substrate, but not with respect to each other. The area within the two-dimensional unit cell of the of the second layer $A_{2nd} = 224.2\,\text{Å}^2$ is also markedly larger than the one of the first layer $A_{1st} = 129.8\,\text{Å}^2$. In fact, there is enough space to accommodate *two* molecules of similar or identical azimuthal rotation within the unit cell of the second layer. In this case, the evaporation duration of $t = 45\,\text{min}$ corresponds to a coverage of about 69 % in the second layer on top of the completed first layer. For comparison, if the molecules would continue growing with the monolayer lattice structure, the coverage would be 80 %. However, if only a single molecule would occupy each second layer unit cell, the coverage of 138 % would clearly exceed the second layer and start a third one. Judging from the intense

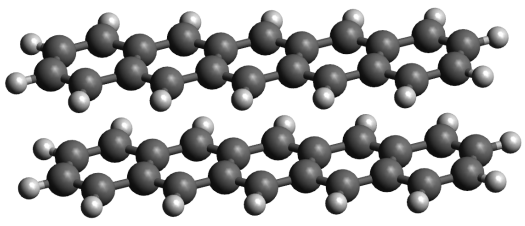

Figure 6.1: Exemplary pentacene dimer structure.

pattern of the first layer in the LEED experiment, we can exclude this possibility and conclude that the first layer is indeed not entirely covered.

Unlike the intra-layer structure, the lateral alignment between both layers is not probed by this LEED experiment and it is not clear whether a specific inter-molecular geometry configuration is present on the sample. On Au(110) however [105], the most prevalent configuration of the second layer pentacene molecules is in a bridge site along the short molecular axis of the molecules below. There is no displacement along the long molecular axis (for the most part) and no additional rotation along the surface normal vector. It is feasible that this configuration is also present when grown on Ag(110) as it is chemically similar and its lattice constant is only $\sim 0.2\,\%$ larger [76, 191].

6.2 Results and discussion

Photoemission experiments on this sample were conducted at the NanoESCA beamline at the ELETTRA synchrotron in Trieste. All measurements were taken while cooling the sample with liquid helium to about $T_{\mathrm{sample}} = 140\,\mathrm{K}$. Fig. 6.2 (b) shows the angle-integrated EDC close to the Fermi edge of a monolayer of pentacene (red) compared to the bilayer (green) atop Ag(110) for a photon energy of $E_{\mathrm{ph}} = 30\,\mathrm{eV}$ and p-polarized light. Compared to the measurement of the monolayer, the partially occupied LUMO ($\mathrm{LUMO}_{1\mathrm{st}}$) at

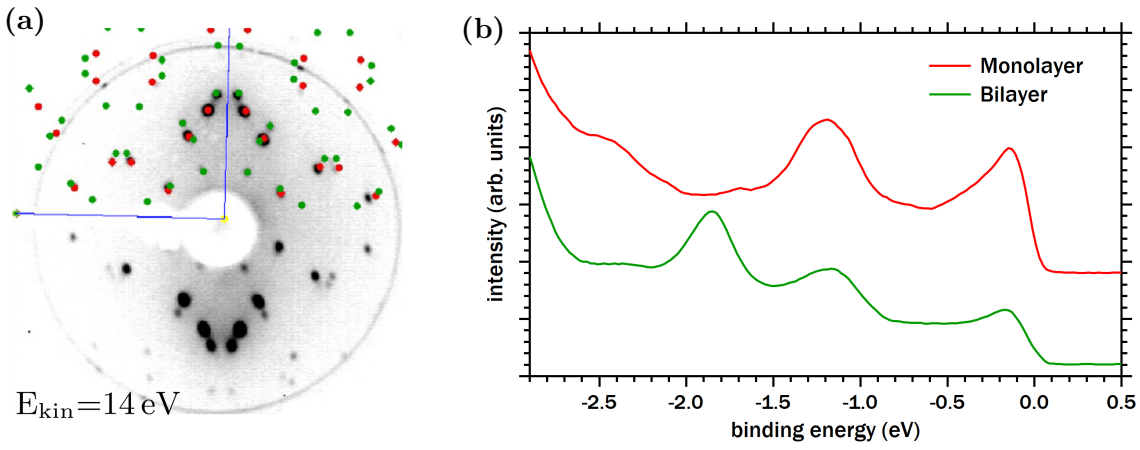

Figure 6.2: (a) LEED pattern of the pentacene bilayer/Ag(110) sample at $E_{\mathrm{kin}} = 14\,\mathrm{eV}$. The unit cell vectors of the first layer are reproduced with the superstructure matrix $M_{1\mathrm{st}} = (3, -1 / -1, 4)$ (red), those of the second layer with $M_{2\mathrm{nd}} = (5, 2 / -2, 3)$ (green). (b) Integrated EDC of the mono- (red) and bilayer (green) of pentacene on Ag(110) with p-polarized light and $E_{\mathrm{ph}} = 30\,\mathrm{eV}$. After evaporation at room temperature, the sample is cooled to $T_{\mathrm{sample}} = 140\,\mathrm{K}$ in both cases.

the Fermi edge is damped, but still clearly visible. This is an indication that the charge transfer from the silver substrate into the first molecular layer is still present, but there is no additional transfer into the second layer. Some of the photoelectrons originating in the first layer scatter inelastically before reaching the vacuum above the sample, reducing the overall $\mathrm{LUMO_{1st}}$ intensity.

While the HOMO signal at $E_\mathrm{B} = 1.2\,\mathrm{eV}$ ($\mathrm{HOMO_{1st}}$) is also similar in both measurements, there is a new intensity maximum in the bilayer sample at $E_\mathrm{B} = 1.8\,\mathrm{eV}$. This feature is tentatively assigned to the HOMO from the second layer ($\mathrm{HOMO_{2nd}}$). The higher binding energy of the HOMO in the second layer is due to the weakened screening of the photohole left behind by the photoelectron [192]: the nearly-free electrons in silver are very effective at screening the core hole in a molecule in immediate contact with the substrate. The screening of a photohole localized in the second layer is significantly less efficient since the localized electrons in neighboring organic molecules do not screen as well and the substrate is not as close to the positive charge. The strength of the photoemission features from the first layer and the absence of any additional signals besides one from the second layer is further evidence of the increased molecule density in the second layer, as determined from fig. 6.2 (a).

Fig. 6.3 displays the constant energy cuts of these three molecular orbitals in the valence regions after applying a fitting routine that averages the photoemission data within $\Delta k_\mathrm{x,y} = 0.05\,\mathrm{\AA}^{-1}$. The fitting procedure contains a Gaussian function for each molecular orbital and an exponential function for the silver background, all of which multiplied by the Fermi-Dirac distribution. The lower end of the intensity color scale is raised from the minimum intensity to suppress the background signal from the silver substrate. There is no discernible energy dispersion of the molecular features within the energy resolution of 70 meV [123]. Each of the PMM is integrated in an energy range of $\pm 100\,\mathrm{meV}$ around its maximum intensity position. The symmetry of the $\mathrm{HOMO_{2nd}}$ (a) and $\mathrm{HOMO_{1st}}$ (b) around the k_x axis does not appear so different from that of the $\mathrm{LUMO_{1st}}$ (c). This outcome is in contrast to the monolayer measurements of chapter 4 (compare fig. 4.5). Curiously, there is a minor photoemission signal at the $k_\mathrm{y} = 0$ nodal plane of the $\mathrm{HOMO_{1st}}$ which is even more pronounced for the $\mathrm{HOMO_{2nd}}$. The PMM also exhibits a lower symmetry than the real space molecular orbitals due to the geometry of the experiment: the photons impinge on the sample at a polar angle of $\Theta = 65\,^\circ$ and towards positive k_y with an azimuthal angle of $2\,^\circ$ from the k_y axis. The p-polarized light is provided by the superposition of two undulators, one set to generate left-circularly polarized light, the other right-circularly polarized light of the same intensity. The technical limitations of the undulators and minor deviations from the delicate alignment of the two beams result in a fraction of the electric light field being s-polarized. By comparing the experimental PMM with simulations of different light polarization, the spurious s-polarization is determined

to be about 8 % of the total field strength that has been determined from a separate measurement. It is nevertheless beneficial to produce the light in this manner because the higher harmonics of the fundamental energy mode are emitted off-axis from the primary beam for circularly polarized light - contrary to linearly polarized light. They thus do not illuminate the sample and cause radiation damage or spurious intensity signals in the photoemission detection.

While the molecular orbitals are still discernible in the PMM, the additional signal at $k_y = 0$ at the HOMO indicates the influence of an effect that is absent in the monolayer. The intensity in between the lobes also scales with that of the main features for PMM at E_{kin} slightly off from the maximum. This implies a molecular instead of a substrate-based cause.

Though some explanations are intuitively more probable than others, we will examine a variety of different mechanisms by comparing their theoretically predicted to the experimentally measured PMM. Not only will this strengthen the final conclusion, but it is also useful to showcase how suitable this technique can be for other systems.

6.2.1 Static molecular distortions

In the discussion of the photoemission patterns so far, the intramolecular structure was assumed to be very close to that of an isolated molecule in the gas phase. This hypothesis is based on the well-known chemical stability and structural rigidity of the aromatic phenylene rings [193], five of which make up the pentacene molecule. It is nevertheless possible that pentacene is slightly distorted by the altered potential surface in its vicinity after adsorption.

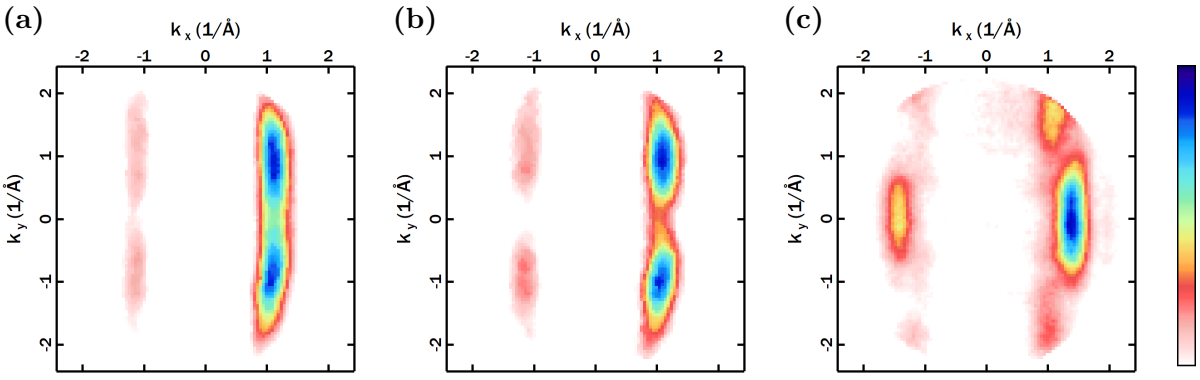

Figure 6.3: Fitted photoemission momentum maps of pentacene on Ag(110) with p-polarized light and $E_{ph} = 30\,eV$. (a) HOMO of the second layer $HOMO_{2nd}$ at $E_B = 1.8\,eV$. (b) HOMO of the first layer $HOMO_{1st}$ at $E_B = 1.2\,eV$. (c) LUMO of the first layer $LUMO_{1st}$ at $E_B = 0.1\,eV$.

On a Cu(110) substrate, Müller et al. [194] predicted a bending of pentacene along its long molecular axis and verified it via scanning tunneling microscopy. According to their DFT calculation, the strong interaction with the substrate pulls the center about 40 pm closer to the surface than the outer parts of the molecule. Contrary to the growth on Ag(110), the long molecular axis on Cu(110) is aligned along the rows in $[1\bar{1}0]$ direction. The spacing of copper atoms $a_{\mathrm{Cu}[1\bar{1}0]} = 2.54\,\text{Å}$ in this direction [76] is only slightly larger than that of the phenylene rings with about 2.47 Å [195]. Due to their chemical similarity, it is conceivable that an analogous displacement takes place in the pentacene/Ag(110) system as well. However, one should keep in mind that there is no accompanying geometric match between the molecule and substrate, since the silver lattice constant in [0 0 1] direction is $a_{\mathrm{Ag}[001]} = 4.08\,\text{Å}$ [76]. As Dauth et al. determined for the comparable molecule PTCDA [38], emission into an anti-symmetry plane of the real space MO is not generally impossible. This displacement therefore might trigger the emission of photoelectrons with $k_{\mathrm{y}} = 0$ despite the HOMO still being anti-symmetric around the $y = 0$ axis. It should be mentioned that this – or any – kind of distortion is evidently not necessary to interpret the PMM of a single monolayer on Ag(110), but the presence of the second layer might sufficiently alter the potential surface.

DFT calculations on the isolated molecule have been computed with the Gaussian 09 software [145]. Just like in the previous chapter, a 6-31G+ basis set and the B3LYP functional was used to determine the initial states [139, 140]. Two different initial conformations have been tested: one with a maximum height difference of 40 pm as seen on Cu(110) [194], and another at 80 pm. The latter distortion is purposefully exaggerated to uncover how the photoemission pattern changes with increasing bending amplitudes.

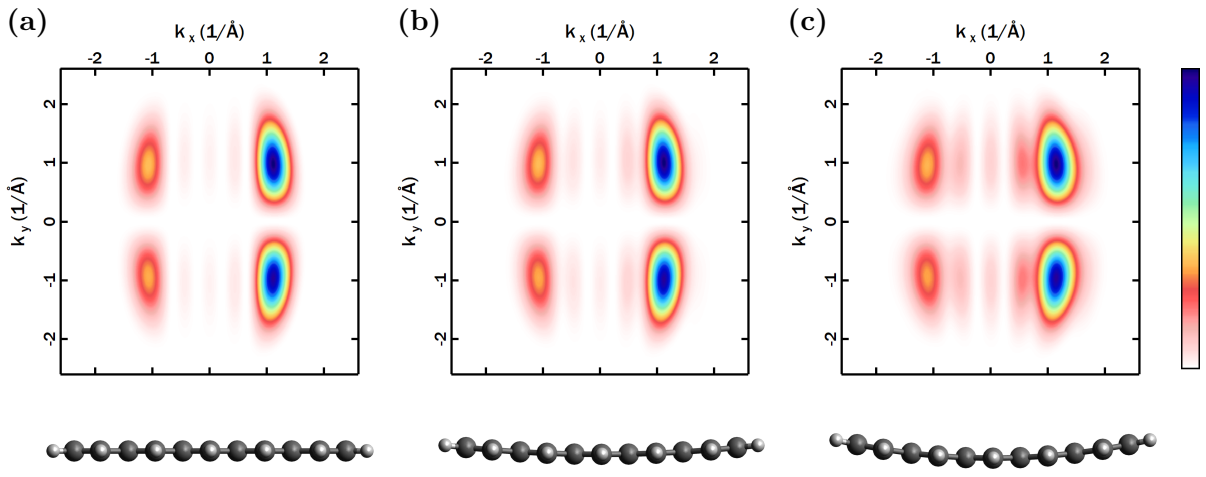

Figure 6.4: Simulated PMM of the HOMO at $E_{\mathrm{ph}} = 30\,\text{eV}$ when the molecule is undistorted (a) and when applying a static curvature with a maximum amplitude of 40 pm (b) and 80 pm (c). The respective profile of the molecule in real space is shown below.

Based on the HOMO initial state and the known experimental parameters of the exciting light, calculations of the entire photoemission process were performed. The chosen resolution in reciprocal space $\Delta\mathrm{k} = 0.008\,\mathrm{\AA}^{-1}$ is similar to the experimental one. In accordance to the best agreement with experiment in preparation of the manuscript for the publication [10] the inner potential was set to $V_0 = -10\,\mathrm{eV}$. Fig. 6.3 displays the simulated PMM (top) and the corresponding real space depiction (bottom) for the flat (a) and bent molecule with a maximum amplitude of 40 pm (b) and 80 pm (c). Comparing the changes caused by the enhanced curvature, the intensity at the main features $(k_\mathrm{x}, k_\mathrm{y}) = (\pm 1.1\,\mathrm{\AA}^{-1}, \pm 1.0\,\mathrm{\AA}^{-1})$ is increasingly spread out in k_x direction. The same conclusion can be drawn for the side features at $(0, \pm 1.0)\,\mathrm{\AA}^{-1}$ and $(\pm 0.5, \pm 1.0)\,\mathrm{\AA}^{-1}$. They are also more intense compared to the main feature in the top right corner. A displacement of this magnitude therefore leaves noticeable traces in the PMM and would be detectable in the measurement. These changes to the PMM however do not fit to the experiment, which is especially crucial around $(\pm 1.1, 0)\,\mathrm{\AA}^{-1}$. While it could be argued that the curvature of pentacene might be too small to visibly increase the intensity at the side features, it does not produce a signal on the k_y axis anyhow. One can therefore definitively exclude that the molecules are displaced in this manner.

6.2.2 Dynamic molecular distortions

A distortion of the molecular frame is not only possible as a static deformation, however. It can also be *dynamic* if a vibrational mode is stimulated alongside the electronic excitation. A coupling between electronic and vibrational excitations through electromagnetic interaction is quite common, since the electrons alter the potential landscape in which the atoms are located. It is the underlying cause of many physical properties, e.g. superconductivity [196] and heavily influences the transport as well as the optical material characteristics [25, 179, 197, 198]. The electron-vibration coupling can also affect the PMM, as has recently been demonstrated by our group on the example of the molecule coronene [199]. Fig. 6.5 displays the governing physical picture – the *Franck-Condon principle* – for the following brief explanation.

The emitted photoelectron can expend some of its kinetic energy to excite the molecular vibration and is thus recorded at a decreased kinetic and thus increased binding energy at the detector. The energy difference between the main feature in the EDC (without an accompanying vibration) and the shifted one from the same molecular orbital is the vibration energy E_vib. E_vib is a function of the vibrational mode and the energy level within that mode. For low-lying levels – when the potential surface can be well approximated by a harmonic oscillator [179, 200]– the different levels are evenly spaced, which benefits the identification of whether different peaks in the EDC belong to the same or different

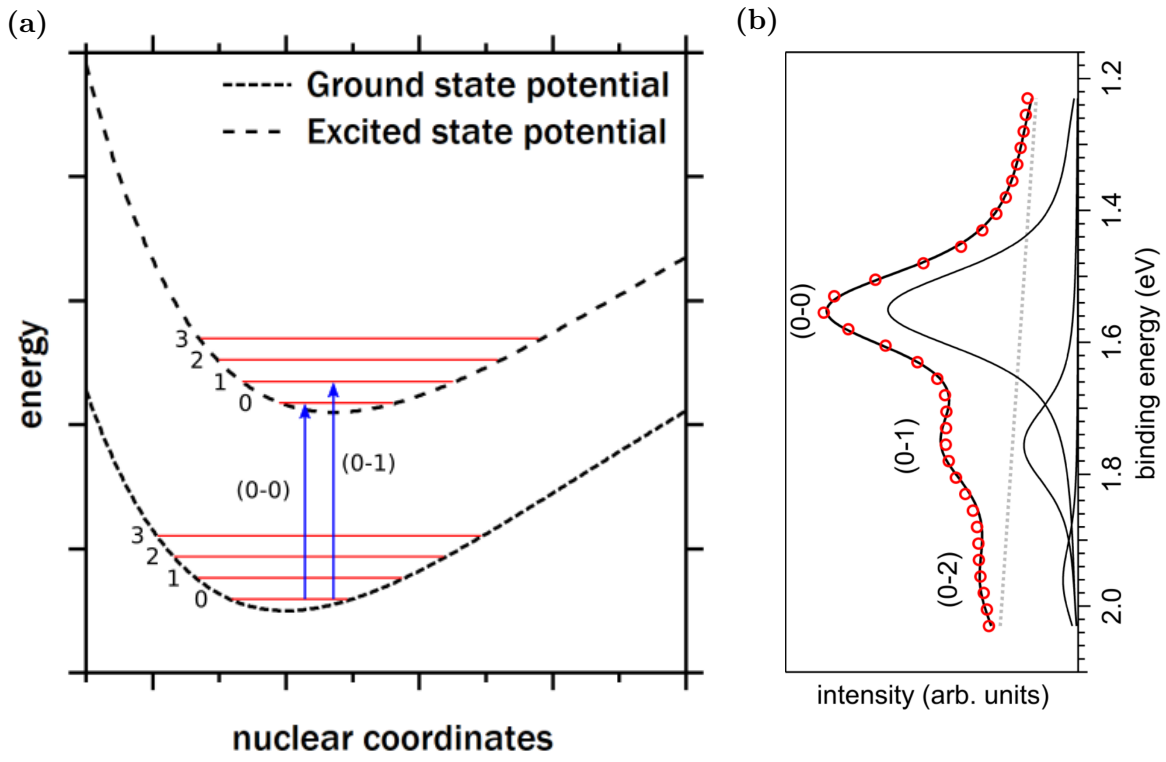

Figure 6.5: (a) Franck-Condon diagram with some vibrational levels drawn as a guide to the eye (adapted from [179]). The electronic excitation changes the potential surface (black dashed lines) and can be accompanied by a transition onto a different vibrational level (red lines). Of the two indicated transitions, the (0-0) does not excite a vibration, while the (0-1) does. The distance between the vibronic states is exaggerated to showcase the non-harmonic behavior of the potential far from the potential minimum. (b) Exemplary EDC of the coronene HOMO (red dots) on an Au(111) substrate that is reproduced by the result of a fit procedure (black lines) at energetic distances that take the vibrational transitions into account [199].

modes. The relative intensity distribution (*vibronic progression*) between different levels is connected to the overlap of the vibronic wave functions before and after excitation. The inverse process of deexciting a vibration for an increased photoelectron kinetic energy is in principle also possible. Due to the high E_{vib} for molecular vibrations compared to the thermal energy at room temperature, the vast majority of molecules are in the vibronic ground state, making this effect negligible in our case.

The motion of the nuclei can usually be decoupled from that of the decidedly lighter electrons, whose reaction to the nuclei is effectively instantaneous (Born-Oppenheimer approximation [201]. If the nuclei are able to move some distance before the photoemission process is completed, the Franck-Condon principle is violated and the measured PMM can be distorted depending on where and how far the atoms have travelled. The vibronic progression can also be affected, since the transitions in fig. 6.5 (a) are no longer perfectly

vertical. While the EDC of the pentacene bilayer does not resemble a "regular" vibronic progression (see Fig. 6.2 (a)), the underlying Franck-Condon principle would be invalid anyhow. This effect has recently been demonstrated by our group in publication [199].

The vibrational modes of a single pentacene molecule have been calculated with Gaussian 09 [145] using a 6-31G+ basis set and the B3LYP functional. There is a total of $3N - 6 = 102$ possible modes with fundamental energies E_{vib} between $\sim 5 - 400\,\mathrm{meV}$. Even though the interaction between the molecules and the noble metal substrate is limited, the real E_{vib} values of the adsorbed molecules presumably differ from the simulated ones. Likewise, the atomic motion is not identical, but comparable [199]. Within the total of 102 modes there are 69 in-plane and 33 out-of-plane vibrations. Due to the geometry of the experiment with the hemispherical analyzer positioned in the out-of-plane direction of the molecules, in-plane vibrations should generally have a greater effect on the PMM. With the assistance of the automated import dialog of the photoemission tool (see appendix A5.1) we are nevertheless able to check every single vibrational mode – even if a mode appears to be an unlikely candidate.

Starting from the output of the vibration simulation, the atomic coordinates of pentacene were distorted according to the direction and amplitude of the respective vibration. These displaced atomic positions were then used as (static) geometry input for the follow-up DFT calculations under otherwise identical simulation parameters. Under some conditions the displacement alters the shape of the orbitals considerably, changing the energetic order of orbitals in the DFT. In no case is the distortion of the orbitals so significant that the HOMO and LUMO cannot be related back to the undistorted, "original" HOMO and LUMO, however.

The majority of excited modes barely alter the resulting PMM, especially when the oscillation is out of the molecular plane and/or mostly hydrogen atoms are involved. Fig. 6.6 (a) shows the resulting PMM for vibration number 82 (ordered from lowest to highest energy in the gas phase) with $E_{\mathrm{vib},82} = 198\,\mathrm{meV}$ for the isolated molecule. The difference to the undistorted PMM in fig. 6.4 (a) is very limited: the minor maximum at $(-1.1, 1.0)\,\mathrm{Å}^{-1}$ is slightly less intense while the one at $(-1.1, -1.0)\,\mathrm{Å}^{-1}$ is unchanged. The six minor features spaced in k_{x} direction between the main maxima gain a little bit of intensity. As is the case for the vast majority of vibrations, there is no photoemission intensity to be detected at $k_{\mathrm{y}} = 0$ though. We can thus safely exclude the coupling of the photoelectron to mode 82 as the cause for the pattern of the measured PMM.

Fig. 6.6 (b) and (c) display mode 85 ($E_{\mathrm{vib},85} = 206\,\mathrm{meV}$) and 88 ($E_{\mathrm{vib},88} = 210\,\mathrm{meV}$), where the electron-vibration coupling leads to a more significant change in the PMM. The four main lobes in the PMM of mode 85 (b) are shifted to slightly smaller k_{y} values and also broadened in k_{y} direction. This results in a finite photoemission signal in between the lobes at $k_{\mathrm{y}} = 0$. Additionally, there are new side maxima at $(\pm 1.7, 0)\,\mathrm{Å}^{-1}$. Both of

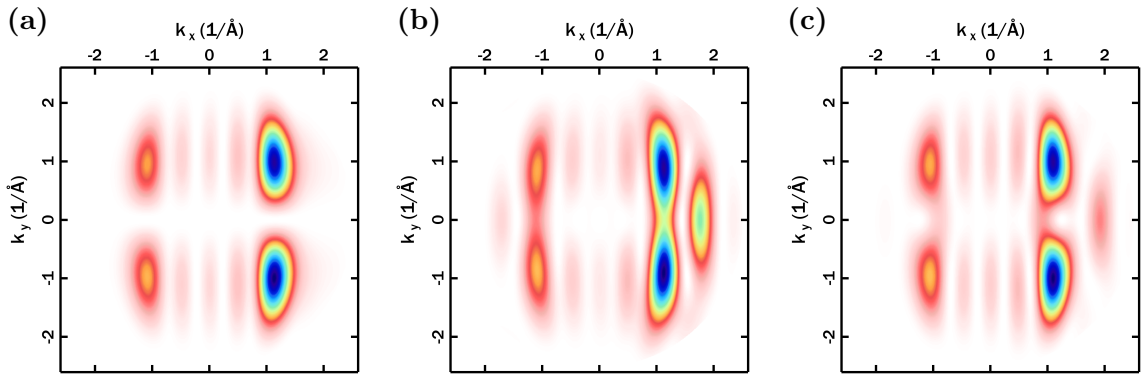

Figure 6.6: Simulated PMM under excitation of a molecular vibration at $E_{\mathrm{ph}} = 30\,\mathrm{eV}$. The molecules have been distorted according to the in-plane vibrations with number 82 (a) 85 (b) and 88 (c). Even though some vibrations result in a finite intensity at $_{\mathrm{y}} = 0$, none of the modes can replicate the pattern found in the experiment in fig. 6.3 (a) and (b).

these changes reflect the broken anti-symmetry axis of the initial state around the $y = 0$. A less drastic change in the PMM can be observed for vibration 88 (c): there are again two minor features at $(\pm\,1.9, 0)\,\mathrm{\AA}^{-1}$, but the main lobes are not shifted inward as much as for vibration 85. The lobes at negative k_{y} values are connected to those at positive k_{y} by an arc with a curvature towards lower $|k_{\mathrm{x}}|$.

While not a perfect fit by any means, these results for vibrations 85 and 88 at $E_{\mathrm{ph}} = 30\,\mathrm{eV}$ warrant a closer look at higher photon energies. The more data sets are compared to the simulation, the less likely it is to draw a wrong conclusion based on a lack of information which strengthens the final result. Fig. 6.7 shows the experimental PMM of the $\mathrm{HOMO}_{\mathrm{2nd}}$ (a) compared to simulations with electron-vibration coupling to mode 85 (b) and 88 (c) for a photon energy of 50 eV with p-polarized light.

The experimental signal-to-noise ratio at $E_{\mathrm{ph}} = 50\,\mathrm{eV}$ is considerably worse than for 30 eV. The main reason is the decreased cross section of the valence molecular orbitals assembled from atomic carbon $2\mathrm{p}_{\mathrm{z}}$ orbitals. The maximum cross section of these molecular orbitals is around 25 eV and quickly declines for higher E_{ph} (see fig. 4.6 of section 4.2). The loss in intensity is related to the behavior of an individual, atomic C-2p orbital which is $\sim 67\,\%$ less intense at $E_{\mathrm{ph}} = 50\,\mathrm{eV}$ compared to 30 eV [202]. Furthermore, the background from the silver 5s bands is only reduced by $\sim 16\,\%$ for the same jump in energy [202]. Since the Ag-5s bands pass through the HOMO features in the PMM, the data evaluation is more intricate and less yielding than at lower E_{ph}. At $E_{\mathrm{ph}} = 50\,\mathrm{eV}$ the molecular features remain at comparable k_{x} values, but are significantly more intense in between two lobes at $k_{\mathrm{y}} = 0$. The molecular feature is also broadened in k_{x} direction at $k_{\mathrm{y}} = 0$.

Comparing the simulations for $E_{\mathrm{ph}} = 50\,\mathrm{eV}$ in fig. 6.7 (b) and (c) with 30 eV all minor features gain in intensity relative to the main lobes around $(1.1, \pm 1.0)\,\mathrm{\AA}^{-1}$. The photoemission horizon is extended towards higher $|\mathrm{k}| \propto \sqrt{E_{\mathrm{kin}}}$ due to the additional kinetic energy of the photoelectrons. There is also an increase in the $|\mathrm{k}_y|$ position of the features by about 10 %. This shift slightly reduces the signal in between the lobes at $(\pm 1.1, 0)\,\mathrm{\AA}^{-1}$ which is opposite to the change in the experimental PMM from $E_{\mathrm{ph}} = 30\,\mathrm{eV}$ to 50 eV. In total, the simulations are not all that different for the raised photon energy, but their match to the measurement is worse.

In summary, some of the vibrational modes would be detectable by the trace they leave in the PMM. None of the possible vibrations produces the pattern that is observed in the experiment, however. A coupling of the emitted photoelectrons to molecular vibrations can therefore be excluded as the origin of the change in the PMM of the valence region when growing a bilayer of pentacene on Ag(110).

6.2.3 Inter- and intramolecular scattering

Another effect that is related to the geometric structure of the sample, but does not require any static or dynamic deformation of the molecules is the elastic scattering of the photoelectrons. Due to the strong dependence of the scattered intensity distribution on the position of the scattering potential around each atom, the analysis of scattered intensity is a common experimental technique in its own right. The photon energies for these **X**-ray **P**hotoelectron **D**iffraction (**XPD**) experiments are in the X-ray range both to boost the electron kinetic energy into the high-energy region with an increased inelastic mean free path [22] and to excite tightly bound states close to the atomic cores.

The measurement at hand differs from these methods in that we use lower photon energies in the UV-range. The decreased inelastic mean free path of the slower electrons

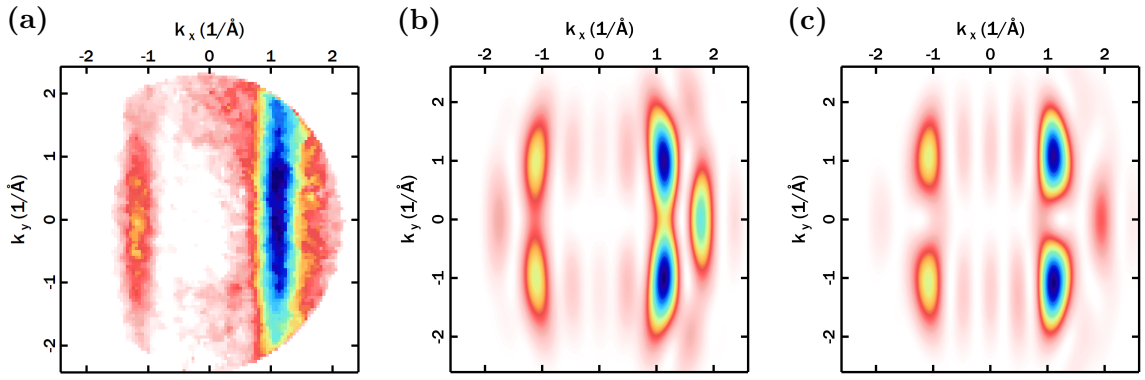

Figure 6.7: Experimental, fitted PMM of the $\mathrm{HOMO}_{2\mathrm{nd}}$ (a) and simulated PMM under excitation of molecular vibration number 85 (b) and 88 (c) at $E_{\mathrm{ph}} = 50\,\mathrm{eV}$.

results in a greater influence of the unscattered electrons on the PMM compared to the scattered electrons that travel a longer distance inside the system before reaching the surface. The excited initial states are also no core levels, but molecular orbitals in the valence region which are spread over the entire molecule. Lastly, the low atomic number of the carbon ($Z = 6$) and hydrogen atoms ($Z = 1$) leads to a smoother potential surface and thus less prominent scattering than for heavier elements. Since the modification of the PMM of the bilayer compared to the monolayer in fig. 4.5 (which can be explained without resorting to any scattering phenomena) is moderate, but not too extreme, the change is nevertheless possibly caused by elastic scattering. We will therefore undertake simulations with the final state described in subsection 2.3.2. The initial state is assembled with a 6-31G+ basis set and the B3LYP functional. After a preliminary assessment, the maximum scatter distance of the emitting to the last scattering atom is set to 12 Å and the electrons can scatter at most twice. The inelastic mean free path $\lambda = 29.2\,\text{Å}$ is deliberately increased from the universal curve value [22] so that the effect of elastically scattered electrons is more prominent. This is to prevent missing the influence of the elastically scattered photoemission due to the large uncertainty of the universal curve. Lastly, the resolution in reciprocal space is reduced to $\Delta\text{k} = 0.04\,\text{Å}^{-1}$ to expedite the elaborate calculations now that elastic scattering is enabled.

The calculated PMM with elastic scattering included in the photoemission matrix element are displayed in fig. 6.8. When only the scattering at the emitting molecule itself is taken into account in fig. 6.8 (a), there are already a few minor differences to the simulated PMM without elastic scattering in fig. 6.3 (a): the lobes at $(\pm 1.1, 1.0)\,\text{Å}^{-1}$ are more intense and connected to the faint signals at $(\pm 1.1, -2)\,\text{Å}^{-1}$. All features are slightly elongated along in k_y direction, but there is no additional signal at the anti-symmetry crossing at $k_\text{y} = 0$.

This first result does not imply that elastic scattering cannot play a role in creating the pattern of the experimental PMM. The angle-dependent intensity distribution of the elastically scattered electrons certainly changes with any adjustments to the scattering atoms. We will therefore expand the scattering cluster in the calculation to include a second pentacene molecule which does not emit any electrons itself, but scatters the electrons emitted from the first molecule. There is an important issue with the geometric alignment of the molecules though: as can be deduced from the LEED pattern in fig. 6.2 (a), the growth of the second layer on top of the first is not commensurate. This means that there is a multitude of possible dimer configurations that would have to be checked. The LEED measurement furthermore only contains information on the periodicity of the lattice lateral to the surface, but none on the spacing and the lateral in-plane alignment between the layers. Without further data on the in- and out-of-plane offset between the layers it

is therefore not possible to replicate the geometric structure of the real system with any certainty.

We can nevertheless begin by making educated guesses based on the published literature of comparable systems. Guaino et al. [105] found a commensurate stacking of several layers of pentacene on top of Au(110) that can serve as a starting point for our approach. In their ordered thin film they verified via STM that the molecules grow predominantly in a bridge site along the short molecular axis between two molecules below. We will therefore focus on this geometry in the evaluation.

Two configurations of the layer by layer growth of Guaino et al. have been tested and are displayed in fig. 6.2: one with the emitting molecule in the first layer and the nearest neighbors as scatterers (b); and a second one with the emitting molecule in the second layer and its respective neighbors as scatterers (c). For now, we disregard the fact that photoelectrons emitted from the HOMO in the first layer are not bound as strongly as those in the second layer. Starting with (b), the PMM is close to the unscattered one except a small shift of the maximum intensity in each lobe by $\sim 0.1\,\text{Å}^{-1}$ towards lower $|k_\text{y}|$ values. The small influence can be expected considering the prevalence of forward scattering at the carbon atoms for this kinetic energy (compare fig. 4.1). There is no additional intensity at $k_\text{y} = 0$, however. In contrast, the photoelectrons emitted from the second layer in (c) cannot reach the detector with forward scattering only. The pattern in the calculated PMM is more clearly distorted, but still identifiable as the pentacene HOMO. The intensity maxima in each lobe are shifted in the opposite direction as in (b) by $\sim 0.5\,\text{Å}^{-1}$ towards higher $|k_\text{y}|$ values. The change in shape from the unscattered calculation is most probably exaggerated and only as intense due to the artificially low inelastic damping. Crucially, there is also no photoemission intensity at $k_\text{y} = 0$.

Even though the tested geometries do not precisely match the real system, we can

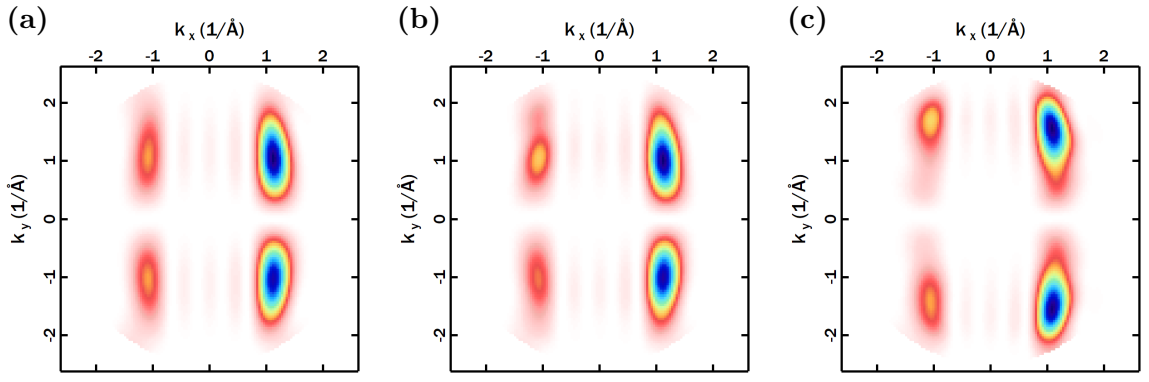

Figure 6.8: Simulated PMM of the HOMO at $E_\text{ph} = 30\,\text{eV}$ when intramolecular scattering is taken into account (a). PMM also including intermolecular scattering at a molecule in the first layer when emitting from the second layer (b) and vice versa (c).

draw some important conclusions from them. First of all, we only considered a single alignment of molecules in between both layers even though the LEED pattern of the first and second layer are not identical. Depending on the lateral offset between the layers, there are many inequivalent adsorption sites even in case of the adsorption of one molecule at a high-symmetry site. The scattered electrons from each dissimilar site will exhibit a different angle-dependence and thus combine to a smoother and fainter PMM of scattered intensity. Given that elastically scattered electrons would also have a smaller impact on the total PMM if the inelastic mean free path was not amplified in the calculation and we considered only a single domain, the actual influence of elastic scattering on the measured PMM is likely not significant. A similar argument can be made for scattering at the silver substrate atoms. While the scattering potential of silver ($Z = 47$) is larger than for carbon and hydrogen, the distance from the molecules to the silver and back through the sample surface greatly reduces the elastically scattered intensity due to inelastic processes.

In conclusion, elastic scattering does not contribute considerably to the measured PMM and is not sufficient to explain the change in the angle-dependent intensity from the mono- to the bilayer.

6.2.4 Molecular tilt

Even though we could exclude the presence of plausible, static deformations in subsection 6.2.1, there is another geometric cause that we did not address yet. One could imagine that the molecules retain their shape upon adsorption, but instead of lying flat on the substrate they acquire a tilt angle with respect to the surface plane. At first sight the gradual phase change from the thin film towards the bulk structure [106, 189] by a progressive increase in tilt angle beyond the first monolayer appears very reasonable [190]. Still, pentacene has a remarkably rich phase space which includes abrupt transitions from one layer to the next [80, 106]. In the following, we will therefore have a closer look into this possible explanation.

Fig. 6.9 displays how the tilting of pentacene affects the PMM. In this example, the monomer in the simulation of fig. 6.9 (a) is rotated by an angle of $\alpha = -11.0\,^\circ$ along the long molecular axis. The calculated PMM of the HOMO under the same excitation parameters as previously and a photon energy of 30 eV is shown. The main difference from the flat-lying molecule is a shift of the molecular features in the direction of the tilt towards higher k_y. This result is easily understood as the result of the rotation of the initial state around this axis. For larger angles, the intensity maxima could even shift beyond the photoemission horizon in this measurement geometry. Since the exciting light field is unaffected by the transformation, the relative intensity distribution between the

features is nevertheless modified.

The two-fold symmetry of the Ag(110) substrate and the first layer means that an adsorption angle that is mirrored around the long molecular axis will have the same adsorption energy and is thus equally likely. The typical domain size is roughly equal to the extend of the substrate terraces, up to $\sim 200\,\mathrm{nm}$ [127, 128]. The reason is the mobility of the molecules at room temperature, which usually begin accumulating at step edges of the substrate and continue growing from there. A spectroscopy method that integrates over a large number of molecules will therefore measure the same amount of molecules in either tilt direction. The PMM of the energetically identical tilt angle of $+11.0\,^\circ$ is shown in fig. 6.9 (a). It exhibits the same behavior as molecules with $\alpha = -11.0\,^\circ$, except the shift is in the direction of lower k_y. If the interaction between neighboring molecules is low – as is the case here – one can approximate the measured PMM by taking the superposition of the monomers of all non-identical molecular alignments in the simulation.

This superposition of pentacene tilted by $\alpha = \pm 11\,^\circ$ is depicted in fig. 6.9 (c). For the particular initial states and excitation parameters of this simulation, the four intensity lobes from an individual monomer blend into one another to form two stripes. Depending on the values for α and E_ph the individual PMM will combine into a total PMM with either two, four, six or eight separate maxima, as the four features of each single PMM will move in reciprocal space.

With this knowledge, we can now make an educated guess on which tilt angles to test against the measurement shown in fig. 6.3. We will start by checking different tilt angles of the pentacene HOMO in the second of the two layers. A brief comparison of fig. 6.3 (a) to the simulation for $\alpha = \pm 11\,^\circ$ in fig. 6.9 (c) indicates that we would have to look at smaller tilt angles. In this vein, fig. 6.10 displays the calculation for $\alpha = \pm 8.0\,^\circ$ (a), $\alpha = \pm 8.5\,^\circ$ (b) and $\alpha = \pm 9.0\,^\circ$ (c) at $E_\mathrm{ph} = 30\,\mathrm{eV}$. Despite the relatively minute geometric differences between the three monomers, there is a noticeable difference in the

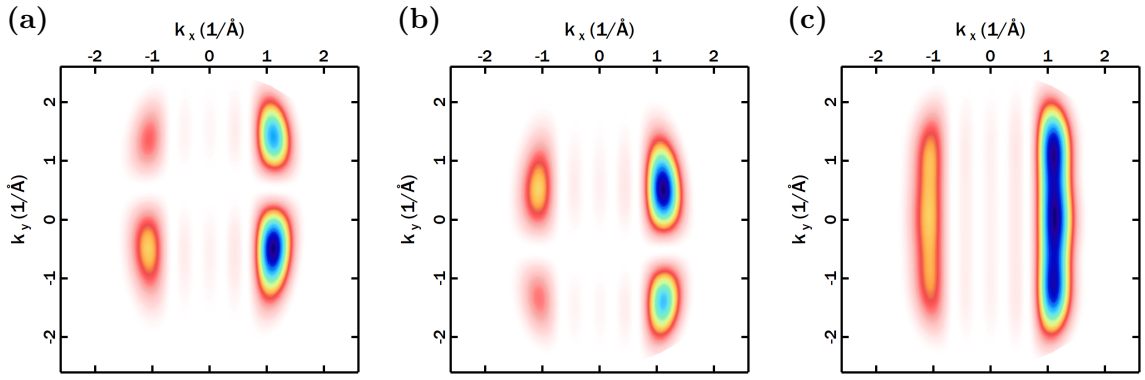

Figure 6.9: Simulated PMM of the pentacene HOMO at $E_\mathrm{ph} = 30\,\mathrm{eV}$ and a tilt angle around the long molecular axis of $-11.0\,^\circ$ (a) $+11.0\,^\circ$ (b) and their superposition (c).

resulting PMM. The main change is found in the overlap region between the main lobes at $(\pm 1.1, 0)\,\text{Å}^{-1}$: the broken asymmetry axis at $y = 0$ results in finite photoemission intensity at $k_y = 0$. While there is no distinct maximum, the signal between the lobes is growing with increasing α. The position of the maxima in reciprocal space also moves to marginally greater $|k_y|$ values.

The intensity in between two lobes at $k_y = 0$ relative to the maxima is the best indicator for the correct tilt angle. In comparison with the experimental PPM in fig. 6.3 (a), the angles $\alpha = 8.5\,^\circ$ (b) and $\alpha = 9.0\,^\circ$ (b) are in very good agreement with the measurement with $\alpha = 8.5\,^\circ$ being the arguably slightly better fit. At lower tilt angles of $\alpha = 8.0\,^\circ$ (a) the signal at $k_y = 0$ is somewhat too low. Taking this into account, the simulation can determine the tilt angle of the second layer to $\alpha_{2\text{nd}} = (8.5 \pm 0.5)\,^\circ$ from this data set at $E_{\text{ph}} = 30\,\text{eV}$. For further tilt angles beyond this selection the inclined reader is referred to appendix A6.1.

The same procedure can be applied to uncover the tilt angles of the molecules in the first layer. The charge transfer from the substrate into the first layer makes it possible to compare the photoemission signal from the (former) $\text{LUMO}_{1\text{st}}$ as well as the $\text{HOMO}_{1\text{st}}$ to the simulations. These are displayed in fig. 6.11 for tilt angles $\pm 6.0\,^\circ$ (left column), $\pm 6.5\,^\circ$ (middle column) and $\pm 7.0\,^\circ$ (right column) for the $\text{HOMO}_{1\text{st}}$ (top row) and $\text{LUMO}_{1\text{st}}$ (bottom row). Again, the photon energy is set to $E_{\text{ph}} = 30\,\text{eV}$.

The difference in the PMM at these three tilt angles is not as striking as for the higher α values in fig. 6.10. This is especially true for the PMM of the $\text{LUMO}_{1\text{st}}$ in the bottom row, where the broadening due to the increased α is concealed by the already widespread molecular features in this direction. Since the real sample is not without some degree of structural disorder, the features in the experimental PMM are additionally broadened by the imperfect order of the molecules. The lack of a clear indicator for the tilt angles means that the geometry determination is less accurate than for the $\text{HOMO}_{2\text{nd}}$ and would

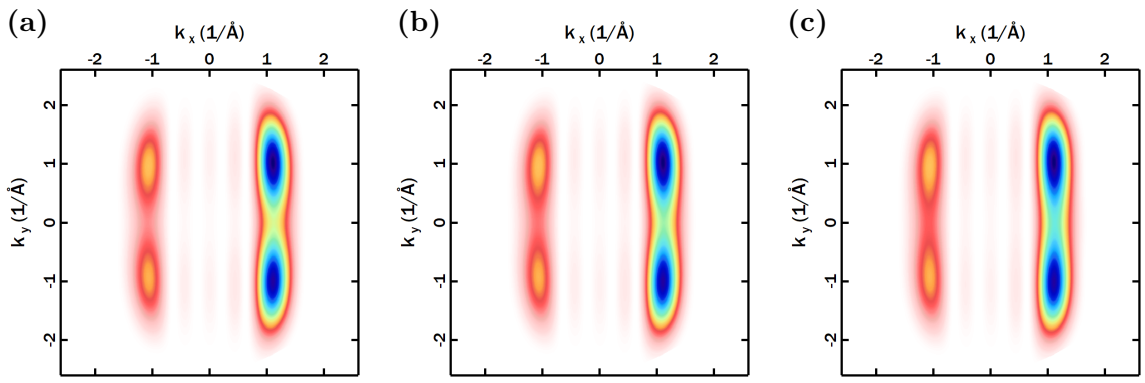

Figure 6.10: Simulated PMM of the $\text{HOMO}_{2\text{nd}}$ at $E_{\text{ph}} = 30\,\text{eV}$ and a tilt angle around the long molecular axis of $8.0\,^\circ$ (a) $8.5\,^\circ$ (b) $9.0\,^\circ$ (c).

have an even greater uncertainty if one would exclusively evaluate the LUMO data.

The difference between the HOMO PMM in the upper row nevertheless permits the determination of the molecular tilt angle in the first layer by contrasting them with the experimental data in fig. 6.3 (b). The best agreement is achieved $\alpha = 6.5\,^\circ$ (b) and $\alpha = 7.0\,^\circ$ (c). In contrast, the intensity at $k_y = 0$ for $\alpha = 6.0\,^\circ$ (a) is clearly below the measured signal. The LUMO exhibits hardly any difference for these set of angles, since they only cause a negligible broadening of the features in k_y direction that pales in comparison to the experimental broadening, e.g. due to the film inhomogeneity.

In order to increase the accuracy of the tilt angle determination, we can evaluate a larger data set and correlate the simulations to experiment at higher photon energies. It is also useful to check the other recorded molecular orbitals, since the tilt will affect their PMM in the similar manner. For this particular system, however, the other orbitals do not help in increasing the precision of the technique. Focusing on the k_y direction that we use for the angle determination, the HOMO-1 shows a pattern that is very close to the HOMO. The same argument can be made for the HOMO-2 and the LUMO. Additionally, the binding energies of identical orbitals in each molecular layer are not as well separated

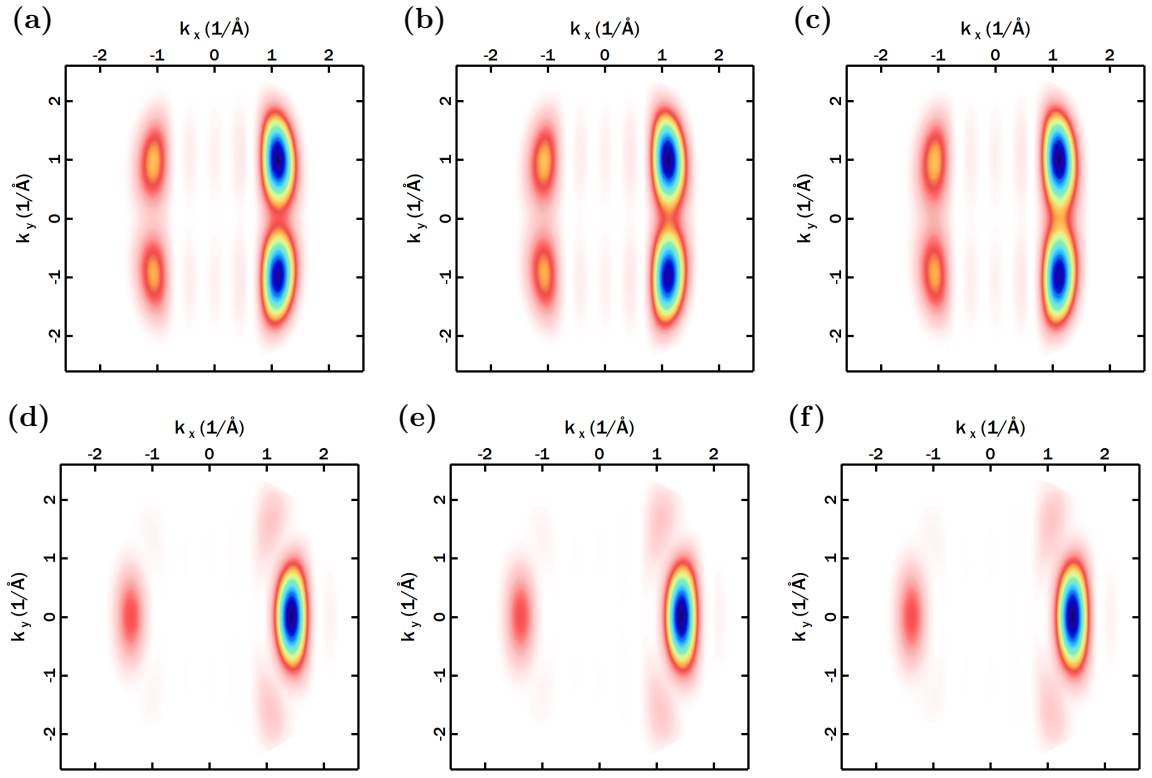

Figure 6.11: Simulated PMM of the pentacene $HOMO_{1st}$ (top row) and $LUMO_{1st}$ (bottom row) at $E_{ph} = 30\,eV$ and a tilt angle around the long molecular axis of $6.0\,^\circ$ (a,d) $6.5\,^\circ$ (b,e) $7.0\,^\circ$ (c,f).

as for the HOMO and the LUMO – see fig. 6.2 (b). They can still be reconstructed from the weighted superposition of the simulations for each of the two tilt angles, but this mixture certainly makes them less valuable to investigate the geometry of each individual layer.

Adding the measurements at higher photon energies to the evaluation is a different story. The initial states of the pentacene layers are essentially two-dimensional since there are no atoms outside the molecular plane that is equal to the (x, y) plane. The $(k_\mathrm{x}, k_\mathrm{y})$ values at which the intensity of a particular molecular orbital is greatest for the flat-lying molecule is therefore largely independent from the total wave vector k of the photoelectron. A higher photon energy and hence photoelectron kinetic energy therefore mainly changes the intensity of the maxima and increases the k_z component at which it is detected. This can easily be understood from the Fourier transformation of the initial state in the plane wave approximation. While we use a more elaborate final state here, the final state of this system is close enough to a plane wave that this reasoning holds up well. If the molecule is now tilted against the reference of the detector plane, a change in k via varying E_ph will appear to move the maxima across the detector so that the photoemission maximum remains at the same $(k_\mathrm{x}, k_\mathrm{y})$ value from the perspective of a tilted molecule. In the reference system of the detector, this corresponds to a shift in $(k_\mathrm{x}, k_\mathrm{y})$. This relation can be exploited by choosing a higher E_ph to increase the shift of the maxima at fixed tilt angles – effectively zooming in to enhance the effect of the shift to increase the accuracy of the angle determination. The downside of using higher E_ph is a drop in the photoemission cross section of the molecular orbitals , see fig. 4.6 of section 4.2. The signal-to-noise ratio thus gets considerably worse and limits the maximum photon energy. For our particular excitation parameters and sample, measurements with $E_\mathrm{ph} > 50\,\mathrm{eV}$ could not be used to any benefit. Hence we will focus on the ARPES data taken at $E_\mathrm{ph} = 50\,\mathrm{eV}$.

Fig. 6.12 shows the experimental PMM of the $\mathrm{HOMO}_{2\mathrm{nd}}$ (a) and $\mathrm{HOMO}_{1\mathrm{st}}$ (b) at a photon energy of 50 eV. As expected, the data quality is reduced and the silver sp-bands are more visible, especially at wave vectors where they cross the molecular features. Nevertheless, in comparison to the experimental data for $E_\mathrm{ph} = 30\,\mathrm{eV}$ in fig. 6.3 the intensity around $k_\mathrm{y} = 0$ is clearly increased for both molecular orbitals. This trend is in accord with the predicted behavior of the photoemission intensity from tilted molecules as laid out above. The signal between the lobes is comparable to the main maxima for the $\mathrm{HOMO}_{2\mathrm{nd}}$ (a), but not quite so for the $\mathrm{HOMO}_{1\mathrm{st}}$ (b).

The experimental data can again be contrasted with simulations for different tilt angles α for the higher photon energy. The simulated PMM for the $\mathrm{HOMO}_{2\mathrm{nd}}$ at $\alpha = \pm 8.0\,^\circ$ (a), $\alpha = \pm 8.5\,^\circ$ (b) and $\alpha = \pm 9.0\,^\circ$ (c) at $E_\mathrm{ph} = 50\,\mathrm{eV}$ is displayed in fig. 6.13. Just like the experiment, the most distinct change in the calculated PMM is the boosted signal at $k_\mathrm{y} = 0$. The difference in the PMM between steps in the tilt angle of $0.5\,^\circ$ is more

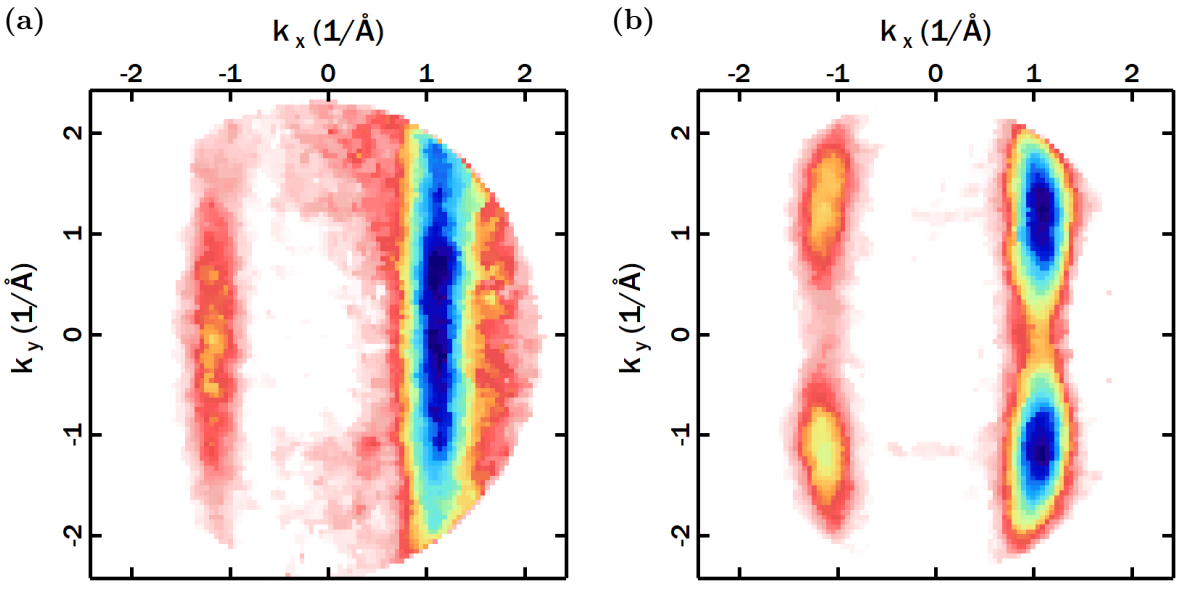

Figure 6.12: Experimental, fitted PMM of the pentacene $HOMO_{2nd}$ (a) and $HOMO_{1st}$ (b) at $E_{ph} = 50\,eV$. The ratio between molecular and background signal is reduced due to the change in cross sections at this higher photon energy.

pronounced, with the $k_y = 0$ feature being less (a), equally (b) and arguably more intense (c) than the main maxima, but still within the estimated error bar. With this additional data, the tilt angle of the molecules in the second pentacene layer is determined to be $\alpha_{2nd} = (8.5 \pm 0.5)^\circ$.

The analogous PMM for the $HOMO_{1st}$ at $E_{ph} = 50\,eV$ for simulated tilt angles of $\alpha = \pm 6.0^\circ$ (a), $\alpha = \pm 6.5^\circ$ (b) and $\alpha = \pm 7.0^\circ$ (c) are shown in fig. 6.14. The dissimilarities between the angles are again enhanced compared to the lower photon energy and the signal at $k_y = 0$ is the clearest indicator for the geometry. The intensity for 7.0° is

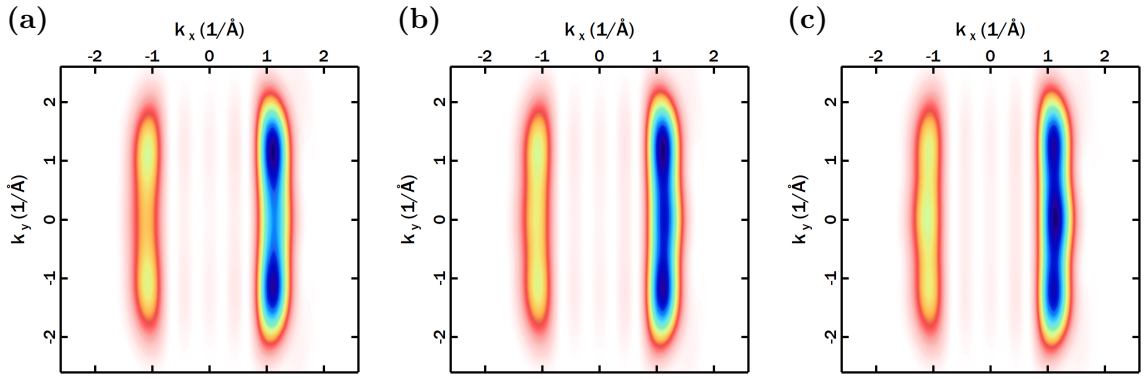

Figure 6.13: Simulated PMM of the pentacene $HOMO_{2nd}$ at $E_{ph} = 50\,eV$ and a tilt angle around the long molecular axis of 8.0° (a), 8.5° (b), 9.0° (c).

too high at this wave vector. On the other hand, the angles 6.0 ° (a) and 6.5 ° (b) are in good agreement with the experiment. The actual tilt angle of the real system is likely in between 6.0 ° and 6.5 °. $\alpha = 6.0\,^\circ$ is still within the uncertainty of the angle determination, so that the tilt angle of the molecules in the first pentacene layer is concluded to be $\alpha_{1st} = (6.5 \pm 0.5)\,^\circ$.

Please note that we draw no conclusion about how any individual molecular domain is structured. Depending on the parameter settings at the NanoESCA beamline, the photoelectrons are gathered from an area of $\sim 10\,\mu m$ or larger [123]. The measurement area is thus considerably larger than the terrace width of $\sim 200\,nm$ of the Ag(110) substrate. Since the nucleation of the molecules is likely to start at step edges of the substrate due to the lateral atomic neighbors at these positions, the measurement integrates over an immense number of molecular domains. It is therefore possible that each domain has only a single molecular tilt direction and the instrument integrates over too many to detect any intensity difference between the signal from each type of domain. Alternatively, both tilt angles could be present in a single domain and possibly arranged in a zig-zag pattern. Since the tilt angles are relatively small, the two possibilities cannot be distinguished from this data set alone.

In conclusion, a tilt of the molecules around the long molecular axis is the cause for the change in the experimental PMM from the mono- to the bilayer system of pentacene on Ag(110). Elastically scattered photoelectrons do not explain the experimental PMM and nor do static distortions of the molecules or the excitation of dynamic vibrations. The best fits are achieved for tilt angles of $\alpha_{1st} = (6.0 \pm 0.5)\,^\circ$ of the first and $\alpha_{2nd} = (8.5 \pm 0.5)\,^\circ$ of the second layer. Perhaps the most remarkable property of this photoemission technique is that the tilt angle of the first layer can be determined with a high precision even though

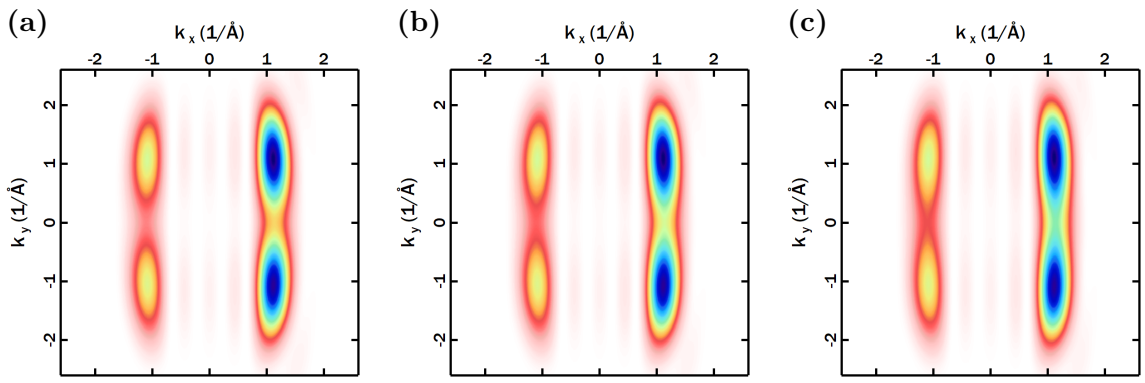

Figure 6.14: Simulated PMM of the pentacene $HOMO_{1st}$ at $E_{ph} = 50\,eV$ and a tilt angle around the long molecular axis of 6.0 ° (a), 6.5 ° (b), 7.0 ° (c).

it is covered by another layer of pentacene.

The method is not limited to this particular system and can be adapted for other organic-inorganic compounds, where some or all of the showcased effects might become relevant.

7 Photoemission from three-dimensional molecules

The plane wave approximation for the photoemission final state was already extensively discussed and utilized in the previous chapters. To recapitulate, the PWA can be used to gain many usefuly insights, but is not universally applicable, see subsection 2.3.3 for further details. In this chapter we will test one of the conditions under which the PWA is thought to be inadequate [11]: non-planar molecules whose molecular orbitals extend in all three spatial dimensions. The lack of data on this issue means that it is still an open question whether this expectation of the community is correct or not. The successful application would expand the orbital tomography technique to the new class of truly three-dimensional molecules.

A monolayer of the close to spherically symmetric fullerene C_{60} on top of an Ag(110) substrate is chosen to examine this topic. A fullerene lends itself as an archetype molecule as they have already been widely researched in the past decades not least because they and their derivates are suitable for a variety of applications [203–205]. C_{60} itself is an organic electron acceptor [206] and resistant against mechanical and environmental strains [207]. It is also already being used in prototype devices [208–210]. Photoemission experiments that were conducted so far shed light on photoemission intensity resonances induced by the geometric shape of C_{60} [47, 211] and the electronic band dispersion in high quality thin films [212]. The structure of C_{60} is displayed in fig. 7.1 (a). The molecule is entirely made up of carbon atoms (black) who form a frame of alternating penta- and hexagons in the shape of a football. C_{60} has a diameter of about 7.1 Å with each carbon atom having three nearest neighbors [213].

The photoemission study presented in this thesis is supported by DFT calculations and simulations of the photoemission matrix elements and its results are published in *Physical Review B* [12]. A complementary analysis of a thick film of C_{60} by Haag et al. is published alongside this work in the same issue [214]. In contrast to our study that focuses on the applicability of the plane wave approximation when the molecules are interacting with the metal surface, they examine a thick film of C_{60} where molecule-molecule interactions and molecular bands play a significant role.

7.1 Sample preparation

The sample is prepared under ultra-high vacuum conditions through the procedures laid out in section 3.2. First, the Ag(110) substrate is cleaned by repeated cycles of Ar^+ ion bombardment with subsequent annealing at elevated temperatures. After verifying the cleanliness of the substrate with a LEED experiment, a monolayer of C_{60} is deposited from a home-made thermal evaporator onto the pristine surface at room temperature. The molecules are commercially available and purchased from Sigma-Aldrich with a purity of 99.9 %. The evaporation rate was calibrated to be 40 min per monolayer with X-ray photoemission spectroscopy and LEED measurements before the main experiment. With the sample at room temperature, the superstructure of the molecular lattice is already visible in the LEED experiment, but fairly diffuse immediately after the evaporation. The sample is therefore annealed at 300 °C for 5 min to increase the homogeneity of the molecular layer.

The LEED pattern of the finalized sample at room temperature and an electron kinetic energy of 12 eV is shown in fig. 7.1 (b). The molecular lattice is reproduced by a (1.67 , 2 / 1.67 , -2) superstructure matrix that is indicated by red circles. The matrix is indication of the interaction between the molecules and the substrate, which promotes the assembly of C_{60} in this higher-order commensurate superstructure. The molecules in this lattice structure are slightly closer to one another than in the bulk structure and have a

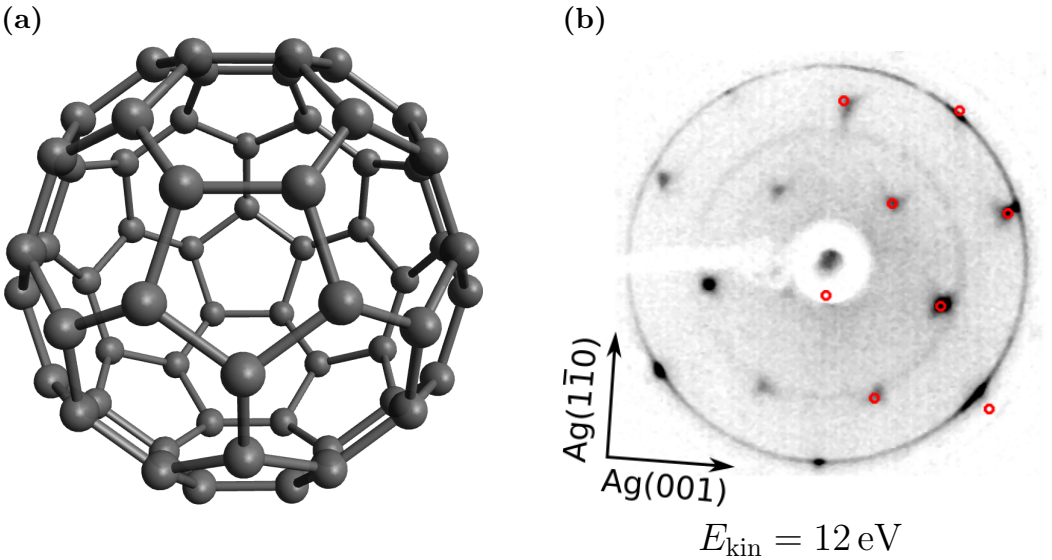

Figure 7.1: (a) Molecular structure of C_{60}. The molecule is solely made up of carbon atoms (black) positioned in the shape of a truncated icosahedron. (b) LEED pattern of a single monolayer of C_{60} on an Ag(110) substrate with a primary electron energy of 12 eV. Positions of constructive interference to be expected with a (1.67 , 2 / 1.67 , -2) superstructure matrix are indicated by red circles.

nearest neighbor spacing of 94 % of the bulk value at room temperature [215].

7.2 Results and discussion

The photoemission experiments were conducted using the PEMM at the NanoESCA beamline at the ELETTRA synchrotron in Trieste [123]. The undulators were set to produce right-circularly polarized light at several photon energies within the range of 20 – 140 eV. The circular polarization has the advantage that the higher harmonics are emitted off-axis at a different angle than the base mode and thus do not cause any spurious photoemission signal or radiation damage. For each photon energy the valence region in the vicinity of the Fermi edge from $E_{\mathrm{bin}} = 4.8$ to -0.5 eV was recorded in steps of $\Delta E = 0.1$ eV. All experiments were performed with the sample at room temperature.

Fig. 7.2 shows the EDC for $E_{\mathrm{ph}} = 42$ eV integrated within $(\pm 0.02\,\mathrm{\AA}^{-1})^2$ around $(k_{\mathrm{x}}, k_{\mathrm{y}}) = (1.00, -0.90)\,\mathrm{\AA}^{-1}$ (red circles). There are several features visible in the EDC which modulate the smooth background from the substrate. Even though the silver sub-

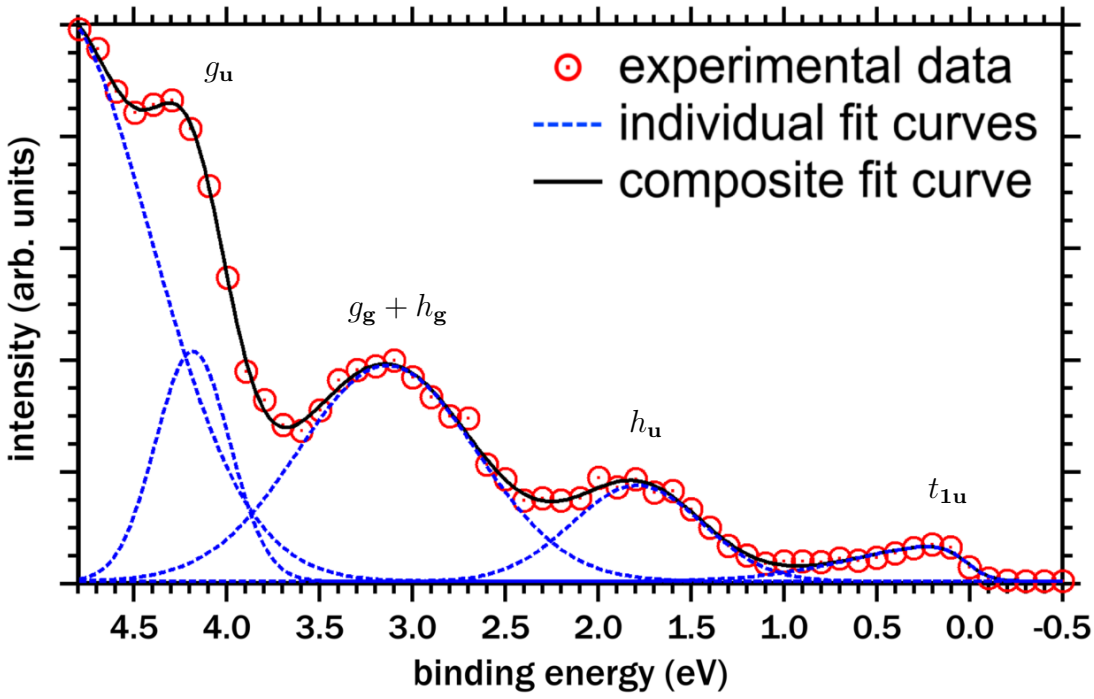

Figure 7.2: EDC with right-circularly polarized light at a photon energy of $E_{\mathrm{ph}} = 42$ eV and integrated within an area of $(\pm 0.02\,\mathrm{\AA}^{-1})^2$ around $(k_{\mathrm{x}}, k_{\mathrm{y}}) = (1.00, -0.90)\,\mathrm{\AA}^{-1}$ (red dots). The EDC is fitted by the black line with the individual fit components represented by dashed blue lines.

strate signal is damped by the adsorbed molecular layer, the sharp increase in intensity from the silver 4d-bands at $E_{\mathrm{bin}} \gtrsim 4\,\mathrm{eV}$ dominates the spectrum at higher binding energies [134]. On top of the substrate signal, there are four additional features in the valence region that can be attributed to the C_{60} monolayer. These features belong to molecular orbitals that are several times degenerate in the gas phase molecule. Even though the molecular symmetry is broken by the presence of the substrate and the adjacent molecules, the lifted degeneracy cannot easily be resolved by this measurement alone and only increases the width of the peaks. Features which cannot be energetically separated within the energy resolution of the experiment are therefore labeled with monikers specifying their combined symmetry in the isolated molecule. The features can be tentatively assigned to the g_{u}, $g_{\mathrm{g}} + h_{\mathrm{g}}$, h_{u} and $t_{1\mathrm{u}}$ orbitals of C_{60} at binding energies around 4.3 eV, 3.2 eV, 1.8 eV and 0.2 eV, respectively. Their corresponding degeneracy in the gas phase is four-fold (g_{u}), four- plus five-fold ($g_{\mathrm{g}} + h_{\mathrm{g}}$), five-fold ($h_{\mathrm{u}}$) and three-fold ($t_{1\mathrm{u}}$). The $t_{1\mathrm{u}}$ orbital at and slightly below the Fermi edge is not occupied in the isolated molecule which means that a moderate amount of charge transfer from the silver substrate into the molecules is taking place. This phenomenon has already been observed at the metal-organic interfaces of the previous chapters and is also frequently detected in similar systems [10, 136].

Before a more detailed data evaluation, the recorded PMM are cleaned of the experimental artifacts described in section 3.3. Since the orbitals have a relevant energetic overlap, they are extracted with a fitting procedure after the correction to separate the molecular features from the substrate and one another. To this end, the EDC at each $(k_{\mathrm{x}}, k_{\mathrm{y}})$ tuple on the MCP and for each photon energy E_{ph} was averaged in k_{x} and k_{y} by $\Delta k = 0.02\,\mathrm{\mathring{A}}^{-1}$ to increase the signal-to-noise ratio. The $t_{1\mathrm{u}}$ orbital close to the Fermi edge can obscure the position of the chemical potential and is therefore established first. This is done by taking the derivative of the averaged EDC and fitting it with the derivative of the Fermi-Dirac distribution. The position of the chemical potential is then saved and used as an input in the main fitting routine, where it can only be moved with a $\pm 20\,\mathrm{meV}$ range. The chemical potential can be determined fairly accurately through this procedure and more so than leaving it entirely to the algorithm of the subsequent fitting.

In the main routine, the averaged EDC is fitted with a Gaussian function for each of the four molecular features plus one for the silver 4d-bands. The features are multiplied by the Fermi-Dirac distribution for the known sample temperature (room temperature) and position from the previous fitting procedure. The width, position and height of all features and the Fermi-Dirac distribution is highly constrained to suppress erroneous results. After the successful convergence, the area under the Gaussian functions is stored as the photoemission intensity of the respective orbital, $(k_{\mathrm{x}}, k_{\mathrm{y}})$ tuple and photon energy. The procedure then moves to the next $(k_{\mathrm{x}}, k_{\mathrm{y}})$ tuple until all recorded wave vectors are

processed. These steps are then repeated for the measurements at all other photon energies. This data treatment is especially crucial for the t_{1u} orbital and at the lower and upper end of the photon energy range, where the intensities are comparatively low due to the reduced photon flux and and the decreased photoemission cross section, respectively.

An exemplary fitting result for $(1.00, -0.90)\,\text{Å}^{-1}$ and $E_{ph} = 42\,\text{eV}$ is shown in fig. 7.2. The individual molecular orbitals and the silver background (dashed blue lines) reproduce the experimental data very well when summed up (black line). As can be seen, the overlap of the individual features with one another is particularly large at higher binding energies. There is no energy dispersion detectable in any of the molecular orbitals within the experimental resolution of $\sim 70\,\text{meV}$ [123].

Fig. 7.3 (a) displays the extracted h_u orbital after applying the fitting procedure over the entire data set at $E_{ph} = 42\,\text{eV}$. The light incidence is towards positive k_y values and the color indicates the photoemission intensity (fitted area) of the orbital. The abrupt drop in intensity at high $k_\parallel$ is not due to the photoemission horizon $k_z = 0$ which lies beyond the detector at this electron kinetic energy. It is instead caused by the finite size of the multi-channel plate detector.

The PMM resembles the molecular frame of C_{60} itself with elevated intensities towards positive k_y which one might expect due to the vector potential $\mathbf{A}$ being larger in this

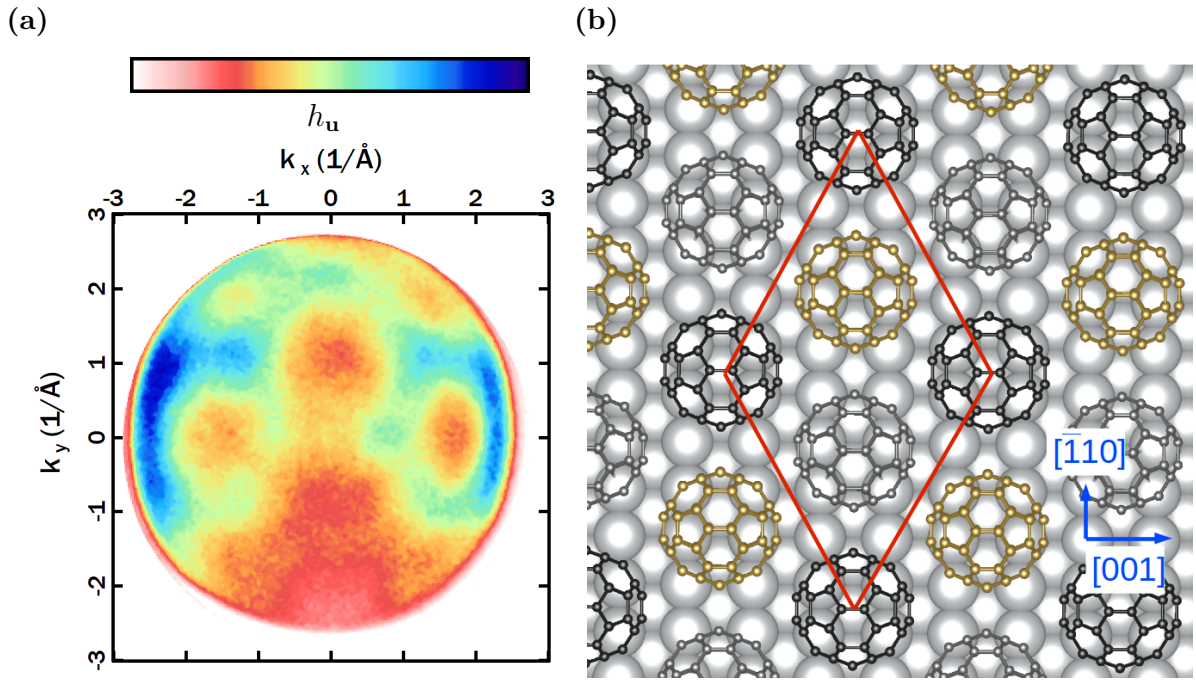

Figure 7.3: (a) Fitted PMM of the photoemission intensity from the C_{60} h_u orbital excited with $E_{ph} = 42\,\text{eV}$. (b) Determined adsorption geometry of C_{60} on Ag(110), showing the three inequivalent C_{60} molecules per unit cell in different colors. The unit cell is indicated by red lines.

area. Nevertheless, there are contrary examples on organic molecules with significant photoemission intensities in regions where $\mathbf{A} \to 0$ [38]. A small misalignment between $(k_\mathrm{x}, k_\mathrm{y}) = (0, 0)$ and the center of the MCP leads to a slightly increased field of view and higher intensities at the edge of the detector in negative k_x direction. The general shape of the emission from the h_u orbital is essentially two-fold symmetric with mirror axes along $k_\mathrm{x} = 0$ and $k_\mathrm{y} = 0$. The pattern strongly suggests that there is only a single azimuthal orientation of the C_{60} molecules present on the Ag(110) substrate at room temperature. Since the measurement integrates over a large amount of domains, molecules with a different azimuthal alignment would have photoemission maxima in directions that are effectively rotated around $(k_\mathrm{x}, k_\mathrm{y}) = (0, 0)$. In the most extreme case of randomly distributed azimuthal orientations, the shape of all PMM from the molecular orbitals would have a radial symmetry. This is actually the case for C_{60} in the bulk structure [216] which indicates a stronger interaction of C_{60} with the Ag(110) substrate than with other molecules in the extended crystal. Note that the same argument is not fully valid for molecules which adsorb at dissimilar polar angles. It is therefore possible that there is more than a single adsorption geometry that is mirrored in other domains due to the two-fold symmetry of the substrate.

The superstructure established via the LEED measurement in fig. 7.1 (b) reveals the structure within the molecular layer, but not the alignment with respect to the silver substrate. To determine the latter, the C_{60} molecules are relaxed on top of the Ag(110) substrate utilizing the VASP code for the DFT calculation [217]. A repeated slab approach is used where the substrate is represented by five metallic layers and a vacuum layer of $\sim 15\,\text{Å}$ is inserted between the slabs for separation. An additional dipole layer is located in the vacuum region to eliminate any spurious electrical fields [218]. The exchange-correlation effects are modelled using the generalized gradient approximation [219]. In the first series of calculations with a single molecule per unit cell, a Monkhorst-Pack grid of $(k_\mathrm{x} \times k_\mathrm{y} \times k_\mathrm{z}) = (10 \times 10 \times 1)$ points is used [220]. For a subsequent second cycle with three molecules per unit cell, a smaller $(6 \times 6 \times 1)$ grid is chosen. The super cell geometry is built according to the experimentally determined $(\,1.67\,,2\,/\,1.67\,,\text{-}2\,)$ superstructure matrix from the LEED measurement. Using the projector augmented wave approach [221], the kinetic energy cutoff is set to $\sim 500\,\text{eV}$. In order to simulate the rigid bulk during the geometry optimization, only the top two silver layers and the atoms of C_{60} are allowed to relax. The van der Waals interactions are accounted for in the calculations using the vdW-surf method according to Tkatchenko and Scheffler [222].

The relaxation is performed with five different initial molecular orientations at four

different adsorption sites in a c(4x4) surface unit cell. After convergence of the calculation, the adsorption energy E_{ads} is computed with the equation

$$E_{\text{ads}} = \frac{E_{\text{system}} - E_{\text{sub}} - nE_{\text{mol}}}{n} \tag{7.1}$$

where E_{system}, E_{sub} and E_{mol} is the ground state energy of the whole system, the silver substrate and the molecule, respectively. n designates the number of molecules included in the unit cell. These calculations were carried out by Mathias Schwendt and Peter Puschnig from the Institut für Physik at the University of Graz.

The resulting adsorption energies E_{ads} in units of eV are listed in tab. 7.1 with the five molecular orientation grouped in the columns and the four adsorption sites in the rows. The labels of the molecular orientation specify which part of C_{60} lies parallel to the substrate surface at the C_{60}/Ag(110) interface. For example, the 6-6 configuration indicates that the molecular axis of two carbon atoms between two hexagon faces is parallel to the [001] direction of the silver substrate. The 6-6 (90°) orientation also has two atoms of the same bridge parallel to the surface, but rotated along the surface normal vector by 90°. Similarly, the 5-6, pentagon and hexagon configurations mean that the bridge between a hexagon and a pentagon face, a pentagon face and a hexagon face are at the very bottom of the molecule, respectively. The adsorption positions separated by different rows in the table define above which substrate site the center of the molecule is located. The labels refer to the hollow site above a silver atom in the second row (H), the top site above a molecule in the second row (T), the short bridge site between two adjacent atoms in the first row along the $[\bar{1}10]$ direction of the substrate (SB) and the long bridge site between two adjacent atoms in the first row along the [001] direction (LB).

As shown in tab. 7.1, the lowest calculated adsorption energy is found for the 6-6 orientation in the hollow adsorption site (H) with $E_{\text{ads,6-6,H}} = -2.06\,\text{eV}$. This most favorable adsorption energy is followed by the 5-6 (H), 6-6 rotated (H) and hexagon (H) configurations. All remaining combinations of molecular orientation and adsorption site are even less favorable in adsorption energy.

For the 6-6 (H) configuration with the lowest adsorption energy a relaxation calculation of the C_{60}/Ag(110) interface with the (1.67 , 2 / 1.67 , -2) superstructure determined by the LEED experiment is carried out. The geometric structure in real space is depicted in fig. 7.3 (b) with the red lines indicating the molecular unit cell. The different colors of the molecules refer to the three different adsorption sites of C_{60} on the silver substrate. Note that only one out of the three molecules in the unit cell is in the 6-6 (H) configuration, since the superstructure matrix is not perfectly commensurate. The other two molecules are close to a LB adsorption site which has an only slightly less favorable adsorption energy of $E_{\text{ads,6-6,LB}} = -1.83\,\text{eV}$ in the c(4x4) cell. Nevertheless, the average adsorp-

Table 7.1: Calculated adsorption energies E_{ads} in units of eV after relaxation of C_{60} in a c(4x4) unit cell of Ag(110) on top of the substrate for five initial C_{60} orientations and four adsorption sites. The orientation labels refer to the edges or faces in parallel with the surface. The columns designate hollow (H), top (T), short bridge (SB) and long bridge (LB) adsorption sites.

	6-6	6-6 (90°)	pentagon	hexagon	5-6
H	-2.06	-1.90	-1.72	-1.88	-1.93
T	-1.52	-1.34	-1.13	-1.16	-1.40
SB	-1.21	-1.43	-1.45	-1.58	-1.50
LB	-1.83	-1.39	-1.72	-1.72	-1.81

tion energy after the converged relaxation is decreased further to $E_{\mathrm{ads}} = -2.71\,\mathrm{eV}$ per molecule, signifying a more favorable and stable structure compared to the larger c(4x4) cell. The small energetic difference between the 6-6 (H) and 6-6 (LB) configurations along with the increased intermolecular interaction between the more densely packed molecules is most likely the cause of the reduced adsorption energy.

While these conclusions strongly imply that C_{60} adsorbs with the 6-6 orientation, the comparison to the photoemission experiment can yield an unambiguous result. First, the two-fold symmetry of the photoemission pattern visible in fig. 7.3 (a) excludes the presence of the pentagon and hexagon orientations on the sample. In contrast, the 6-6 and 6-6 (90°) orientations have a two-fold symmetry when viewed from the curved plane at fixed electron kinetic energy in the experiment. The one-fold symmetric 5-6 orientation in combination with the two-fold symmetric Ag(110) substrate could also produce an two-fold symmetric pattern when integrating over both equivalent adsorption sites.

To determine the correct adsorption orientation, the PMM of the h_{u} orbital from isolated C_{60} with these orientations are computed with the photoemission tool in the IAC approximation. The DFT calculation for the initial state is performed with a 6-31G+ basis set and the B3LYP functional. The two equivalent domains of the 5-6 orientations are calculated separately and subsequently summed up. Since the h_{u} is five-fold degenerate in the gas phase and the individual orbitals cannot be disentangled within the experimental resolution, the superposition of the five composite molecular orbitals is used to form the integrated h_{u} intensity.

The resulting PMM for the photoemission from the h_{u} orbital is displayed in fig. 7.4 for the 6-6 (a), 6-6 (90°) (b) and 5-6 orientation (c). The respective real space view of C_{60} from the top-down view on the sample is displayed below each PMM. Just like in the experiment, the two-fold symmetry of the molecule is broken in the photoemission process due to the right-circularly polarized light impinging towards the positive k_{y} direction.

As can be seen from the comparison to the experimental PMM in fig. 7.3 (a), the 6-6

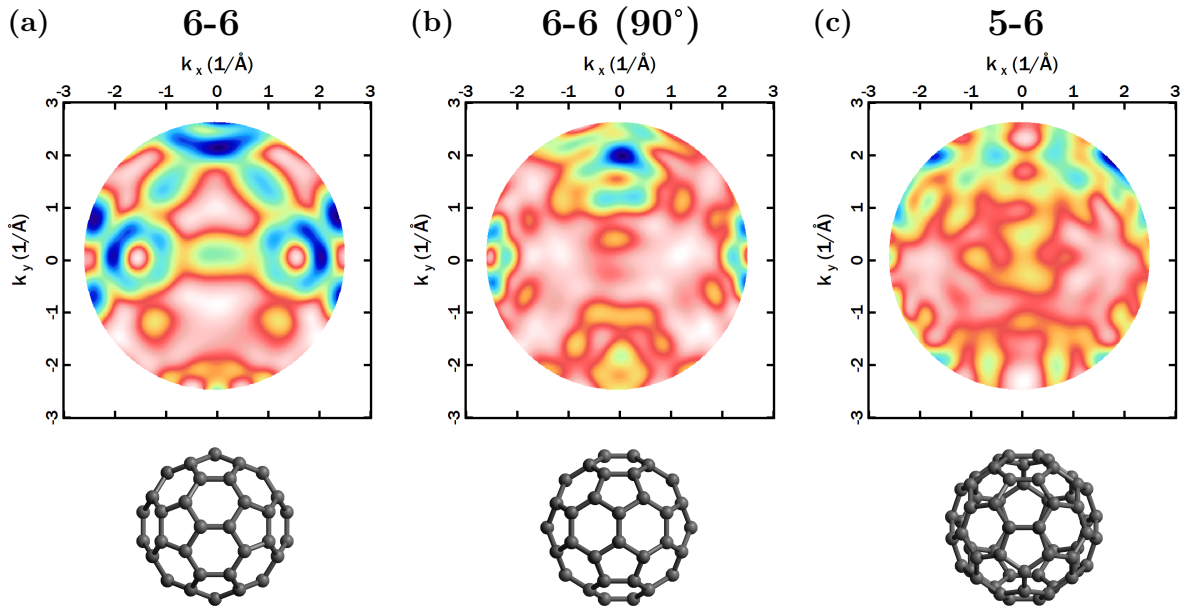

Figure 7.4: Photoemission calculations for the h_u orbital at $E_{ph} = 42\,eV$ with an isolated C_{60} molecule in the 6-6 (a), 6-6 (90°) (b) and 5-6 (c) orientation. The top-down view of the molecule in real space is depicted below the PMM. Only the 6-6 configuration in (a) fits to the experimental data shown in fig. 7.3 (a). The two-fold symmetry of the initial state wave function is broken in the photoemission process due to the right-circularly polarized light impinging in direction of positive k_y values.

(90°) (b) and 5-6 (c) orientations can clearly be ruled out. The 6-6 (90°) orientation (b) does not exhibit the main intensity features at the correct $k_{\parallel}$ values and is most intense close to the edges of the detector plate. The result for the 5-6 orientation (c) is even further off from and has no discernible shapes that can be clearly related to the experiment. On the other hand, the simulated PMM for the 6-6 orientation (a) agrees well with the experiment. The goggle-shape of the experiment is well reproduced, albeit at slightly smaller $|k_{\parallel}|$ values. The heightened relative intensity at large $|k_x|$ and positive k_y values also matches the experiment.

In combination with the structure relaxation, the determined geometry of the adsorbed monolayer of C_{60} on Ag(110) is a 6-6 adsorption orientation with molecules at three inequivalent adsorption sites per unit cell. One of the molecules occupies a hollow site (H) while the other two are located close to a long bridge (LB) site. This result is also depicted in fig. 7.3 (b).

The three-dimensional geometry of C_{60} results in a considerable photoemission intensity redistribution under changing photon energies which is unlike the behavior of planar molecules [61, 73]. This is showcased on the h_u orbital for various photon energies in fig. 7.5. The upper row displays the fitted PMM compared to the simulated ones in the

lower row for $E_{\mathrm{ph}} = 32\,\mathrm{eV}$ (a,d), 50 eV (b,e) and 60 eV (c,f). The goggle shaped pattern that resembles the molecular frame of C_{60} is visible over a wide range of photon energies. At higher photon energies the intensity gradually shifts away from the center towards higher $|k_{\mathrm{x}}|$ values. Starting at $E_{\mathrm{ph}} \approx 50\,\mathrm{eV}$ and towards higher photon energies the experimental data exhibits a strong increase in intensity at the edge of the detector plate around $k_{\mathrm{x}} \approx -2.5\,\text{Å}$. The trend is already visible in (b) and even more so in at $E_{\mathrm{ph}} = 60\,\mathrm{eV}$ (c). This behavior is not intrinsic to the photoemission experiment on the sample, but an experimental artifact that is caused by a misalignment of the photon spot on the sample and the detector column above. Excluding this artifact, the agreement between experiment and simulation is generally decent. The shape of the photoemission intensity is well reproduced in the simulation and the relative intensities of the features are also mostly close to the experiment.

In order to evaluate the applicability of the plane wave approximation, further photo-

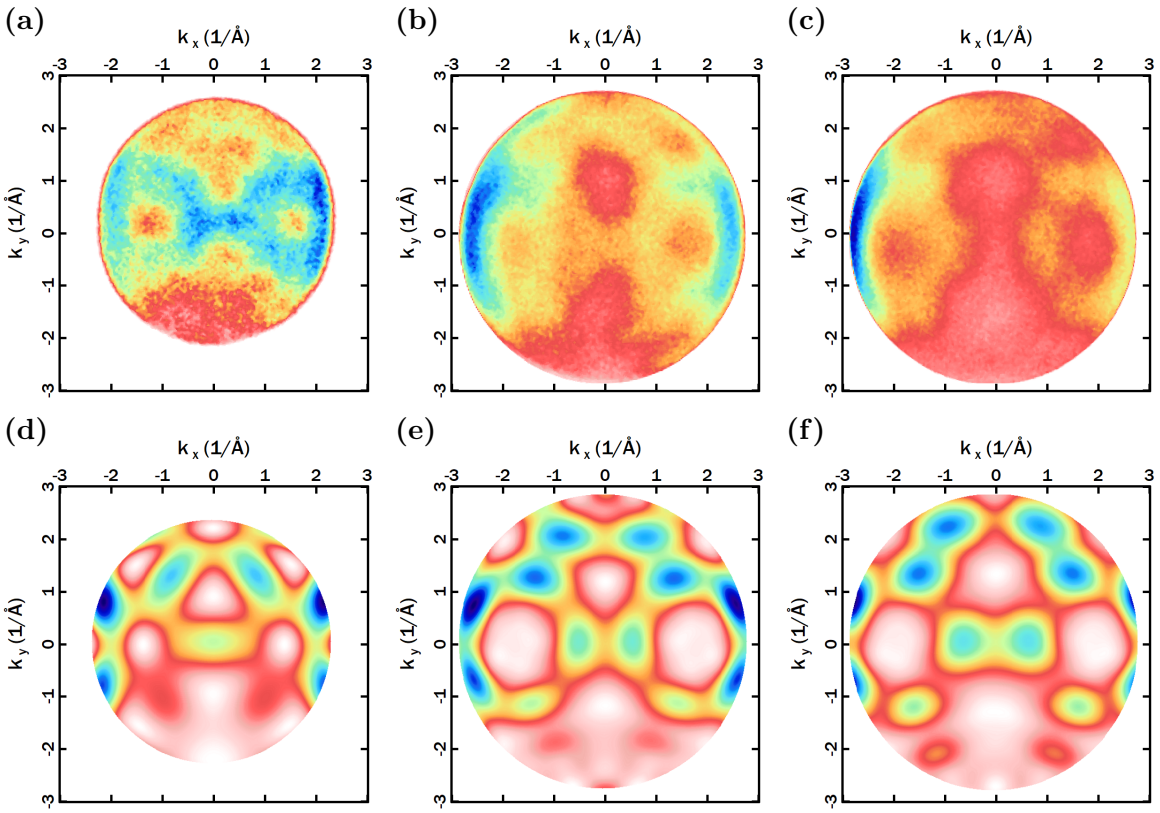

Figure 7.5: Comparison of experimental photoelectron momentum maps (top row) to simulations with the IAC approximation (bottom row) for the h_{u}-orbital illuminated with right-circularly polarized light at a photon energy of 32 eV (left column), 50 eV (middle column), 60 eV (right column). In contrast to planar molecules [61,73], the shape underlying the photoemission pattern is notably dependent on the photon energy.

emission calculations are performed on the relaxed C_{60} geometry for $E_{ph} = 40\,eV$. Simulations with the PWA and the IAC approximation for the 6-6 orientation are compared to the fitted measurement data in fig. 7.6. The left column shows the $g_g + h_g$ orbital of the experiment (a), the calculation with a plane wave final state (c) and with a IAC-based final state (e). The analogous results for the h_u orbital are displayed in the right column for the experimental (b), plane-wave- (d) and IAC-based (e) PMM. The goggle-shaped features of the experiment are reproduced fairly well by both types of simulations, with only small differences in the relative intensities between the approximations. In general, the IAC-based simulations manage to reproduce the relative intensities at different $k_{\parallel}$ slightly better. This largely good agreement between simulation and experiment is also maintained at other photon energies, as shown for the IAC-based final state in fig. 7.5.

The IAC-based simulations are computed with an isolated molecule, which permits an assertion about the hybridization and the molecular deformation upon adsorption. Despite the charge transfer from the substrate into the organic monolayer, the hybridization with neighboring C_{60} molecules and the Ag(110) substrate is evidently not strong enough to substantially alter the character of these valence orbitals. Neither is there any atomic displacement on the silver surface large enough to affect the PMM. This conclusion is consistent with the well-established rigidity of C_{60} [223].

The DFT calculations of the relaxed molecule on the silver surface performed with the VASP code predict the charge transfer into the molecules that is confirmed by the experiment (see Fig. 7.2). Furthermore, while the symmetry breaking upon adsorption does not influence the $g_g + h_g$ and h_u photoemission, it has another impact: the calculations reveal a small energetic redistribution of the formerly three-fold degenerate t_{1u} which lifts the degeneracy of the three orbitals, shown in Fig. 7.7 (a). Integrating the fractional occupation of the three components results in a relative occupation of 39 %, 31 % and 30 % with respect to each other.

Further photoemission calculations of the t_{1u} can be conducted and correlated to the experiment based on this finding. Fig. 7.7 (b) shows the measured photoemission intensity at 40 eV compared to the fitted (c) with simulations of the t_{1u} with the IAC approximation. The fractional occupation numbers have been taken into account by multiplying the PMM of the three components by their respective factor. Note that the relatively small charge transfer into the t_{1u} (see Fig. 7.1 (b)) results in a low signal-to-noise ratio, making the quantitative analysis more demanding.

Both PMM show goggle shaped features with increased intensity towards higher $|k_x|$ and from low to high k_y values. The drop in intensity around $k_x = \pm 1.7\,\text{Å}^{-1}$ and $k_y = 0$ is also visible in both PMM. Even though the match between experiment and theory is not as good as for the $g_g + h_g$ and h_u under these conditions, the general shape and intensity distribution fits moderately well, corroborating the DFT result from the relaxed molecule.

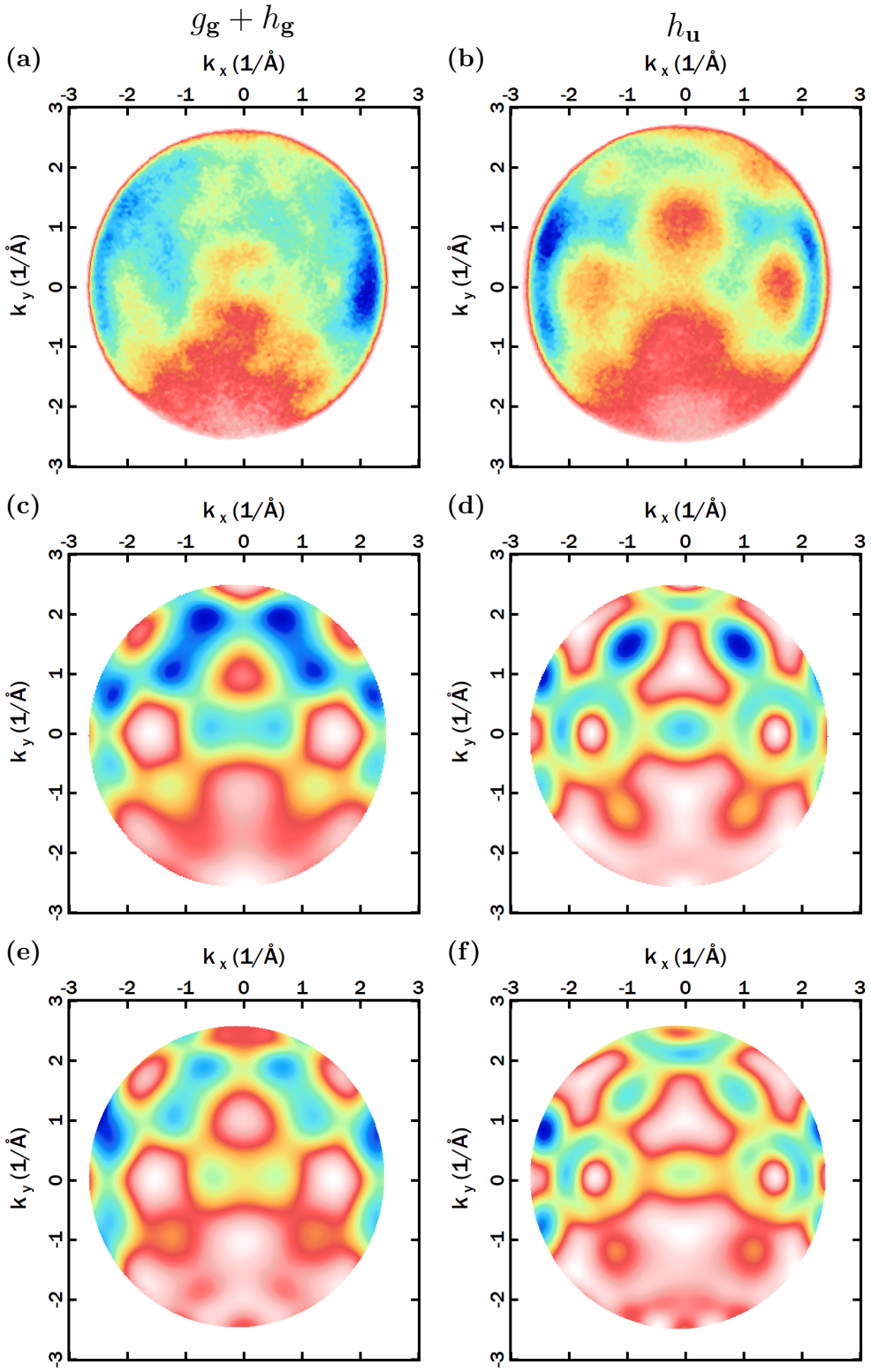

Figure 7.6: Comparison of experimental PMM (top) to simulations with final states based on the plane wave approximation (middle) and the IAC approximation (bottom) at 40 eV photon energy. The left column shows the C_{60} $g_g + h_g$, the right column the h_u orbitals. Both types of simulations fit well to the experimental data with only minor deviations in intensity.

In conclusion, the evaluation of the evaporated monolayer of C_{60} adsorbed on Ag(110) demonstrates that despite previous reservations [11] the plane wave final state can be successfully applied in photoemission calculations for non-planar molecules at the metal-organic interface. The comparison of simulations with the plane wave final state with an IAC final state and the experiment show a decent agreement. The C_{60}/Ag(110) interface is characterized through angle-resolved photoemission spectroscopy in a combined approach of state-of-the-art measurements, intricate data evaluation and theoretical simulations. The adsorption site, deformation and orientation of C_{60} are computed and the latter confirmed experimentally. A weak hybridization between substrate and molecules is revealed and DFT calculations of the redistributed density of states of the formerly degenerate t_{1u} are verified in the experiment. The molecules are only negligibly distorted upon adsorption and do not hybridize significantly with each other.

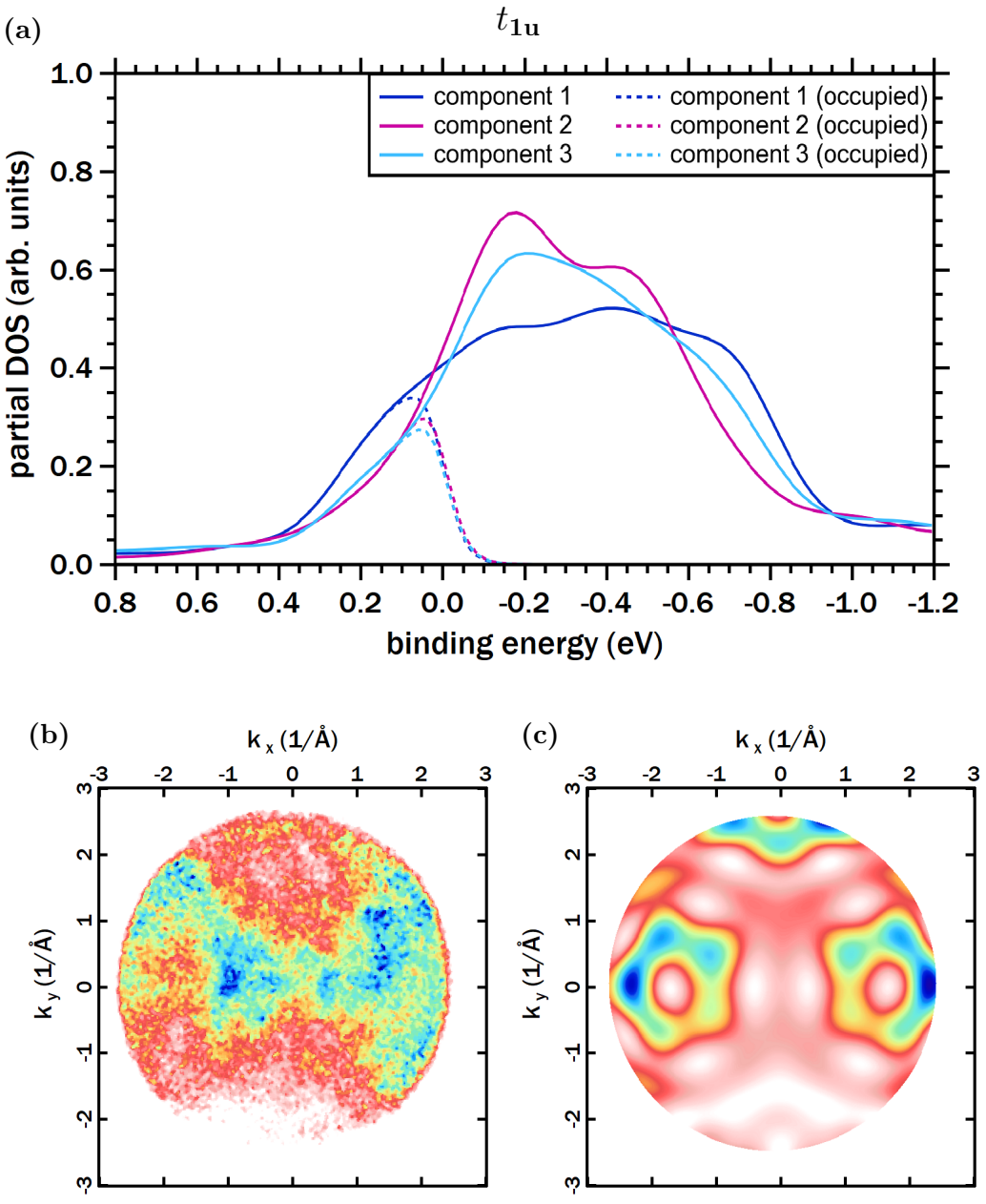

Figure 7.7: (a) Calculated projected density of states (DOS) of the C_{60}/Ag(110) system. The degeneracy of the t_{1u} orbitals is clearly lifted upon adsorption. Comparison of the PMM of the measured t_{1u} orbital (b) to an IAC-based simulation (c) for a photon energy of 40 eV.

8 Conclusion and outlook

The overarching topic of this thesis was the study of organic molecules at metal-organic interfaces using several angle-resolved photoemission techniques. Of particular significance was the description of the final state in calculations of the photoemission process which has to be chosen in accordance with the experiment to extract as much information as possible. Relevant material properties were already obtained with a simple plane wave final state. Beyond the limitations of a plane wave, however, a more complex final state description based on the independent atomic center approximation was successfully employed in further photoemission studies. Advances in this kind of fundamental science are a crucial step to tailor materials for specific needs and applications. In the end, a detailed understanding of elementary processes within a prototype sample in the laboratory promotes the efficiency of current devices or even permits the emergence of entirely novel applications with unprecedented material properties.

The value of the plane wave approximation was evaluated on the valence orbitals of a monolayer of pentacene on an Ag(110) substrate with photon energies between $E_{\mathrm{ph}} = 20-140\,\mathrm{eV}$. There are significant deviations from the expected E_{ph} dependence of the measured intensity of the molecular orbitals compared to calculations with a plane wave final state. The variations in intensity are indication that the final state might be influenced by shape resonances [61] and/or increased elastic scattering in the Bragg gap of the substrate [141]. To settle this question, theoretical calculations on the pentacene/Ag(110) system are required. Next, the phase information was retrieved from a two-dimensional excerpt of the three-dimensional experimental data set of the pentacene HOMO. With the information from the two-dimensional reconstruction, the entire molecular orbital was reconstructed in three dimensions. The experimental result is in good agreement with the prediction from DFT calculations points, but does not fully match it. The dissimilarities point to a small hybridization of the molecular orbital, but nevertheless, this analysis would also profit from the aforementioned theoretical calculations.

The appealing simplicity of the plane wave approximation is connected to its limited applicability [11]. It is thus crucial to be able to resort to a more complex final state if a system requires it. A photoemission tool with final states based on the independent atomic

center approximation was developed and implemented in *WaveMetrics IGOR Pro* to this end [144]. The initial state wave functions can be calculated externally with DFT programs like *Gaussian 09* [145] and subsequently imported via an automated procedure in the tool. The program also comes with a user interface that is straightforward to operate even for users unfamiliar with the theory behind it. To verify the correct implementation, the tool was successfully tested against the pentacene molecular orbitals measured in the previous chapter, chapter 4. After this brief replication, the tool was used to discover the adsorption structure of a pyrphyrin monolayer on top of Ag(110). The final examination was to determine the adsorption geometry of a sub-monolayer of carbon monoxide adsorbed on Pt(111). This study was ambitious due to the intention to use angle-resolved photoemission data from a molecular orbital under excitation of light with comparably low energy. Despite this challenge and the early state of the photoemission tool when enabling elastically scattered photoelectrons, the geometry was successfully established in agreement with literature.

Understanding the structural and electronic properties of molecules at interfaces was also the target of the next study. A combined experimental and theoretical technique for the geometry determination was showcased on the example of a bilayer of pentacene adsorbed on an Ag(110) substrate [10]. After an initial photoemission survey of the molecular valence states the angle-dependent intensity distribution of the energetically non-degenerate HOMO orbitals of each layer was compared to simulations with the photoemission tool. A static deformation of the molecules, the excitation of molecular vibrations, the influence elastically scattered electrons, and a tilt of the molecules were assessed and evaluated next to the experiment. The latter was found to be the sole cause of the change in the photoemission pattern from the mono- to the bilayer of pentacene on Ag(110). The tilt angles even of the first layer buried beneath the second could be determined with a high precision of $\pm 0.5\,^{\circ}$. The approach taken in this study can readily be adapted for other samples.

Lastly, the applicability of the plane wave approximation was examined on the non-planar molecule C_{60} and compared to calculations with the independent atomic center approximation [12]. The work demonstrated that the simple, yet powerful plane wave approximation can indeed be successfully employed for truly three-dimensional molecules, despite justified reservations in literature [11]. Calculations with the plane wave approximation were in good agreement with the experiment and found to give predictions similar to the more complex independent atomic center approximation. With accompanying DFT simulations, the adsorption geometry of C_{60} on the Ag(110) substrate could be determined. The presence of the substrate breaks the symmetry of the formerly unoccupied and threefold degenerate t_{1u} orbital and results in an unequal charge transfer from the substrate into the three composite molecular orbitals. The measured angle-resolved photoemission

intensity distribution is in agreement with the calculations for these molecular orbitals.

A promising next step is expanding these photoemission techniques techniques to include the time-dependent evolution of a system under excitation with an external stimulus. Time-resolved photoemission can be performed by using two pulsed photon sources in a pump-probe scheme and varying the delay time between them [167, 224]. Recording and understanding the inherent time-dependence of any physical phenomenon is beneficial to any study, but even more so in multi-step processes that are not as easily deciphered with time-integrating methods. These include for example the singlet fission of excited electrons in pentacene which conceivably enable overcoming the Shockley-Queisser limit of solar cells [225, 226] or catalytic reaction as in the reduction of carbon monoxide on Pt(111), see section 5.3.

Another fascinating way forward that builds upon the projects in this thesis is combining the knowledge on organic molecules and the presented photoemission techniques with novel topological materials. Adsorbed molecules are ideally suited to alter the properties of topological surface states since they are easier to grow in an ordered and adjustable fashion on a variety of substrates. This can enable e.g. the controlled surface doping in low concentrations of topological insulators with metal-containing molecules that is tough to achieve with pure metals. A variety of organic materials lend themselves to systematically study this interaction, like transition metal phthalocyanines and porphyrins that can be synthesized to contain different metal atoms.

Appendix

A5 The expanded photoemission simulation tool

Upon starting the photoemission tool, the main window shown in fig. A5.1 with most calculation parameters is opened. In the figure the tool is in the "Stationary kPEEM Scan" mode which is used to simulate the photoemission intensities as they would be measured in a PEMM setup (see chapter 3.3). In the second mode ("Rotary Azimuthal Scan", not shown), the polar and azimuthal angles Θ and ϕ of an azimuthal scan can be set instead of k_x and k_y – more of this difference will be clarified later. The two modes are almost identical besides this axis transformation and can be toggled by clicking the top center "Stationary kPEEM Scan" button. Before going into detail of all the available parameters, we will first examine how the DFT data is loaded into the procedure.

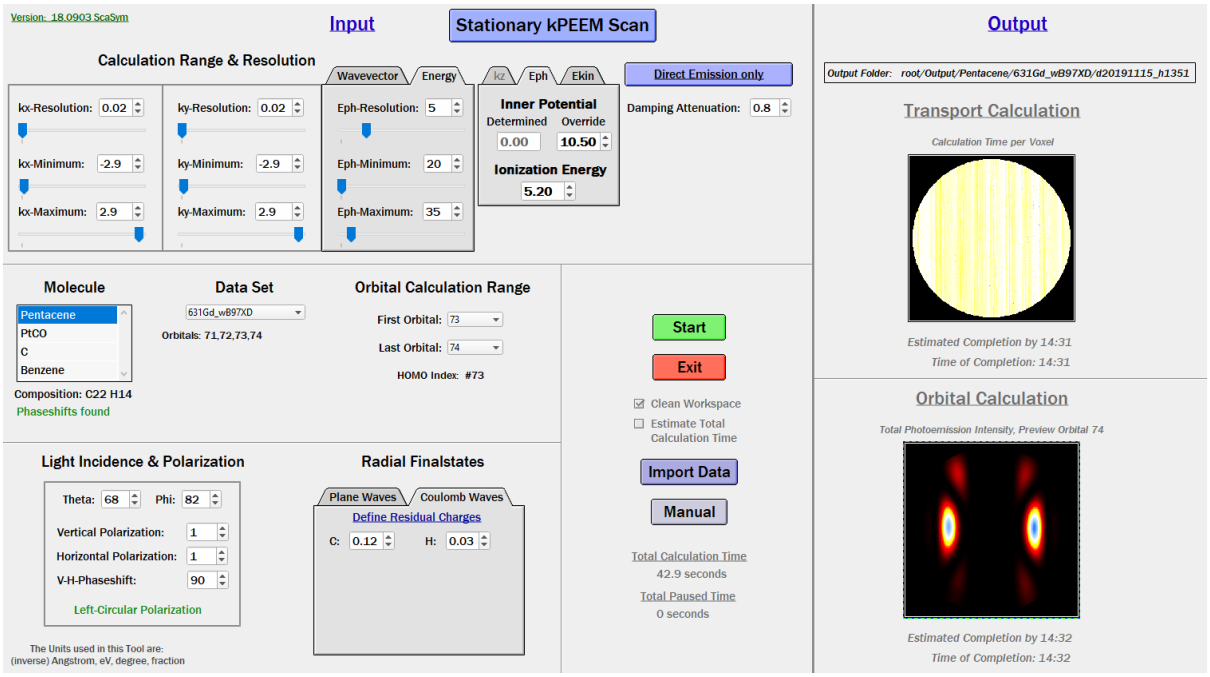

Figure A5.1: Main window of the photoemission tool in PEMM mode showcasing most of the available parameters and optional settings.

A5.1 Input preparation

In preparation of a photoemission calculation, the molecular initial states have to be read from the DFT output created by Gaussian 09. The Gaussian output file is recorded in plain text and as such too large and unwieldy to use as an input right away. The photoemission tool therefore includes an auxiliary function that reads and converts the relevant data in the raw output into several files within IGOR Pro that are of manageable size. This procedure is mostly automated and accessed by clicking the "Import Data" button in the bottom center of the main window in fig. A5.1.

Pushing the button opens a dialog window (see fig. A5.2) with brief instructions and a few hints on its usage. Next, the user picks a Gaussian output file from a drive on the computer by clicking the "Select File" button. This triggers the first phase of the automated import process: reading the file and analyzing it with respect to certain keywords.

The readout takes less than a second and leads to one of two panels shown in fig. A5.3. During this time the procedure attempts to load the parameters in four stages:

Gaussian Keywords

This is a copy of main command line in the Gaussian input file. It contains all information on how the DFT is performed – including basis set, functional, geometry optimization and which data is to be recorded in the output. Every valid output contains this line as it is are mandatory for the DFT calculation itself.

Molecular Structure

The atomic number and Cartesian coordinates of each atom are also part of any authentic output. If a geometry optimization has been performed by Gaussian, the procedure detects the optimized coordinates separately from the original ones.

LCAO-Coefficients

The LCAO coefficients $c_{a,j}$ described in eq. (2.15) are fundamental to the initial state wave function. Only those orbitals whose coefficients have been printed into the output can be loaded into the photoemission tool. To simplify the navigation through the orbital indices, all available orbitals and the index of the HOMO are displayed here as well. The procedure will also differentiate between the spin-dependent wave functions in case the molecular orbitals are not spin-degenerate. If the geometry has been optimized, both sets of coefficients will be detected and assigned to their respective structural data from the previous stage.

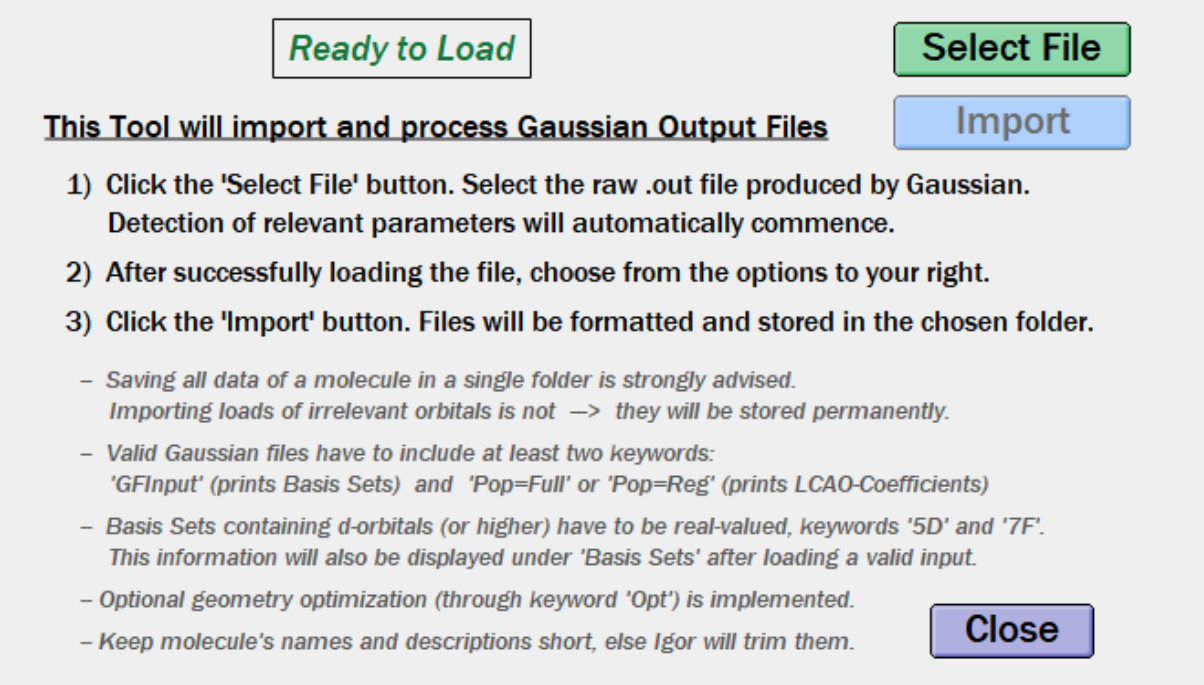

Figure A5.2: Import dialog that is opened after clicking the ”Import Data” button in the main window. The dialog displays a short guideline and helpful comments on its usage.

Basis Sets

The basis set defines the radial wave function in eq. (2.16). In combination with the spherical harmonics of the angular wave function and LCAO coefficients above they make up the initial state wave function.

Fig. A5.3 (a) displays a successful readout of a spin-dependent DFT calculation where a second DFT run was carried out after the atomic coordinates of the input were energetically optimized. In fig. A5.3 (b) a dummy text file unrelated to a DFT calculation was loaded and thus failed at every readout. Note that the import of a file is prevented if the initialization of *any* of the four stages fails.

There are only two mandatory keywords that must be included in the Gaussian DFT to produce a valid output: First, the parameters of the chosen basis set have to be recorded with the keyword ”GFInput”. This is necessary to reconstruct the atomic wave functions with eq. (2.16). Second, the LCAO coefficients $c_{a,j}$ of the molecular orbitals must be printed into the file as well so that the initial state wave function can later be compiled with eq. (2.15) and (2.16). The most convenient keyword here is ”Pop=Full”, which lists the LCAO coefficients of every single molecular orbital into the output. The import procedure can detect and process any basis set that comes with Gaussian 09 plus any basis sets that have been manually defined by the user. In the current version, the wave func-

(a)

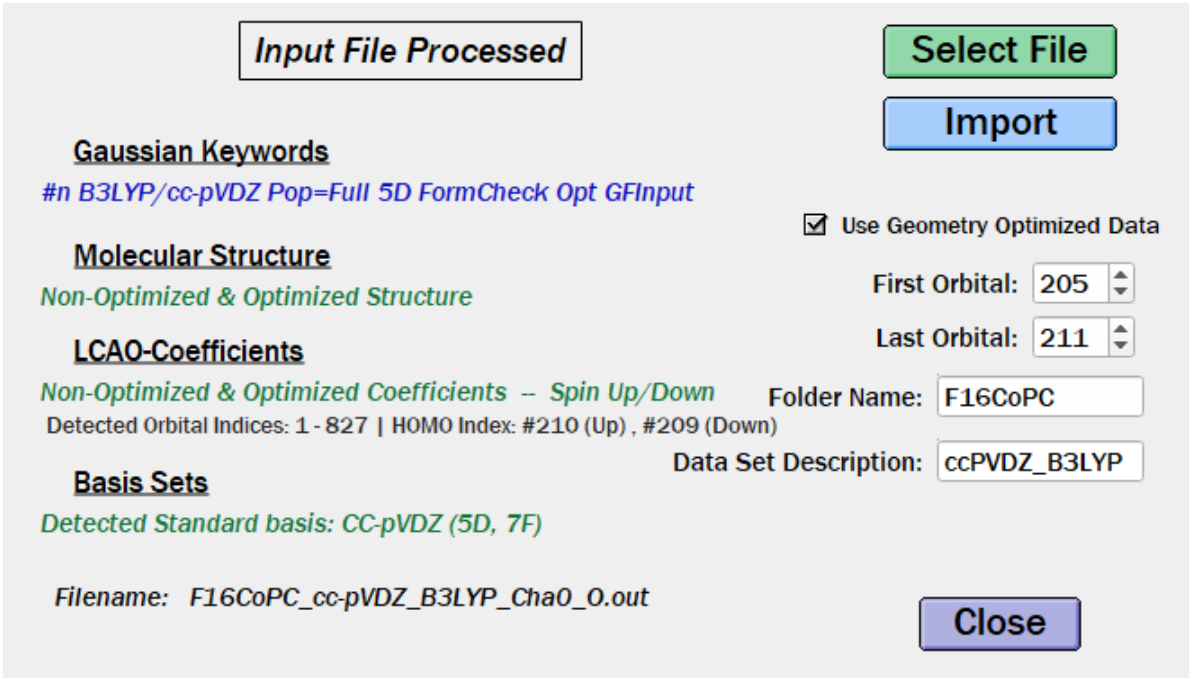

(b)

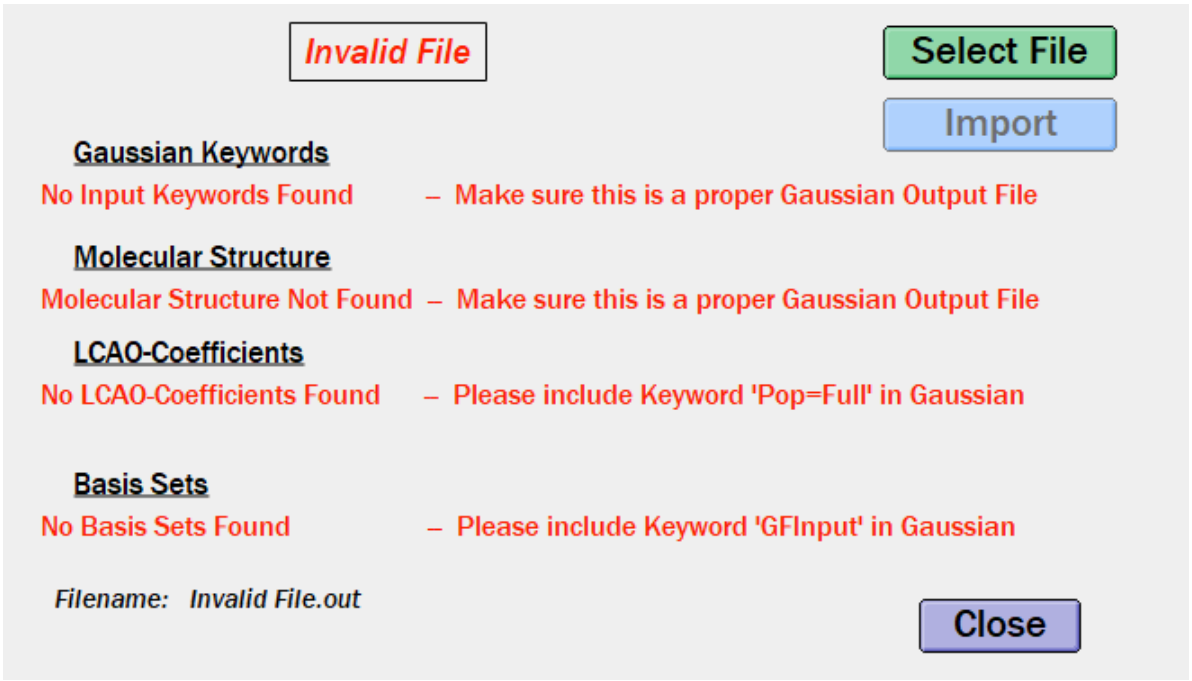

Figure A5.3: Import dialog after loading a valid DFT input with all optional Gaussian keywords enabled (a). The detected keywords are shown for each phase in the readout process. The input parameters can be set on the right side of the dialog and imported with the "Import" button. (b) Import dialog after loading a (fully) invalid file. If the readout fails at any step, the dialog will display what went wrong. Since the input is not a Gaussian output file, none of the four phases are successful and the "Import" button is disabled.

tions have to be expressed with real-valued spherical harmonics, though this is ensured by using keywords ”5D” and ”7F”. The choice of DFT functional is also not restricted in any way. Hence, both the basis set and the functional can be picked freely depending on the system in question and the desired complexity.

If the readout in the first phase is successful, the user can choose how to import the data in the right-hand side of the panel (see fig. A5.3 (a)). Going from top to bottom the procedure can import either the initial or the geometry optimized parameters. Naturally, the checkbox ”Use Geometry Optimized Data” is only activated if an optimized structure was actually detected. Which of the orbitals are loaded can be set in the next two fields. Any orbital in between and including ”First Orbital” and ”Last Orbital” are imported. While the molecular orbital files have a very small size on the order of a few kilobytes, it is just inconvenient to load hundreds of irrelevant files into the program. Lastly, the storage folder in the IGOR file and the moniker of the data set has to be picked in the fields ”Folder Name” and ”Data Set Description”. With everything set up, the import is concluded by pushing the ”Import” button.

In the current version of the code, the import procedure loads every essential input file with the exception of the phase shifts. This is because they are generated separately from the DFT with Gaussian from spherically symmetric muffin-tin potentials with the software *Electron Diffraction in Atomic Clusters* (EDAC) [101]. EDAC is a freeware code that can be used to simulate the multiply scattered photoelectron diffraction signal [227]. To do so, it calculates the phase shifts $\delta_a^l(\mathrm{k})$ of an electron that is elastically scattered at the potential around an atom a (compare subsection 2.3.2). For our purposes, we run the simulation with the same atomic coordinates as in the photoemission calculation and only extract the phase shifts from the program. The $\delta_a^l(\mathrm{k})$ matrix is loaded into IGOR Pro and used alongside the DFT input.

A5.2 Procedure details

With all input files in place, we can now look into the calculation of photoelectron matrix elements. As explained at the beginning of the chapter, there are two different modes: the first one is for the stationary geometry that is found at a PEMM (”Stationary kPEEM Scan”). The angle between the incoming light and the sample is constant for every calculated tuple in reciprocal space. The second mode (”Rotary Azimuthal Scan”) simulates a photoemission measurement where different azimuthal angles ϕ are accessed by rotating the sample while the intensity along the polar angle Θ is recorded with a one-dimensional detector. The angle between incoming photons and the sample is therefore *not* constant in this mode. All other settings and internal calculations are identical, so to avoid redun-

dancy only the "Stationary kPEEM Scan" mode will be described in the following.

The input parameters are defined to the left and center of the main window in the input section, see fig. A5.4 (a). Starting in the top row from the left, the first three panels control the extent and resolution of the three-dimensional grid in reciprocal space, for which the photoemission intensity will be calculated. All values of wave vectors here and everywhere else in the tool are given in units of Å^{-1}. For the third dimension, the user can choose between k_z and energy. Selecting "Wavevector" leads to an orthogonal coordinate system, while picking "Energy" results in spherical cuts at fixed energy in reciprocal space. The latter is more convenient when comparing experimental data at a fixed kinetic E_{kin} or binding energy E_{bin} to the simulation. Similarly to the units of the wave vector, all energies in the tool are standardized to be in units of eV. The fourth panel determines whether the energies in the third panel refer to the photon energy E_{ph} or the electron kinetic energy E_{kin} outside the sample if energies are set in the third panel. There is no analogous choice when using an orthogonal coordinate system with k_z. This is also where the inner potential V_0 is set (see eq. (2.10)). When selecting E_{ph} one also needs to provide the ionization energy in order to work out the correct kinetic energy of the electrons inside the system.

In the fifth and last panel of the row a factor of the inelastic mean free path $\lambda(E_{\text{kin}})$ is set. The initial value for $\lambda(E_{\text{kin}})$ is calculated using the universal curve for the inelastic mean free path of organic compounds from Seah et al. [22]. The multiplicative factor is indispensable since Seah's data set is lacking in the energetic range of typical ARPES experiments and the universal curve has a huge relative error bar, which makes $\lambda(E_{\text{kin}})$ strongly dependent on the exact material anyhow. Elastic scattering is turned on by pressing the "Direct Emission only" button to the very right. The theory behind the the calculation of the elastically scattered amplitude is described in subsection 2.3.2. Clicking the button activates the additional parameters shown in fig. A5.4 (b): "Max. Scatter Distance" determines in units of Å how far the emitting atom can at most be from the last scatterer to be included in the simulation. An electron can scatter a maximum of "Max. Scatter Order" times. The last setting on this row is a checkbox on whether to included "external" scatterers. These are atoms which have not been part of the DFT calculation, but nevertheless scatter the emitted electrons. They can be provided manually within the data folder of the input automatically imported with the import procedure in appendix A5.1. This setting is highly useful e.g. to simulate the elastically scattered photoemission pattern from a substrate which is too large for the Gaussian DFT to handle. Please note that in order to determine the scattered intensity, phase shift files of every element in the external scattering cluster have to be provided. The program will automatically look for these files and only enable the checkbox upon a successful readout. Enabling elastic scattering greatly increases the calculation time. It is also less accurate than the unscat-

tered amplitude because it relies on a lot of approximations and has only recently been implemented into the program. This option is still very much under construction, but already functional for some initial applications.

The second row in the main window contains the selection of the DFT initial states. The folder within IGOR that contains the data set is chosen under "Molecule". Upon picking a folder, a procedure looks for the composition of the molecule and all necessary phase shift files – just like for the "External Scatterers" above. If phase shift matrices are missing for a particular element, there are some backups that will be provided by the program. These include metal substrate elements and elements commonly found in organic molecules. The latter obviously vary from compound to compound, but are generally quite similar for molecules mainly based on cyclic components. The backups are usually sufficient for a rough and fast evaluation before importing the correct phase shift files. The moniker "Molecule" above the list is used because it makes sense to save all data of a particular molecule in one folder, since they can share the same phase shifts. One panel to the right, the user picks one or more data sets within this "Molecule" folder. The name of the data set corresponds to the on given under "Data Set Description" in the import procedure (see fig. A5.3). Data sets usually differ in the DFT functional, basis set and/or geometry. When a data set is selected, another automated procedure looks for LCAO coefficients of the molecular initial states. The orbital indices of all detected initial states are then available in the rightmost panel "Orbital Calculation Range". Keep in mind that the ionization energy or electron kinetic energy has to be set according to the chosen orbitals in the panel above. Calculating several orbitals with the same energy values at once is mostly useful for degenerate orbitals or a quick assessment.

The third row holds the geometric parameters of the exciting light on the left, and the radial final states to the right. First, the polar ("Theta") and azimuthal angle ("Phi") with respect to the molecule are set in units of degrees. The next three lines define the amplitude of the vertical and horizontal component of the electric field as well as the phase shift between them in degrees. Using these three numbers, any arbitrarily polarized light field can be applied in the simulation. The bottom line is a readout which helps to verify that the desired polarization has been set. In the second panel, the user can choose to use the spherical Bessel functions of a plane wave ("Plane Wave", see eq. (2.17)) or Coulomb waves as radial final states. Only when selecting Coulomb waves the user has to supply the residual charge per element Z_{ion} to calculate α with eq. (2.18).

There are three notable reasons for providing this choice, even though Coulomb waves should always be closer to the experiment: Using spherical Bessel functions saves a significant amount of time in the calculation of the radial component of the integral over all of real space in eq. (2.5). This is because these integrals are solved analytically, while the

(a)

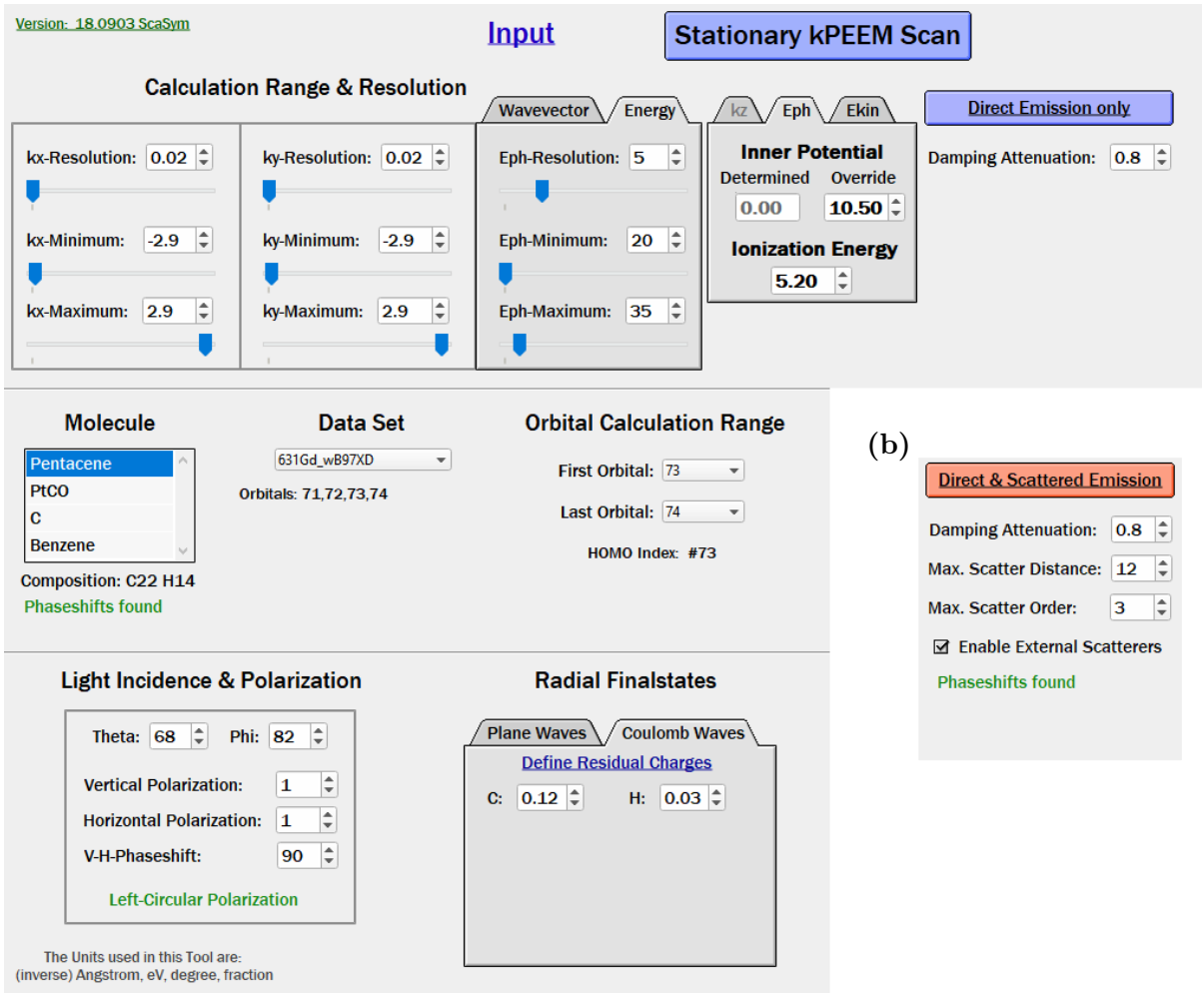

(b)

Figure A5.4: (a) Input section of the main window in "Stationary kPEEM Scan" mode is split into three panels: The simulation range and resolution plus the energy and scattering parameters (top), the imported data set (middle), and the excitation and final state values (bottom). (b) Scattering parameters located in the top center of the main window when elastic scattering is turned on. The phase shifts used for scattering are identical to the ones in the calculation of the unscattered emission. External scatterers are optionally provided atoms which have not been included in the ground state DFT, but with which the electrons can interact during the emission process.

integrals over Coulomb waves have to be determined numerically. The radial component at each atom is also entirely separated from the angular one. Many ARPES projects focus on the angle-dependence at a fixed photon energy and the binding energy of an orbital without explicitly evaluating the E_{kin} dependence. The radial wave function can usually be neglected in these cases, since it scales the photoemission intensity equally at every angle. Note that the angular dependence is still affected if there is more than a single type of orbital and/or element with a relevant share in the initial state. Lastly, the difference between both radial wave functions gets progressively smaller for higher electron kinetic energies and larger molecules, as the residual charge is spread over an increasing number of atoms. The minute difference between the final states might thus not justify the larger computational cost. With all these settings in place the input section is concluded.

Fig. A5.5 shows the control panel in the center of the main window while the calculation is idle (a), running (b) and finished (c). When everything has been set up in the input section, the calculation can be started here with the "Start" button. This is also the place where the program can be exited and a running calculation can be paused

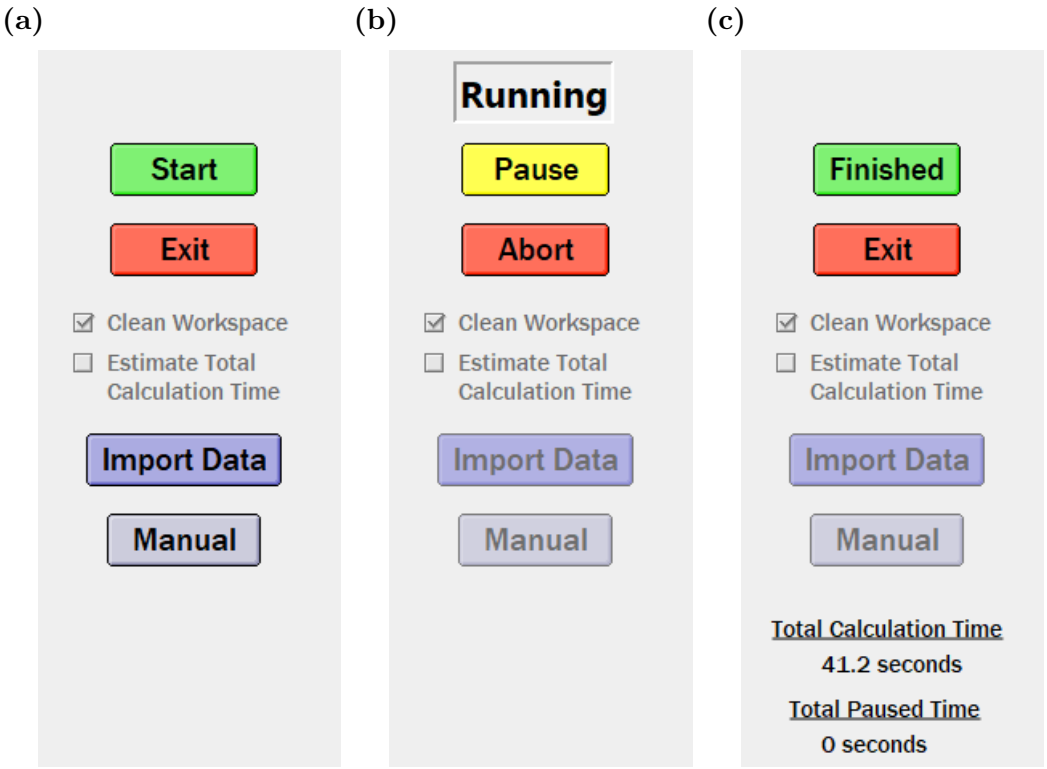

Figure A5.5: Control panel of the main window before (a) during (b) and after completing the simulation (c). The calculation can be started, paused or aborted with the two buttons on the top. The lower two buttons access the import dialog shown in fig. A5.2 and a brief manual with helpful advice. After a simulation is finished, the elapsed time since starting the procedure is displayed below.

to temporarily free up resources of the CPU. Pressing the "Import Data" button opens the import dialog described in appendix A5.1, and clicking the "Manual" button below displays a text window with a short manual and advice.

Upon starting the simulation, the output section on the right-hand side of the main window becomes relevant (see fig. A5.6). It is split between an upper panel where the transport properties of the electrons inside the system are determined, and a lower panel where the LCAO coefficients and a couple more parameters are fed into the procedure. At the very top is the path to an automatically created folder where all output files will be stored at the end of the run. Splitting the simulation into two steps is entirely due to technical reasons, since it accelerates the calculation in proportion to the number of orbitals. While the upper panel is active, the transport properties of the electrons inside the system are calculated. This is done by solving part of the matrix element in eq. (2.5) with the LCAO initial state from eq. (2.16) and final state eq. (2.20) when elastic scattering disabled, or eq. (2.25) when enabled. Excluded in this step are the LCAO coefficients, the phase shift due to the different atomic locations and a few constants. During the calculation, the image under "Transport Calculation" will gradually fill up from top to bottom and left to right. Each pixel in the image corresponds to a $(\mathrm{k}_x, \mathrm{k}_y)$ tuple and its color to the duration it took to determine the transport of all k_z (or E_{kin} / E_{ph}) values at this tuple. The result is subsequently passed to the lower "Orbital Calculation" panel. This second phase is usually a lot faster than the first one and feeds the missing parameters into the matrix element.

After it has done so for an orbital, it will preview the resulting photoelectron momentum map in a false color illustration. When all orbitals are done, the output will be saved and all temporary auxiliary files cleaned up. While the calculation is running, the program estimates the time it takes until its conclusion. This is helpful at the very beginning to adjust the parameters in such a way, that the program is done by some requested time while having the best possible resolution. Non-scattering calculations with a resolution close to most experiments (0.01 – $0.03\,\mathrm{Å}^{-1}$) commonly take only a few minutes to an hour on a commercially available laptop. However, when elastic scattering is enabled with a high accuracy, the runtime can get almost arbitrarily long. The output code saves the direct and the elastically scattered intensity both in a separate file and combined into one. This can aid in assigning individual features in the PMM to the initial state or the influence of scattering atoms.

Fig. A5.7 displays a flowchart describing every step in the photoemission simulation. Briefly recapitulated, the input is prepared by Gaussian and EDAC outside of the tool.

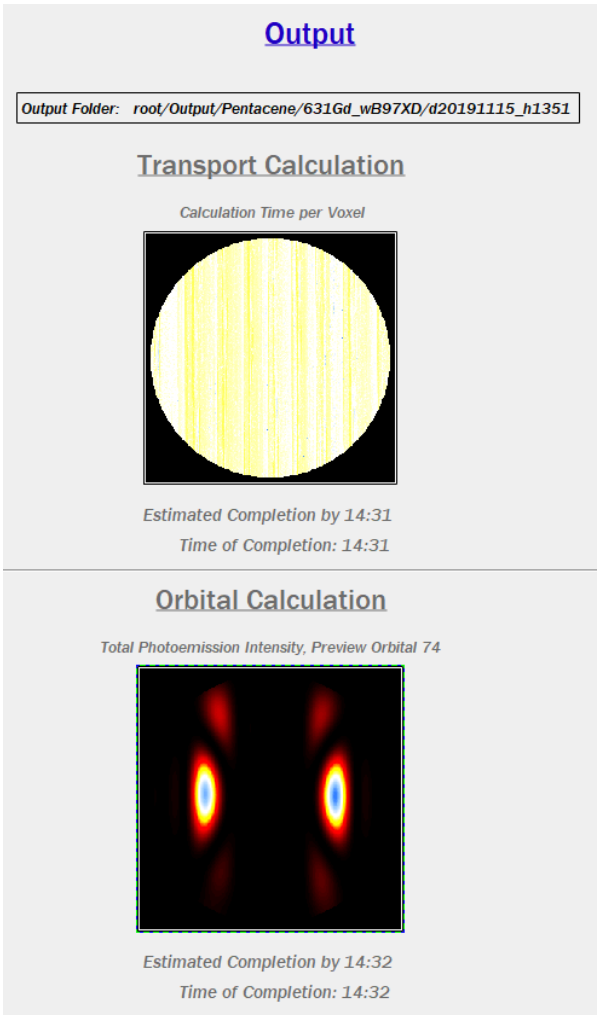

Figure A5.6: The output section of the main window in "Stationary kPEMM Scan" mode is divided into two panels. The upper "Transport Calculation" is active while the transport properties of the electrons inside the system are calculated. During the second "Orbital Calculation" phase the remaining parameters are incorporated and the simulation is concluded.

Their output is then imported with a tool-assisted procedure and the desired photoemission matrix elements are determined with the main program.

The photoemission tool is still work in progress and updated with new features and improvements. These include some features which are partially implemented in the user interface, but have not been discussed since they are disabled in the current version – e.g. the two inactive checkboxes in the center of fig. A5.5.

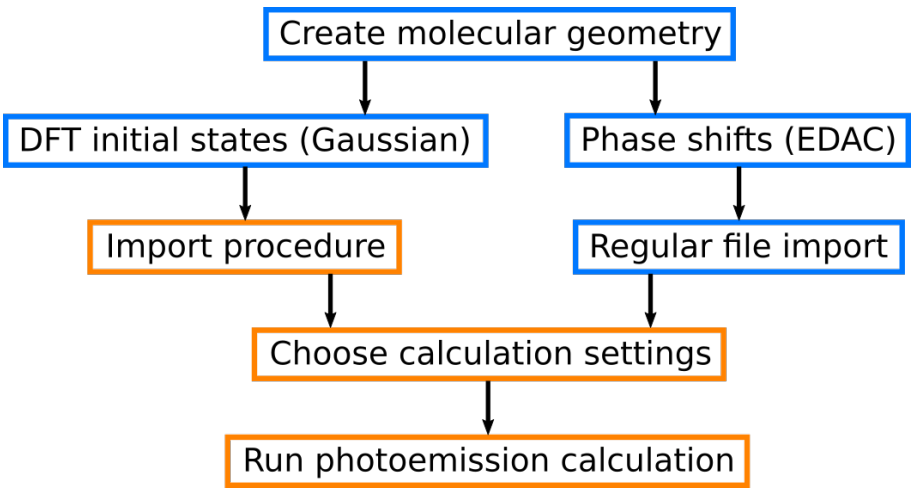

Figure A5.7: Flowchart of the entire photoemission simulation process. Blue steps are performed outside of the photoemission tool, orange ones within.

A6 Structure determination of adsorbates in multilayer films

A6.1 Photoelectron momentum maps of pentacene tilt angles

Fig. A6.1 shows the experimental, fitted PMM of the pentacene HOMO of the first (a) and second layer (b) compared to simulations for the tilted molecule for $\alpha = 6.0\,^\circ$ to $9.5\,^\circ$ (c-j) as described in subsection 6.2.4 for $E_{\mathrm{ph}} = 30\,\mathrm{eV}$.

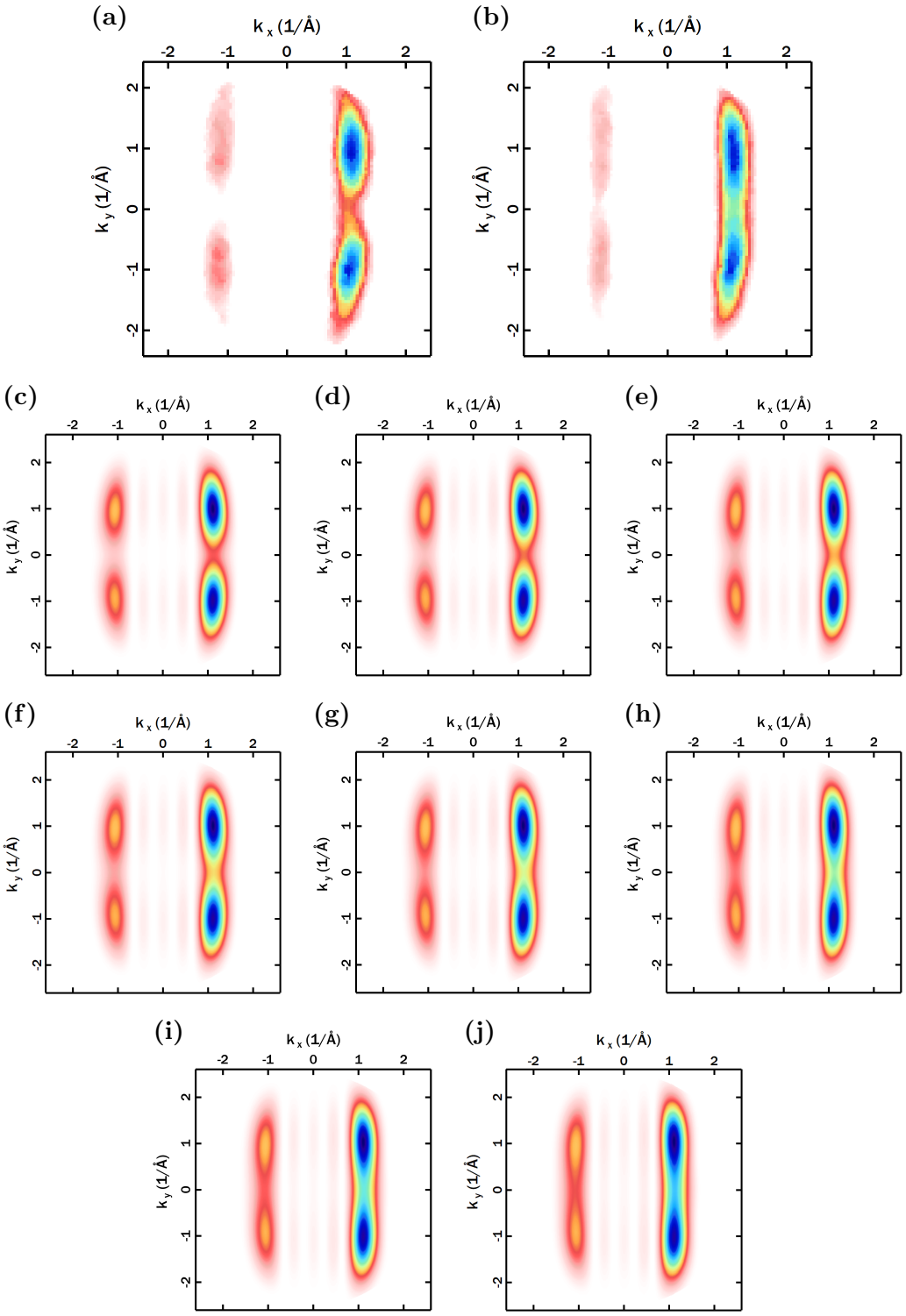

Figure A6.1: Experimental, fitted PMM of a pentacene bilayer on Ag(110) from the $HOMO_{1st}$ (a) and $HOMO_{2nd}$ (b) compared to simulations of an isolated, tilted pentacene molecule at $E_{ph} = 30\,eV$ for $\alpha = 6.0\,^\circ$ (c), $6.5\,^\circ$ (d), $7.0\,^\circ$ (e), $7.5\,^\circ$ (f), $8.0\,^\circ$ (g), $8.5\,^\circ$ (h), $9.0\,^\circ$ (i), $9.5\,^\circ$ (j).

Bibliography

[1] H. Klauk, *Organic Electronics: Materials, Manufacturing, and Applications*. John Wiley & Sons, 2006.

[2] K. T. Kamtekar, A. P. Monkman, and M. R. Bryce, "Recent Advances in White Organic Light-Emitting Materials and Devices (WOLEDs)," *Advanced Materials*, vol. 22, no. 5, pp. 572–582, 2010.

[3] Y.-L. Chang and Z.-H. Lu, "White Organic Light-Emitting Diodes for Solid-State Lighting," *Journal of Display Technology*, vol. 9, no. 6, pp. 459–468, 2013.

[4] Z. R. Li, *Organic Light-Emitting Materials and Devices*. CRC Press, 2017.

[5] M. C. Scharber, D. Mühlbacher, M. Koppe, P. Denk, C. Waldauf, A. J. Heeger, and C. J. Brabec, "Design Rules for Donors in Bulk-Heterojunction Solar Cells—Towards 10% Energy-Conversion Efficiency," *Advanced Materials*, vol. 18, no. 6, pp. 789–794, 2006.

[6] L. Meng, Y. Zhang, X. Wan, C. Li, X. Zhang, Y. Wang, X. Ke, Z. Xiao, L. Ding, R. Xia, *et al.*, "Organic and solution-processed tandem solar cells with 17.3% efficiency," *Science*, vol. 361, no. 6407, pp. 1094–1098, 2018.

[7] S. Bewick, R. Parsons, T. Forsythe, S. Robinson, and J. Dupon, *CK12 Chemistry*. CK-12 Foundation, 2020. Available at `https://www.ck12.org/book/ck-12-chemistry-concepts-intermediate/r34/section/25.1/`, last checked on 28.09.2020.

[8] J. Ziroff, F. Forster, A. Schöll, P. Puschnig, and F. Reinert, "Hybridization of organic molecular orbitals with substrate states at interfaces: PTCDA on silver," *Physical Review Letters*, vol. 104, no. 23, p. 233004, 2010.

[9] P. Puschnig, E.-M. Reinisch, T. Ules, G. Koller, S. Soubatch, M. Ostler, L. Romaner, F. S. Tautz, C. Ambrosch-Draxl, and M. G. Ramsey, "Orbital tomography: Deconvoluting photoemission spectra of organic molecules," *Physical Review B*, vol. 84, no. 23, p. 235427, 2011.

[10] M. Grimm, C. Metzger, M. Graus, M. Jugovac, G. Zamborlini, V. Feyer, A. Schöll, and F. Reinert, "Molecular orbital imaging beyond the first monolayer: Insights into

the pentacene/Ag(110) interface," *Physical Review B*, vol. 98, no. 19, p. 195412, 2018.

[11] A. M. Bradshaw and D. P. Woodruff, "Molecular orbital tomography for adsorbed molecules: is a correct description of the final state really unimportant?," *New Journal of Physics*, vol. 17, no. 1, p. 013033, 2015.

[12] C. Metzger, M. Graus, M. Grimm, G. Zamborlini, V. Feyer, M. Schwendt, D. Lüftner, P. Puschnig, A. Schöll, and F. Reinert, "Plane-wave final state for photoemission from nonplanar molecules at a metal-organic interface," *Physical Review B*, vol. 101, no. 16, p. 165421, 2020.

[13] H. Hertz, "Ueber einen Einfluss des ultravioletten Lichtes auf die electrische Entladung," *Annalen der Physik*, vol. 267, no. 8, pp. 983–1000, 1887.

[14] W. Hallwachs, "Ueber den Einfluss des Lichtes auf electrostatisch geladene Körper," *Annalen der Physik*, vol. 269, no. 2, pp. 301–312, 1888.

[15] P. Lenard, "Ueber die lichtelektrische Wirkung," *Annalen der Physik*, vol. 313, no. 5, pp. 149–198, 1902.

[16] A. Einstein, "Über einen die Erzeugung und Verwandlung des Lichtes betreffenden heuristischen Gesichtspunkt," *Annalen der Physik*, vol. 322, no. 6, pp. 132–148, 1905.

[17] S. Hüfner, *Photoelectron spectroscopy: principles and applications*. Springer Science & Business Media, 2013.

[18] S. Moser, "An experimentalist's guide to the matrix element in angle resolved photoemission," *Journal of Electron Spectroscopy and Related Phenomena*, vol. 214, pp. 29–52, 2017.

[19] F. Reinert and S. Hüfner, "Photoemission spectroscopy — from early days to recent applications," *New Journal of Physics*, vol. 7, no. 1, p. 97, 2005.

[20] K. Siegbahn, *ESCA : atomic, molecular and solid state structure studied by means of electron spectroscopy*. Almqvist and Wiksell, 1967.

[21] K. Siegbahn, *ESCA applied to free molecules*. North-Holland Publishing, 1969.

[22] M. P. Seah and W. Dench, "Quantitative electron spectroscopy of surfaces: A standard data base for electron inelastic mean free paths in solids," *Surface and Interface Analysis*, vol. 1, no. 1, pp. 2–11, 1979.

[23] T. Graber, F. Forster, A. Schöll, and F. Reinert, "Experimental determination of the attenuation length of electrons in organic molecular solids: The example of PTCDA," *Surface Science*, vol. 605, no. 9-10, pp. 878–882, 2011.

[24] A. Damascelli, "Probing the electronic structure of complex systems by ARPES," *Physica Scripta*, vol. 2004, no. T109, p. 61, 2004.

[25] A. Tejeda and D. Malterre, *A Primer in Photoemission: Concepts and Applications*. EDP sciences, 2019.

[26] O. Gunnarsson and K. Schönhammer, "Electron spectroscopies for Ce compounds in the impurity model," *Physical Review B*, vol. 28, no. 8, p. 4315, 1983.

[27] D. Malterre, M. Grioni, and Y. Baer, "Recent developments in high-energy spectroscopies of Kondo systems," *Advances in Physics*, vol. 45, no. 4, pp. 299–348, 1996.

[28] M. Dauth, M. Wiessner, V. Feyer, A. Schöll, P. Puschnig, F. Reinert, and S. Kümmel, "Angle resolved photoemission from organic semiconductors: orbital imaging beyond the molecular orbital interpretation," *New Journal of Physics*, vol. 16, no. 10, p. 103005, 2014.

[29] E. Schrödinger, "An undulatory theory of the mechanics of atoms and molecules," *Physical Review*, vol. 28, no. 6, p. 1049, 1926.

[30] C. Fiolhais, F. Nogueira, and M. A. Marques, *A primer in density functional theory*, vol. 620. Springer Science & Business Media, 2003.

[31] K. Capelle, "A bird's-eye view of density-functional theory," *Brazilian Journal of Physics*, vol. 36, no. 4A, pp. 1318–1343, 2006.

[32] P. Fulde, *Electron Correlations in Molecules and Solids*, vol. 100. Springer Science & Business Media, 2012.

[33] W. Kohn, "Nobel Lecture: Electronic structure of matter—wave functions and density functionals," *Reviews of Modern Physics*, vol. 71, no. 5, p. 1253, 1999.

[34] W. Kohn and L. J. Sham, "Self-consistent equations including exchange and correlation effects," *Physical Review*, vol. 140, no. 4A, p. A1133, 1965.

[35] J. E. Lennard-Jones, "The electronic structure of some diatomic molecules," *Transactions of the Faraday Society*, vol. 25, pp. 668–686, 1929.

[36] R. A. Evarestov, *Quantum chemistry of solids: LCAO treatment of crystals and nanostructures*, vol. 153. Springer Science & Business Media, 2013.

[37] C. A. Ullrich, *Time-dependent density-functional theory: concepts and applications*. OUP Oxford, 2011.

[38] M. Dauth, M. Graus, I. Schelter, M. Wießner, A. Schöll, F. Reinert, and S. Kümmel, "Perpendicular emission, dichroism, and energy dependence in angle-resolved photoemission: The importance of the final state," *Physical Review Letters*, vol. 117,

no. 18, p. 183001, 2016.

[39] W. D. Grobman, "Angle-resolved photoemission from molecules in the independent-atomic-center approximation," *Physical Review B*, vol. 17, no. 12, p. 4573, 1978.

[40] P. Puschnig, S. Berkebile, A. J. Fleming, G. Koller, K. Emtsev, T. Seyller, J. D. Riley, C. Ambrosch-Draxl, F. P. Netzer, and M. G. Ramsey, "Reconstruction of molecular orbital densities from photoemission data," *Science*, vol. 326, no. 5953, pp. 702–706, 2009.

[41] R. Mehrem, "The plane wave expansion, infinite integrals and identities involving spherical Bessel functions," *Applied Mathematics and Computation*, vol. 217, no. 12, pp. 5360–5365, 2011.

[42] L. D. Landau and E. M. Lifshitz, *Quantum mechanics: non-relativistic theory*, vol. 3. Elsevier, 2013.

[43] S. Gozem, A. O. Gunina, T. Ichino, D. L. Osborn, J. F. Stanton, and A. I. Krylov, "Photoelectron wave function in photoionization: Plane wave or Coulomb wave?," *The Journal of Physical Chemistry Letters*, vol. 6, no. 22, pp. 4532–4540, 2015.

[44] C. L. Lamont and J. Wilkes, "Attenuation length of electrons in self-assembled monolayers of n-alkanethiols on gold," *Langmuir*, vol. 15, no. 6, pp. 2037–2042, 1999.

[45] A. Liebsch, "Theory of photoemission from localized adsorbate levels," *Physical Review B*, vol. 13, no. 2, p. 544, 1976.

[46] S. Hasegawa, S. Tanaka, Y. Yamashita, H. Inokuchi, H. Fujimoto, K. Kamiya, K. Seki, and N. Ueno, "Molecular orientation in thin films of bis (1, 2, 5-thiadiazolo)-p-quinobis (1, 3-dithiole) on graphite studied by angle-resolved photoelectron spectroscopy," *Physical Review B*, vol. 48, no. 4, p. 2596, 1993.

[47] S. Hasegawa, T. Miyamae, K. Yakushi, H. Inokuchi, K. Seki, and N. Ueno, "Origin of the photoemission intensity oscillation of C60," *Physical Review B*, vol. 58, no. 8, p. 4927, 1998.

[48] J. W. Gadzuk, "Surface molecules and chemisorption. II. Photoemission angular distributions," *Physical Review B*, vol. 10, no. 12, p. 5030, 1974.

[49] S. Goldberg, C. Fadley, and S. Kono, "Photoelectric cross-sections for fixed-orientation atomic orbitals: Relationship to the plane-wave final state approximation and angle-resolved photoemission," *Solid State Communications*, vol. 28, no. 6, pp. 459–463, 1978.

[50] N. Richardson, "Comments on angle-resolved photoemission from oriented films of lead phthalocyanine on a Cu100 surface," *Chemical Physics Letters*, vol. 102, no. 4,

pp. 390–391, 1983.

[51] M. Wießner, D. Hauschild, A. Schöll, F. Reinert, V. Feyer, K. Winkler, and B. Krömker, "Electronic and geometric structure of the PTCDA/Ag (110) interface probed by angle-resolved photoemission," *Physical Review B*, vol. 86, no. 4, p. 045417, 2012.

[52] B. Stadtmüller, M. Willenbockel, E. Reinisch, T. Ules, F. Bocquet, S. Soubatch, P. Puschnig, G. Koller, M. Ramsey, F. Tautz, *et al.*, "Orbital tomography for highly symmetric adsorbate systems," *EPL (Europhysics Letters)*, vol. 100, no. 2, p. 26008, 2012.

[53] V. Feyer, M. Graus, P. Nigge, M. Wießner, R. Acres, C. Wiemann, C. Schneider, A. Schöll, and F. Reinert, "Adsorption geometry and electronic structure of iron phthalocyanine on Ag surfaces: A LEED and photoelectron momentum mapping study," *Surface Science*, vol. 621, pp. 64–68, 2014.

[54] K. Kambe and M. Scheffler, "Theory of photoexcitation of adsorbates: An analysis of atomic, adlayer, and substrate effects," *Surface Science*, vol. 89, no. 1-3, pp. 262–273, 1979.

[55] S. Goldberg, C. Fadley, and S. Kono, "Photoionization cross-sections for atomic orbitals with random and fixed spatial orientation," *Journal of Electron Spectroscopy and Related Phenomena*, vol. 21, no. 4, pp. 285–363, 1981.

[56] M. Wießner, D. Hauschild, C. Sauer, V. Feyer, A. Schöll, and F. Reinert, "Complete determination of molecular orbitals by measurement of phase symmetry and electron density," *Nature Communications*, vol. 5, p. 4156, 2014.

[57] D. Lüftner, S. Weiß, X. Yang, P. Hurdax, V. Feyer, A. Gottwald, G. Koller, S. Soubatch, P. Puschnig, M. G. Ramsey, *et al.*, "Understanding the photoemission distribution of strongly interacting two-dimensional overlayers," *Physical Review B*, vol. 96, no. 12, p. 125402, 2017.

[58] M. Dauth, T. Körzdörfer, S. Kümmel, J. Ziroff, M. Wiessner, A. Schöll, F. Reinert, M. Arita, and K. Shimada, "Orbital density reconstruction for molecules," *Physical Review Letters*, vol. 107, no. 19, p. 193002, 2011.

[59] M. Wießner, N. R. Lastra, J. Ziroff, F. Forster, P. Puschnig, L. Dössel, K. Müllen, A. Schöll, and F. Reinert, "Different views on the electronic structure of nanoscale graphene: aromatic molecule versus quantum dot," *New Journal of Physics*, vol. 14, no. 11, p. 113008, 2012.

[60] M. Willenbockel, B. Stadtmüller, K. Schönauer, F. Bocquet, D. Lüftner, E. Reinisch, T. Ules, G. Koller, C. Kumpf, S. Soubatch, *et al.*, "Energy offsets within a molecular

monolayer: the influence of the molecular environment," *New Journal of Physics*, vol. 15, no. 3, p. 033017, 2013.

[61] S. Weiß, D. Lüftner, T. Ules, E. Reinisch, H. Kaser, A. Gottwald, M. Richter, S. Soubatch, G. Koller, M. Ramsey, *et al.*, "Exploring three-dimensional orbital imaging with energy-dependent photoemission tomography," *Nature Communications*, vol. 6, p. 8287, 2015.

[62] P. Kliuiev, T. Latychevskaia, G. Zamborlini, M. Jugovac, C. Metzger, M. Grimm, A. Schöll, J. Osterwalder, M. Hengsberger, and L. Castiglioni, "Algorithms and image formation in orbital tomography," *Physical Review B*, vol. 98, no. 8, p. 085426, 2018.

[63] D. Lüftner, T. Ules, E. M. Reinisch, G. Koller, S. Soubatch, F. S. Tautz, M. G. Ramsey, and P. Puschnig, "Imaging the wave functions of adsorbed molecules," *Proceedings of the National Academy of Sciences*, vol. 111, no. 2, pp. 605–610, 2014.

[64] J. Miao, P. Charalambous, J. Kirz, and D. Sayre, "Extending the methodology of X-ray crystallography to allow imaging of micrometre-sized non-crystalline specimens," *Nature*, vol. 400, no. 6742, pp. 342–344, 1999.

[65] R. Harder, M. Liang, Y. Sun, Y. Xia, and I. Robinson, "Imaging of complex density in silver nanocubes by coherent x-ray diffraction," *New Journal of Physics*, vol. 12, no. 3, p. 035019, 2010.

[66] J. R. Fienup, "Phase retrieval algorithms: a comparison," *Applied Optics*, vol. 21, no. 15, pp. 2758–2769, 1982.

[67] S. Marchesini, "Invited article: A unified evaluation of iterative projection algorithms for phase retrieval," *Review of Scientific Instruments*, vol. 78, no. 1, p. 011301, 2007.

[68] P. Kliuiev, T. Latychevskaia, J. Osterwalder, M. Hengsberger, and L. Castiglioni, "Application of iterative phase-retrieval algorithms to ARPES orbital tomography," *New Journal of Physics*, vol. 18, no. 9, p. 093041, 2016.

[69] J. R. Fienup, "Reconstruction of an object from the modulus of its Fourier transform," *Optics Letters*, vol. 3, no. 1, pp. 27–29, 1978.

[70] S. Marchesini, H. He, H. N. Chapman, S. P. Hau-Riege, A. Noy, M. R. Howells, U. Weierstall, and J. C. Spence, "X-ray image reconstruction from a diffraction pattern alone," *Physical Review B*, vol. 68, no. 14, p. 140101, 2003.

[71] J. Miao, D. Sayre, and H. Chapman, "Phase retrieval from the magnitude of the Fourier transforms of nonperiodic objects," *JOSA A*, vol. 15, no. 6, pp. 1662–1669, 1998.

[72] J. Miao, T. Ishikawa, E. H. Anderson, and K. O. Hodgson, "Phase retrieval of diffraction patterns from noncrystalline samples using the oversampling method," *Physical Review B*, vol. 67, no. 17, p. 174104, 2003.

[73] M. Graus, C. Metzger, M. Grimm, P. Nigge, V. Feyer, A. Schöll, and F. Reinert, "Three-dimensional tomographic imaging of molecular orbitals by photoelectron momentum microscopy," *The European Physical Journal B*, vol. 92, no. 4, p. 80, 2019.

[74] M. A. VanHove, W. H. Weinberg, and C.-M. Chan, *Low-energy electron diffraction: experiment, theory and surface structure determination*, vol. 6. Springer Science & Business Media, 2012.

[75] L. De Broglie, "Waves and quanta," *Nature*, vol. 112, no. 2815, pp. 540–540, 1923.

[76] W. P. Davey, "Precision measurements of the lattice constants of twelve common metals," *Physical Review*, vol. 25, no. 6, p. 753, 1925.

[77] P. Bayersdorfer, "Spot-Plotter Version 1.2.1.4," 2008. Available at `https://spot-plotter.software.informer.com`, last checked on 28.09.2020.

[78] M. I. Haftel, "Surface reconstruction of platinum and gold and the embedded-atom model," *Physical Review B*, vol. 48, no. 4, p. 2611, 1993.

[79] J. F. Moulder, W. F. Stickle, P. E. Sobol, and K. D. Bomben, "Handbook of X-ray photoelectron spectroscopy," 1992.

[80] S. Söhnchen, S. Lukas, and G. Witte, "Epitaxial growth of pentacene films on Cu (110)," *The Journal of Chemical Physics*, vol. 121, no. 1, pp. 525–534, 2004.

[81] C. Tusche, A. Krasyuk, and J. Kirschner, "Spin resolved bandstructure imaging with a high resolution momentum microscope," *Ultramicroscopy*, vol. 159, pp. 520–529, 2015.

[82] F. Hadjarab and J. L. Erskine, "Image properties of the hemispherical analyzer applied to multichannel energy detection," *Journal of Electron Spectroscopy and Related Phenomena*, vol. 36, no. 3, pp. 227–243, 1985.

[83] M. Escher, N. Weber, M. Merkel, C. Ziethen, P. Bernhard, G. Schönhense, S. Schmidt, F. Forster, F. Reinert, B. Krömker, *et al.*, "NanoESCA: a novel energy filter for imaging x-ray photoemission spectroscopy," *Journal of Physics: Condensed Matter*, vol. 17, no. 16, p. S1329, 2005.

[84] J. Kirschner, F. Giebels, H. Gollisch, and R. Feder, "Spin-polarized electron scattering from pseudomorphic Au on Ir (001)," *Physical Review B*, vol. 88, no. 12, p. 125419, 2013.

[85] M. Seah, "XPS reference procedure for the accurate intensity calibration of electron spectrometers—results of a BCR intercomparison co-sponsored by the VAMAS SCA TWA," *Surface and Interface Analysis*, vol. 20, no. 3, pp. 243–266, 1993.

[86] G. Drera, G. Salvinelli, J. Åhlund, P. Karlsson, B. Wannberg, E. Magnano, S. Nappini, and L. Sangaletti, "Transmission function calibration of an angular resolved analyzer for X-ray photoemission spectroscopy: Theory vs experiment," *Journal of Electron Spectroscopy and Related Phenomena*, vol. 195, pp. 109–116, 2014.

[87] R. Hesse, P. Streubel, and R. Szargan, "Improved accuracy of quantitative XPS analysis using predetermined spectrometer transmission functions with UNIFIT 2004," *Surface and Interface Analysis*, vol. 37, no. 7, pp. 589–607, 2005.

[88] H.-J. Hagemann, W. Gudat, and C. Kunz, "Optical constants from the far infrared to the x-ray region: Mg, Al, Cu, Ag, Au, Bi, C, and Al2O3," *JOSA*, vol. 65, no. 6, pp. 742–744, 1975.

[89] B. L. Henke, E. M. Gullikson, and J. C. Davis, "X-ray interactions: photoabsorption, scattering, transmission and reflection E=50-30,000 eV, Z=1-92," *Atomic Data and Nuclear Data Tables*, vol. 54, no. 2, 1993.

[90] B. Henke, J. Davis, E. Gullikson, and R. Perera, "A preliminary report on x-ray photoabsorption coefficients and atomic scattering factors for 92 elements in the 10–10,000 eV region," tech. rep., Lawrence Berkeley Lab., 1988.

[91] B. L. Henke, J. Knauer, and K. Premaratne, "The characterization of x-ray photocathodes in the 0.1–10-keV photon energy region," *Journal of Applied Physics*, vol. 52, no. 3, pp. 1509–1520, 1981.

[92] A. Owens, S. Bayliss, G. Fraser, and S. Gurman, "On the relationship between total electron photoyield and X-ray absorption coefficient," *Nuclear Instruments and Methods in Physics Research Section A: Accelerators, Spectrometers, Detectors and Associated Equipment*, vol. 385, no. 3, pp. 556–558, 1997.

[93] A. Gerlach, G. Meister, R. Matzdorf, and A. Goldmann, "High-resolution photoemission study of the $\bar{\mathrm{Y}}$ surface state on Ag (110)," *Surface Science*, vol. 443, no. 3, pp. 221–226, 1999.

[94] E. Bauer, "The resolution of the low energy electron reflection microscope," *Ultramicroscopy*, vol. 17, no. 1, pp. 51–56, 1985.

[95] P. Krüger, "Photoelectron diffraction from valence states of oriented molecules," *Journal of the Physical Society of Japan*, vol. 87, no. 6, p. 061007, 2018.

[96] J. Minár, J. Braun, S. Mankovsky, and H. Ebert, "Calculation of angle-resolved photo emission spectra within the one-step model of photo emission—Recent de-

velopments," *Journal of Electron Spectroscopy and Related Phenomena*, vol. 184, no. 3-6, pp. 91–99, 2011.

[97] J. Faye, "Copenhagen Interpretation of Quantum Mechanics," in *The Stanford Encyclopedia of Philosophy* (E. N. Zalta, ed.), Metaphysics Research Lab, Stanford University, winter 2019 ed., 2019.

[98] S. Siddiqui and C. Singh, "How diverse are physics instructors' attitudes and approaches to teaching undergraduate level quantum mechanics?," *European Journal of Physics*, vol. 38, no. 3, p. 035703, 2017.

[99] W. E. Schwarz, "Measuring orbitals: provocation or reality?," *Angewandte Chemie International Edition*, vol. 45, no. 10, pp. 1508–1517, 2006.

[100] J. Repp, G. Meyer, S. M. Stojković, A. Gourdon, and C. Joachim, "Molecules on insulating films: scanning-tunneling microscopy imaging of individual molecular orbitals," *Physical Review Letters*, vol. 94, no. 2, p. 026803, 2005.

[101] F. G. de Abajo, M. Van Hove, and C. Fadley, "Electron Diffraction in Atomic Clusters (EDAC)," 1999. Available at `http://garciadeabajos-group.icfo.es/widgets/edac/`, last checked on 28.09.2020.

[102] H. Klauk, M. Halik, U. Zschieschang, G. Schmid, W. Radlik, and W. Weber, "High-mobility polymer gate dielectric pentacene thin film transistors," *Journal of Applied Physics*, vol. 92, no. 9, pp. 5259–5263, 2002.

[103] M. Klues and G. Witte, "Crystalline packing in pentacene-like organic semiconductors," *CrystEngComm*, vol. 20, no. 1, pp. 63–74, 2018.

[104] D. Lubert-Perquel, E. Salvadori, M. Dyson, P. N. Stavrinou, R. Montis, H. Nagashima, Y. Kobori, S. Heutz, and C. W. Kay, "Identifying triplet pathways in dilute pentacene films," *Nature Communications*, vol. 9, no. 1, pp. 1–10, 2018.

[105] P. Guaino, D. Carty, G. Hughes, O. McDonald, and A. Cafolla, "Long-range order in a multilayer organic film templated by a molecular-induced surface reconstruction: Pentacene on Au (110)," *Applied Physics Letters*, vol. 85, no. 14, pp. 2777–2779, 2004.

[106] R. Ruiz, D. Choudhary, B. Nickel, T. Toccoli, K.-C. Chang, A. C. Mayer, P. Clancy, J. M. Blakely, R. L. Headrick, S. Iannotta, *et al.*, "Pentacene thin film growth," *Chemistry of Materials*, vol. 16, no. 23, pp. 4497–4508, 2004.

[107] F.-J. M. Zu Heringdorf, M. Reuter, and R. Tromp, "Growth dynamics of pentacene thin films," *Nature*, vol. 412, no. 6846, pp. 517–520, 2001.

[108] W. H. Mills and M. Mills, "CCXXX.—The synthetical production of derivatives of dinaphthanthracene," *Journal of the Chemical Society, Transactions*, vol. 101,

pp. 2194–2208, 1912.

[109] S. Yoo, B. Domercq, and B. Kippelen, "Efficient thin-film organic solar cells based on pentacene/C 60 heterojunctions," *Applied Physics Letters*, vol. 85, no. 22, pp. 5427–5429, 2004.

[110] A. K. Pandey and J.-M. Nunzi, "Efficient flexible and thermally stable pentacene/C 60 small molecule based organic solar cells," *Applied Physics Letters*, vol. 89, no. 21, p. 213506, 2006.

[111] J. Yang and T.-Q. Nguyen, "Effects of thin film processing on pentacene/C60 bilayer solar cell performance," *Organic Electronics*, vol. 8, no. 5, pp. 566–574, 2007.

[112] X. Zhang, M. Li, C. Dall'Agnese, G. Chen, X.-F. Wang, and T. Miyasaka, "Thermo-evaporated pentacene and perylene as hole transport materials for perovskite solar cells," *Dyes and Pigments*, vol. 160, pp. 285–291, 2019.

[113] S. Wang, T. Miyadera, T. Minari, Y. Aoyagi, and K. Tsukagoshi, "Correlation between grain size and device parameters in pentacene thin film transistors," *Applied Physics Letters*, vol. 93, no. 4, p. 282, 2008.

[114] M. F. Mabrook, Y. Yun, C. Pearson, D. A. Zeze, and M. C. Petty, "A pentacene-based organic thin film memory transistor," *Applied Physics Letters*, vol. 94, no. 17, p. 122, 2009.

[115] J. H. Lee, Y. Seo, Y. D. Park, J. E. Anthony, D. H. Kwak, J. A. Lim, S. Ko, H. W. Jang, K. Cho, and W. H. Lee, "Effect of crystallization modes in TIPS-pentacene/insulating polymer blends on the gas sensing properties of organic field-effect transistors," *Scientific Reports*, vol. 9, no. 1, pp. 1–9, 2019.

[116] F. Yakuphanoglu and W. A. Farooq, "Flexible pentacene organic field-effect phototransistor," *Synthetic Metals*, vol. 161, no. 5-6, pp. 379–383, 2011.

[117] S. Lee, H. Seong, S. G. Im, H. Moon, and S. Yoo, "Organic flash memory on various flexible substrates for foldable and disposable electronics," *Nature Communications*, vol. 8, no. 1, pp. 1–9, 2017.

[118] D. W. Kim, S.-Y. Min, Y. Lee, and U. Jeong, "Transparent Flexible Nanoline Field-Effect Transistor (NL-FET) Array with High-Integration in Large-Area," *ACS Nano*, 2020.

[119] N. Onojima, Y. Mori, T. Ozawa, T. Sugai, N. Akiyama, and S. Obata, "Flexible organic field-effect transistors based on 6, 13-bis (triisopropylsilylethynyl) pentacene/polystyrene blend film prepared by electrostatic spray deposition," *Japanese Journal of Applied Physics*, vol. 59, no. SD, p. SDDA13, 2020.

[120] X. Hou, Y. Xia, S. C. Ng, J. Zhang, and J. S. Chang, "Formulation of novel screen-printable dielectric ink for fully-printed TIPs-pentacene OFETs," *RSC Advances*, vol. 4, no. 71, pp. 37687–37690, 2014.

[121] F. Shiono, H. Abe, T. Nagase, T. Kobayashi, and H. Naito, "Optical memory characteristics of solution-processed organic transistors with self-organized organic floating gates for printable multi-level storage devices," *Organic Electronics*, vol. 67, pp. 109–115, 2019.

[122] W. Tang, Y. Huang, L. Han, R. Liu, Y. Su, X. Guo, and F. Yan, "Recent progress in printable organic field effect transistors," *Journal of Materials Chemistry C*, vol. 7, no. 4, pp. 790–808, 2019.

[123] C. Schneider, C. Wiemann, M. Patt, V. Feyer, L. Plucinski, I. Krug, M. Escher, N. Weber, M. Merkel, O. Renault, *et al.*, "Expanding the view into complex material systems: From micro-ARPES to nanoscale HAXPES," *Journal of Electron Spectroscopy and Related Phenomena*, vol. 185, no. 10, pp. 330–339, 2012.

[124] R. Koch, S. Moser, S. Ulstrup, L. Moreschini, C. Jozwiak, A. Bostwick, and E. Rotenberg, "The new nanoARPES at MAESTRO of the ALS," *Bulletin of the American Physical Society*, vol. 62, 2017.

[125] B. Rösner, P. Dudin, J. Bosgra, M. Hoesch, and C. David, "Zone plates for angle-resolved photoelectron spectroscopy providing sub-micrometre resolution in the extreme ultraviolet regime," *Journal of Synchrotron Radiation*, vol. 26, no. 2, 2019.

[126] R. Tromp, "Selected-area diffraction and spectroscopy in LEEM and PEEM," *Ultramicroscopy*, vol. 120, pp. 73–77, 2012.

[127] MaTecK – Material-Technologie und Kristalle GmbH, "Silver single crystal," 2020. Available at `https://mateck.com/info/silver-single-crystal-47ag107-870.html`, last checked on 28.09.2020.

[128] MTI Corporation, "Gold(111) single crystal," 2020. Available at `https://www.mtixtl.com/MC-Au-c-101005-S1.aspx`, last checked on 28.09.2020.

[129] P. Heimann, H. Neddermeyer, and H. Roloff, "Ultraviolet photoemission for intrinsic surface states of the noble metals," *Journal of Physics C: Solid State Physics*, vol. 10, no. 1, p. L17, 1977.

[130] A. McLachlan, J. Liesegang, R. Leckey, and J. Jenkin, "40.81-eV photoelectron study of Cu, Ag, and Au surfaces," *Physical Review B*, vol. 11, no. 8, p. 2877, 1975.

[131] Y. Wang, W. Ji, D. Shi, S. Du, C. Seidel, Y. Ma, H.-J. Gao, L. Chi, and H. Fuchs, "Structural evolution of pentacene on a Ag (110) surface," *Physical Review B*, vol. 69, no. 7, p. 075408, 2004.

[132] K. Glöckler, C. Seidel, A. Soukopp, M. Sokolowski, E. Umbach, M. Böhringer, R. Berndt, and W.-D. Schneider, "Highly ordered structures and submolecular scanning tunnelling microscopy contrast of PTCDA and DM-PBDCI monolayers on Ag (111) and Ag (110)," *Surface Science*, vol. 405, no. 1, pp. 1–20, 1998.

[133] G. Panaccione, G. Cautero, M. Cautero, A. Fondacaro, M. Grioni, P. Lacovig, G. Monaco, F. Offi, G. Paolicelli, M. Sacchi, *et al.*, "High-energy photoemission in silver: resolving d and sp contributions in valence band spectra," *Journal of Physics: Condensed Matter*, vol. 17, no. 17, p. 2671, 2005.

[134] L. Giovanelli, F. Bocquet, P. Amsalem, H.-L. Lee, M. Abel, S. Clair, M. Koudia, T. Faury, L. Petaccia, D. Topwal, *et al.*, "Interpretation of valence band photoemission spectra at organic-metal interfaces," *Physical Review B*, vol. 87, no. 3, p. 035413, 2013.

[135] C. Wiemann, M. Patt, I. P. Krug, N. B. Weber, M. Escher, M. Merkel, and C. M. Schneider, "A new nanospectroscopy tool with synchrotron radiation: NanoESCA@ Elettra," *e-Journal of Surface Science and Nanotechnology*, vol. 9, pp. 395–399, 2011.

[136] A. Mugarza, R. Robles, C. Krull, R. Korytár, N. Lorente, and P. Gambardella, "Electronic and magnetic properties of molecule-metal interfaces: Transition-metal phthalocyanines adsorbed on Ag (100)," *Physical Review B*, vol. 85, no. 15, p. 155437, 2012.

[137] M. Graus, C. Metzger, M. Grimm, V. Feyer, P. Puschnig, A. Schöll, and F. Reinert, "Degeneracy lifting of adsorbate orbitals imaged by high-resolution momentum microscopy," *Journal of the Physical Society of Japan*, vol. 87, no. 6, p. 061009, 2018.

[138] S. Erker and O. T. Hofmann, "Fractional and Integer Charge Transfer at Semiconductor/Organic Interfaces: The Role of Hybridization and Metallicity," *The Journal of Physical Chemistry Letters*, vol. 10, no. 4, pp. 848–854, 2019.

[139] A. D. Becke, "Density-functional thermochemistry. III. The role of exact exchange," *The Journal of Chemical Physics*, vol. 98, no. 7, pp. 5648–5652, 1993.

[140] C. Lee, W. Yang, and R. G. Parr, "Development of the Colle-Salvetti correlation-energy formula into a functional of the electron density," *Physical Review B*, vol. 37, no. 2, p. 785, 1988.

[141] H. Bentmann, H. Maaß, E. E. Krasovskii, T. R. Peixoto, C. Seibel, M. Leandersson, T. Balasubramanian, and F. Reinert, "Strong linear dichroism in spin-polarized photoemission from spin-orbit-coupled surface states," *Physical Review*

Letters, vol. 119, no. 10, p. 106401, 2017.

[142] Scienta Omicron GmbH, "Computer Ethernet Rack upgrade," 2019. `https://www.scientaomicron.com/Services%26Support/ServiceUpgrades/ESPEC/ComputerEthernetRack.pdf`, last checked on 22.01.2020.

[143] WaveMetrics, Inc., "IGOR Pro 6," 2013.

[144] WaveMetrics, Inc., "IGOR Pro 8," 2018.

[145] M. Frisch, G. Trucks, H. Schlegel, G. Scuseria, M. Robb, J. Cheeseman, G. Scalmani, V. Barone, B. Mennucci, G. Petersson, *et al.*, "Gaussian, Inc., Wallingford CT, Gaussian 09 (Revision A.02)," *Inc., Wallingford CT*, 2009.

[146] M. Frisch, G. Trucks, H. Schlegel, G. Scuseria, M. Robb, J. Cheeseman, G. Scalmani, V. Barone, G. Petersson, H. Nakatsuji, *et al.*, "Gaussian, Inc., Wallingford CT, Gaussian 16 (Revision C.01)," *Inc., Wallingford CT*, 2016.

[147] P. Kliuiev, G. Zamborlini, M. Jugovac, Y. Gurdal, K. von Arx, K. Waltar, S. Schnidrig, R. Alberto, M. Iannuzzi, V. Feyer, *et al.*, "Combined orbital tomography study of multi-configurational molecular adsorbate systems," *Nature Communications*, vol. 10, 2019.

[148] M. Willenbockel, D. Lüftner, B. Stadtmüller, G. Koller, C. Kumpf, S. Soubatch, P. Puschnig, M. Ramsey, and F. Tautz, "The interplay between interface structure, energy level alignment and chemical bonding strength at organic–metal interfaces," *Physical Chemistry Chemical Physics*, vol. 17, no. 3, pp. 1530–1548, 2015.

[149] N. Koch, "Energy levels at interfaces between metals and conjugated organic molecules," *Journal of Physics: Condensed Matter*, vol. 20, no. 18, p. 184008, 2008.

[150] S. Duhm, A. Gerlach, I. Salzmann, B. Bröker, R. Johnson, F. Schreiber, and N. Koch, "PTCDA on Au (1 1 1), Ag (1 1 1) and Cu (1 1 1): Correlation of interface charge transfer to bonding distance," *Organic Electronics*, vol. 9, no. 1, pp. 111–118, 2008.

[151] A. Schöll, L. Kilian, Y. Zou, J. Ziroff, S. Hame, F. Reinert, E. Umbach, and R. Fink, "Disordering of an organic overlayer on a metal surface upon cooling," *Science*, vol. 329, no. 5989, pp. 303–305, 2010.

[152] M. Marks, N. L. Zaitsev, B. Schmidt, C. Schwalb, A. Schöll, I. Nechaev, P. Echenique, E. Chulkov, and U. Höfer, "Energy shift and wave function overlap of metal-organic interface states," *Physical Review B*, vol. 84, no. 8, p. 081301, 2011.

[153] S. Duhm, C. Bürker, J. Niederhausen, I. Salzmann, T. Hosokai, J. Duvernay, S. Kera, F. Schreiber, N. Koch, N. Ueno, *et al.*, "Pentacene on Ag (111): Correla-

tion of Bonding Distance with Intermolecular Interaction and Order," *ACS Applied Materials & Interfaces*, vol. 5, no. 19, pp. 9377–9381, 2013.

[154] Q. Guo, Y. Xu, B. Xiao, B. Zhang, E. Zhou, F. Wang, Y. Bai, T. Hayat, A. Alsaedi, and Z. Tan, "Effect of energy alignment, electron mobility, and film morphology of perylene diimide based polymers as electron transport layer on the performance of perovskite solar cells," *ACS Applied Materials & Interfaces*, vol. 9, no. 12, pp. 10983–10991, 2017.

[155] S. Ogawa, R. Narushima, and Y. Arai, "Aza macrocycle that selectively binds lithium ion with color change," *Journal of the American Chemical Society*, vol. 106, no. 19, pp. 5760–5762, 1984.

[156] S. Ogawa, T. Uchida, T. Uchiya, T. Hirano, M. Saburi, and Y. Uchidac, "Lithium complexation of configurational isomers of tetra-aza macrocycle containing 2, 2-bipyridine. X-Ray molecular structure of the trans-isomer of a dibutyl dicyano macrocycle," *Journal of the Chemical Society, Perkin Transactions 1*, no. 6, pp. 1649–1653, 1990.

[157] Y. Gurdal, S. Luber, J. Hutter, and M. Iannuzzi, "Non-innocent adsorption of Co-pyrphyrin on rutile (110)," *Physical Chemistry Chemical Physics*, vol. 17, no. 35, pp. 22846–22854, 2015.

[158] E. Joliat, S. Schnidrig, B. Probst, C. Bachmann, B. Spingler, K. K. Baldridge, F. von Rohr, A. Schilling, and R. Alberto, "Cobalt complexes of tetradentate, bipyridine-based macrocycles: their structures, properties and photocatalytic proton reduction," *Dalton Transactions*, vol. 45, no. 4, pp. 1737–1745, 2016.

[159] G. Mette, D. Sutter, Y. Gurdal, S. Schnidrig, B. Probst, M. Iannuzzi, J. Hutter, R. Alberto, and J. Osterwalder, "From porphyrins to pyrphyrins: adsorption study and metalation of a molecular catalyst on Au (111)," *Nanoscale*, vol. 8, no. 15, pp. 7958–7968, 2016.

[160] S. Losse, J. G. Vos, and S. Rau, "Catalytic hydrogen production at cobalt centres," *Coordination Chemistry Reviews*, vol. 254, no. 21-22, pp. 2492–2504, 2010.

[161] J. Venables and G. Spiller, "Nucleation and growth of thin films," in *Surface Mobilities on Solid Materials*, pp. 341–404, Springer, 1983.

[162] Z. Zhang and M. G. Lagally, "Atomistic processes in the early stages of thin-film growth," *Science*, vol. 276, no. 5311, pp. 377–383, 1997.

[163] C. Westphal, "The study of the local atomic structure by means of X-ray photoelectron diffraction," *Surface Science Reports*, vol. 50, no. 1-3, pp. 1–106, 2003.

[164] S. Eich, A. Stange, A. Carr, J. Urbancic, T. Popmintchev, M. Wiesenmayer, K. Jansen, A. Ruffing, S. Jakobs, T. Rohwer, *et al.*, "Time-and angle-resolved photoemission spectroscopy with optimized high-harmonic pulses using frequency-doubled Ti: Sapphire lasers," *Journal of Electron Spectroscopy and Related Phenomena*, vol. 195, pp. 231–236, 2014.

[165] Y. Liu, J. E. Beetar, M. M. Hosen, G. Dhakal, C. Sims, F. Kabir, M. B. Etienne, K. Dimitri, S. Regmi, Y. Liu, *et al.*, "Extreme ultraviolet time-and angle-resolved photoemission setup with 21.5 meV resolution using high-order harmonic generation from a turn-key Yb: KGW amplifier," *Review of Scientific Instruments*, vol. 91, no. 1, p. 013102, 2020.

[166] A. Damascelli, D. J. Jones, and A. K. Mills, "Cavity-enhanced high-harmonic generation for XUV time-resolved ARPES: quantitative determination electron-phonon coupling in the time domain (Conference Presentation)," in *Ultrafast Phenomena and Nanophotonics XXIV*, vol. 11278, p. 1127818, International Society for Optics and Photonics, 2020.

[167] J. Rossbach, J. R. Schneider, and W. Wurth, "10 years of pioneering X-ray science at the Free-Electron Laser FLASH at DESY," *Physics Reports*, vol. 808, pp. 1–74, 2019.

[168] D. Kutnyakhov, R. P. Xian, M. Dendzik, M. Heber, F. Pressacco, S. Y. Agustsson, L. Wenthaus, H. Meyer, S. Gieschen, G. Mercurio, *et al.*, "Time-and momentum-resolved photoemission studies using time-of-flight momentum microscopy at a free-electron laser," *Review of Scientific Instruments*, vol. 91, no. 1, p. 013109, 2020.

[169] M. A. Newton, D. Ferri, G. Smolentsev, V. Marchionni, and M. Nachtegaal, "Room-temperature carbon monoxide oxidation by oxygen over Pt/Al2O3 mediated by reactive platinum carbonates," *Nature Communications*, vol. 6, no. 1, pp. 1–7, 2015.

[170] M. A. Van Spronsen, J. W. Frenken, and I. M. Groot, "Observing the oxidation of platinum," *Nature Communications*, vol. 8, no. 1, pp. 1–7, 2017.

[171] J. Neugebohren, D. Borodin, H. W. Hahn, J. Altschäffel, A. Kandratsenka, D. J. Auerbach, C. T. Campbell, D. Schwarzer, D. J. Harding, A. M. Wodtke, *et al.*, "Velocity-resolved kinetics of site-specific carbon monoxide oxidation on platinum surfaces," *Nature*, vol. 558, no. 7709, pp. 280–283, 2018.

[172] H.-J. Krebs and H. Lüth, "Evidence for two different adsorption sites of CO on Pt (111) from infrared reflection spectroscopy," *Applied Physics*, vol. 14, no. 4, pp. 337–342, 1977.

[173] H. Steininger, S. Lehwald, and H. Ibach, "On the adsorption of CO on Pt (111)," *Surface Science*, vol. 123, no. 2-3, pp. 264–282, 1982.

[174] M. Gajdoš, A. Eichler, and J. Hafner, "CO adsorption on close-packed transition and noble metal surfaces: trends from ab initio calculations," *Journal of Physics: Condensed Matter*, vol. 16, no. 8, p. 1141, 2004.

[175] M. Muntwiler, J. Zhang, R. Stania, F. Matsui, P. Oberta, U. Flechsig, L. Patthey, C. Quitmann, T. Glatzel, R. Widmer, *et al.*, "Surface science at the PEARL beamline of the Swiss Light Source," *Journal of Synchrotron Radiation*, vol. 24, no. 1, pp. 354–366, 2017.

[176] J. Biberrian and M. Van Hove, "A new model for CO ordering at high coverages on low index metal surfaces: A correlation between LEED, HREELS and IRS: II. CO adsorbed on fcc (111) and hep (0001) surfaces," *Surface Science*, vol. 138, no. 2-3, pp. 361–389, 1984.

[177] T. D. Thomas, "X-Ray Photoelectron Spectroscopy of Carbon Monoxide," *The Journal of Chemical Physics*, vol. 53, no. 5, pp. 1744–1749, 1970.

[178] T. Yanai, D. P. Tew, and N. C. Handy, "A new hybrid exchange–correlation functional using the Coulomb-attenuating method (CAM-B3LYP)," *Chemical Physics Letters*, vol. 393, no. 1-3, pp. 51–57, 2004.

[179] N. Ueno and S. Kera, "Electron spectroscopy of functional organic thin films: deep insights into valence electronic structure in relation to charge transport property," *Progress in Surface Science*, vol. 83, no. 10-12, pp. 490–557, 2008.

[180] J. Kuügel, M. Karolak, J. Senkpiel, P.-J. Hsu, G. Sangiovanni, and M. Bode, "Relevance of hybridization and filling of 3d orbitals for the Kondo effect in transition metal phthalocyanines," *Nano Letters*, vol. 14, no. 7, pp. 3895–3902, 2014.

[181] M. Wießner, J. Ziroff, F. Forster, M. Arita, K. Shimada, P. Puschnig, A. Schöll, and F. Reinert, "Substrate-mediated band-dispersion of adsorbate molecular states," *Nature Communications*, vol. 4, p. 1514, 2013.

[182] Y. D. Park, J. A. Lim, H. S. Lee, and K. Cho, "Interface engineering in organic transistors," *Materials Today*, vol. 10, no. 3, pp. 46–54, 2007.

[183] L. Vitali, G. Levita, R. Ohmann, A. Comisso, A. De Vita, and K. Kern, "Portrait of the potential barrier at metal–organic nanocontacts," *Nature Materials*, vol. 9, no. 4, pp. 320–323, 2010.

[184] L. Romaner, G. Heimel, J.-L. Brédas, A. Gerlach, F. Schreiber, R. L. Johnson, J. Zegenhagen, S. Duhm, N. Koch, and E. Zojer, "Impact of bidirectional charge transfer and molecular distortions on the electronic structure of a metal-organic

interface," *Physical Review Letters*, vol. 99, no. 25, p. 256801, 2007.

[185] H. Kroemer, "Quasi-Electric Fields and Band Offsets: Teaching Electrons New Tricks (Nobel Lecture)," *ChemPhysChem*, vol. 2, pp. 490–499, 09 2001.

[186] B. Voigtländer, *Scanning probe microscopy: Atomic force microscopy and scanning tunneling microscopy*. Springer, 2015.

[187] J. Stöhr, *NEXAFS spectroscopy*, vol. 25. Springer Science & Business Media, 2013.

[188] D. Woodruff, "Surface structure determination using x-ray standing waves," *Reports on Progress in Physics*, vol. 68, no. 4, p. 743, 2005.

[189] C. C. Mattheus, A. B. Dros, J. Baas, A. Meetsma, J. L. De Boer, and T. T. Palstra, "Polymorphism in pentacene," *Acta Crystallographica Section C: Crystal Structure Communications*, vol. 57, no. 8, pp. 939–941, 2001.

[190] J. Smerdon, M. Bode, N. Guisinger, and J. Guest, "Monolayer and bilayer pentacene on Cu (111)," *Physical Review B*, vol. 84, no. 16, p. 165436, 2011.

[191] Element Collection, Inc, "Lattice Constants of the elements," 2020. Available at `https://periodictable.com/Properties/A/LatticeConstants.html`, last checked on 28.09.2020.

[192] B. Stadtmüller, I. Kröger, F. Reinert, and C. Kumpf, "Submonolayer growth of CuPc on noble metal surfaces," *Physical Review B*, vol. 83, no. 8, p. 085416, 2011.

[193] M. Lee, *Analytical chemistry of polycyclic aromatic compounds*. Elsevier, 2012.

[194] K. Müller, A. Kara, T. K. Kim, R. Bertschinger, A. Scheybal, J. Osterwalder, and T. A. Jung, "Multimorphism in molecular monolayers: Pentacene on Cu (110)," *Physical Review B*, vol. 79, no. 24, p. 245421, 2009.

[195] R. Campbell, J. M. Robertson, and J. Trotter, "The crystal and molecular structure of pentacene," *Acta Crystallographica*, vol. 14, no. 7, pp. 705–711, 1961.

[196] A. G. Lebed, *The physics of organic superconductors and conductors*, vol. 110. Springer, 2008.

[197] V. Čápek and E. A. Silinsh, "Dynamics of electronic polarization in molecular crystals," *Chemical Physics*, vol. 200, no. 3, pp. 309–318, 1995.

[198] D. M. Adams, L. Brus, C. E. Chidsey, S. Creager, C. Creutz, C. R. Kagan, P. V. Kamat, M. Lieberman, S. Lindsay, R. A. Marcus, *et al.*, "Charge transfer on the nanoscale: current status," *The Journal of Physical Chemistry B*, vol. 107, no. 28, pp. 6668–6697, 2003.

[199] M. Graus, M. Grimm, C. Metzger, M. Dauth, C. Tusche, J. Kirschner, S. Kümmel, A. Schöll, and F. Reinert, "Electron-vibration coupling in molecular materials:

assignment of vibronic modes from photoelectron momentum mapping," *Physical Review Letters*, vol. 116, no. 14, p. 147601, 2016.

[200] S. Kera, H. Yamane, and N. Ueno, "First-principles measurements of charge mobility in organic semiconductors: Valence hole–vibration coupling in organic ultrathin films," *Progress in Surface Science*, vol. 84, no. 5-6, pp. 135–154, 2009.

[201] M. Born and R. Oppenheimer, "Zur quantentheorie der molekeln," *Annalen der Physik*, vol. 389, no. 20, pp. 457–484, 1927.

[202] J. Yeh and I. Lindau, "Atomic subshell photoionization cross sections and asymmetry parameters: 1<Z<103," *Atomic Data and Nuclear Data Tables*, vol. 32, no. 1, pp. 1–155, 1985.

[203] H. W. Kroto, J. R. Heath, S. C. O'Brien, R. F. Curl, and R. E. Smalley, "C60: Buckminsterfullerene," *Nature*, vol. 318, no. 6042, p. 162, 1985.

[204] Y. Zhao, Y. Gai, S. Jin, X. Tong, J. Zhang, and E. Yifeng, "Synthesis of C60 Nanorods and Its Application as Glucose Sensors," *Science of Advanced Materials*, vol. 11, no. 4, pp. 502–506, 2019.

[205] Y. Ishikawa, T. Hasegawa, and C. Joachim, "A nano-mechanical device using a Ag2S–C60 system," *Japanese Journal of Applied Physics*, vol. 58, no. SD, p. SDDF02, 2019.

[206] J. L. Segura, N. Martín, and D. M. Guldi, "Materials for organic solar cells: the C60/π-conjugated oligomer approach," *Chemical Society Reviews*, vol. 34, no. 1, pp. 31–47, 2005.

[207] S. Günes, H. Neugebauer, and N. S. Sariciftci, "Conjugated polymer-based organic solar cells," *Chemical Reviews*, vol. 107, no. 4, pp. 1324–1338, 2007.

[208] R. Haddon, A. Perel, R. Morris, T. T. Palstra, A. Hebard, and R. Fleming, "C60 thin film transistors," *Applied Physics Letters*, vol. 67, no. 1, pp. 121–123, 1995.

[209] K. Wojciechowski, T. Leijtens, S. Siprova, C. Schlüter, M. T. Hörantner, J. T.-W. Wang, C.-Z. Li, A. K.-Y. Jen, T.-L. Lee, and H. J. Snaith, "C60 as an efficient n-type compact layer in perovskite solar cells," *The Journal of Physical Chemistry Letters*, vol. 6, no. 12, pp. 2399–2405, 2015.

[210] W. Lv, Y. Liang, Q. Dai, J. Zhou, Z. Zhou, F. Lu, S. Xu, H. Zhang, L. Sun, and Y. Peng, "Influence of C60 acceptor layer position on near infrared photosensitive organic field-effect transistors based on tri-layer planar heterojunction," *Synthetic Metals*, vol. 250, pp. 131–135, 2019.

[211] Y. Xu, M. Tan, and U. Becker, "Oscillations in the photoionization cross section of C60," *Physical Review Letters*, vol. 76, no. 19, p. 3538, 1996.

[212] D. W. Latzke, C. Ojeda-Aristizabal, S. M. Griffin, J. D. Denlinger, J. B. Neaton, A. Zettl, and A. Lanzara, "Observation of highly dispersive bands in pure thin film C60," *Physical Review B*, vol. 99, no. 4, p. 045425, 2019.

[213] E. A. Katz, "Fullerene thin films as photovoltaic material," in *Nanostructured materials for solar energy conversion*, pp. 361–443, Elsevier, 2006.

[214] N. Haag, D. Lüftner, F. Haag, J. Seidel, L. L. Kelly, G. Zamborlini, M. Jugovac, V. Feyer, M. Aeschlimann, P. Puschnig, *et al.*, "Signatures of an atomic crystal in the band structure of a C 60 thin film," *Physical Review B*, vol. 101, no. 16, p. 165422, 2020.

[215] P. A. Heiney, J. E. Fischer, A. R. McGhie, W. J. Romanow, A. M. Denenstein, J. P. McCauley Jr, A. B. Smith, and D. E. Cox, "Orientational ordering transition in solid C60," *Physical Review Letters*, vol. 66, no. 22, p. 2911, 1991.

[216] C. Yannoni, R. Johnson, G. Meijer, D. Bethune, and J. Salem, "Carbon-13 NMR study of the C60 cluster in the solid state: molecular motion and carbon chemical shift anisotropy," *The Journal of Physical Chemistry*, vol. 95, no. 1, pp. 9–10, 1991.

[217] G. Kresse and J. Furthmüller, "Efficiency of ab-initio total energy calculations for metals and semiconductors using a plane-wave basis set," *Computational Materials Science*, vol. 6, pp. 15–20, 1996.

[218] J. Neugebauer and M. Scheffler, "Adsorbate-substarte and adsorbate-adsorbate interactions of Na and K adlayers on Al(111)," *Physical Review B*, vol. 46, pp. 16067–16080, 1992.

[219] J. P. Perdew, K. Burke, and M. Ernzerhof, "Generalized Gradient Approximation Made Simple," *Physical Review Letters*, vol. 77, pp. 3865–3868, 1996.

[220] M. Methfessel and A. T. Paxton, "High-precision sampling for Brillouin-zone integration in metals," *Physical Review B*, vol. 40, pp. 3616–3621, 1989.

[221] G. Kresse and D. Joubert, "From ultrasoft pseudopotentials to the projector augmented-wave method," *Physical Review B*, vol. 59, no. 3, p. 1758, 1999.

[222] A. Tkatchenko and M. Scheffler, "Accurate molecular van der Waals interactions from ground-state electron density and free-atom reference data," *Physical Review Letters*, vol. 102, no. 7, p. 073005, 2009.

[223] G. Luengo, S. E. Campbell, V. I. Srdanov, F. Wudl, and J. N. Israelachvili, "Direct measurement of the adhesion and friction of smooth C60 surfaces," *Chemistry of Materials*, vol. 9, no. 5, pp. 1166–1171, 1997.

[224] E. Carpene, E. Mancini, C. Dallera, G. Ghiringhelli, C. Manzoni, G. Cerullo, and S. De Silvestri, "A versatile apparatus for time-resolved photoemission spectroscopy

via femtosecond pump-probe experiments," *Review of Scientific Instruments*, vol. 80, no. 5, p. 055101, 2009.

[225] J. Zirzlmeier, D. Lehnherr, P. B. Coto, E. T. Chernick, R. Casillas, B. S. Basel, M. Thoss, R. R. Tykwinski, and D. M. Guldi, "Singlet fission in pentacene dimers," *Proceedings of the National Academy of Sciences*, vol. 112, no. 17, pp. 5325–5330, 2015.

[226] K. Broch, J. Dieterle, F. Branchi, N. Hestand, Y. Olivier, H. Tamura, C. Cruz, V. Nichols, A. Hinderhofer, D. Beljonne, *et al.*, "Robust singlet fission in pentacene thin films with tuned charge transfer interactions," *Nature Communications*, vol. 9, no. 1, pp. 1–9, 2018.

[227] F. G. de Abajo, M. Van Hove, and C. Fadley, "Multiple scattering of electrons in solids and molecules: A cluster-model approach," *Physical Review B*, vol. 63, no. 7, p. 075404, 2001.

Own Publications

M. Scholz, K. Baumgärtner, **C. Metzger**, D. Kutnyakhov, M. Heber, C.H. Min, T.R.F. Peixoto, M. Reiser, C. Kim, W. Lu, W. M. Izquierdo, F. Roth, F. Pressacco, A. Schöll, S. Molodtsov, W. Wurth, F. Reinert, and A. Madsen, "Ultrafast molecular orbital tomography of a pentacene thin film using time-resolved momentum microscopy at a free-electron laser", *Nature Communications*, under review.

P. Kretz, K. Waltar, Y. Geng, **C. Metzger**, M. Graus, A. Schöll, F. Reinert, S. Liu, S. Decurtins, M. Hengsberger, J. Osterwalder, and L. Castiglioni, "Adsorption geometry and electronic structure of a charge-transfer-complex: TTF-PYZ2 on Ag(110)", *New Journal of Physics*, vol. 23, no. 1, p. 013002, 2021.

C. Metzger, M. Graus, M. Grimm, G. Zamborlini, V. Feyer, M. Schwendt, D. Lüftner, P. Puschnig, A. Schöll, and F. Reinert, "The plane-wave final state for photoemission from nonplanar molecules at the metal-organic interface", *Physical Review B*, vol. 101, no. 16, p. 165421, 2020.

M. Graus, **C. Metzger**, M. Grimm, P. Nigge, V. Feyer, A. Schöll, and F. Reinert, "Three-dimensional Tomographic Imaging of Molecular Orbitals by Photoelectron Momentum Microscopy", *The European Physical Journal B*, vol. 92, no. 4, p. 80, 2019.

M. Grimm, **C. Metzger**, M. Graus, M. Jugovac, G. Zamborlini, V. Feyer, A. Schöll, and F. Reinert, "Molecular orbital imaging beyond the first monolayer: Insights into the pentacene/Ag(110) interface", *Physical Review B*, vol. 98, no. 19, p. 195412, 2018.

P. Kliuiev, T. Latychevskaia, G. Zamborlini, M. Jugovac, **C. Metzger**, M. Grimm, A. Schöll, J. Osterwalder, M. Hengsberger, L. Castiglioni, "Algorithms and image formation in orbital tomography", *Physical Review B*, vol. 98, no. 8, p. 085426, 2018.

M. Graus, **C. Metzger**, M. Grimm, V. Feyer, P. Puschnig, A. Schöll, F. Reinert, "Degeneracy lifting of adsorbate orbitals imaged by high-resolution momentum microscopy", *Journal of the Physical Society of Japan*, vol. 187, no. 6, p. 0601009, 2018.

M. Graus, M. Grimm, **C. Metzger**, M. Dauth, C. Tusche, J. Kirschner, S. Kümmel, A. Schöll, F. Reinert, "Electron-Vibration coupling in molecular materials: Assignment of vibronic modes from photoelectron momentum mapping", *Physical Review Letters*, vol.

116, no. 14, p. 147601, 2016.

Acknowledgement

First of all I would like to thank the supervisor of my thesis, PD Dr. Achim Schöll. He always provided me with direction, but still managed to leave me with plenty of freedom to pursue whatever I was most interested in. He was never discouraged even when my venture into theory and programming sidetracked other projects and produced no tangible results while I learned the ropes. His close supervision and the weekly groups meetings fostered a perfect work environment in our small group.

Thank You also to Prof. Friedrich Reinert for his support and advice as well as the opportunity to be a part of his chair. His broad expertise in all things photoemission and beyond along with his open door policy were greatly appreciated. Besides physics, I remember many intriguing conversations about politics and music during lunch and coffee breaks that I often continued to mull over long after.

I am grateful to Prof. Bert Hecht for taking over the second report on my thesis without hesitation despite his busy schedule. His own research and knowledge on organic materials made him an obvious choice as a second reviewer.

I would also like to thank my colleagues in the organic part of the group with whom I spent the majority of my time at the university:
Dr. Martin Graus for the entertaining beamtimes in Trieste and Halle plus the many, many engaging conversations we had on all kinds of topics over the years. No matter how absurd or ridiculous a question was, he never once failed to entertain it and provide profound and amusing insights. A great deal of the understanding of molecular physics and photoemission that I have today is the result of his input. Dr. Manuel Grimm with whom I had several great beamtimes in Trieste, Halle and Didcot. His experimental work on pentacene bilayers made the project a success and the help besides the work place was always appreciated. Kiana Baumgärtner for the great teamwork that propelled past and upcoming projects forward and the awesome time both in and out of work. The atmosphere in the office was simply amazing and just like the beamtimes in Hamburg a genuine delight. An additional thanks for reading and suggesting corrections on a draft of this thesis. I also express my gratitude to my outstanding bachelor student Julian Wienand

for the insightful physical discussions and uncomplicated work together in the lab.

I am very grateful to all coworkers and secretaries at the Experimentelle Physik 7 that I did not mention by name, but made the time spent at the university a pleasure. Most days were so enjoyable that they did not feel like work at all. A special thanks to Dr. Sebastian Fiedler who got me acquainted with working in an UHV lab and was determined to make sure that I would not turn out to be a "Pfuscher". His bleak and pessimistic outlook on life left a lasting mark towards the opposite on me.

The success of this thesis also hinged on the input from many collaboration partners outside of Würzburg that I am happy to acknowledge:
Prof. Satoshi Kera, Dr. Matthias Meissner and Dr. Keiichirou Yonezawa from the Institute for Molecular Science in Okazaki for the fruitful and extremely friendly collaboration. A personal Thank You to Satoshi for suggesting the subsequently successful application for a JSPS scholarship that allowed me to spend a fascinating summer in Okazaki.
Dr. Markus Scholz from the European XFEL in Schenefeld for the very close and amiable collaboration on time-dependent photoemission projects as well as insider advice on a career as a scientist.
Dr. Luca Castiglioni, Dr. Pavlo Kliuiev and Dr. Kay Waltar from the Osterwalder Group at the University of Zürich for the collaboration on both experimental and theoretical issues. I am particularly grateful for the numerous ideas in both physics and everyday life that I have picked up from Luca.
Prof. Peter Puschnig, Dr. Daniel Lüftner and Mathias Schwendt from the Institut für Physik at the University of Graz for the fruitful cooperation and the warm welcome in Graz.
Dr. Vitaliy Feyer and Dr. Giovanni Zamborlini from the NanoESCA beamline at the ELETTRA synchrotron in Trieste for their tireless support during our beamtimes there.
Prof. Kaori Niki and Dr. Naoki Komiya from the Department of Chemistry at Chiba University and Prof. Peter Krüger from the Department of Materials Science at Chiba University for their help in understanding the photoemission theory behind the program I wanted to design.
Prof. Torsten Fritz und Maximilian Schaal from the Institut für Festkörperphysik at the University of Jena for the warm welcome in Jena and the great time in Japan.

Lastly a heartfelt Thank You to my family and friends for their personal support in a multitude of ways that I could always count on.